From Serendipity to the Rational Design of Protein–Protein Interface Modulators Targeting a tRNA-Modifying Enzyme

Dissertation

zur
Erlangung des Doktorgrades
der Naturwissenschaften
(Dr. rer. nat.)

dem
Fachbereich Pharmazie der
Philipps-Universität Marburg
vorgelegt von

Dzung Nguyen

aus
Sangerhausen

Marburg, 2021

Die Untersuchungen zur vorliegenden Arbeit wurden in der Zeit von April 2017 bis November 2020 unter der Leitung von Herrn Prof. Dr. Gerhard Klebe am Institut für Pharmazeutische Chemie des Fachbereichs Pharmazie der Philipps-Universität Marburg angefertigt.

Erstgutachter: Prof. Dr. Gerhard Klebe
Institut für Pharmazeutische Chemie
Philipps-Universität Marburg

Zweitgutachter: Prof. Dr. Klaus Reuter
Institut für Pharmazeutische Chemie
Philipps-Universität Marburg

Eingereicht am: 27. November 2020
Tag der mündlichen Prüfung: 15. Januar 2021
Hochschulkennziffer: 1180

cc BY NC ND

Für meine Ma
Cho mẹ con

Danksagung

Auf diesen Seiten möchte ich meine Dankbarkeit gegenüber wichtigen Menschen zum Ausdruck bringen, denn ohne sie wäre die vorliegende Arbeit nicht möglich gewesen. An oberster Stelle möchte ich mich bei Prof. Dr. **Gerhard Klebe** für die Betreuung und große Unterstützung während meiner Promotion bedanken. Sie haben Ihr umfangreiches Wissen mit mir geteilt und immer Vertrauen in meine Ideen gehabt, was ich besonders schätze. Ich hätte mir keinen besseren Betreuer für diese Arbeit vorstellen können.

Ich danke Prof. Dr. **Klaus Reuter** für die Übernahme des Zweitgutachtens sowie für das Teilen seiner langjährigen Expertise bezüglich der TGT und jeglichen biologischen Fragestellungen. Prof. Dr. **Andreas Heine** danke ich für die Einweisung in die Proteinkristallographie sowie für die Hilfe bei allen kristallographischen Herausforderungen. Weiterhin danke ich **Lydia Hartleben**, **Hans-Dieter Gerber**, **Stefanie Dörr**, **Christian Sohn**, **Frank Balzer**, **Victor Lim**, Dr. **Tobias Hüfner** und Dr. **Alexander Metz** für ihre Hilfe bei allen administrativen und technischen Fällen sowie für die Instandhaltung der Labore und Computerserver.

Ebenfalls bedanken möchte ich mich bei allen Mitgliedern der **AG Klebe** für die stets angenehme Arbeitsatmosphäre. Spezieller Dank gilt hierbei meinen Vorgängern Dr. **Frederik Ehrmann** und **Phong Nguyen** für die damalige Einführung in das molekularbiologische Arbeiten sowie in das TGT-Projekt. Besonders bedanken möchte ich mich bei meinem langjährigen TGT-Kollegen und Co-Sensei unseres Nguyen-Dojos Dr. **Andreas „Andy“ Nguyen** für die vielen Gespräche, die zu produktiven Ideen und Inputs bezüglich unserer Projekte geführt haben und durch die wir beide wachsen konnten. Die gemeinsame Zeit im Büro 02A14 sowie die weiten Reisen werden mir stets in Erinnerung bleiben. Zudem möchte ich mich meinen Praktikanten und Praktikantinnen, **Jessica Pilgram**, **Rebecca Feyh**, **Sandrine Ngaha**, **Shaochen You**, **Peihong Luo**, **Mujia „Jenny“ Li** und **Raquel „Rocky“ Reilly**, für ihre tatkräftige Unterstützung bei den Projekten bedanken.

Ein außerordentlicher Dank gilt unseren Kollaborationspartnern, die mir gezeigt haben, dass eine gute wissenschaftliche Partnerschaft der Schlüssel ist, um ehrgeizige Forschungsziele zu erreichen und ohne die kein Projekt in dieser Arbeit realisierbar gewesen wäre. Vorausgehend danke ich unseren langjährigen Partnern der Arbeitsgruppe von Prof. Dr. **François Diederich**, insbesondere Dr. **Toni Pfaffeneder**, Dr. **Luzi Barandun**, Dr. **Christoph Hohn**, Dr. **Levon Movsisyan** und **Jorna Kalim**, für die hochaufwendige Synthese der zahlreichen TGT-Inhibitoren. Für die gemeinsame Arbeit am *Twisted Dimer*-Projekt, die dazugehörigen zahlreichen Experimente und für die tolle Gastfreundschaft danke ich im großen Maße den EPR-Experten Dr. **Dinar Abdullin**, **Caspar Heubach** und Prof. Dr. **Olav Schiemann** von der Rheinischen Friedrich-Wilhelms-Universität Bonn.

Für die Arbeit am *Covalent Dimer*-Projekt danke ich besonders Dr. **Xiulan Xie** für die essentiellen NMR-Messungen und ebenso für die angenehmen Teestunden und gemeinsamen Gespräche. Für die Hilfe zu den Berechnungen der Solvenskanälen danke ich **Katharina Holzapfel** und Dr. **Serghei Glinca** (CrystalsFirst). Zudem danke ich herzlich Dr. **Vitalii Palchykov** von der University of Texas at Dallas für die Bereitstellung neuer Proben. Ein großer Dank geht auch an **Lea Albert**, **Van Tuan „Marco“ Trinh** und Prof. Dr. **Olalla Vázquez** vom Fachbereich Chemie sowie an **Thuy Van Lam van** und Prof. Dr. **Torsten Steinmetzer** vom Institut für Pharmazeutische Chemie der Philipps-Universität Marburg für ihr Vertrauen und ihre Expertise im *Interface Peptides*-Projekt. Ebenfalls innerhalb dieses Projektes danke ich Dr. **Khang Ngo** und Dr. **Steffen Glöckner** für die Einführung in die ITC sowie Dr. **Andreas Langer** und Dr. **Franziska Tippel** (NanoTemper Technologies) für das Messen unserer Proben und das tolle MST-Training. Für die Einweisung in das Arbeiten im S2-Labor am Biomedizinischen Forschungszentrum und für die große Unterstützung beim *Shigella*-Invasionsassay möchte ich mich bei Dr. **Harshavardhan „Harsha“ Janga** und Prof. Dr. **Leon Schulte** vom Institut für Lungenforschung bedanken. Weiterhin danke ich **Ralf Pöschke** für die Hilfe beim Aufsetzen des Kristallisationsscreens am MarXtal sowie dem Service-Team der Massenabteilung um Dr. **Uwe Linne** für die massenspektrometrischen Messungen zahlreicher Proteinproben.

Von ganzem Herzen danke ich meinen Freunden, besonders **Michael „Micha“ Nguyen**, **Odysseas „Ody“ Anastasiadis**, **Samuel „Sam“ Jäger**, **Suat Chousein** und **Yasin Kelleci** für die einzigartigen gemeinsamen Jahre in Marburg. Selbst in den kritischsten Zeiten, konnten wir aufeinander zählen, uns gegenseitig aufbauen, über viele Dinge lachen und zusammen wachsen. Danke, dass ihr mir gezeigt habt, wie wichtig das Leben außerhalb der Universität ist.

Weiterhin danke ich **Ody**, **Rocky**, **Xiulan** und **Andy**, für ihre investierte Mühe und Zeit für das Lesen der ersten Entwürfe dieser Arbeit und vor allem für die wertvollen Tipps wie man die Arbeit noch besser aussehen lassen kann.

Ein ganz besonderer Dank geht an meine wundervolle **Ma** und meinen kleinen Schwestern **Emily** und **Elisa**. Ohne eure unermüdliche Unterstützung wären das gesamte Studium und vieles andere nicht möglich gewesen.

Zum Schluss möchte mich bei meiner besseren Hälfte, **Eleen Birnschein**, bedanken. Und zwar für all die schönen Erinnerungen, die wir bisher zusammen erleben durften und auch dafür, dass du mich durch die harten Phasen des Lebens geleitet. Dank dir bin ich der Mensch, der ich heute bin, und ich freue mich auf die Momente, die noch vor uns stehen.

Aus dieser Dissertation hervorgegangene Publikationen und Konferenzbeiträge

Titel der Publikation und Journal	**Autoren**
The Importance of Charge in Perturbing the Aromatic Glue Stabilizing the Protein–Protein Interface of Homodimeric tRNA-Guanine Transglycosylase *ACS Chemical Biology* **2020**, *15*, 3021–3029. *bioRxiv* **2020**, DOI: 10.1101/2020.09.01.277731v1.	A. Nguyen*, **D. Nguyen***, T. X. P. Nguyen, M. Sebastiani, S. Dörr, O. Hernandez-Alba, F. Debaene, S. Cianférani, G. Klebe, A. Heine, K. Reuter
Unraveling a Ligand-Induced Twist of a Homodimeric Enzyme by Pulsed Electron–Electron Double Resonance (Manuskript in Bearbeitung)	D. Abdullin*, **D. Nguyen***, A. Nguyen, T. Pfaffeneder, A. Heine, F. Diederich, O. Schiemann, G. Klebe
Targeting a Transient Binding Pocket by Disulfide-Induced Break-Up of the Homodimeric TGT Interface (Manuskript in Bearbeitung)	**D. Nguyen***, X. Xie, S. Jakobi, A. Nguyen, T. X. P. Nguyen, F. Terwesten, A. Heine, K. Reuter, G. Klebe

* Diese Autoren haben einen gleichwertigen Beitrag geleistet.

Titel des Vortrages (V) oder Posters (P) und Angaben zur Konferenz	**Autoren**
P: Design of Carbamate-protected *lin*-Benzoguanines as Prodrug Candidates against *Shigella* Infections *Frontiers in Medicinal Chemistry* **2020**, Freiburg, Deutschland (abgesagt wegen COVID-19)	**D. Nguyen**, F. R. Ehrmann, C. Hohn, V. Micallef, H. Janga, L. N. Schulte, K. Reuter, F. Diederich, G. Klebe
V+P: Uncovering a Ligand-induced Twisted State of a Homodimeric Enzyme by Pulsed Electron-Electron Double Resonance *Biophysics in Drug Discovery – 7th NovAliX Conference Asian Edition* **2019**, Kyōto, Japan	**D. Nguyen**, A. Nguyen, D. Abdullin, F. R. Ehrmann, T. Pfaffeneder, J. Kalim, L. J. Barandun, F. Diederich, O. Schiemann, G. Klebe
P: ^{19}F NMR Unveils Conformational Changes at Homodimer Contacts of tRNA-Guanine Transglycosylase *Biophysics in Drug Discovery – 7th NovAliX Conference Asian Edition* **2019**, Kyōto, Japan	A. Nguyen, **D. Nguyen**, G. Gemmecker, F. R. Ehrmann, J. Kalim, T. Pfaffeneder, L. J. Barandun, F. Diederich, M. Sattler, G. Klebe
V: Exploring a Transient Binding Pocket at the Dimerization Interface of TGT *Tongji / UMR Scientific Symposium* **2018**, Shanghai, China	**D. Nguyen**, A. Nguyen, T. X. P. Nguyen, S. Jakobi, F. Terwesten, G. Klebe
V+P: Towards a Novel Inhibitory Mechanism of tRNA-Guanine Transglycosylase *Tongji / UMR Interdisciplinary Summer School* **2017**, Marburg, Deutschland	**D. Nguyen**, A. Nguyen, L. Movsisyan, F. R. Ehrmann, F. Immekus, L. J. Barandun, F. Diederich, G. Klebe

Contents

Abstract V

Kurzfassung VI

List of Abbreviations and Acronyms IX

List of Units, Variables and Constants XIII

Amino Acids XV

List of Figures XVII

List of Tables XXI

1 General Introduction 1
- 1.1 Serendipity in Drug Discovery . . . 1
- 1.2 tRNA-Guanine Transglycosylase as a Shigellosis Target . . . 2
  - 1.2.1 Role of TGT in *Shigella* pathogenesis . . . 2
  - 1.2.2 Structure of TGT and the TGT–tRNA complex . . . 4
  - 1.2.3 Mechanism of the nucleobase exchange catalyzed by TGT . . . 5
- 1.3 Structure-based Design of TGT Inhibitors . . . 7
  - 1.3.1 Competitive inhibition by active-site blocking . . . 7
  - 1.3.2 Design of spiking ligands for homodimer destabilization . . . 8
  - 1.3.3 Fragment-based screening for the discovery of new hit compounds . . . 9
- 1.4 Thesis Outline . . . 10

2 Unraveling the Ligand-Induced Twist of Homodimeric TGT by PELDOR 11
- 2.1 Introduction . . . 11
  - 2.1.1 Discovery of the twisted TGT homodimer . . . 12
  - 2.1.2 Nanometer distance measurements via EPR and PELDOR spectroscopy . . . 13
- 2.2 Results and Discussion . . . 14
  - 2.2.1 Preface . . . 14

2.2.2 Search for the best spin labeling positions in TGT 15
2.2.3 Biophysical characterization of spin-labeled TGT variants 15
2.2.4 Assignment of PELDOR distance distributions 17
2.2.5 Ligand-dependent formation of the twisted dimer 20
2.2.6 PELDOR measurements in dependence of incubation time 22
2.2.7 Orthogonal spin labeling and mixing experiments for the elucidation of the twisting mechanism 22
2.3 Conclusion 24
2.4 Experimental Section 26
2.4.1 Mutagenesis and recombinant production of *Z. mobilis* TGT 26
2.4.2 Spin labeling of TGT variants 27
2.4.3 Crystallization and structure determination 29
2.4.4 Analytical gel filtration 29
2.4.5 Preparation of tRNA^{Tyr} 29
2.4.6 PELDOR spectroscopy and data analysis 31

3 Disulfide-Induced Break-Up of the Homodimeric TGT Interface 37
3.1 Introduction 37
3.1.1 Discovery of a pseudomonomeric TGT variant 38
3.1.2 Druggability of the β1α1-loop 39
3.2 Results and Discussion 41
3.2.1 Preface 41
3.2.2 Design and characterization of a stabilized disulfide-linked TGT variant . 41
3.2.3 Soaking of sulfoxide fragments 44
3.2.4 Solvent channel and soakability analysis 46
3.2.5 Soaking of sulfone fragments 49
3.2.6 Soaking of cyclic diols and other sulfolane derivatives 52
3.2.7 ^{19}F NMR experiments 55
3.2.8 PFG diffusion studies 60
3.3 Conclusion 65
3.4 Experimental Section 67
3.4.1 Mutagenesis and recombinant production of *Z. mobilis* TGT 67
3.4.2 Crystallization and fragment soaking 68
3.4.3 Data collection and structure determination 69
3.4.4 Analytical gel filtration 69
3.4.5 Thermal shift assay 72
3.4.6 NMR spectroscopy 72
3.4.7 List of investigated compounds 80

4 Disrupting the Bacterial TGT Homodimer with Interface-Derived Peptides 83
4.1 Introduction . . . 83
4.1.1 Peptides as homodimer disruptors . . . 84
4.1.2 Discovery of an interface target site in homodimeric TGT occupied by structural peptide motifs . . . 84
4.2 Results and Discussion . . . 85
4.2.1 Preface . . . 85
4.2.2 Epitope mapping and peptide design using peptide microarrays . . . 86
4.2.3 Peptide binding by fluorescence polarization . . . 87
4.2.4 Crystallization trials and characterization of $\mathrm{TGT}^{\mathrm{Y330D}}$ . . . 99
4.2.5 Assessment of TGT dimerization constants . . . 101
4.2.6 Development of a *Shigella* host cell invasion assay . . . 105
4.3 Conclusion . . . 107
4.4 Experimental Section . . . 108
4.4.1 Preparation of *Z. mobilis* TGT . . . 108
4.4.2 Crystallization and structure determination . . . 109
4.4.3 Preparation of $\mathrm{tRNA}^{\mathrm{Tyr}}$ . . . 109
4.4.4 Enzyme kinetic characterization . . . 113
4.4.5 Analytical gel filtration . . . 113
4.4.6 Peptide microarray . . . 113
4.4.7 Fluorescence polarization . . . 116
4.4.8 Isothermal dilution calorimetry . . . 116
4.4.9 Thermal shift assay . . . 116
4.4.10 MicroScale thermophoresis . . . 117
4.4.11 *Shigella* host cell invasion . . . 118
4.4.12 Flow cytometry . . . 119

Bibliography 121

Appendix A Construct Summary 131

Appendix B Materials 133

Appendix D Erklärung gemäß § 10 Abs. 1 der Promotionsordnung 137

Abstract

Serendipity has played a historically significant role in science and especially in the discovery of new drugs. Chance discoveries have led to important drug developments that characterize the pharmaceutical industry and our current health care system. Over the last decades, the concept of rational drug design has developed into one of the key approaches to the research of new and specific drugs. Nevertheless, the development of inhibitors for protein–protein interactions, especially oligomeric protein contact surfaces, remains challenging. The bacterial enzyme, tRNA-guanine transglycosylase (TGT), is an example of a homodimer protein and serves as model target protein in this work. This thesis summarizes three projects that were created from serendipitous discoveries of previous studies to develop new approaches for the modulation of the TGT homodimer interface and thus lay out the basis for alternative inhibition pathways in oligomeric enzymes.

A previous crystallographic study of TGT–inhibitor complexes revealed an unexpected, twisted arrangement of the TGT homodimer. However, data from the obtained X-ray crystal structures can neither exclude crystallographic artifacts resulting from crystal packing forces nor study the transition between the two dimeric end states. Therefore, a method based on electron paramagnetic resonance (EPR) was established to study this ligand-induced rearrangement mechanism of the TGT homodimer in a solution equilibrium (Chapter 2). For this purpose, paramagnetic spin markers were introduced via site-directed cysteine mutations on the protein surface. The following pulsed EPR techniques enabled the observation of inter-spin distance distributions within the TGT homodimer. During the study, a pyranose-substituted *lin*-benzoguanine inhibitor was identified to be superior in transforming the functional TGT dimer to its twisted state. Thus, the developed method can be used to distinguish between the functional and twisted TGT dimer species upon ligand addition in a solution equilibrium.

A second project comprises the search of small molecule fragments that target a newly discovered transient binding pocket at the homodimer interface of TGT (Chapter 3). In an earlier mutational study, a new crystal form of the TGT dimer was discovered, in which the two protomers are covalently linked by an introduced disulfide bridge. This arrangement breaks up the original dimer interface and exposes a small hydrophobic binding pocket through an extended movement of the nearby β1α1-loop motif. Surprisingly, the newly formed pocket was occupied by a dimethyl sulfoxide molecule. In this work, a further stabilized variant of the disulfide-linked dimer was designed for subsequent fragment soaking studies to target the interface binding pocket.

In the course of the soaking experiments, the solvent channels of the covalently linked TGT dimer were analyzed *in silico* to estimate the putative cutoff radii of small molecules that are capable of freely traversing through the protein crystal. The structural characterization of initial fragment hits led to the rational design of compounds with optimized functionalities which are able to modulate the β1α1-loop. Furthermore, fragment binding studies were attempted by nuclear magnetic resonance (NMR) techniques. Although no binding could be detected using a ^{19}F-based method, the binding constants of two fragments were successfully estimated in the micromolar range using diffusion-ordered spectroscopy (DOSY). While DOSY provides binding data on two of the investigated fragments, structure determination by X-ray crystallography combined with soaking experiments proves to be superior in the identification of fragment binding events. This study highlights the difficulties in characterizing weak binders to a transient interface pocket within the TGT homodimer.

The last project initiated the design of peptide-based modulators derived from the interface of the TGT homodimer (Chapter 4). The idea for this approach was inspired by a crystal structure from the second project in which N-terminal residues of TGT, which were usually ill-defined in the electron density, were structurally resolved and stabilized by the exposed dimer contact surface of a crystallographic symmetry mate. In the functional dimer, the position of this particular N-terminal tail is occupied by helix αE, which contains two aromatic residues of the dimer-stabilizing hot spot. This served as a starting point for the development of helical peptides, that are capable to compete with the native dimer partner at the contact surface. A peptide microarray was used to determine the binding epitope to TGT. Subsequently, the most promising peptides were synthesized and characterized with respect to their binding properties by fluorescence polarization. An optimization approach by peptide stapling was attempted. In order to determine the modulation of TGT dimerization, two biophysical assays each based on MicroScale thermophoresis and isothermal titration calorimetry were developed to track changes in the dimerization constants of TGT. Furthermore, a *Shigella* host cell invasion assay was established to investigate the invasion pathogenicity of a *Shigella flexneri* Δ*tgt* mutant strain. Henceforth, the established *in vitro* assays can be further used to characterize potential peptides and drug candidates for TGT inhibition.

In conclusion, serendipitous discoveries served as a foundation for the projects discussed in this thesis. It was demonstrated that accidental findings in basic research can be used and acted upon to uncover novel mechanisms of action or for the design of new small molecule fragments and peptides as starting points with the common goal of modulating challenging protein–protein interactions.

Kurzfassung

Der Begriff der Serendipität spielt in der Wissenschaft und insbesondere bei der Entdeckung neuer Medikamente eine historisch bedeutsame Rolle. So führten Zufallsentdeckungen zu wichtigen Arzneimittelentwicklungen, die die pharmazeutische Industrie sowie unser heutiges Gesundheitssystem prägen. In den letzten Jahrzehnten entwickelte sich das rationale Wirkstoffdesign zu einem der Schlüsselansätze zur Erforschung neuer und spezifischer Arzneistoffe. Dennoch stellt die Inhibitorentwicklung für Protein–Protein-Interaktionen, insbesondere von oligomeren Proteinkontaktflächen, eine besondere Herausforderung dar. Das bakterielle Enzym, tRNA-Guanin-Transglycosylase (TGT), ist ein Beispiel für ein homodimeres Protein und dient in dieser Arbeit als Modell-Zielprotein. Diese Arbeit fasst drei Projekte zusammen, die aus zufälligen Entdeckungen früherer Studien entstanden sind, um neue Ansätze für die Modulation der Homodimerkontaktfläche von TGT zu entwickeln und damit die Grundlage für alternative Inhibitionswege in oligomeren Enzymen zu legen.

Eine frühere kristallographische Studie von TGT–Inhibitor-Komplexen enthüllte eine unerwartete, verdrehte Anordnung des TGT-Homodimers. Die gewonnenen Informationen aus den Röntgenkristallstrukturen können jedoch weder kristallographische Artefakte von Kristallpackungskräften ausschließen noch den Übergang zwischen den beiden dimeren Endzuständen aufklären. Daher wurde eine auf der Elektronenspinresonanz (EPR) basierende Methode etabliert, um diesen liganden-induzierten Umlagerungsmechanismus des TGT-Homodimers in Lösung zu untersuchen (Kapitel 2). Zu diesem Zweck wurden paramagnetische Spinmarker über ortsgerichtete Cystein-Mutationen auf der Proteinoberfläche eingeführt. Die folgenden gepulsten EPR-Techniken ermöglichten die Beobachtung von Inter-Spin-Abstandsverteilungen innerhalb des Homodimers. Während der Studie wurde ein Pyranose-substituierter *lin*-Benzoguanin-Inhibitor als bester Ligand für die Umwandlung des funktionalen TGT-Dimers in seinen verdrehten Zustand identifiziert. Somit kann die entwickelte Methode zur Differenzierung zwischen der funktionalen und verdrehten TGT-Dimerspezies bei Zugabe von Liganden im Lösungsgleichgewicht eingesetzt werden.

Ein zweites Projekt umfasst die Suche nach kleinen Molekülfragmenten, die auf eine neu entdeckte transiente Bindungstasche in der Homodimerkontaktfläche von TGT abzielen (Kapitel 3). In einer früheren Mutationsstudie wurde eine neue Kristallform des TGT-Dimers entdeckt, in der die beiden Protomere durch eine eingeführte Disulfidbrücke kovalent miteinander verknüpft sind. Diese Anordnung bricht die ursprüngliche Dimerkontaktfläche auf und legt eine kleine hydrophobe Bindetasche durch eine Konformationsänderung der nahegelegenen β1α1-Schleife frei.

Überraschenderweise war die neu gebildete Tasche von einem Dimethylsulfoxid-Molekül besetzt. In dieser Arbeit wurde eine weitere stabilisierte Variante des Disulfid-gebundenen Dimers für nachfolgende Fragment-*Soaking*-Studien entworfen, um die neue Bindungstasche zu adressieren. Im Verlauf der *Soaking*-Experimente wurden die Solvenskanäle des kovalent verknüpften TGT-Dimers *in silico* analysiert, um die mutmaßlichen Cutoff-Radien kleiner Moleküle abzuschätzen, die in der Lage sind, frei durch den Proteinkristall zu diffundieren. Die strukturelle Charakterisierung der ersten Hits führte zum rationalen Design von Fragmenten mit optimierten Funktionalitäten, die in der Lage sind, die β1α1-Schleife zu modulieren. Darüber hinaus wurden Bindungsstudien mittels magnetischer Kernspinresonanz (NMR)-Techniken durchgeführt. Obwohl mit einer ^{19}F-basierten Methode keine Bindung nachgewiesen werden konnte, wurden die Bindungskonstanten zweier Fragmente mit Hilfe der diffusionsgeordneten Spektroskopie (DOSY) erfolgreich im mikromolaren Bereich abgeschätzt. Während DOSY für zwei der untersuchten Fragmente Bindungsdaten liefert, erweist sich die Röntgenkristallstrukturbestimmung in Kombination mit *Soaking*-Experimenten als überlegen bei der Identifizierung von Bindungsereignissen von Fragmenten mit niedriger Affinität. Diese Studie verdeutlicht die Herausforderung bei der Charakterisierung schwacher Binder an einer transienten Bindetasche innerhalb des TGT-Homodimers.

Das letzte Projekt initiierte das Design von peptidbasierten Modulatoren, die von der Kontaktfläche des TGT-Dimers abgeleitet wurden (Kapitel 4). Die Idee für diesen Ansatz wurde durch eine Kristallstruktur aus dem zweiten Projekt inspiriert, in der N-terminale Aminosäuren, die zuvor undefiniert in der Elektronendichte vorlagen, durch die exponierte Dimerkontaktfläche eines kristallographischen Symmetriepartners strukturell aufgelöst und stabilisiert wurden. Im funktionalen Dimer wird die Position dieses N-terminalen Anhangs von Helix αE eingenommen, die zwei aromatische Reste des dimerstabilisierenden Hotspots enthält. Dies diente als Ausgangspunkt für die Entwicklung von helikalen Peptiden, die in der Lage sind, mit dem nativen Dimerpartner an der Kontaktfläche zu konkurrieren. Zur Bestimmung des Bindungsepitops an der TGT wurde ein Peptid-Microarray verwendet. Anschließend wurden die vielversprechendsten Peptide synthetisiert und durch Fluoreszenzpolarisation in ihrem Bindungsverhalten charakterisiert. Ein Optimierungsansatz wurde durch konformative Peptidzyklisierung unternommen. Um die Modulation der TGT-Dimerisierung zu untersuchen, wurden zwei biophysikalische, jeweils auf *MicroScale*-Thermophorese und isothermale Titrationskalorimetrie basierende, Assays entwickelt mit denen Änderungen in den Dimerisierungskonstanten verfolgt werden konnten. Darüber hinaus wurde ein *Shigella*-Wirtszellinvasionsassay etabliert, um die Pathogenität zweier *Shigella flexneri*-Stämme zu untersuchen. In Zukunft können die etablierten *in-vitro*-Assays verwendet werden, um Peptide und Wirkstoffkandidaten für die TGT-Inhibition zu testen.

Zusammenfassend kann gesagt werden, dass Serendipität als Grundlage für die in dieser Arbeit diskutierten Projekte diente. Es konnte gezeigt werden, dass zufällige Entdeckungen aus der Grundlagenforschung genutzt und umgesetzt werden können, um neue Wirkmechanismen aufzudecken oder um neue kleine Molekülfragmente und Peptide als Ausgangspunkt für das gemeinsame Ziel der Modulation herausfordernder Protein–Protein-Interaktionen zu entwerfen.

List of Abbreviations and Acronyms

Ac	acetyl group
Ahx	6-aminohexanoic acid
Amp	ampicillin
aPP	avian pancreatic polypeptide
ATAD2	ATPase family, AAA domain containing 2
BESSY	Berlin Electron Storage Ring Society for Synchrotron Radiation (German: *Berliner Elektronenspeicherring-Gesellschaft für Synchrotronstrahlung*)
Bn	benzyl group
BSA	bovine serum albumin
ca.	approximately (lat. *circa*)
Caco-2	Caucasian colon adenocarcinoma 2
Cam	chloramphenicol
CD	circular dichroism
CK2β	casein kinase 2 subunit β
CO_2	carbon dioxide
CPP	cell-penetrating peptide
CR	Congo red
cryo-EM	cryo-electron microscopy
ctrl	control
CW	continuous wave
D_2O	deuterium oxide
ddH_2O	double-distilled water
DESY	German Electron Synchrotron (German: *Deutsches Elektronen-Synchrotron*)
DMF	dimethylformamide
DMSO	dimethylsulfoxide
DNA	deoxyribonucleic acid
DOI	digital object identifier
DOSY	diffusion-ordered spectroscopy
DTT	dithiothreitol
Δ*tgt*	deletion of *tgt* gene
EC	enzyme commission
E. coli	*Escherichia coli*
EDTA	ethylenediamine tetraacetic acid
e. g.	for example (Latin: *exempli gratia*)
EMBL	European Molecular Biology Laboratory
EPR	electron paramagnetic resonance

eq.	equivalent(s)
ESEEM	electron spin echo envelope modulation
et al.	and others (Latin: *et alii*)
FACS	fluorescence-activated cell sorting
FAM	5(6)-carboxyfluorescein
FAXS	fluorine chemical shift anisotropy and exchange for screening
FCS	fetal calf serum
FP	fluorescence polarization
FPLC	fast protein liquid chromatography
Grb2	growth factor receptor-bound protein 2
^{3}H	tritium
H_2O	water
HEPES	2-[4-(2-hydroxyethyl)piperazin-1-yl]ethanesulfonic acid
HPLC	high-performance liquid chromatography
HRP	horseradish peroxidase
HSQC	heteronuclear single quantum coherence
IPTG	isopropyl-β-D-thiogalactopyranoside
ITC	isothermal titration calorimetry
KCl	potassium chloride
KRAS	Kirsten rat sarcoma
KSHV	Kaposi's sarcoma-associated herpesvirus
LB	lysogeny broth
Li-TryR	*Leishmania infantum* trypanothione reductase
MEM	minimum essential medium
MERS-CoV	Middle East respiratory syndrome-related coronavirus
MES	2-(*N*-morpholino)ethanesulfonic acid
$MgCl_2$	magnesium chloride
M. musculus	*Mus musculus*
MOI	multiplicity of infection
mRNA	messenger ribonucleic acid
MS	mass spectrometry
MST	microscale thermophoresis
MTSL	methanethiosulfonate spin label
MW	molecular weight
MWCO	molecular weight cut-off
NaCl	sodium chloride
nanoESI-MS	nano-electrospray ionization mass spectrometry
NaOH	sodium hydroxide
NMR	nuclear magnetic resonance
No.	number
NTP	nucleoside triphosphate
OD	optical density
PAGE	polyacrylamide gel electrophoresis

PBS	phosphate-buffered saline
PCR	polymerase chain reaction
PDB	Protein Data Bank
PEG	polyethylene glycol
PELDOR	pulsed electron–electron double resonance
PFG	pulsed field gradients
PPI	protein–protein interaction
preQ_1	pre-queuine
QTRT1	queuine tRNA-ribosyltransferase catalytic subunit 1
R	(organic) residue
rmsd	root-mean-square deviation
RNA	ribonucleic acid
RPMI	Roswell Park Memorial Institute
SAR	structure–activity relationship
SDSL	site-directed spin labeling
SEC	size-exclusion chromatography
S. dysenteriae	*Shigella dysenteriae*
S. flexneri	*Shigella flexneri*
SLC26	solute carrier family 26
SOD1	superoxide dismutase 1
SPR	surface plasmon resonance
TBS	TRIS-buffered saline
TBS-T	TRIS-buffered saline with Tween® 20
TCEP	tris(2-carboxyethyl)phosphine
TES	2-[[1,3-dihydroxy-2-(hydroxymethyl)propan-2-yl]amino]ethanesulfonic acid
TFA	trifluoroacetic acid
TGT	tRNA-guanine transglycosylase
TOTD	4,7,10-trioxa-1,13-tridecanediamine
6-TramTO-3	4-((1*E*,3*Z*)-3-(3-(6-(4-(aminomethyl)-1*H*-1,2,3-triazol-1-yl)hexyl)benzo[*d*]thiazol-2(3*H*)-ylidene)prop-1-en-1-yl)-1-ethylquinolin-1-ium iodide
TRIS	tris(hydroxymethyl)aminomethane
tRNA	transfer ribonucleic acid
UV	ultraviolet
virF	virulence factor F gene
Vis	visible
vs.	versus
WT	wild type
Z. mobilis	*Zymomonas mobilis*

List of Units, Variables and Constants

$a\ b\ c$	unit cell axes
A	anisotropy
A_b	anisotropy of bound ligand
A_f	anisotropy of free ligand
AU	absorbance unit
Å	ångström
$\alpha\ \beta\ \gamma$	unit cell angles
B**-factor**	Debye–Waller factor
cal	calorie
Ci	curie
CV	column volume
°C	degree Celsius
d	day
D	diffusion coefficient
D_b	diffusion coefficient of bound ligand
D_f	diffusion coefficient of free ligand
D_o	observed diffusion coefficient
Da	dalton
DP	differential power
δ	gradient pulse duration
Δ	diffusion delay
ΔG	change in Gibbs free energy
ΔH	change in enthalpy
ΔS	change in entropy
ε	molar extinction coefficient
η	viscosity
F	fraction or structure factor
F_b	fraction of bound ligand
F_c	calculated structure factor
F_f	fraction of free ligand
F_o	observed structure factor
g	gram
g	gravitational force; gradient strength
γ	gyromagnetic ratio
h	hour
I	intensity
I_0	intensity in absence of applied gradient
$I_{\parallel}$	intensity in parallel plane
$I_{\perp}$	intensity in perpendicular plane
J	joule

K	kelvin
k_{cat}	turnover number
K_{d}	dissociation constant
K_{i}	inhibition constant
K_{m}	Michaelis-Menten constant
L	liter
L_{tot}	total ligand concentration
λ	wavelength
m	meter
m	mass
M	molar
min	minute
mol	mole
mP	millipolarization
MW	molecular weight
m/z	mass-to-charge ratio
v	frequency
OD	optical density
P	polarization
pD	potential of deuterium
pH	potential of hydrogen
P_{tot}	total protein concentration
r	distance
R	universal gas constant $R = 8.314\,\mathrm{J\,mol^{-1}\,K^{-1}}$
R**-factor**	residual or reliability factor
rpm	revolutions per minute
ρ	rotational relaxation time
s	second
σ	standard deviation
t	time
T	temperature
T_2	spin–spin relaxation time
T_{m}	melting temperature
τ	time constant
U	enzyme unit
V	volt
V	volume
ζ	angle between excitation and emission dipoles

Amino Acids

The following figures show the uncharged chemical structures of the 20 proteogenic amino acids including their three- and one-letter codes (shown in parentheses).

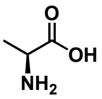

alanine
(Ala, A)

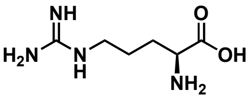
NH
H2N
N
H
O
OH
NH2

arginine
(Arg, R)

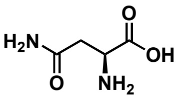
H2N
O
O
OH
NH2

asparagine
(Asn, N)

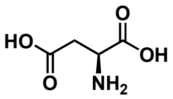

aspartic acid
(Asp, D)

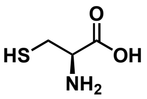

cysteine
(Cys, C)

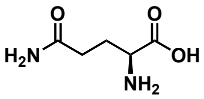
O
H2N
O
OH
NH2

glutamine
(Gln, Q)

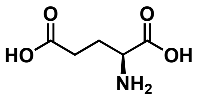

glutamic acid
(Glu, E)

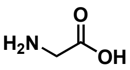

glycine
(Gly, G)

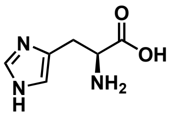

histidine
(His, H)

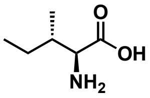

isoleucine
(Ile, I)

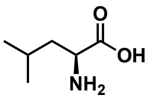

leucine
(Leu, L)

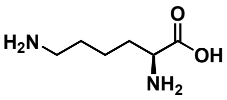

lysine
(Lys, K)

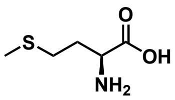

methionine
(Met, M)

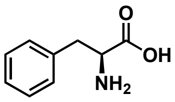

phenylalanine
(Phe, F)

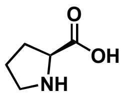

proline
(Pro, P)

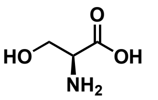

serine
(Ser, S)

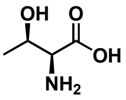

threonine
(Thr, T)

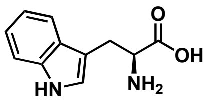

tryptophan
(Trp, W)

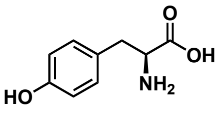

tyrosine
(Tyr, Y)

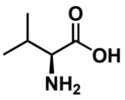

valine
(Val, V)

List of Figures

1.1 Chemical structures of penicillin, chlordiazepoxide, and sildenafil. 2
1.2 Nucleobase exchange reaction from guanine to preQ$_1$ catalyzed by TGT and subsequent modification to queuine. 3
1.3 Ribbon representation of the homodimeric *Z. mobilis* TGT crystal structure. 4
1.4 Ribbon representation of the TGT homodimer in complex with a tRNA stem loop. 5
1.5 Proposed mechanism of the TGT-catalyzed nucleobase exchange reaction. 6
1.6 Design of *lin*-benzoguanine inhibitors. 7
1.7 Perturbation of the TGT homodimer interface dimer by spiking ligand **1.6**. 8
1.8 From fragment-based screening to addressing a novel transient pocket of TGT. . . 9

2.1 Chemical structures of twist-inducing *lin*-benzoguanine inhibitors **2.1** and **2.2**, and structural comparison of the functional and twisted TGT homodimer. 12
2.2 Examples of cysteine spin labeling strategies. 14
2.3 Search for the best spin labeling positions in TGT using the program *MtsslWizard*. 16
2.4 Structural comparison of the functional wild type TGT homodimer with TGT^{G87R1} and TGT^{H319R1} and gel filtration elution profiles of TGT variants at 10 µM. 17
2.5 The spin labeling sites G87C and H319C of the functional and twisted TGT homodimers and chemical structures of ligands **2.1**–**2.4**. 18
2.6 PELDOR results on TGT^{G87R1} and TGT^{H319R1} incubated over 24 h with ligands **2.1**–**2.4** or tRNA. 19
2.7 Structural comparison of the functional *apo* TGT structure with the ligand-bound structures of TGT–**2.1**, TGT–**2.2**, and TGT–**2.3**. 21
2.8 The relative amount of the functional and twisted TGT homodimers in dependence of the ligand incubation time. 22
2.9 Chromatograms from desalting steps with parallel detection of two wavelengths. . 23
2.10 Inter-spin distance predictions for the TGT^{G87R1}–TGT^{H319R1} heterodimer as well as the TGT^{G87R1}–TGT^{G87R1} and TGT^{H319R1}–TGT^{H319R1} homodimers calculated by *MtsslWizard*. 24
2.11 Mass spectra and deconvoluted spectra of TGT^{G87R1} and TGT^{H319R1}. 28
2.12 PELDOR results on TGT^{G87R1} incubated over 24 h with ligands **2.1**–**2.4** or tRNA. . 32

2.13 PELDOR results on TGT^{H319R1} incubated over 24 h with ligands **2.1**–**2.4** or tRNA. . 33
2.14 PELDOR results on TGT^{G87R1} incubated over 1, 24, and 72 h with ligand **2.1**. 34
2.15 PELDOR results on TGT^{G87R1} incubated over 1, 24, and 72 h with ligand **2.2**. 35
2.16 PELDOR results on TGT^{G87R1} incubated over 1, 24, and 72 h with ligand **2.3**. 36

3.1 Structural comparison of TGT^{Y330C} in the functional vs. disulfide-linked dimer. . . 39
3.2 Detailed view of the opened interface binding pocket of TGT^{Y330C} occupied by a DMSO molecule and chemical structures of the investigated sulfoxide fragments. . 40
3.3 Structural and biophysical characterization of TGT$^{330/333}$ and the interface binding pocket. 43
3.4 Detailed view of the occupied interface binding pocket and interaction network of complexes TGT^{Y330C}–**3.1**, TGT$^{330/333}$–**3.1**, and TGT$^{330/333}$–**3.2**. 44
3.5 Depiction of the stabilizing interaction between the N-terminal tail and the opened dimer interface in TGT$^{330/333}$–**3.2**. 45
3.6 Detailed view of the guanine-34/preQ$_1$ binding pocket of the TGT$^{330/333}$ variant occupied by *lin*-benzoguanine inhibitor **3.3** via soaking. 46
3.7 Two perspectives on the solvent channels in *apo* TGT$^{330/333}$ along the *c*-axis and *b*-axis of the unit cell. 47
3.8 Detailed view of the interface binding pocket accessibility and the surrounding solvent channels in the *apo* TGT$^{330/333}$ crystal structure. 49
3.9 Detailed view of the occupied interface binding pocket and interaction network of complexes TGT$^{330/333}$–**3.4**, TGT$^{330/333}$–**3.5**, and TGT$^{330/333}$–**3.6**. 50
3.10 Detailed view and interaction network of fragments **3.5** and **3.6** binding on the surface of TGT$^{330/333}$. 52
3.11 Detailed view of the occupied interface binding pocket and interaction network of complexes TGT$^{330/333}$–**3.7** and TGT$^{330/333}$–**3.8** and chemical structures of other investigated derivatives. 53
3.12 Detailed view and interaction network of fragments (*R*,*R*)-**3.7** and (*S*,*S*)-**3.8** binding on the surface of TGT$^{330/333}$. 54
3.13 Gel filtration elution profiles of TGT variants at 10 mg mL^{-1}. 56
3.14 ^{19}F spectra of inhibitor **3.14** and inhibitor **3.14** with 20 µM TGT^{H333D} in D$_2$O buffer at 298 K. 57
3.15 ^{19}F spectra of 0.5 mM *rac-trans*-**3.8** and 1.0 mM **3.15** in D$_2$O buffer at 298 K. 58
3.16 ^{19}F spectra of 0.5 mM *rac-trans*-**3.8** and 0.5 mM **3.15** mixed with and without 20 µM TGT^{H333D} in D$_2$O buffer at 298 K. 59
3.17 Stejskal-Tanner plot of the solvent D$_2$O, TGT^{H333D}, the free fragment *rac-trans*-**3.8** and its mixture with TGT^{H333D} in D$_2$O buffer at 298 K. 61

3.18 Simulated dependency of the fraction of bound ligand and the expected change in diffusion coefficient of the ligand on the ligand concentration. 63
3.19 Mass spectrum and deconvoluted spectrum of TGT$^{C158S/C281S/Y330C/H333A}$. 69
3.20 ^{1}H and ^{1}H–^{13}C HSQC spectra of 1 mM *rac-trans*-**3.7** in D_2O buffer at 298 K. 73
3.21 ^{1}H and ^{1}H–^{13}C HSQC spectra of 1 mM *rac-trans*-**3.8** in D_2O buffer at 298 K. 74
3.22 ^{1}H and ^{1}H–^{13}C HSQC spectra of 1 mM *cis*-**3.8** in D_2O buffer at 298 K. 75
3.23 ^{1}H and ^{1}H–^{13}C HSQC spectra of 1 mM *rac-trans*-**3.12** in D_2O buffer at 298 K. 76
3.24 ^{1}H and ^{1}H–^{13}C HSQC spectra of 1 mM *rac-cis*-**3.12** in D_2O buffer at 298 K. 77
3.25 ^{1}H and ^{1}H–^{13}C HSQC spectra of 1 mM *rac-trans*-**3.13** in D_2O buffer at 298 K. 78
3.26 ^{1}H spectra of 381 µM TGT^{H333D} and 459 µM TGT^{Y330D} in D_2O buffer at 298 K. . . . 79

4.1 Starting points for the study of putative interface-binding peptides. 85
4.2 Peptide array results with TGT^{H333A}, TGT^{Y330D}, and wild type TGT. 87
4.3 Schematic representation of the basic principle behind fluorescence polarization measurements. 89
4.4 Saturation binding curve of 1 µM tracer **4.1** with wild type TGT and dose-response curve for the same FP experiment. 90
4.5 Saturation binding curve of 50 nM tracer **4.1** with TGT^{Y330D} and dose-response curve for the same FP experiment. 90
4.6 Saturation binding curve of 20 nM tracer **4.2** with TGT^{Y330D} and dose-response curve for the same FP experiment. 91
4.7 Helical wheel diagram of the YIHHLIRAGE peptide sequence. 92
4.8 Saturation binding curves of 20 nM tracer **4.3** and 20 nM tracer **4.4** with TGT^{Y330D} and dose-response curves for the same FP experiments. 92
4.9 Saturation binding curves of 20 nM tracer **4.1** and 20 nM tracer **4.4** with TGT^{H333D} and dose-response curves for the same FP experiments. 93
4.10 Saturation binding curves of 5 nM tracer **4.4** from an old and freshly prepared stock solution with TGT^{H333D} and dose-response curves for the same FP experiments. . 94
4.11 HPLC chromatograms of tracer **4.4** prepared from the old and new stock solution each treated without and with 10 mM DTT. 96
4.12 Mass spectra of tracer **4.4** prepared from the old and new stock solution each treated without and with 10 mM DTT. 98
4.13 Optimization of crystallization conditions for TGT^{Y330D}. 99
4.14 Structural comparison of TGT^{Y330D} with the dimeric structures of wild type *Z. mobilis* TGT and *M. musculus* QTRT1. 100
4.15 Progress curves and the resulting Michaelis-Menten plots of wild type TGT and TGT^{Y330D}. 101

4.16 Raw thermogram and integrated raw data with the corresponding isotherm of the TGT^{H333D} dissociation ITC experiment. 103
4.17 Validation of structural integrity of labeled and unlabeled TGT variants. 104
4.18 Dose-response curves of TGT dimerization measured by MST. 104
4.19 Congo red agar plates with grown *S. flexneri* 2a 2457T and Δ*tgt* strains. 105
4.20 Representative dot plots of FACS analysis of untreated versus bacteria-treated Caco-2 cells at MOI of 100 and 500. 106
4.21 Infection rate of *S. flexneri* 2a strains and representative dot plots of FACS analysis of Caco-2 cells treated with 2457T and Δ*tgt* each at MOI of 100. 106
4.22 Mass spectrum and deconvoluted spectrum of wild type TGT. 110
4.23 Mass spectrum and deconvoluted spectrum of TGT^{Y330D}. 111
4.24 Mass spectrum and deconvoluted spectrum of TGT^{H333D}. 112
4.25 Thermal melting curves with intrinsic fluorescence tracked at wavelengths of 330 nm and 350 nm. 117
4.26 Capillary scan and time traces of the MST experiment with wild type TGT. 117
4.27 Capillary scan and time traces of the MST experiment with TGT^{H333D}. 118
4.28 Representative forward vs. side scatter plot of Caco-2 cells. 119

List of Tables

2.1 DNA primer sequences used for mutagenesis. 27
2.2 Crystallographic data collection, processing and refinement statistics of PDB entries 6YGR, 7APL and 7APM. 30

3.1 Solvent channel analysis of the apo TGT$^{330/333}$ structure by *MAP_CHANNELS*. . . 48
3.2 DOSY results in D_2O buffer at 298 K. 64
3.3 DNA primer sequences used for mutagenesis. 68
3.4 Crystallographic data collection, processing and refinement statistics of PDB entries 7ADN, 7A4X, 7A4K and 7A9E. 70
3.5 Crystallographic data collection, processing and refinement statistics of PDB entries 7A3X, 7A3V, 7A0B and 7A6D. 71
3.6 Chemical structures and size descriptors of investigated compounds. 80

4.1 Peptides for FP binding studies. 89
4.2 DNA primer sequences used for mutagenesis. 109
4.3 Peptide sequences of the first peptide array design. 114
4.4 Peptide sequences of the second peptide array design. 115

S1 Summary of recombinant *Z. mobilis* TGT constructs. 131
S2 List of used devices and instruments. 133
S3 List of used chemicals. 135

1

General Introduction

1.1 Serendipity in Drug Discovery

The discovery of penicillin by Sir Alexander Fleming (1881–1955) was unarguably a milestone in pharmaceutical history. After returning from summer vacation in 1928, Fleming observed a contaminated and moldy *Staphylococcus aureus* culture on a Petri dish, in which no bacteria grew near the mold area. Further investigations showed that the mold "juice" produced by this fungus, later identified as *Penicillium notatum*, also inhibited the growth of other common infectious bacteria. Fleming named the active ingredient "penicillin" (**1.1**, Figure 1.1) which launched the era of modern antibiotic research and represents one of the best known example of a serendipitous discovery.[1] Another well-known example of serendipity is the discovery of the potent tranquilizer chlordiazepoxide, also known as Librium® (**1.2**, Figure 1.1) by Leo Sternbach (1908–2005) and chemists from Hofmann-La Roche during the 1950s. An unexpected chemical rearrangement resulted in the first synthesis of benzodiazepines with excellent pharmacological characteristics leading to the successful development of several psychotropic drugs within the pharmaceutical industry.[2] How serendipity can emerge from a rational drug search context, initially sought for, was impressively shown by the discovery of sildenafil (**1.3**, Figure 1.1). Originally, in search of phosphodiesterase inhibitors to treat angina pectoris, sildenafil was not showing pharmacologically interesting results. However, after the side effect of distinct penile erection of male patients was recognized, the drug was repurposed to treat erectile dysfunction.[3,4] Quickly after market launch by Pfizer as Viagra®, sildenafil developed into a "blockbuster" drug worth billions of dollars.

These are only three examples from a long list of similar happy accidents in science. Notably, they all share a common trait: none of them were the product of aimlessness and pure luck but rather they were acknowledged, reviewed and further advanced by their discoverers thus verifying their validity towards the statement "le hasard ne favorise que les esprits préparés" [chance only favors the prepared mind] by Louis Pasteur (1822–1895).[5,6]

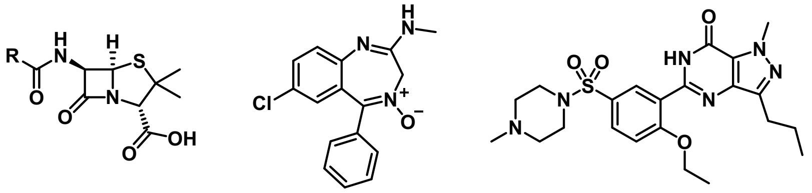

1.1 penicillin

1.2 chlordiazepoxide

1.3 sildenafil

Figure 1.1: Chemical structures of penicillin (**1.1**), chlordiazepoxide (**1.2**), and sildenafil (**1.3**).

Today, such chance discoveries are explored by modern and more rational techniques such as high-throughput screening of large compound libraries comprising million of molecular entries. This allows the systematic identification of so-called "hits" as starting points for further optimization into potent drug candidates during pre-clinical drug development. Within the early development process, several binding properties of specific ligands to their target macromolecule, such as binding thermodynamics and kinetics, can be assessed by biochemical and biophysical methods. In combination with *in silico* predictions and experimental validations of the ligand binding modes by structural techniques such as X-ray crystallography, nuclear magnetic resonance (NMR), and cryo-electron microscopy (cryo-EM), the gained knowledge on the target–ligand interaction can be exploited to guide the development of drug candidates in the context of structure-based drug design.

Yet, despite the big leap in technology in the last decades, serendipity remains one of the several contributors in drug discovery and basic research. Nonetheless, the process of a serendipitous scientific discovery should not be confused with coincidences based on random luck. Quite the contrary, it depends on the ability to recognize the potential of the chance encounter and subsequently act upon it based in a critical manner. This highlights the crucial combination of intuition and open-mindedness based on the past and present experience of the researcher.

1.2 tRNA-Guanine Transglycosylase as a Shigellosis Target

1.2.1 Role of TGT in *Shigella* pathogenesis

During an epidemic in Japan in 1897, the cause of bacillary dysentery, responsible for >90 000 cases with a mortality rate of ~30 %, was discovered by bacteriologist Kiyoshi Shiga (1871–1957).[7,8]

In his honor, the causative agent, initially termed *Shiga bacillus*, now belongs to the established genus *Shigella* consisting of four species with multiple serotypes within the first three groups: *Shigella dysenteriae* (group A), *Shigella flexneri* (group B), *Shigella boydii* (group C), and *Shigella sonnei* (group D). *S. dysenteriae* type 1, the bacterium originally discovered by Shiga, causes the most severe disease. Shigellosis still presents a high disease burden especially in developing countries, responsible for almost 270 million cases and roughly 212 000 deaths from which over 63 000 occured among children younger than 5 years in 2016.[9] As few as 10 to 100 *Shigella* bacteria are sufficient to cause an infection.[10] The disease can cause outbreaks in low-resource settings including regions inflicted by war regions or natural disasters, refugee camps, and generally areas with poor sanitation and hygiene standards or undersupply of clean water.[11] The bacteria are spread predominantly by faecal-oral contact or ingested with contaminated food and water.[11,12] After surviving the acidic conditions of the stomach, *Shigella* bacteria ultimately penetrate the endothelial cells in the intestinal mucosa.[12,13]

In order to develop the essential virulence factors for mucous cell invasion, a post-transcriptional incorporation of a modified nucleobase, queuine, into the anticodon wobble position of specific bacterial transfer RNAs (tRNAs) is required. In a first step, this modification depends on the functionality of the enzyme tRNA-guanine transglycosylase (TGT, EC 2.4.2.29) which catalyzes the nucleobase exchange from guanine to the queuine precursor preQ$_1$ at position 34 of tRNAs specific for Asp, Asn, Tyr, and His. Further modifications of preQ$_1$ by downstream enzymes ultimately yield the queuine-incorporated tRNA (Figure 1.2).

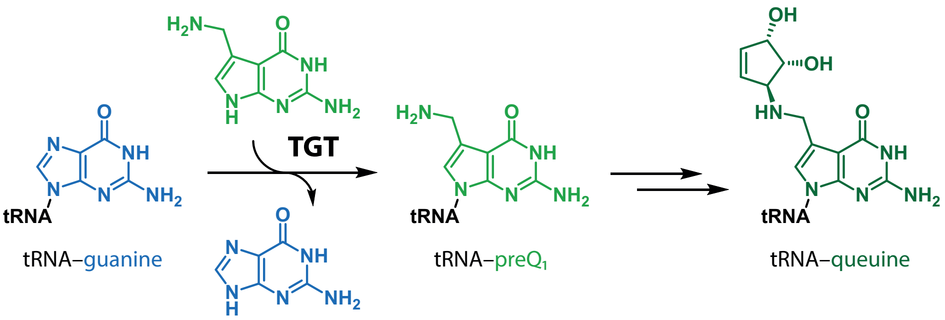

Figure 1.2: Nucleobase exchange reaction from guanine (blue) to preQ$_1$ (green) catalyzed by TGT and subsequent modification to queuine (dark green).

Recent studies have shown that queuine modification of tRNAs is linked to the maintenance of the translation process in terms of accuracy and speed.[14,15] Inactivation of the *tgt* gene, initially termed *vacC*, impairs the efficient translation of the transcriptional regulator-encoding *virF* messenger RNA (mRNA) resulting in a decreased expression of the virulence phenotype in *S. flexneri*.[16,17] Thus, TGT represents a putative target for the rational design of anti-virulence compounds with novel modes of action to fight shigellosis.

1.2.2 Structure of TGT and the TGT–tRNA complex

In 1996, the first high-resolution crystal structure of TGT from *Zymomonas mobilis* was reported by Romier *et al.*[18] The following series of molecular and structural investigations led to bacterial TGT becoming one of the most extensively studied tRNA-modifying enzymes to date. The functional enzyme exhibits a homodimeric quarternary structure consisting of two identical subunits each adopting a $(\beta/\alpha)_8$-barrel fold (Figure 1.3). The homodimer forms a large continuous interface spanning a contact area of 1667 $Å^2$.[18] Furthermore, a C-terminal insertion serves as a zinc-binding subdomain which also contributes to the composition and stability of the TGT dimer interface. The zinc ion is tetrahedrally coordinated by three cysteines (Cys318, Cys320, Cys323) and one histidine (His349). In addition to the zinc-binding subdomain, a structural loop–helix motif (residues Gly46–Thr62) largely contributes to the formation of the dimer interface.

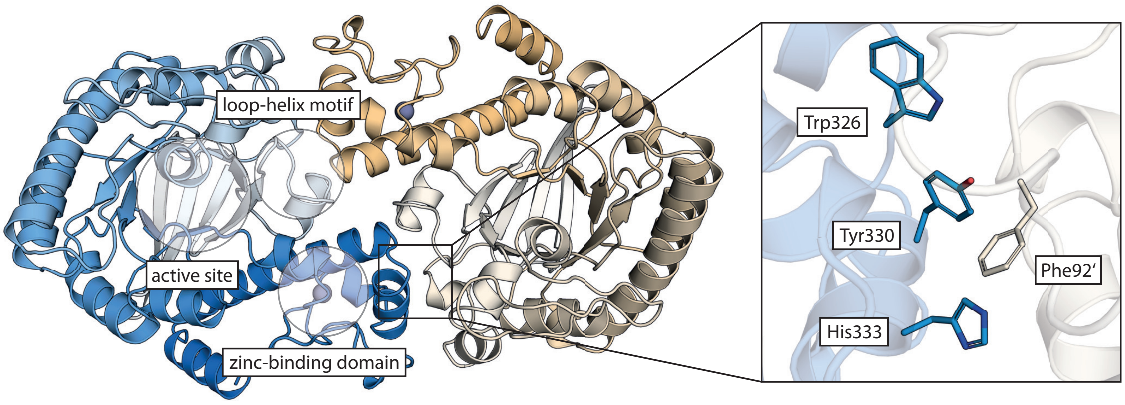

Figure 1.3: Ribbon representation of the homodimeric *Z. mobilis* TGT crystal structure (PDB ID: 1PUD[18]). Important structural motifs are encircled. Zinc ions are shown as dark gray spheres. The aromatic hot spot residues are shown as sticks in the subpanel.

Seven years later, Xie *et al.* determined the crystal structure of *Z. mobilis* TGT in complex with a 20-mer RNA oligonucleotide mimicking the anticodon $tRNA^{Tyr}$ stem loop (Figure 1.4).[19] The structural analysis of the complex provided deeper insights into the binding mode of the tRNA substrate. The structure revealed that although both subunits each contain a catalytic center capable of performing the exchange reaction, only one tRNA molecule is able to bind to the enzyme in a 2:1 fashion (TGT dimer-to-tRNA monomer). Later, Ritschel *et al.* used native nano-electrospray ionization mass spectrometry (nanoESI-MS) to verify the oligomeric state of TGT and the TGT–tRNA binding stoichiometry. These findings explain that a second tRNA molecule is unable to bind due to sterical reasons as both active sites of each TGT monomer are located on the same dimer surface site.[20] This suggests that catalysis is performed only by one monomer subunit while the other one positions and stabilizes the tRNA substrate in the correct orientation.

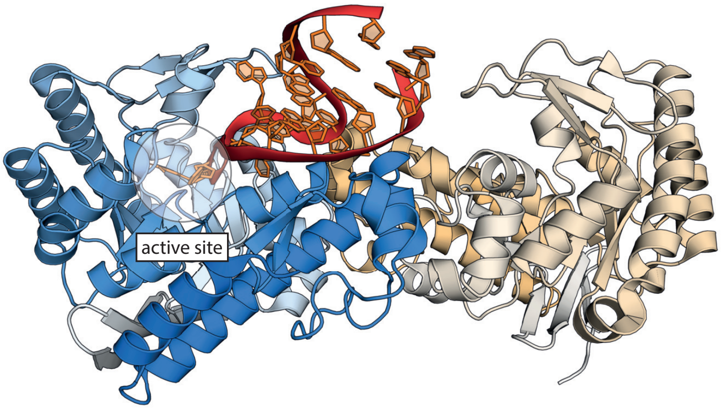

Figure 1.4: Ribbon representation of the *Z. mobilis* TGT homodimer in complex with a tRNA stem loop. One monomer subunit performs catalysis (blue) and the other subunit (orange) stabilizes the tRNA stem loop (red) in its orientation (PDB ID: 1Q2S[19]).

These results have prompted a number of investigations to dissect the stabilizing forces for the formation of the TGT homodimer interface. Computational analysis and subsequent validation by mutagenesis studies revealed a hydrophobic cluster consisting of four aromatic residues, Trp326, Tyr330, His333, and Phe92', which largely contribute to the stabilization of the dimer interface. While three out of four residues, Trp326, Tyr330, and His333, are located in close proximity of or in the α-helix αE of one monomer unit, the aromatic patch is completed by Phe92' of the adjacent dimer mate (indicated by an apostrophe ('), Figure 1.3 right). NanoESI-MS experiments of several mutated TGT variants showed that mutations of the so-called "hot spot" residues resulted in a shift of the TGT dimer–monomer equilibrium towards the monomeric species.[21,22] Additionally, recent studies indicated a strong dependence of the pH value on the structural stability of the homodimer although a reduced dimer stability is not directly correlated with a reduction in enzymatic activity.[23] The early investigations on the structure and function of TGT as well as the rapid progress in protein production technology and availability of well-diffracting TGT crystals have led to TGT as a suitable target for further structure-based drug design efforts.

1.2.3 Mechanism of the nucleobase exchange catalyzed by TGT

The kinetic mechanism of the TGT-catalyzed base exchange reaction was previously described as a ping-pong mechanism.[24,25] After binding of the tRNA substrate to TGT, the guanosine-34 nucleoside unfolds from the tRNA molecule and is specifically recognized in the guanine-34/preQ$_1$ binding pocket by residues Asp102, Asp156, Gln203, Gly230, and Ala232. Asp280 acts as a nucleophile attacking the carbon C1 of ribose-34 (Figure 1.5a). Subsequently, the glycosidic bond of guanosine-34 is cleaved and a covalent TGT–tRNA intermediate is formed (Figure 1.5b). The cleaved guanine molecule leaves the binding pocket after a proton is entrapped.

Originally, Asp102 was assumed to be the proton donor[19] but a more recent mechanistic study led by Biela *et al.*[25] suggested a water molecule bound to Ala232 fulfills this function instead. It was hypothesized that the water molecule is also responsible for the irreversibility of the base exchange reaction by formation of hydroxide ions (Figure 1.5b) and oxonium ions (Figure 1.5d). Mutual neutralization removes both ions from the equilibrium thus preventing the reverse reaction. Additionally, due to the exocyclic amino group of preQ$_1$, the water molecule cannot be located in the pocket at the same time as the modified base.

After guanine and the water molecule have left the binding pocket, preQ$_1$ binds resulting in a flip of the peptide backbone amide of Leu231/Ala232. The carbonyl group of Leu231 can then act as an electron donor to form a new hydrogen bond with the exocylic amine of preQ$_1$ (Figure 1.5c). This induced-fit adaptation is stabilized by Glu235 which can interact with both, the amide carbonyl of Leu231 and amide nitrogen of Ala232, depending on the protonation state of Glu235. The release of a proton, coupled with the formation of an oxonium ion, leads to a nucleophilic attack of the anomeric carbon of ribose-34 by the basic nitrogen N9 of preQ$_1$ (Figure 1.5c). This final step results in the cleavage of the TGT–tRNA intermediate and release of the preQ$_1$-modified tRNA (Figure 1.5d).

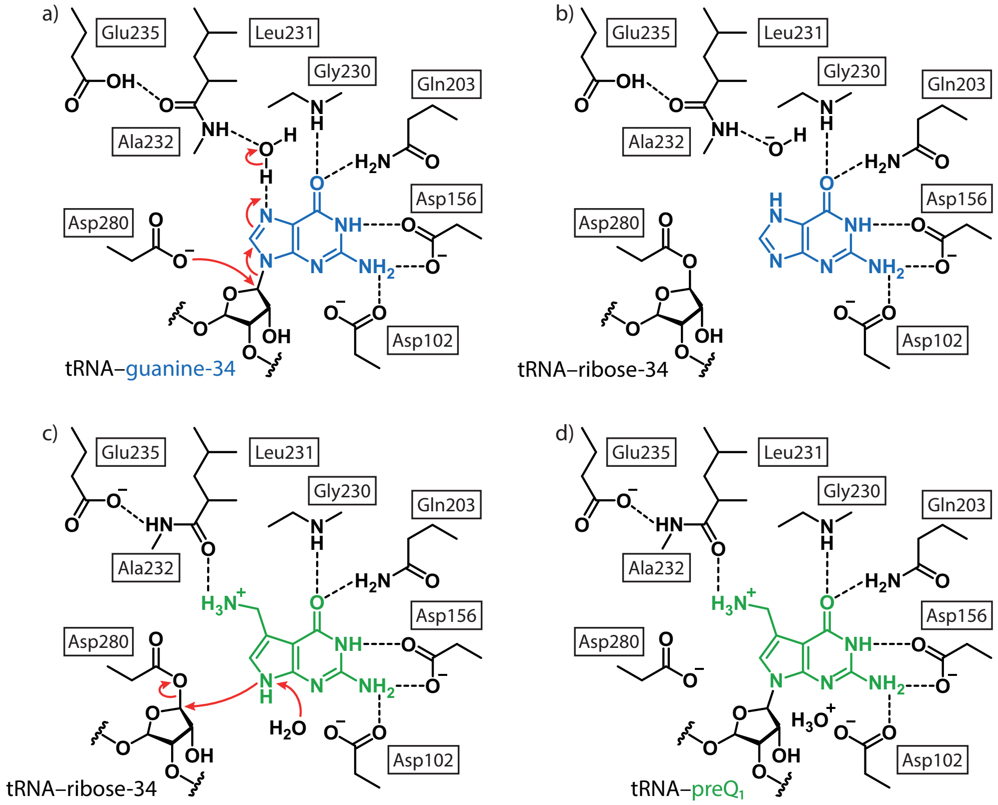

Figure 1.5: Proposed mechanism of the TGT-catalyzed nucleobase exchange reaction by Biela *et al.*[25] a, b) Recognition of guanine-34 (blue) and cleavage of guanosine-34 by nucleophilic attack of Asp280 resulting in formation of a covalent TGT–tRNA intermediate. c, d) Exchange by preQ$_1$ (green) through nucleophilic attack on anomeric carbon of ribose-34 by N9 of preQ$_1$ yielding the modified tRNA.

1.3 Structure-based Design of TGT Inhibitors

1.3.1 Competitive inhibition by active-site blocking

In close collaboration with the research group of François Diederich (1952–2020, ETH Zürich), *lin*-benzoguanines have been developed as starting compounds to enhance TGT inhibition and binding affinity by addressing adjacent hydrophobic pockets. Structural analysis of the TGT–tRNA complex indicated that in addition to the guanine-34/preQ$_1$ binding pocket, the adjacent subpockets, occupied by the ribose units of uridine-33 and guanosine-34 (Figure 1.6a), can be targeted by adding extended moieties to the *lin*-benzoguanine core scaffold **1.4** (K_i = 4.1 ± 1.0 µM). While hydrophobic extensions to the ribose-33 subpocket yielded inhibitors with improved affinities in the nanomolar range,[26] extensions towards the ribose-34 subpocket unexpectedly led to an affinity decrease. This could be explained by the disruption of a nearby water cluster, which can be observed in the unsubstituted *lin*-benzoguanine **1.4** (Figure 1.6b). The water molecules bridge the hydrophobic subpocket between Asp102 and Asp280 and are likely responsible for the solvation contribution while buffering the high charge of these two polar residues. Hydrophobic moieties addressing the ribose-34 subpocket would inevitably destroy the water cluster, hence leading to an affinity loss due to entropic penalty.[27] The introduction of an amino group to the substituted moiety enabled an ionic interaction to Asp280. The additional salt bridge overcompensated the decrease in entropy, and together these findings led to the design of the highly potent nanomolar inhibitor **1.5** (K_i = 4 ± 2 nM, Figure 1.6c).[27]

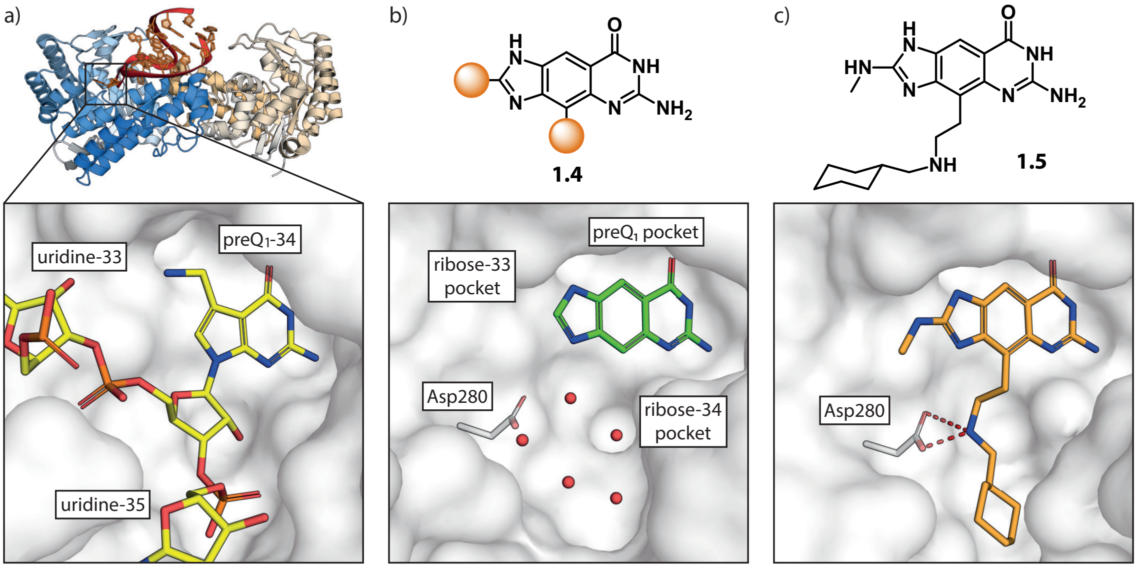

Figure 1.6: Design of *lin*-benzoguanine inhibitors. a) Detailed view of the substrate binding site of the TGT–tRNA^{Tyr} complex with tRNA shown as sticks (PDB ID: 1Q2S[19]). b) Occupation of the guanine-34/preQ$_1$ pocket by the core scaffold **1.4** with adjacent water molecules shown as red spheres (PDB ID: 2BBF[28]). Positions for moiety extensions are highlighted as orange spheres in the chemical structure. c) Example of substituted inhibitor **1.5** addressing the adjacent ribose-33 and ribose-34 pockets (PDB ID: 3EOS[27]). For reasons of clarity, residues Tyr106 and Ser110 are not shown.

1.3.2 Design of spiking ligands for homodimer destabilization

Since the guanine-34/preQ$_1$ binding pocket is not far positioned from the homodimer interface, a series of "spiking" ligands based on the substituted *lin*-benzoguanine inhibitor **1.5** were characterized.[29] Further elongated moieties targeting beyond the ribose-34 subpocket were designed to pierce into the homodimer interface hence disturbing its formation. The destabilizing effect on the TGT homodimer was investigated by native nanoESI-MS with the ethyne-linked pyridyl-substituted ligand **1.6** showing the most promising shift towards monomeric species of TGT (Figure 1.7a). Furthermore, the mode of action was investigated by X-ray crystallographic analysis. The missing electron density of the inhibitor pyridyl moiety from the co-crystallized ligand **1.6**-bound TGT complex indicated multiple conformations or high residual mobility of the substituent in accordance with observed elevated *B*-factors (Figure 1.7b). Importantly, an induced shift of residues Val45–Thr47 and a collapse of the loop–helix motif along with changes in the crystal lattice, compared to usual TGT crystals of the *C*2 space group, were observed due to the close proximity to the extended inhibitor substituent (Figure 1.7b). Meanwhile, the adjacent helix–turn–helix motif of the dimer mate (residues Arg328'-Ser366') remains largely unaffected. As the results of this proof of concept study suggest, rational perturbation of the structural loop–helix motif by small molecules represents a potential approach to modulate the interface formation of bacterial homodimeric TGT.

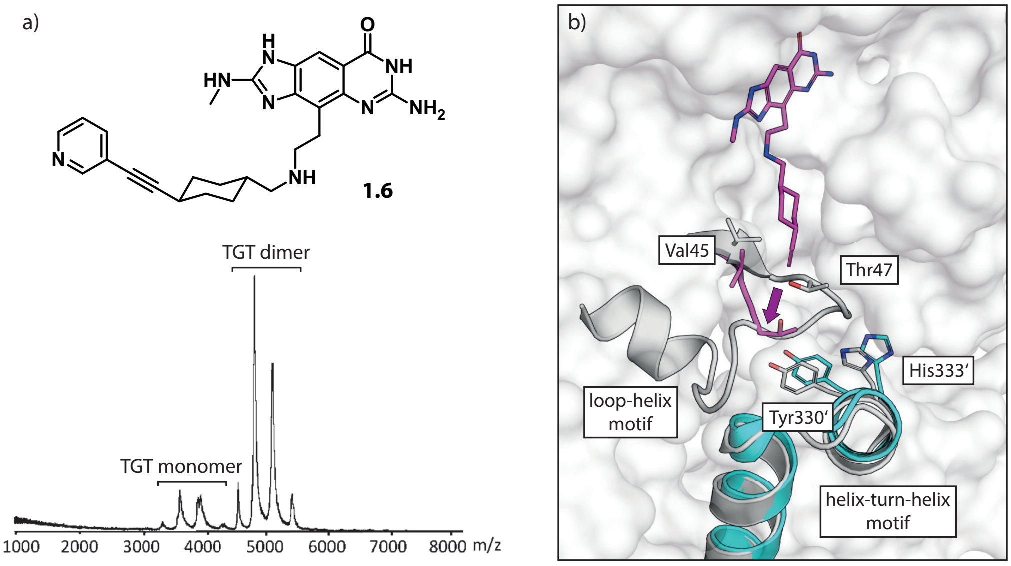

Figure 1.7: Perturbation of the TGT homodimer interface dimer by spiking ligand **1.6**. a) Chemical structure of ligand **1.6** and corresponding nanoESI-MS spectrum at a TGT concentration of 1 µM and a TGT–**1.6** molar ratio of 1:10. Adapted from Immekus *et al.*[29] b) Conformational collapse of the loop–helix motif induced by ligand **1.6** (purple, PDB ID: 4FR6[29]) compared to the *apo* structure of TGT (gray, PDB ID: 1PUD). The shift of residues Val45–Thr47 is indicated by a purple arrow. The helix-turn-helix motif of the dimer mate remains unaffected (cyan, PDB ID: 4FR6[29]).

1.3.3 Fragment-based screening for the discovery of new hit compounds

Fragment-based screening approaches have been widely used to find new starting points for lead development or to explore novel ligand binding sites. In the course of a comparative analysis led by Hassaan *et al.*[30], TGT was chosen as a target and screened against our in-house 96-fragment library which was developed in collaboration with the Helmholtz-Zentrum Berlin.[31] Out of the 96 library entries, 8 hit compounds were identified by X-ray crystallography (Figure 1.8a) with most of them binding to the active site while some also bound to the protein surface of the enzyme. Screens of the same library based on NMR and surface plasmon resonance (SPR) yielded 23 and 10 hits, respectively. Astoundingly, no hit overlap was detected between all three methods indicating that X-ray crystallography may be superior in detecting weak binders that would be missed by other biophysical assays.[30]

Surprisingly, one fragment hit, L-canavanine **1.7**, opened a previously unknown transient sub-pocket adjacent to the preQ$_1$ recognition site by inducing a rearrangement of nearby residues that enlarged the guanine-34/preQ$_1$ binding pocket (Figure 1.8a). This discovery led to the design of dihydroimidazoquinazoline-based inhibitor **1.7** that is capable of opening the transient pocket and displacing a conserved water cluster in a favorable manner (Figure 1.8b).[32] Due to the pocket opening, Cys158, a cysteine residue only present in bacterial TGTs, becomes addressable, e. g. by electrophilic ligands. This finding provides the basis for the design of covalent inhibitors that selectively target bacterial TGTs.

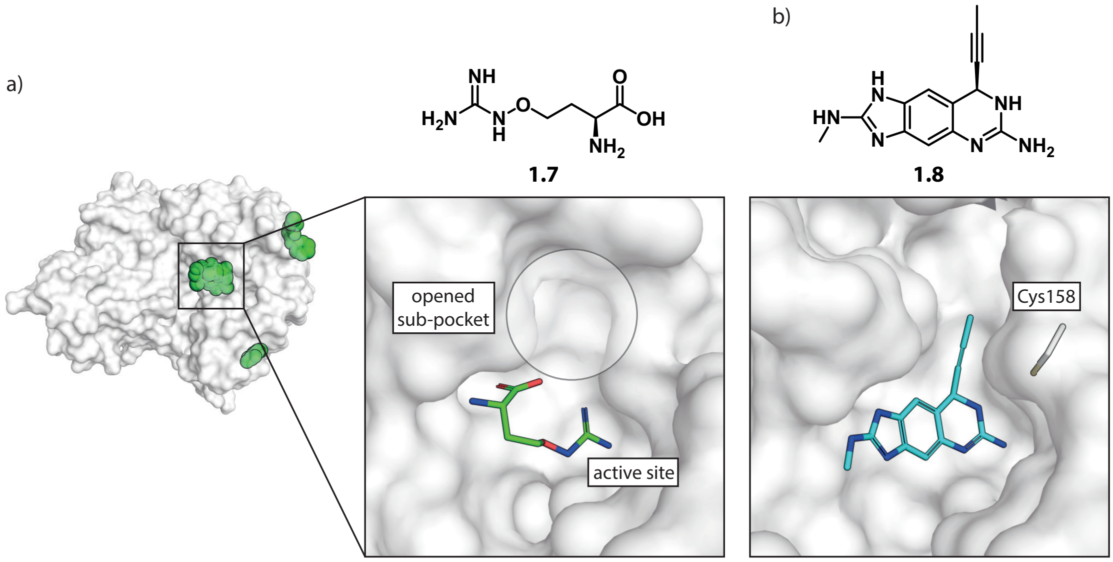

Figure 1.8: From fragment-based screening to addressing a novel transient pocket of TGT. a) Superposition of crystallographic fragment hits (shown as green spheres) by Hassaan *et al.* and detailed view of the guanine-34/preQ$_1$ pocket extension by L-canavanine **1.7** (green, PDB ID: 5UTI[30]). b) View of the novel subpocket addressed by dihydroimidazoquinazoline **1.8** (cyan) with the adjacent Cys158 (PDB ID: 6RKQ[32]). For reasons of clarity, residues Tyr106 and Ser110 are not shown.

1.4 Thesis Outline

This thesis compiles the work of three projects based on a series of serendipitous discoveries within the functional and structural investigation of the TGT homodimer and its inhibitors. A summary of the key findings and potential directions for future research are discussed in each chapter. The gained knowledge from these projects display a coherent image and shall ultimately contribute to the development of novel approaches for rational design of TGT homodimer modulators.

In **Chapter 2**, an electron paramagnetic resonance-based approach is introduced to investigate a ligand-induced rearrangement of the functional TGT homodimer. The newly developed method was used to verify a twisted state of dimeric TGT observed from crystal structures of previous studies.[33,34] Site-directed spin labeling and pulsed electron–electron double resonance methods were applied to measure the distance between two labeled TGT monomers. By adding a twist-inducing inhibitor, we observed a shift in the interspin distance distributions. In this study, we identified a pyranose-substituted *lin*-benzoguanine inhibitor as superior in forming the twisted species therefore verifying this novel mode of inhibition in a solution equilibrium.

Chapter 3 describes the story of finding new small-molecule binders of the β1α1-loop motif of TGT. A study by Jakobi *et al.* discovered an alternative crystal structure of a mutant variant of TGT with a new solvent-exposed interface hence representing a "pseudomonomeric" structure. The β1α1-loop adopts a new conformation thereby opening a transient binding pocket which is occupied by a dimethyl sulfoxide (DMSO) molecule. Remarkably, DMSO was not part of the crystallization condition but was soaked into the crystal as part of the cryoprotecting procedure before flash freezing. We hypothesized that DMSO binds as a fragment to the pocket and stabilizes it. The stabilized loop conformation would clash into the other dimer mate thus dimer formation could be impaired by stabilization of the β1α1-loop motif with small molecules. A fragment-based approach via fragment soaking was used to screen for hit compounds.

Chapter 4 illustrates the journey to the first peptide-based TGT inhibitors that target the homodimer interface. One structure of the pseudomonomeric TGT mutant showed an extended and stabilized N-terminal helix. We hypothesized that the sequence is stabilized by binding to the interface of another crystal mate. In comparison with the wild type structure, we identified helix αE binding to the dimer mate in a similar fashion. Initial peptides derived from helix αE and the N-terminus were screened using a peptide microarray. The most promising peptides were then synthesized and their binding to TGT was characterized using fluorescence polarization (FP). To provide a screening platform for further investigations on the influence of TGT homodimerization, two assays based on MicroScale thermophoresis (MST) and dissociation isothermal calorimetry (ITC) were established. Also, the development of an assay to study host cell invasion by *S. flexneri* is described, which can be used for cellular screening of dimer-disrupting peptides and other TGT inhibitors.

2

Unraveling the Ligand-Induced Twist of Homodimeric TGT by Pulsed Electron–Electron Double Resonance

2.1 Introduction

A large number of proteins undergoes a carefully arranged interplay with other macromolecules in order to perform biological functions accurately. Self-association into oligomeric states via protein–protein interactions (PPIs) represents one feature to the functional regulation of proteins as, e. g., specific enzymes can only perform catalysis in their homooligomeric arrangement.[35–37] Disturbing oligomerization with small molecules and peptides/peptidomimetics is therefore a promising concept to modulate and inhibit the function of such enzymes as could be shown for the dimeric Kaposi's sarcoma-associated herpesvirus protease (KSHV).[38,39] Less exploited strategies such as transferring or stabilizing a protein in a non-functional oligomeric state can represent an attractive approach for drug design. This concept has been exemplified by the development of the small molecule BI-2852 that successfully stabilizes a non-functional dimeric form of KRAS, a member of the GTPase protein family and the most frequently mutated proto-oncogene in human cancers.[40] Another example, displaying the discovery of orthosteric PPI stabilizers of the dimeric N-terminal domain of the MERS-CoV nucleocapsid protein, demonstrated that the stabilization of non-native PPIs might serve as targets for the design of novel antivirals.[41]

2.1.1 Discovery of the twisted TGT homodimer

In a recent study led by Ehrmann *et al.*, a functionalized *lin*-benzoguanine inhibitor **2.1** was designed that is capable of stabilizing a novel “twisted” dimer state of TGT (Figure 2.1a).[34] The rational design of the inhibitor was based on a serendipitous finding during a comparative study of ligand soaking versus co-crystallization methods of several TGT–inhibitor complexes. Unexpectedly, one inhibitor of the *lin*-benzoguanine series (inhibitor **2.2**) was found to induce a rearranged dimer packing and a newly observed $P2_1$ crystal space group for TGT (Figure 2.1c).[33] Surprisingly, the sugar-substituted derivative **2.1** co-crystallized with the enzyme in both dimer states, functional and twisted, side by side in the same crystallization well indicating the presence of a ligand-dependent equilibrium between both states.

Crystal structure analysis of the twisted dimer revealed a difference by rotation of approximately 130° of a monomer subunit compared to the functional dimer (Figure 2.1b and c). Interestingly, the dimer interface does hardly differ in size with 1619 vs. 1644 Å^2 for the functional and twisted dimer interface area, respectively.[34] However, while the functional dimer forms a continuous interface (Figure 2.1b), the interface of the twisted dimer is split into four smaller patches (Figure 2.1c). The helix αE forms a new aromatic contact with the dimer mate which involves positional adaptations of the hotspot residues. Phe92’, a hotspot residue complementing Trp326, Tyr330, and His333 in the functional enzyme (Figure 2.1b), is replaced by Tyr72’ in the twisted arrangement (Figure 2.1c).

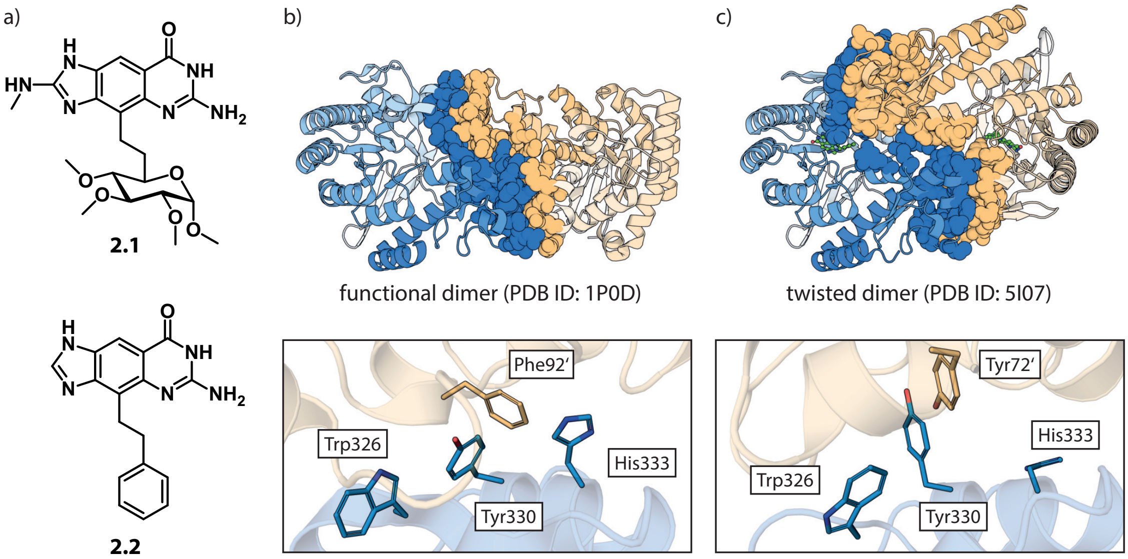

Figure 2.1: a) Chemical structures of twist-inducing *lin*-benzoguanine inhibitors **2.1** and **2.2**. Structural comparison of the b) functional (PDB ID: 1P0D[42]) and c) ligand-bound twisted (PDB ID: 5I07[33]) TGT homodimer. Interface residues are shown as spheres. The bound inhibitor **2.2** is shown in green as a ball-and-stick model. Detailed view of the hotspot residue compositions (shown as sticks) of both dimer species are displayed in subpanels.

By analysis of the twisted TGT dimer structure, Ehrmann *et al.* hypothesized that the twisted dimer is not capable to bind and process the tRNA substrates due to steric reasons, hence rendering the enzyme inactive in this state. Therefore, stabilization of this novel twisted dimer state by small molecule ligands adds an additional opportunity to inhibit the function of TGT. However, the detection of subtle changes in the tertiary structure along with the geometrical characterization of the mechanisms behind the transformation into a non-functional state remains challenging.

2.1.2 Nanometer distance measurements via electron paramagnetic resonance and pulsed electron–electron double resonance spectroscopy

Electron paramagnetic resonance (EPR) spectroscopy has been applied to give closer insights into complex biomolecular systems, such as the mechanism behind molecular oxygen formation of the photosynthetic protein complex photosystem II.[43] The most frequently used EPR spectroscopic method is continuous wave (CW) EPR, whereby a sample is irradiated with constant microwaves. This allows the detection and study of molecules containing unpaired electrons. However, the absence of paramagnetic centers in most biomolecules, such as specific transition metals or naturally occuring radicals, limited the application to a small subset of biological studies.[44] The invention of site-directed spin labeling (SDSL) provided a way to introduce artificial spin labels to a biological system thus expanding the application scope when combined with EPR spectroscopy.[45–47] In case two or more spin labels are present, pulsed electron–electron double resonance (PELDOR or DEER) experiments can be applied to capture precise information about inter-spin distance changes in the range of 15 to 60 Å. This provides a powerful tool to investigate conformational dynamics and transformations of macromolecular systems in solution under static equilibrium conditions.[48–50] Most commonly, nitroxide spin labels such as MTSL (methanethiosulfonate spin label) are used, which react selectively with the thiol group of cysteines forming disulfide bridges (Figure 2.2a).[51–53] Site specificity is achieved by mutating cysteines into the protein sequence at the desired positions and mutating unwanted cysteines to e. g. alanine or serine. Alternatively, novel functionalized tetrathiatriarylmethyl (trityl) radicals[54–56] (Figure 2.2b), based on the so-called Finland Trityl (patented in 1996[57]), extend the repertoire of spin labels allowing distance measurements at physiological conditions[58,59], and enabling in-cell applications[54,56,60] as well as orthogonal spin labeling approaches[59,61].

PELDOR has been successfully applied to resolve structural details within integrative structural biology approaches, e. g., for the elucidation of SLC26 transporters and their functional dimeric states.[62] It has to be noted that PELDOR experiments are usually conducted using flash-frozen solution and, thus, have the potential to study the representative end states of the solution equilibrium. Furthermore, PELDOR can be used as a complementary method to X-ray crystallography to obtain data on conformational heterogeneity of protein samples.[63] Here, we report on a method that uses a combination of MTSL and trityl labeling together with PELDOR experiments to unravel details about a ligand-induced dynamic transformation of the TGT homodimer in solution.

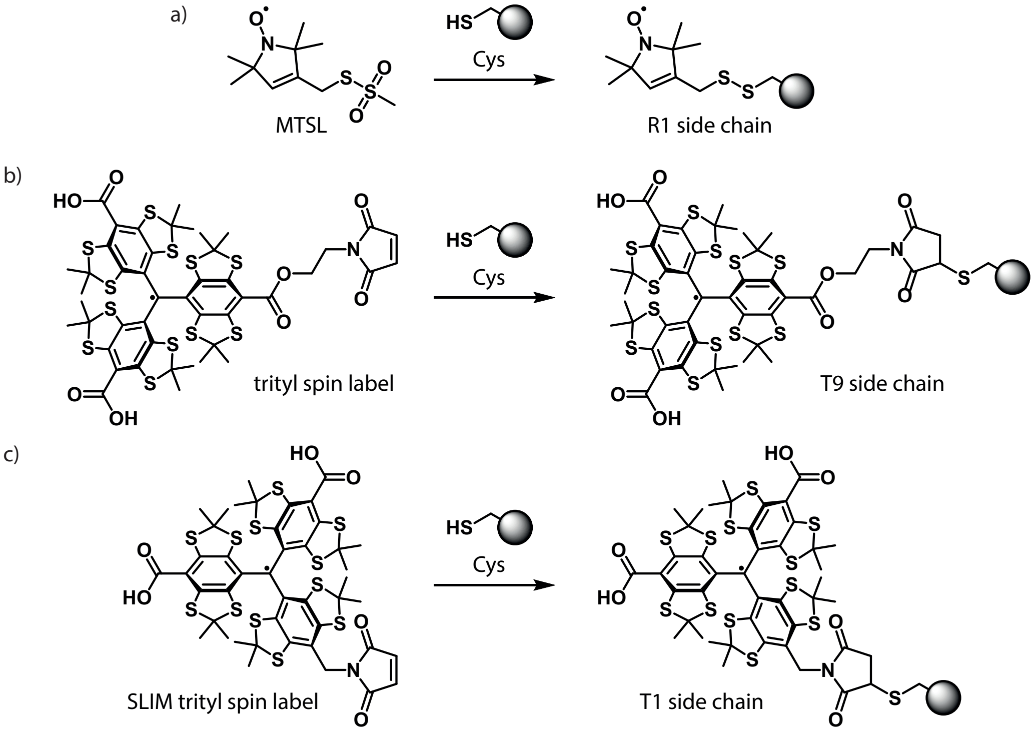

Figure 2.2: Examples of cysteine spin labeling strategies. a) Bioconjugation of MTSL to a cysteine residue under cleavage of sulfinic acid resulting in the R1 side chain. b, c) Bioconjugation of trityl spin labels to a cysteine residue via maleimide-based Michael addition resulting in the T9 and T1 side chains.

2.2 Results and Discussion

2.2.1 Preface

In this work, PELDOR spectroscopy was applied to unravel the conformational states of TGT in solution and to study its geometrical transformation from the functional to the twisted state in dependence of ligand binding. The recombinant expression and purification, nitroxide spin labeling and biophysical characterization of the protein samples were performed by the author of this thesis. Distance predictions of ligand-bound TGT are based on co-crystal structures reported by **Frederik R. Ehrmann** from the group of **Gerhard Klebe** (Philipps-Universität Marburg). In the course of the present work, an additional co-crystal structure of the ligand **2.2**-bound functional TGT dimer (PDB ID: 6YGR[64]) has been reported by **Andreas Nguyen** from the same group. The PELDOR experiments including the prior *in silico* distance predictions and data analysis were done by **Dinar Abdullin** while trityl spin labeling approaches with TGT were performed by **Caspar A. Heubach** from the group of **Olav Schiemann** (University of Bonn). The used *lin*-benzoguanine inhibitors were synthesized by members of the group of **François Diederich** (ETH Zürich) including **Toni Pfaffeneder**, **Luzi J. Barandun** and **Emmanuel A. Meyer**.

2.2.2 Search for the best spin labeling positions in TGT

To enable PELDOR measurements, the diamagnetic protein was spin-labeled with the nitroxide-based tag MTSL. Since TGT is overwhelmingly present in solution in its homodimeric form[20], the spin labeling of a single TGT residue is sufficient to enable the inter-monomer distance measurements via PELDOR. Crystal structures of both protein states, the functional state and the twisted state, allowed the systematic search for the best spin labeling sites using the *in silico* spin labeling program *MtsslWizard*[65]. The following criteria had to be considered for the search:

(1) The selected site has to be accessible for the spin label in both protein states.

(2) The distance r between two spin-labeled sites should be in the range of 15 to 60 Å in both protein states.

(3) r should differ between the functional and twisted states by more than 5 Å.

The first criterion is necessary for obtaining good labeling efficiency and also minimizes the probability of the local structural changes of the protein due to the introduction of the spin label. The second ensures that the inter-nitroxide distances will be in the sensitivity range of PELDOR. Finally, the last criterion allows a clear differentiation between both protein states. The details of the *in silico* simulations and the full set of selected spin labeling positions are given in Figure 2.3.

2.2.3 Biophysical characterization of spin-labeled TGT variants

Importantly, two of the selected positions, namely 87 and 319, were used for further experiments. Each of these positions was mutated to a cysteine to enable labeling via its reactive thiol group. To avoid the formation of unspecific modifications and intermolecular disulfide linkages between the TGT monomers, the conservative mutations C158S and C281S were introduced, yielding the variants $\text{TGT}^{\text{G87C/C158S/C281S}}$ and $\text{TGT}^{\text{C158S/C281S/H319C}}$. Then, Cys87 and Cys319 were spin-labeled via a covalent attachment of MTSL, respectively. The spin-labeled variants will be denoted in the following as $\text{TGT}^{\text{G87R1}}$ and $\text{TGT}^{\text{H319R1}}$, where R1 stands for the MTSL-attached cysteine residue (Figure 2.2a). To ensure comparable structural and oligomerization states, both mutants were successfully crystallized in the functional state (Figure 2.4a). Only marginal perturbations could be observed in the overall tertiary structure compared to the functional dimer (PDB ID: 1PUD). In case of $\text{TGT}^{\text{G87R1}}$, no electron density was observed for the R1-spin label indicating high residual flexibility and the existence of multiple conformations whereas in $\text{TGT}^{\text{H319R1}}$ the spin label could be successfully resolved after initial refinement (Figure 2.4a). It should be noted that both variants differ in their crystallization conditions (see Experimental Section 2.4.3). Furthermore, the homodimeric states in solution of $\text{TGT}^{\text{G87R1}}$ and $\text{TGT}^{\text{H319R1}}$ were verified by gel filtration compared to homodimeric wild type (WT) TGT and the mainly monomeric $\text{TGT}^{\text{Y330D}}$ mutant[22] (Figure 2.4).

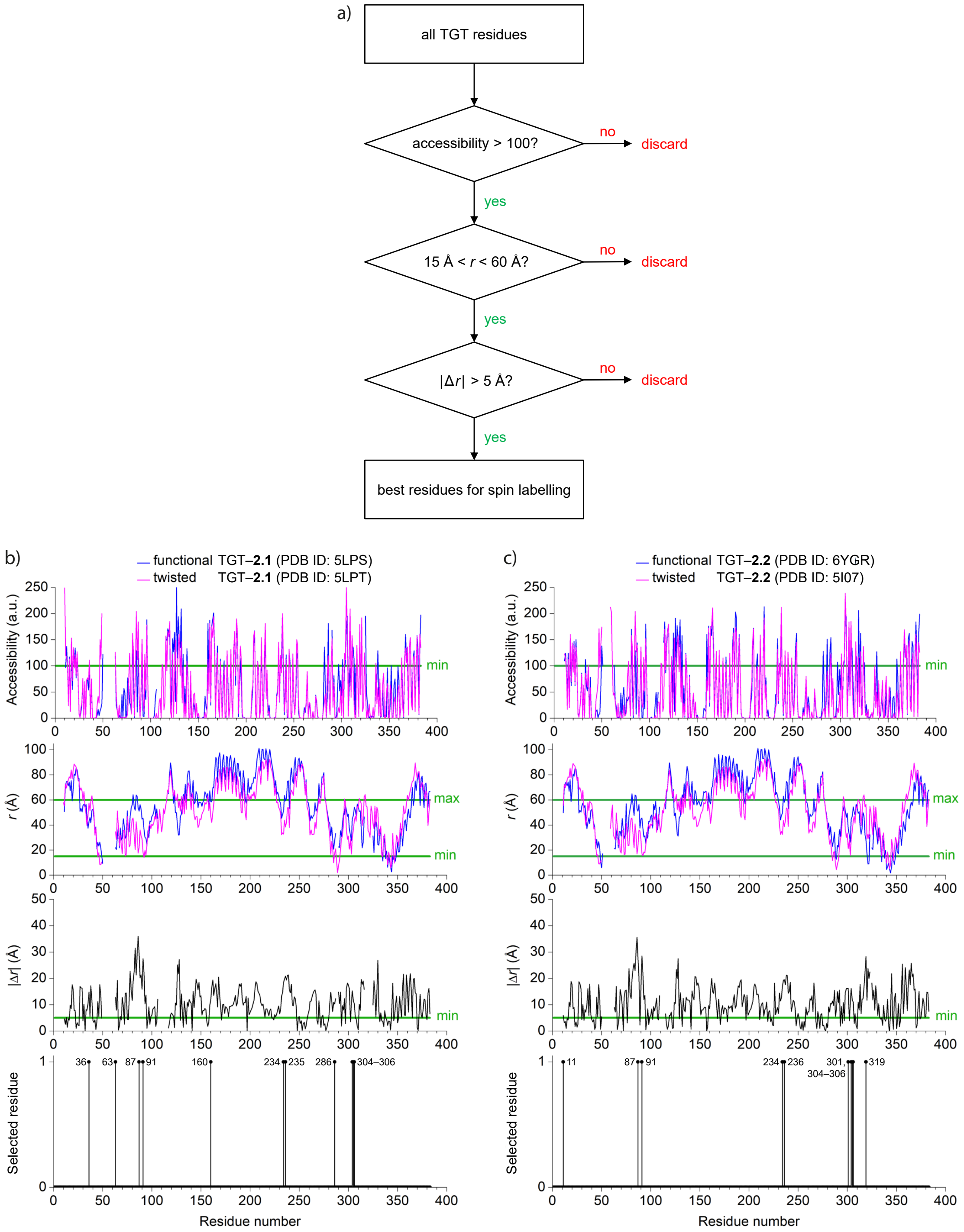

Figure 2.3: Search for the best spin labeling positions in TGT using the program *MtsslWizard*. a) The search algorithm with the search results for b) TGT–**2.1** (PDB IDs: 5LPS[34] and 5LPT[34]) and c) TGT–**2.2** (PDB IDs: 6YGR[64] and 5I07[33]). r denotes the distance between two spin-labeled sites of two equally single-labeled TGT monomers within each TGT homodimer. Δr denotes the difference in r between the functional and twisted states of TGT. Line breaks indicate residues ill-defined in the electron density of the used protein models.

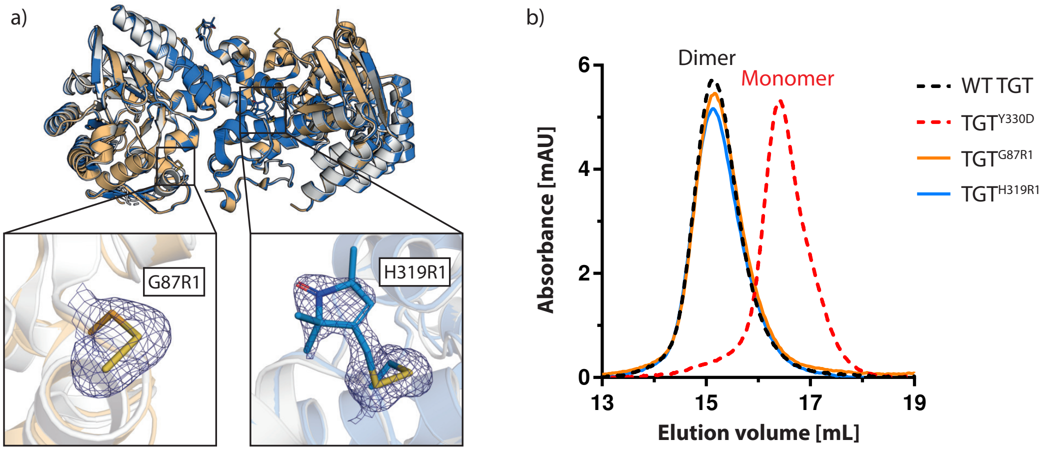

Figure 2.4: a) Structural comparison of the functional wild type TGT homodimer (gray, PDB ID: 1P0D[42]) with TGT^{G87R1} (orange, PDB ID: 7APL) and TGT^{H319R1} (blue, PDB ID: 7APM). Labeling positions are highlighted in subpanels with R1-label side chains shown as sticks and corresponding electron densities from $2mF_o - DF_c$ map contoured at 1.0 σ. b) Gel filtration elution profiles of TGT variants at 10 µM.

2.2.4 Assignment of PELDOR distance distributions

The PELDOR measurements were carried out on the ligand-free and ligand-bound forms of TGT^{G87R1} and TGT^{H319R1} (Figure 2.5a). The ligand-bound form was obtained after incubation of each mutant with either 3 eq. of ligands **2.1**–**2.4** (Figure 2.5b) or 1.5 eq. of tRNA over 24 h at room temperature. The amount of added ligands was chosen in accordance to their binding affinities[34] and was estimated to be sufficient to completely occupy both preQ$_1$ binding pockets of the TGT homodimer. The amount of added tRNA was half the amount of the ligands, because only one tRNA molecule binds to dimeric TGT.

The resulting distance distributions of the PELDOR measurements on the ligand-free and ligand-bound forms of TGT^{G87R1} and TGT^{H319R1} are depicted in Figure 2.6. The PELDOR time traces are shown in Figures 2.12 and 2.13 (Experimental Section 2.4.6) and have a good modulation depth, a clear dipolar oscillation and an excellent signal-to-noise ratio. This allowed an accurate conversion of the primary PELDOR data into inter-nitroxide distance distributions depicted in Figure 2.6a. Figure 2.6a reveals that the distance distribution determined for the ligand-free TGT^{G87R1} mutant contains a single unimodal peak at ~54 Å, whereas the distance distribution of ligand-free TGT^{H319R1} is bimodal and has two maxima at ~28 Å and ~34 Å. Most likely, the bimodality results from two different conformational ensembles of the spin labels at the position 319. Importantly, the distance distributions of both ligand-free mutant variants are in good agreement with the inter-nitroxide distance predictions obtained from the crystal structure of the functional TGT dimer (Figure 2.6a, rows 9–11). This allows assigning the obtained distance distributions to the functional state. The same assignment can also be done for the samples of both mutants incubated with tRNA and ligand **2.4**, because their distance distributions are identical to the ones of both ligand-free TGT variants.

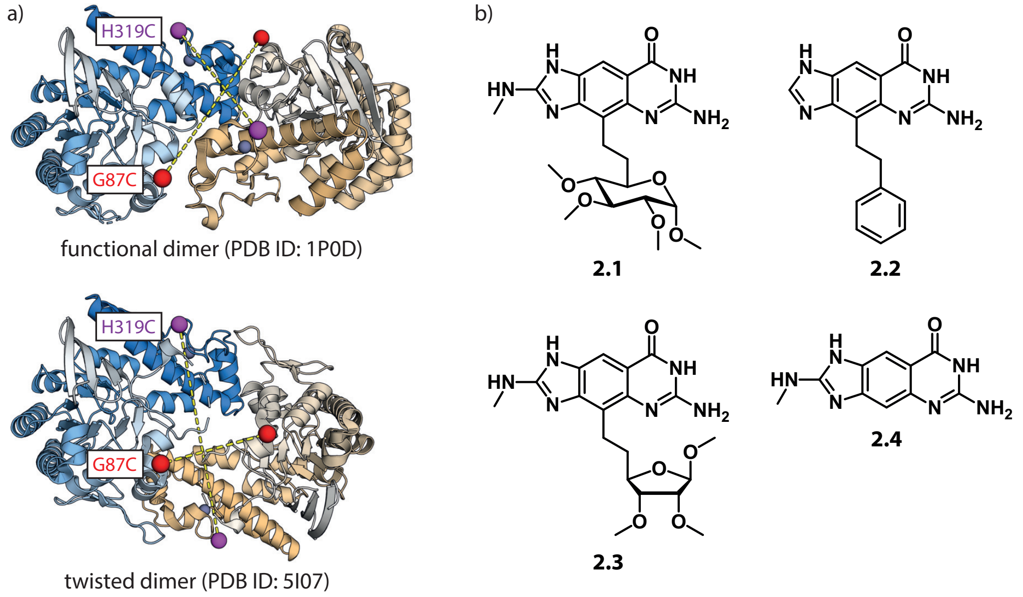

Figure 2.5: a) The spin labeling sites G87C (red spheres) and H319C (purple spheres) shown together with the crystal structures of the functional (top, PDB ID: 1P0D[42]) and twisted (bottom, PDB ID: 5I07[33]) TGT homodimers. Zinc ions are shown as dark gray spheres. Yellow dashed lines connect the spin labeling sites, between which the PELDOR-based distance measurements were carried out. b) Chemical structures of ligands **2.1**–**2.4**.

A pronounced difference was observed in the ligand-bound versus ligand-free distance distributions if both mutants were incubated with ligand **2.1**. In addition to the distance distribution, found for the ligand-free state, a further peak appears around 28 Å for the variant TGT$^{\mathrm{G87R1}}$–**2.1** and around 46 Å for TGT$^{\mathrm{H319R1}}$–**2.1**. Comparing with the computed distribution of possible inter-nitroxide distances based on the crystal structures of the functional and twisted TGT homodimer (Figure 2.6a, rows 7–8 and 9–11, respectively), the additional distance peak for TGT$^{\mathrm{G87R1}}$–**2.1** can be assigned to the presence of the twisted homodimer (Figure 2.6a, row 1). For TGT$^{\mathrm{H319R1}}$–**2.1**, an analogous additional distance maximum is detected that is also assignable to the twisted homodimer. However, it is less obvious, because the maximum of this distribution is shifted from the computationally predicted most probable distance by 14 Å (Figure 2.6a). A closer comparison of the *apo* TGT crystal structure (PDB ID: 1P0D[42]) with the ligand **2.1**-bound functional dimer (PDB ID: 5LPS[34]) reveals that the zinc-binding subdomain, which hosts residue 319, is very flexible as the residues Glu317–Gln324 are not resolved in the structure and the zinc ion is only occupied at 21 % (compared to 100 % in the *apo* structure). Although the subdomain is resolved in the twisted dimer, it does not exclude that this results from crystal packing forces of an adjacent crystal mate. Since the conformational flexibility of the protein was not taken into account in the *in silico* simulations, the predicted distances might be affected by this simplification, which could explain the deviation of the predicted from the measured PELDOR results.

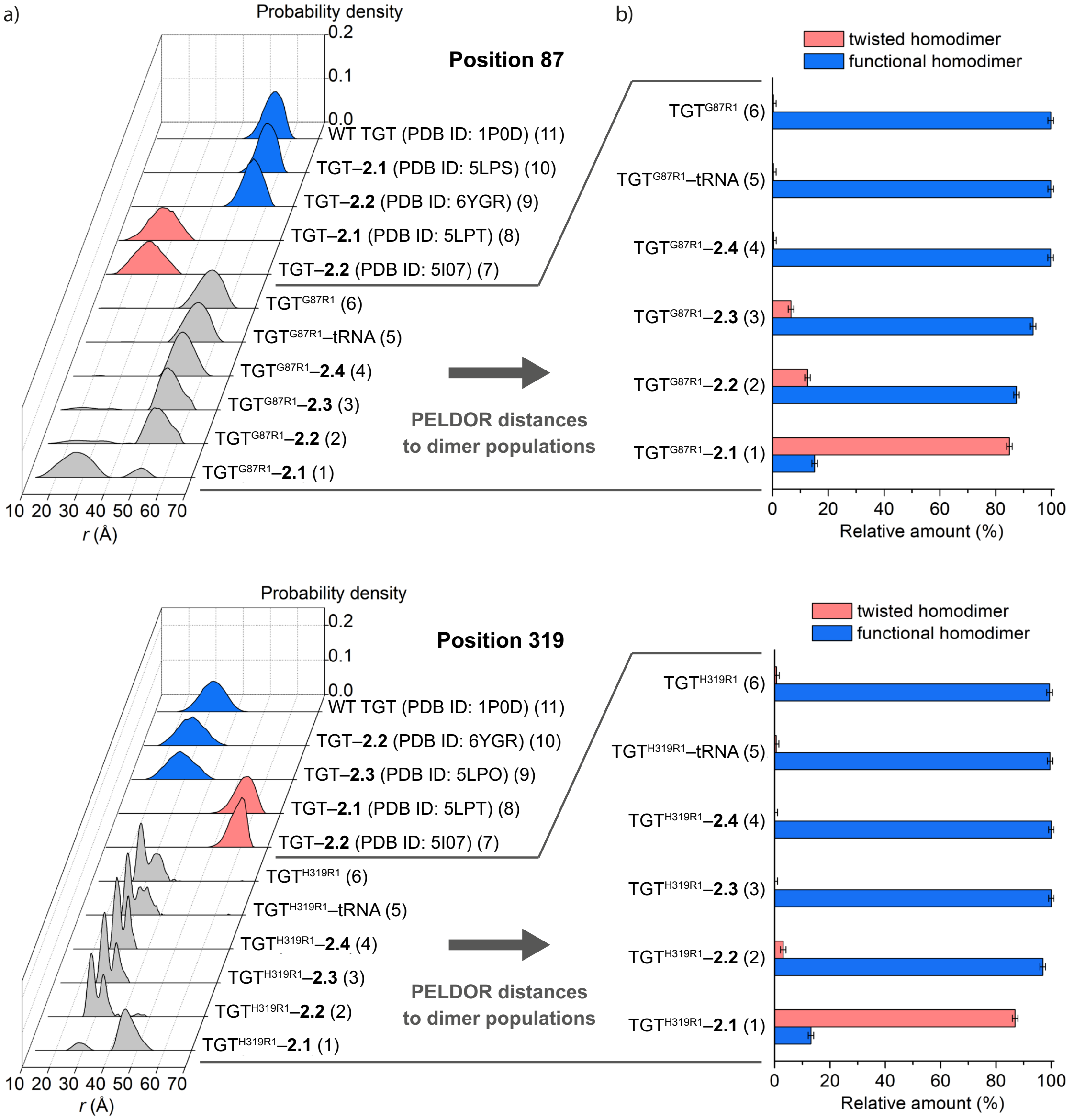

Figure 2.6: PELDOR measurements on TGT^{G87R1} (top) and TGT^{H319R1} (bottom) incubated over 24 h with ligands **2.1**–**2.4** or tRNA. a) PELDOR-based inter-nitroxide distance distributions (rows 1–6, gray) and their *in silico* predictions based on the crystal structures of the twisted (rows 7–8, rose) and functional (rows 9–11, blue) TGT homodimers. The row numbers are indicated in parentheses. The original PELDOR time traces and the error estimates for the PELDOR-derived distributions are given in Figures 2.12 and 2.13 (Experimental Section 2.4.6). b) The relative amount of the functional (blue) and twisted (rose) TGT homodimers as derived from the PELDOR-based distance distributions. For TGT^{G87R1}, the inter-nitroxide distances below and above 40 Å were assigned to the twisted and functional homodimers, respectively. Inversed distance ranges were used for the assignment of the twisted and functional homodimers of TGT^{H319R1}.

2.2.5 Ligand-dependent formation of the twisted dimer

Finally, all distance distributions, identified for the TGT variants bound to ligand **2.1**, are also observed for those found by binding ligands **2.2** and **2.3** to the corresponding variants (Figure 2.6a, rows 2–3). However, in each case, the relative intensity of the peak corresponding to the twisted homodimer is strongly dependent on the ligand. For the variants incubated with ligands **2.2** and **2.3**, the distance peaks assigned to the functional homodimer are dominant, compared to the twisted homodimer. Thus, the situation is reversed compared to ligand **2.1**, where the twisted state is higher populated. Since the distance distributions mutually assigned to the two forms do not overlap, integration over both states allows determining the relative ratio of functional and twisted homodimers in the different samples (Figure 2.6b). The ligand-free samples contain only the functional homodimers, which is also the only species populated with bound tRNA and ligand **2.4** (Figure 2.6b, rows 4–6). No twisted dimer formation is observed upon incubation with tRNA as it only binds and stabilizes the functional TGT homodimer. Obviously, the lack of a substituent, which penetrates into the ribose-34 binding pocket, avoids triggering the formation of the twisting rearrangement of the homodimer as observed by the *lin*-benzoguanine parent scaffold **2.4**. In contrast, ligands **2.1**–**2.3** induce partial conformational transformation, simultaneously populating both homodimeric states in solution (Figure 2.6b, rows 1–3). Likely, this also explains why both homodimeric forms could be crystallized with ligands **2.1** and **2.2** under the same crystallization conditions.[34] Surprisingly, the relative population of both states depends on the bound ligand. With ligand **2.1**, the twisted homodimer dominates with 86 ± 1 %, but it is only minor present for ligands **2.2** and **2.3** (8 ± 5 % and 4 ± 3 %, respectively).

A further look into the ligand binding site reveals structural details of the rearrangement from the functional into the twisted TGT homodimer. Notably, the moieties of ligands **2.1**–**2.3** clash with the hydrophobic residues Val45, Leu68, and Val282 at the bottom of the ribose-34 subpocket. As a consequence, the loop–helix motif, which shields the aromatic hotspot from water access, adopts a perturbed conformation in the ligand-bound functional as well as twisted dimer state (Figure 2.7a–c). Besides the increased flexibility of the loop–helix motif, a tilt movement of helix αA (residues Gly105–Leu111) can be observed between the two dimeric end states (Figure 2.7a and b). The helix hosts residue Tyr106 which recognizes the tricyclic core of the *lin*-benzoguanine scaffold via π–π stacking. Furthermore, the structural adaptation allows the formation of a new interface contact via hydrogen bonding between Gln107 and Glu339’ in the twisted dimer. In the functional TGT complex structures with ligands **2.2** and **2.3**, helix αA adopts a similar conformation as in the *apo* structure. However, in case of ligand **2.1**, this helix is disordered in the functional TGT form and not resolved in the structure indicating higher structural flexibility (Figure 2.7a). This can be explained by a steric clash of residue Gln107 with the anomeric methoxy group of the pyranose substituent that points toward helix αA (Figure 2.7a and d). Ligands **2.2** and **2.3** lack this extension allowing Gln107 and helix αA to adopt a stable conformation in the structure.

Presumably, in addition to the collapse of the loop–helix motif, a destabilization of helix αA aids the formation of the twisted dimer. Furthermore, the zinc-binding domain becomes increasingly destabilized when the functional TGT dimer is bound to ligand **2.1** as evidenced by the ill-defined residues Glu317–Gln324 (Figure 2.7e) and a lower zinc occupancy compared to the complex with ligand **2.2** (21 % vs. 44 %, respectively). These findings could explain the high population of the twisted dimer species upon addition of ligand **2.1**.

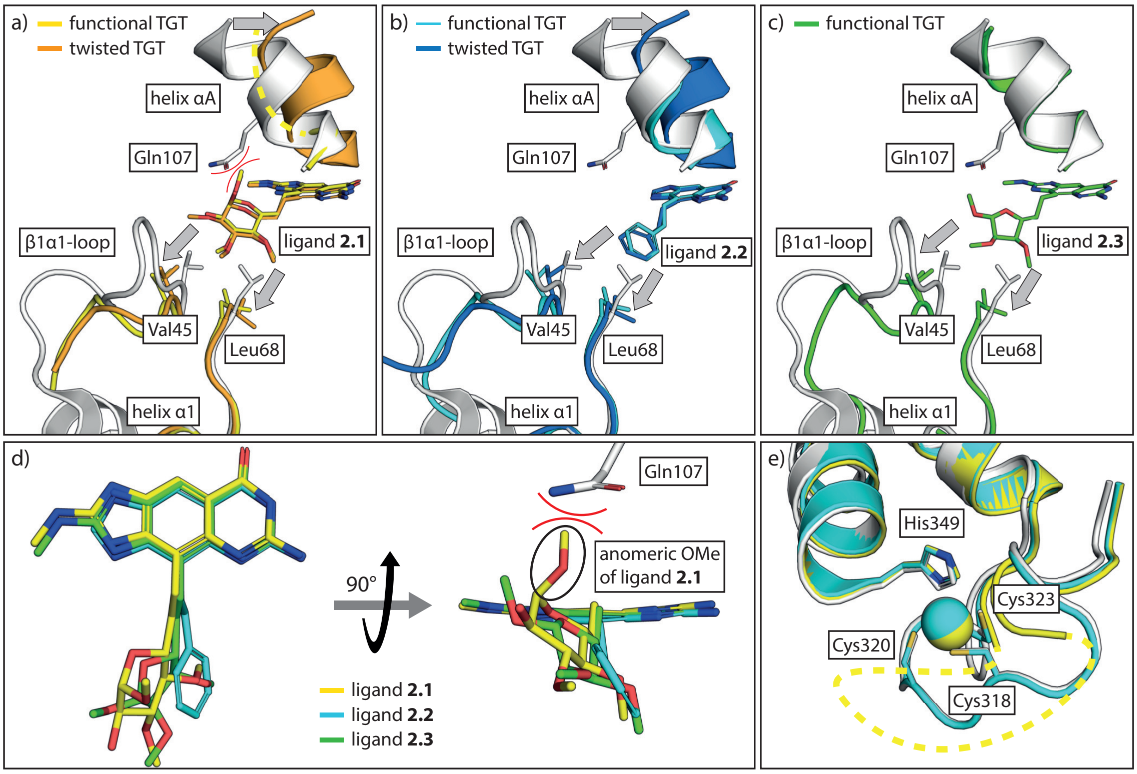
a)
functional TGT
twisted TGT
helix αA
Gln107
β1α1-loop
ligand **2.1**
Val45
Leu68
helix α1
b)
functional TGT
twisted TGT
helix αA
Gln107
β1α1-loop
ligand **2.2**
Val45
Leu68
helix α1
c)
functional TGT
helix αA
Gln107
β1α1-loop
ligand **2.3**
Val45
Leu68
helix α1
d)
Gln107
anomeric OMe
of ligand **2.1**
90°
ligand **2.1**
ligand **2.2**
ligand **2.3**
e)
His349
Cys323
Cys320
Cys318

Figure 2.7: Structural comparison of the functional *apo* TGT structure (gray, PDB ID: 1P0D[42]) with the ligand-bound structures of a) TGT–**2.1** (functional: yellow, PDB ID: 5LPS[34]; twisted: orange, PDB ID: 5LPT[34]), b) TGT–**2.2** (functional: cyan, PDB ID: 6YGR[64]; twisted: blue, PDB ID: 5I07[33]), and c) TGT–**2.3** (functional: green, PDB ID: 5LPO[34]). Structural movements from the functional to the twisted state are indicated by gray arrows. Only one of two equally possible conformations of ligand **2.1** is shown. Ill-defined residues in TGT–**2.1** are indicated as yellow dashes. d) Structural comparison of ligands **2.1**–**2.3** from their ligand-bound functional dimer structures. The anomeric methoxy group of ligand-**2.1** is encircled and its steric clash with Gln107 from *apo* TGT is indicated by red arcs. e) Detailed view of the zinc-binding subdomain of TGT–**2.1** (yellow, PDB ID: 5LPS[34]) and TGT–**2.2** (cyan, PDB ID: 6YGR[64]) compared to the *apo* TGT structure (gray, PDB ID: 1P0D[42]). Zinc ions are shown as spheres and the zinc-coordinating residues are shown as sticks. Ill-defined residues in TGT–**2.1** are indicated as yellow dashes.

2.2.6 PELDOR measurements in dependence of incubation time

In order to check whether the incubation time of 24 h was sufficient to reach the equilibrium, the PELDOR measurements were repeated on ligand-bound samples of TGT^{G87R1} equilibrating for 1, 24, and 72 h (Figure 2.8 and Figures 2.14–2.16, Experimental Section 2.4.6). Remarkably, the relative amount of twisted homodimers increases with incubation time for ligands **2.1**–**2.3** from 1 to 72 h. After 24 h, the system seems fully equilibrated as no further increase is recorded. Possibly, the relative ratio by how much the two states are populated indicates the energetic stabilization of the two TGT forms with respect to the bound ligand. An explanation for this difference can not be given yet, however, a ligand with a C4-substituent, which occupies the ribose-34 subpocket, seems to be essential to induce the transformation between both states.

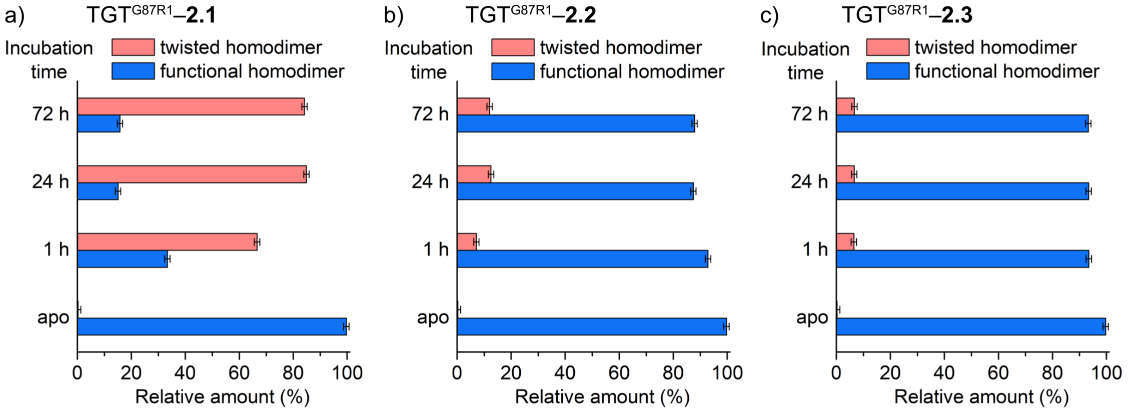

Figure 2.8: The relative amount of the functional (blue) and twisted (rose) TGT^{G87R1} homodimers bounds to ligands a) **2.1**, b) **2.2**, and c) **2.3** in dependence of the ligand incubation time. The original PELDOR time traces and the error estimates for the PELDOR-derived distributions are given in Figures 2.14–2.16 (Experimental Section 2.4.6).

2.2.7 Orthogonal spin labeling and mixing experiments for the elucidation of the twisting mechanism

Importantly, the data in Figure 2.8 discloses that the conversion of functional to twisted homodimer equilibrates slowly within hours. Given the fact that ligand binding to TGT occurs on very short time scale, ligand accommodation cannot be the rate-determining step. Thus, the observed conversion rate must agree with a slow structural re-organization mechanism of the TGT homodimers. Two mechanisms can be considered: (1) an intramolecular twisting rotation of the two TGT monomers against each other or (2) a dissociation/association process proceeding via intermediately fully separated monomers. In order to determine, which of these two mechanisms takes place, an orthogonal spin labeling approach was attempted by labeling the mutant TGT$^{G87C/C158S/C281S}$ independently with two different tags.

Initial spin labeling attempts with the maleimide-conjugated Finland trityl radical spin label SLIM[56], with the aim to yield the TGT$^{G87T1/C158S/C281S}$ variant (Figure 2.2c), failed due to low labeling efficiency (~15 %, Figure 2.9a). Interestingly, a change of color from the expected trityl brown towards a pinkish color was observed during the labeling procedure. This led us to additionally investigate the potential unspecific binding of the trityl core to the protein, e. g. via hydrophobic interaction, by labeling experiments with a non-bioconjugatable Finland trityl radical on TGT$^{G87C/C158S/C281S}$. No absorbance at 459 nm could be detected after desalting and filtering the reaction mixture, hence unspecific binding of the trityl core can be excluded. Furthermore, unspecific reactivity of the maleimide moiety was investigated by incubating an ester-linked maleimide trityl spin label (Figure 2.2b) with the TGT$^{C158S/C281S}$ variant which does not contain addressable cysteine residues. Although, no reaction was expected between the two components, a similar color change from brown to pink was observed as in the initial labeling experiments with TGT$^{G87C/C158S/C281S}$ and SLIM. Additionally, the trityl label could not be completely seperated from TGT$^{C158S/C281S}$ in the filtering process through a desalting column (Figure 2.9b). This indicates that unspecific binding of the label could be related to its maleimide moiety.

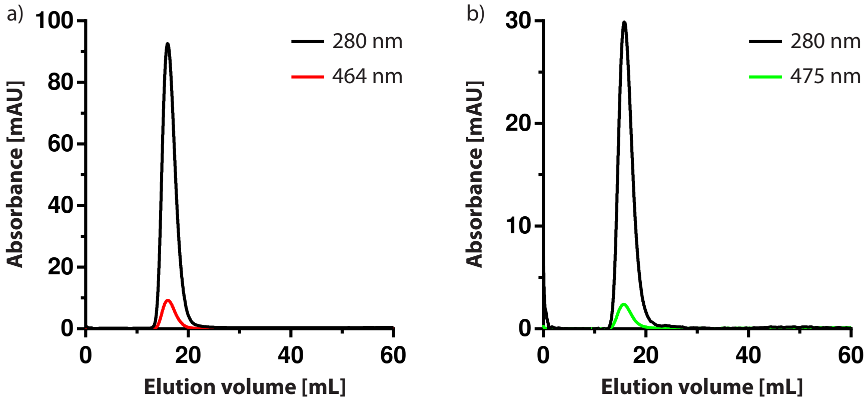

Figure 2.9: Chromatograms from desalting steps with parallel detection of two wavelengths for a) TGT$^{G87C/C158S/C281S}$ with the SLIM trityl label and b) TGT$^{C158S/C281S}$ with the ester-linked maleimide trityl label.

Alternatively, besides the detection of distances between two independently spin-labeled TGT monomers, a mixing experiment between the TGT^{G87R1} and TGT^{H319R1} variants also represents a viable approach. In case of an intra-dimer rotational mechanism, the immediate formation of a TGT^{G87R1}–TGT^{H319R1} heterodimer would be absent, hence, no distance distribution should be observed for the heterodimeric species upon ligand addition. Likely, the detection of a distance distribution corresponding to the twisted heterodimeric species would indicate a mechanism based on the dissociation of the functional dimers followed by the re-association into their twisted states (Figure 2.10).

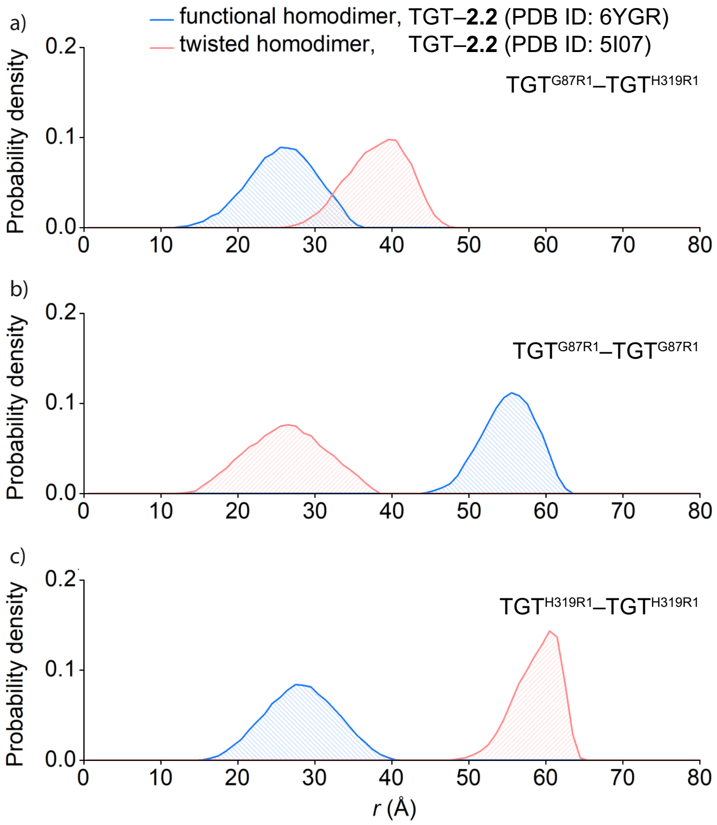

Figure 2.10: Inter-spin distance predictions for the a) TGT^{G87R1}–TGT^{H319R1} heterodimer as well as the b) TGT^{G87R1}–TGT^{G87R1} and c) TGT^{H319R1}–TGT^{H319R1} homodimers calculated by *MtsslWizard*[65].

2.3 Conclusion

In this study, we designed an EPR-based approach to uncover the twisted TGT dimer formation in a solution equilibrium. Therefore, potential spin labeling sites were first evaluated *in silico* and two spin-labeled mutants, TGT^{G87R1} and TGT^{H319R1}, were designed. The PELDOR distance distributions fit well with the predicted distances from previously obtained crystal structures thus verifying that the twisted dimer exists as a species in solution and is not an artifact resulting from crystal packing forces. However, under the experimental conditions of the PELDOR measurements, only with ligand **2.1** the two separated species can be recorded, while ligands **2.2** and **2.3** only marginally show the transformed twisted state besides the higher populated functional dimer. Contrary, protein-observed ^{19}F NMR results have demonstrated that ligands **2.2** and **2.3** show a similar effect in the transformation regulation.[64] Since the PELDOR experiments were performed on flash-frozen samples after incubation at room temperature, a shift in the equilibrium between the functional and twisted dimer states during the freezing process cannot be ruled out.

We hypothesize that a small structural detail of ligand **2.1**, the anomeric methoxy group, is able to displace the nearby helix αA and thereby favor the rearrangement into the twisted dimer. Ligands with substituents occupying a similar or even larger space as this methoxy group might be worth for further investigations. The low population of the twisted dimer species in case of ligand **2.2** indicates, that crystallization conditions might additionally play a role in the equilibrium between both dimer states. Besides a difference in buffer and salt compositions, the distinct difference in pH between the crystallization and PELDOR setup (5.5 vs. 7.4, respectively) could explain the low population of the twisted dimer upon incubation with ligand **2.2**. Preceding mutagenesis studies have shown that the loop–helix motif is destabilized at slightly acidic conditions which is putatively linked to a destabilization of the TGT homodimer.[20,23] Nevertheless, co-crystal structures of the twisted dimer species with ligands **2.1** and **2.2** have been obtained and structurally characterized, independent of the relative population amount as seen in the results of the PELDOR measurements. We suggest that, once a twist-inducing ligand is present in the TGT solution, the crystallization of the twisted dimer removes the species from the solution equilibrium. Subsequently, this leads to an increased transformation of the functional into the twisted dimer in order to restore the equilibrium between both species.

Ligands **2.1**–**2.3** are capable of displacing the loop–helix motif by occupation of the ribose-34 subpocket. Moreover, previous ligand binding studies via isothermal calorimetry (ITC) showed that the binding of ligands **2.1**–**2.3** is largely entropically driven likely due to the destabilization of the loop–helix motif. Additionally, a perturbed zinc-binding subdomain is observed. We suggest that a ligand-induced destabilization of the dimer contact is the first step in the rearrangement mechanism to form the twisted dimer, which is accompanied by re-localization of helix αA. The differentiation of the two possible twisting mechanisms by PELDOR spectroscopy remains to be elucidated. Once the trityl labeling is successful, the PELDOR measurements will be performed with 1:1 mixtures of the nitroxide-labeled $\text{TGT}^{\text{G87R1/C158S/C281S}}$ and the trityl-labeled $\text{TGT}^{\text{G87T1/C158S/C281S}}$ variants. Alternatively, a mixing experiment with $\text{TGT}^{\text{G87R1}}$ and $\text{TGT}^{\text{H319R1}}$ could be performed. In case of a dissociation/association mechanism, mixed distances of a nitroxide–trityl or $\text{TGT}^{\text{G87R1}}$–$\text{TGT}^{\text{H319R1}}$ heterodimer should be observed while these should be absent in case of an intra-dimer rotational mechanism.

To summarize, we demonstrated that PELDOR spectroscopy is a valuable technique to elucidate structurally observed phenomena of the TGT homodimer. The results verify the ligand-induced formation of a twisted dimer species in a solution equilibrium, thus, confirming the previously characterized TGT–ligand co-crystal structures. The pyranose-substituted *lin*-benzoguanine ligand **2.1** proved to be superior, compared to ligands **2.2** and **2.3**, in shifting the equilibrium between the two dimer states towards the twisted dimer form. Combined with our structural analysis, we believe that an additional displacement of helix αA, which is caused by the geometric orientation of the pyranose substituent in ligand **2.1**, favors the formation of the twisted TGT dimer.

2.4 Experimental Section

2.4.1 Mutagenesis and recombinant production of *Z. mobilis* TGT

Mutagenesis and expression of the *Z. mobilis tgt* gene and its mutated variants were performed as previously described by site-directed mutation and plasmid-based expression of the vector pPR-IBA2 (IBA Lifesciences).[22] Plasmids encoding the required mutated TGT variants were prepared using the PureYield™ Plasmid Miniprep System (Promega). Based on the $\mathrm{TGT}^{\mathrm{F92C/C158S/C281S}}$ construct,[22] a reverse C92F and single-site surface cysteine mutations were introduced via the QuikChange Lightning Site-Directed Mutagenesis Kit (Agilent) according to the vendor instructions. DNA primers were purchased from Eurofins Genomics (Ebersberg, Germany) and are summarized in Table 2.1. In each case, the new construct was re-sequenced by Eurofins Genomics to confirm the presence of the desired mutations as well as the absence of any further unwanted mutation. The final constructs were each transformed into *Escherichia coli* BL21-CodonPlus (DE3)-RIPL cells (Agilent).

A single colony was picked from the freshly transformed agar plate and grown overnight in 100 mL of lysogeny broth (LB) medium supplemented with 100 µg mL^{-1} ampicillin and 34 µg mL^{-1} chloramphenicol while shaking at 37 °C. The next day, a large-scale culture in LB medium, supplemented with 100 µg mL^{-1} ampicillin and 34 µg mL^{-1} chloramphenicol, was inoculated with 10 mL of overnight culture per liter. The culture was grown at 37 °C by shaking at 140 rpm until the optical density at 600 nm (OD_{600}) reached a value between 0.6 to 0.7 and was then cooled to 16 °C while shaking. After 1 h, overnight protein expression was induced by the addition of 1 mM IPTG. The cells were harvested the next day by centrifugation using a JA-10 rotor (Beckman Coulter) at 4 °C and 10 000 rpm for 10 min. The collected cells were disrupted by sonication using a Branson Sonifier™ 250 in 100 mL lysis buffer (20 mM TRIS, pH 7.8, 10 mM EDTA, 1 mM DTT and 1 cOmplete™-Protease Inhibitor Cocktail Tablet (Roche) per 4 L of bacterial culture). Subsequently, the cell debris was removed by centrifugation using a JA-25.50 rotor (Beckman Coulter) at 4 °C and 20 000 rpm for 1 h. The supernatant was collected and loaded onto a Q Sepharose® Fast Flow anion exchange column (XK 26/15, GE Healthcare) conditioned with buffer A (10 mM TRIS, pH 7.8, 1 mM EDTA, 1 mM DTT). After washing with buffer A, the target protein was eluted by applying a linear NaCl gradient from 0 to 100 % (v/v) buffer B (buffer A plus 1 M NaCl). The protein-containing fractions, endowed with an N-terminal Strep-tag® II, were then loaded onto a Strep-Tactin® Superflow® column (XK 16/10, IBA Lifesciences) conditioned with buffer W (100 mM TRIS, pH 7.8, 1 mM EDTA, 1 M NaCl). After washing the column with buffer W, the protein was eluted with buffer E (buffer W plus 2.5 mM D-desthiobiotin). All chromatographic steps were carried out at room temperature using an ÄKTAprime™ plus FPLC system (GE Healthcare). All TGT-containing fractions were combined and concentrated to ca. 2 mg mL^{-1} in high-salt buffer (10 mM TRIS, pH 7.8, 1 mM EDTA, 2 M NaCl) using Vivaspin® 20 centrifugal concentrators (30 000 MWCO, Sartorius). Subsequently, the Strep-tag® II was chipped off and separated from the target protein by means of the Thrombin Cleavage Capture Kit (Novagen®) according to the manufacturer's instructions.

Table 2.1: DNA primer sequences used for mutagenesis. Nucleobases deviating from the original *tgt* sequence are underlined.

Mutation / Primer ID	Sequence
G87C_f	5’-GTATTGCAAAACTG$\underline{\text{T}}$GTGGTCTGCATAGC-3’
G87C_r	5’-GCTATGCAGACCAC$\underline{\text{A}}$CAGTTTTGCAATAC-3’
H319C_f	5’-GGATAGCGAATGT$\underline{\text{TGC}}$TGTGCAGTTTGTC-3’
H319C_r	5’-GACAAACTGCACA$\underline{\text{GCA}}$ACATTCGCTATCC-3’
C92F_f	5’-GTGGTCTGCATAGCT$\underline{\text{T}}$TATGGGTTGGGATC-3’
C92F_r	5’-GATCCCAACCCATA$\underline{\text{A}}$AGCTATGCAGACCAC-3’

2.4.2 Spin labeling of TGT variants

Nitroxide spin labeling

After tag cleavage, the protein was spin-labeled by incubation with 10 eq. of MTSL overnight at room temperature. In case of $\text{TGT}^{\text{H319R1}}$, prior to spin labeling, the protein was treated with 10 mM DTT for 2 h at room temperature and DTT was removed by filtering through an illustra™ NAP™-25 column (GE Healthcare) pre-equilibrated with high-salt buffer. After spin labeling, the sample was filtered through the same column to remove unbound MTSL. Spin labeling efficiencies were determined by mass spectrometry to 100 % and 90 % for $\text{TGT}^{\text{G87R1}}$ and $\text{TGT}^{\text{H319R1}}$, respectively (Figure 2.11). Prior to the PELDOR experiments, the sample was dialyzed against deuterated PELDOR buffer (50 mM TES, pH 7.4, 2 M NaCl in D_2O) and concentrated via Vivaspin® 20 centrifugal concentrators to ca. 10 mg mL^{-1}. 100 µL aliquots of the samples were flash-frozen in liquid nitrogen and stored at −80 °C until further usage.

Trityl spin labeling

Prior to labeling with trityl spin labels, the protein was diluted to a final amount of 12 nmol in labeling buffer (10 mM HEPES, pH 6.8, 1 mM EDTA, 2 M NaCl) and subsequently treated with 1 mM TCEP for 1.5 h at room temperature. The mixture was then desalted through a PD-10 column (GE Healthcare) and 5 eq. of spin label (from DMSO stock) were added to the eluate. For the binding test between the trityl core and the protein, the non-bioconjugatable Finland trityl radical was used instead of a spin label. The labeling reaction mixture was incubated for 1 h at 4 °C or 16 h at room temperature. Excess label was removed using a PD-10 column and absorbance was tracked at 280 nm as well as at the absorption maximum of the respective spin label. Labeling efficiency was calculated by measuring the absorbance at the absorption maximum using the respective extinction coefficients for the TGT variants and the spin labels (SLIM[56]: $\varepsilon_{459} = 0.02099\ \text{L}\ \mu\text{mol}^{-1}\ \text{cm}^{-1}$, $\varepsilon_{280} = 0.05152\ \text{L}\ \mu\text{mol}^{-1}\ \text{cm}^{-1}$; ester-linked maleimide trityl spin label[54]: $\varepsilon_{467} = 0.0075\ \text{L}\ \mu\text{mol}^{-1}\ \text{cm}^{-1}$, $\varepsilon_{280} = 0.0193\ \text{L}\ \mu\text{mol}^{-1}\ \text{cm}^{-1}$).

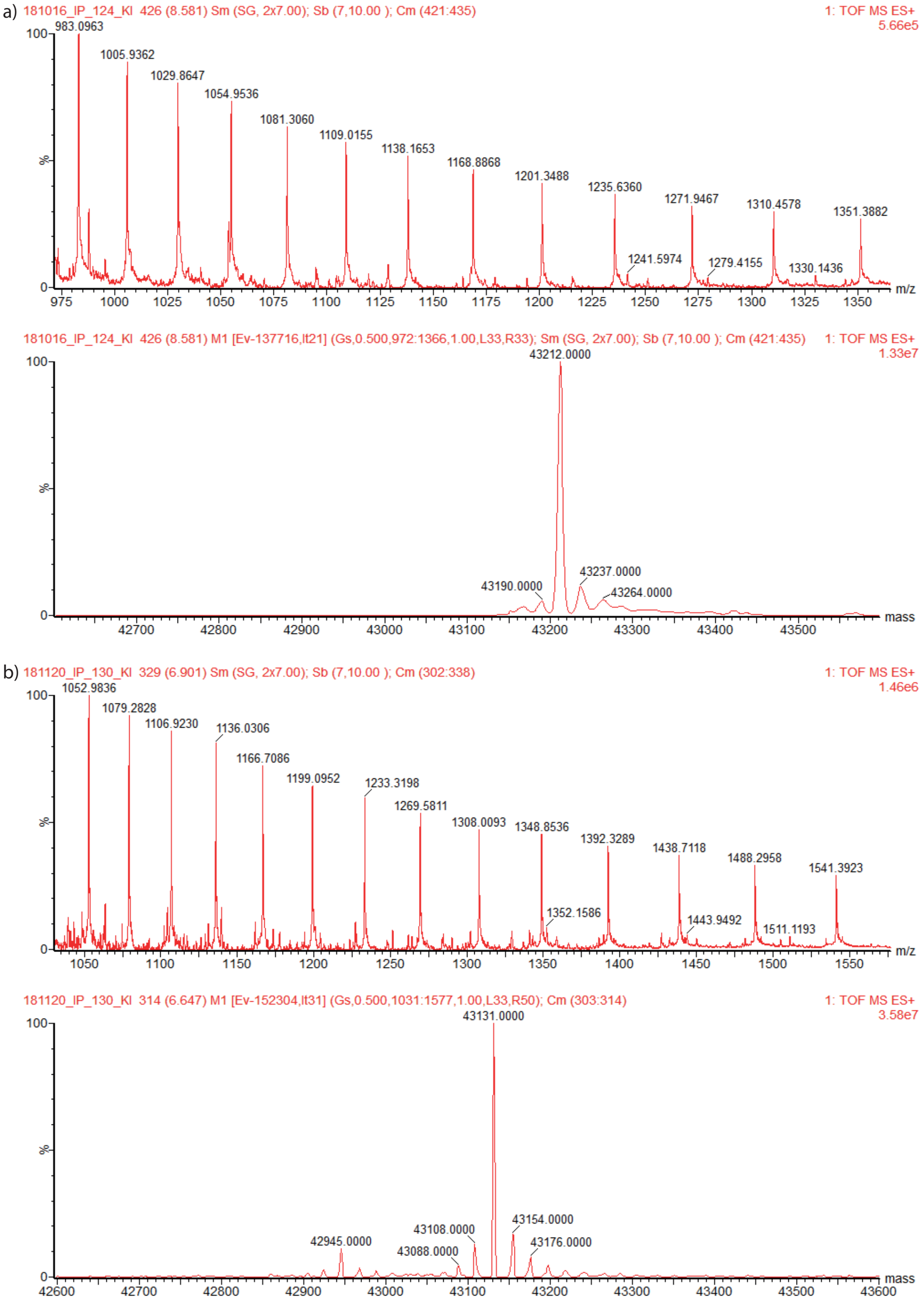

Figure 2.11: Mass spectra and deconvoluted spectra of a) TGT$^{G87R1/C158S/C281S}$ (calculated mass: 43 212.1 Da (labeled), 43 027.8 Da (unlabeled)) and b) TGT$^{C158S/C281S/H319R1}$ (calculated mass: 43 132.0 Da (labeled), 42 947.7 Da (unlabeled)).

2.4.3 Crystallization and structure determination

Crystallization of TGT was performed using the hanging-drop vapor diffusion method at 18 °C. For the R1-labeled TGT variants, the protein solutions (10 mg mL^{-1} in high-salt buffer) were each mixed with reservoir solution (0.1 M TRIS, pH 8.5, 10 % (v/v) DMSO, 7 % (w/v) PEG 8000 or 0.1 M MES, pH 5.5, 0.5 mM DTT, 10 % (v/v) DMSO, 13 % (w/v) PEG 8000) in a 1:1 volume ratio. In case of the functional TGT–**2.2** co-crystallization, the protein solution (31 mg mL^{-1} in high-salt buffer) was mixed with a DMSO stock containing 10 mM of ligand **2.2** yielding a final ligand concentration of 1.6 mM. The protein–inhibitor mixture was then mixed with reservoir solution (0.1 M MES, pH 5.5, 0.5 mM DTT, 10 % (v/v) DMSO, 13 % (w/v) PEG 8000) in a 1:2 volume ratio. Crystals grew within two weeks in the presence of 500 or 650 µL reservoir solution in the plate wells. Prior to data collection, the crystals were transferred to a reservoir solution containing 30 % (v/v) glycerol as cryo-protectant for a few seconds and vitrified in liquid nitrogen. Diffraction data were collected at a wavelength of 0.91841 Å and temperature of 100 K at the synchrotron beamline 14.1 at BESSY II (Helmholtz-Zentrum Berlin). Indexing, processing and scaling of the diffraction images were done using *XDS*[66] and *XDSAPP*[67]. The structures were determined via molecular replacement using the program *Phaser*[68] from the *CCP4 suite*[69] with the PDB entry 1P0D[42] or 1PUD[18] as initial search model. Model building was done in *Coot*[70] and the program *PHENIX*[71] was used for structure refinement. Data collection and refinement statistics are summarized in Table 2.2.

2.4.4 Analytical gel filtration

Analytical size exclusion chromatography was performed using an ÄKTAprime™ plus FPLC system (GE Healthcare) at room temperature. The protein samples were diluted to 10 µM in assay buffer (10 mM HEPES, pH 7.4, 1 M NaCl) and 100 µL of each sample was loaded onto a pre-equilibrated Superdex™ 200 10/300 GL column. The samples were run at a flowrate of 0.5 mL min^{-1} and protein absorbance was tracked at 280 nm wavelength. Data were processed with *GraphPad Prism 6*.

2.4.5 Preparation of tRNA^{Tyr}

The *E. coli* tRNA^{Tyr} (ECY2[75]) was synthesized by *in vitro* transcription using T7 RNA polymerase. The reaction mixture (30 µg of linearized DNA template, 3.75 mM of NTPs, and 1 µM of T7 RNA polymerase in 20 mM $MgCl_2$, 80 mM HEPES, pH 7.5, 1 mM spermidine, 5 mM DTT, 0.05 U pyrophosphatase) was incubated for 4 h at 37 °C. The tRNA transcript was extracted in a 1:1 mixture of acidic phenol/chloroform, pH 4.5, and precipitated upon addition of a 1:20 mixture comprising 3 M sodium acetate, pH 5.2, and ethanol. After centrifugation for 10 min at 16 500 *g*, 4 °C, the supernatant was discarded. The pellet was dried, dissolved in ddH_2O and the tRNA was purified via preparative denaturing (with 8 M urea) 8 % polyacrylamide electrophoresis (PAGE). The tRNA was eluted from the excised gel slice in 1 M sodium acetate, pH 5.2, overnight while shaking at 900 rpm, 4 °C. The purified tRNA was again precipitated using the above described procedure and finally dried *in vacuo*.

Table 2.2: Crystallographic data collection, processing and refinement statistics of PDB entries 6YGR, 7APL and 7APM.

Protein / Ligand	TGT–**2.2**	TGT$^{G87R1/C158S/C281S}$	TGT$^{C158S/C281S/H319R1}$
PDB ID	**6YGR**[64]	**7APL**	**7APM**
(A) Data collection and processing			
Collection site	BESSY II MX 14.1	BESSY II MX 14.1	BESSY II MX 14.1
Wavelength [Å]	0.91841	0.91841	0.91841
Unit cell parameters:			
Space group	$C2$ (5)	$C222_1$ (20)	$C2$ (5)
a, b, c [Å]	83.92 65.02 71.10	64.54 90.95 167.82	91.91 65.06 70.81
α, β, γ [°]	90.0 93.9 90.0	90.0 90.0 90.0	90.0 96.3 90.0
(B) Overall diffraction data (values for highest resolution shell in parentheses)			
Resolution range [Å]	41.86–1.70 (1.81–1.70)	44.59–1.99 (2.11–1.99)	45.68–1.66 (1.76–1.66)
No. of unique reflections	40707 (6285)	35628 (5311)	47688 (7302)
R_{sym}[a] [%]	5.1 (49.9)	6.3 (49.8)	7.5 (46.6)
Completeness [%]	97.5 (93.4)	97.9 (97.6)	97.6 (92.8)
Multiplicity	3.4 (3.4)	5.1 (5.6)	3.4 (3.2)
Mean I/σ	15.3 (2.2)	15.2 (2.8)	10.4 (2.1)
R_{meas}[a] [%]	6.1 (59.3)	7.0 (55.0)	9.0 (56.0)
$CC_{1/2}$ [%]	99.9 (80.2)	99.8 (88.7)	99.7 (82.0)
Matthews coefficient [Å^3 Da^{-1}]	2.3	2.9	2.4
Solvent content [%]	45.4	56.8	49.5
Wilson B-factor [Å^2]	21.8	33.8	18.5
No. of proteins in asymmetric unit	1	1	1
(C) Refinement with *PHENIX*[71] (version 1.16_3549)			
Resolution range [Å]	41.86–1.71	44.59–1.99	45.68–1.66
No. of used reflections	40699	33624	47683
R_{work}[b] / R_{free}[c] [%]	18.2 / 22.1	17.2 / 20.9	13.9 / 17.6
No. of atoms (non-hydrogen):			
Protein atoms	2698	2913	2960
Water molecules	215	173	319
Zinc	1	1	1
Solvent ligand atoms	-	12	19
Ligand atoms	23	-	-
rmsd from ideal values:			
Bond lengths [Å]	0.006	0.006	0.008
Bond angles [°]	0.8	0.8	0.9
Ramachandran plot[d]:			
Most favored [%]	94.7	94.4	94.4
Additionally allowed [%]	5.0	5.0	5.0
Generously allowed [%]	0.3	0.6	0.6
Mean *B*-factors[e] [Å^2]:			
Protein atoms	25.9	42.5	22.9
Water molecules	33.5	44.7	31.8
Zinc ion	20.5	28.8	17.4
Solvent ligand atoms	-	53.3	33.5
Ligand atoms	21.7	-	-

[a] $R_{sym} = \dfrac{\sum_{hkl}\sum_i |I_{hkl,i} - \langle I_{hkl}\rangle|}{\sum_{hkl}\sum_i I_{hkl,i}}$; $R_{meas} = \dfrac{\sum_{hkl}\sqrt{\frac{n}{n-1}}\sum_i |I_{hkl,i} - \langle I_{hkl}\rangle|}{\sum_{hkl}\sum_i I_{hkl,i}}$.[72]

[b] $R_{work} = \dfrac{\sum_{hkl}|F_o - F_c|}{\sum_{hkl} F_o}$.[72]

[c] R_{free} was calculated as R_{work} but on 5 % of the data excluded from the refinement.

[d] Calculated via *PROCHECK*[73].

[e] Calculated via *MOLEMAN*[74].

2.4.6 PELDOR spectroscopy and data analysis

For the PELDOR experiments, the protein was diluted to a final monomer concentration of 120 µᴍ with deuterated PELDOR buffer (50 mᴍ TES, pH 7.4, 2 ᴍ NaCl in D_2O). In case of the ligand-bound TGT samples, 3 eq. of one of the ligands **2.1**–**2.4** (from 10 mᴍ stock in DMSO) or 1.5 eq. of tRNA (from 3 mᴍ stock in the deuterated PELDOR buffer) were added to the protein to a final sample volume of 100 µL. If not mentioned explicitly, the samples were incubated for 24 h and then transferred into a Q-band EPR tube and flash-frozen in liquid nitrogen until further usage.

The PELDOR measurements were carried out on an ELEXSYS E 580 (Bruker) spectrometer using a FlexLine probe head with a Q-band resonator ER5106QT-2 (Bruker). All microwave pulses were amplified via a 150 W TWT amplifier (model 187Ka). To obtain the working temperature of 50 K, a continuous flow helium cryostat CF935 (Oxford Instruments) and a temperature control system iTC 503S (Oxford Instruments) were employed.

The PELDOR experiments were performed with the standard four-pulse sequence $\pi/2\,(\nu_{\mathrm{det}}) - \tau_1 - \pi\,(\nu_{\mathrm{det}}) - (\tau_1 + t) - \pi\left(\nu_{\mathrm{pump}}\right) - (\tau_2 - t) - \pi\,(\nu_{\mathrm{det}}) - \tau_2 - t$-echo. The frequency of the pump pulse and the magnetic field were adjusted to be on resonance with the maximum of the nitroxide spectrum, whereas the frequency of the detection pulse was set 100 MHz lower than the frequency of the pump pulse. All PELDOR measurements were performed with pulse lengths of 12 and 24 ns for the detection $\pi/2$- and π-pulses, respectively. The pump pulse was 14–16 ns long. The detection $\pi/2$-pulse was phase-cycled to eliminate receiver offsets. The τ_1 interval was set to a starting value of 240 ns and was incremented during each experiment 8 times with a step of 16 ns, in order to suppress deuterium electron spin echo envelope modulation (ESEEM). The τ_2 interval was set to 5–7 µs. The position of the pump pulse relative to the primary echo was incremented with a step of 8 ns. All PELDOR spectra were recorded at 50 K with a repetition time of 3 ms. The signal was averaged over 50–200 runs to achieve a good signal-to-noise ratio.

The PELDOR time traces were converted into the distance distributions by means of the program *DeerAnalysis2019*.[76] The background correction was done using a three-dimensional homogeneous background. The Tikhonov regularization was applied using the L-curve criterion. The optimized regularization parameter felt into the range of 100–10 000. The error of the *DeerAnalysis*-based distance distributions was estimated using the Validation tool. In each validation run, the noise level, the starting position for the background correction and the background dimension were varied in the ranges [original noise level, 1.5 original noise level], [1 µs, 4 µs], and [2.0, 3.0], respectively. Data were processed with *OriginPro 8*.

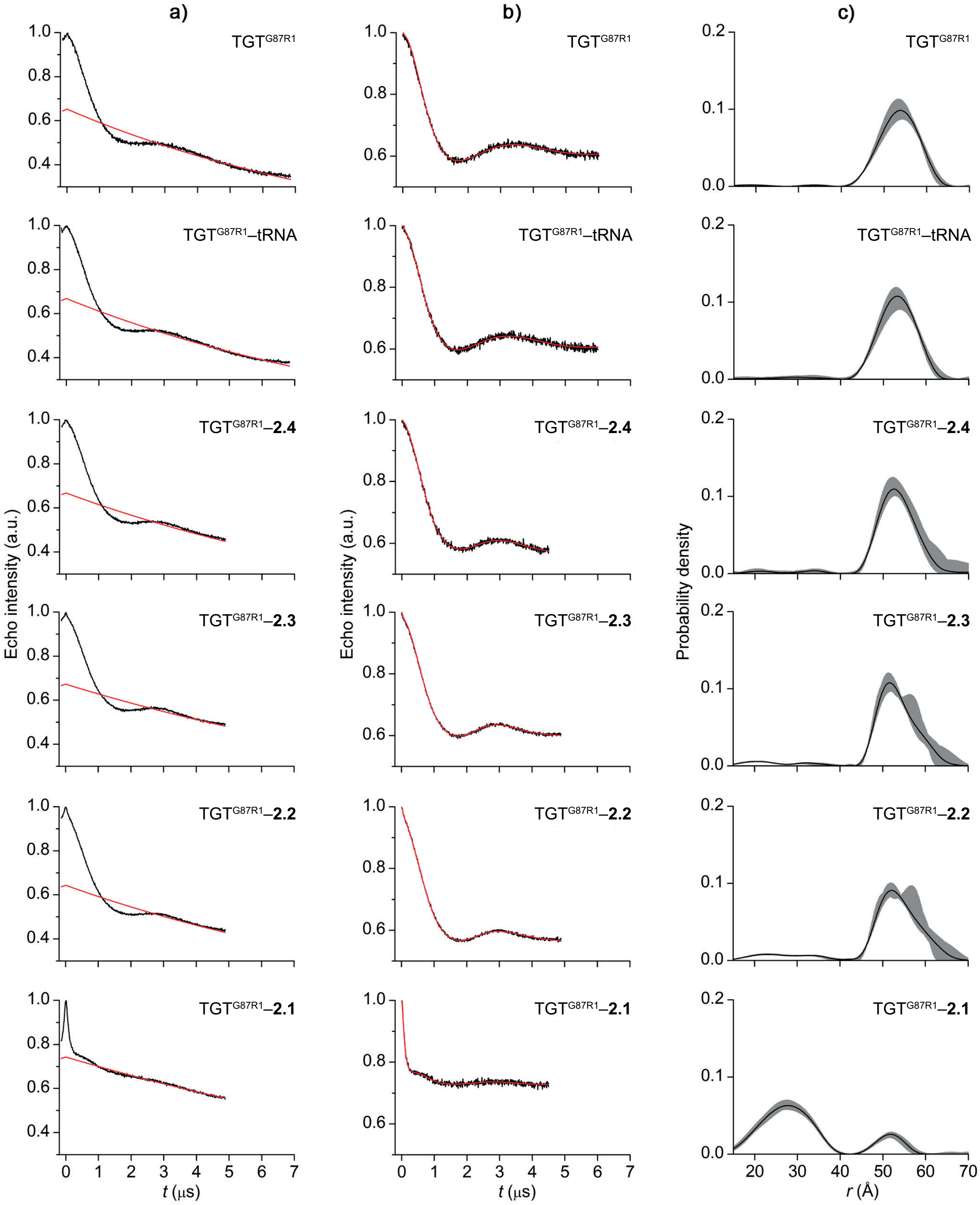

Figure 2.12: PELDOR measurements on TGT^{G87R1} incubated over 24 h with ligands **2.1**–**2.4** or tRNA. a) Original PELDOR time traces (black lines) and their background fits (red lines). b) Background-corrected PELDOR time traces and their fits (red lines). c) PELDOR-derived inter-nitroxide distance distributions (black lines). Gray shades depict the error estimates for the distance distributions.

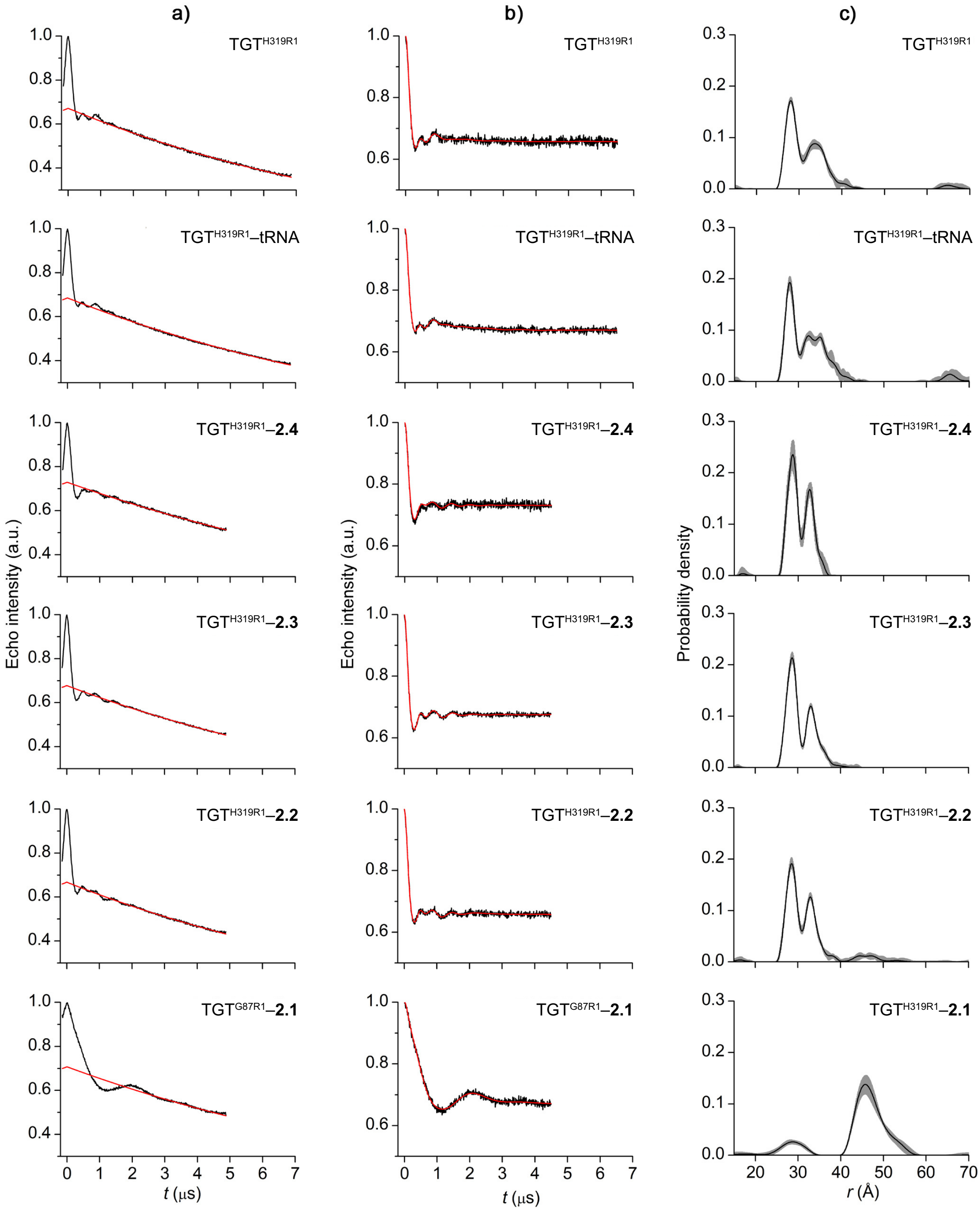

Figure 2.13: PELDOR measurements on TGT^{H319R1} incubated over 24 h with ligands **2.1**–**2.4** or tRNA. a) Original PELDOR time traces (black lines) and their background fits (red lines). b) Background-corrected PELDOR time traces and their fits (red lines). c) PELDOR-derived inter-nitroxide distance distributions (black lines). Gray shades depict the error estimates for the distance distributions.

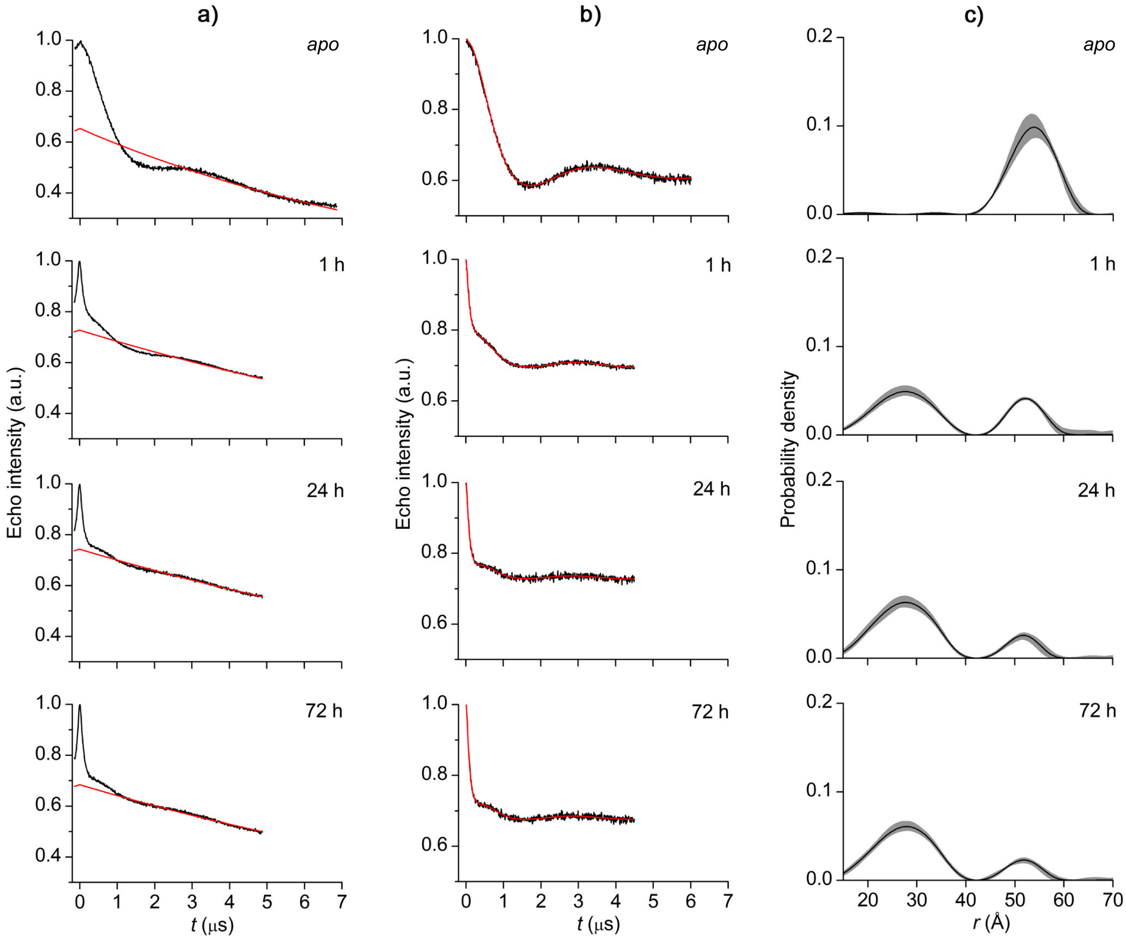

Figure 2.14: PELDOR measurements on TGT^{G87R1} incubated over 1, 24, and 72 h with ligand **2.1**. a) Original PELDOR time traces (black lines) and their background fits (red lines). b) Background-corrected PELDOR time traces and their fits (red lines). c) PELDOR-derived inter-nitroxide distance distributions (black lines). Gray shades depict the error estimates for the distance distributions.

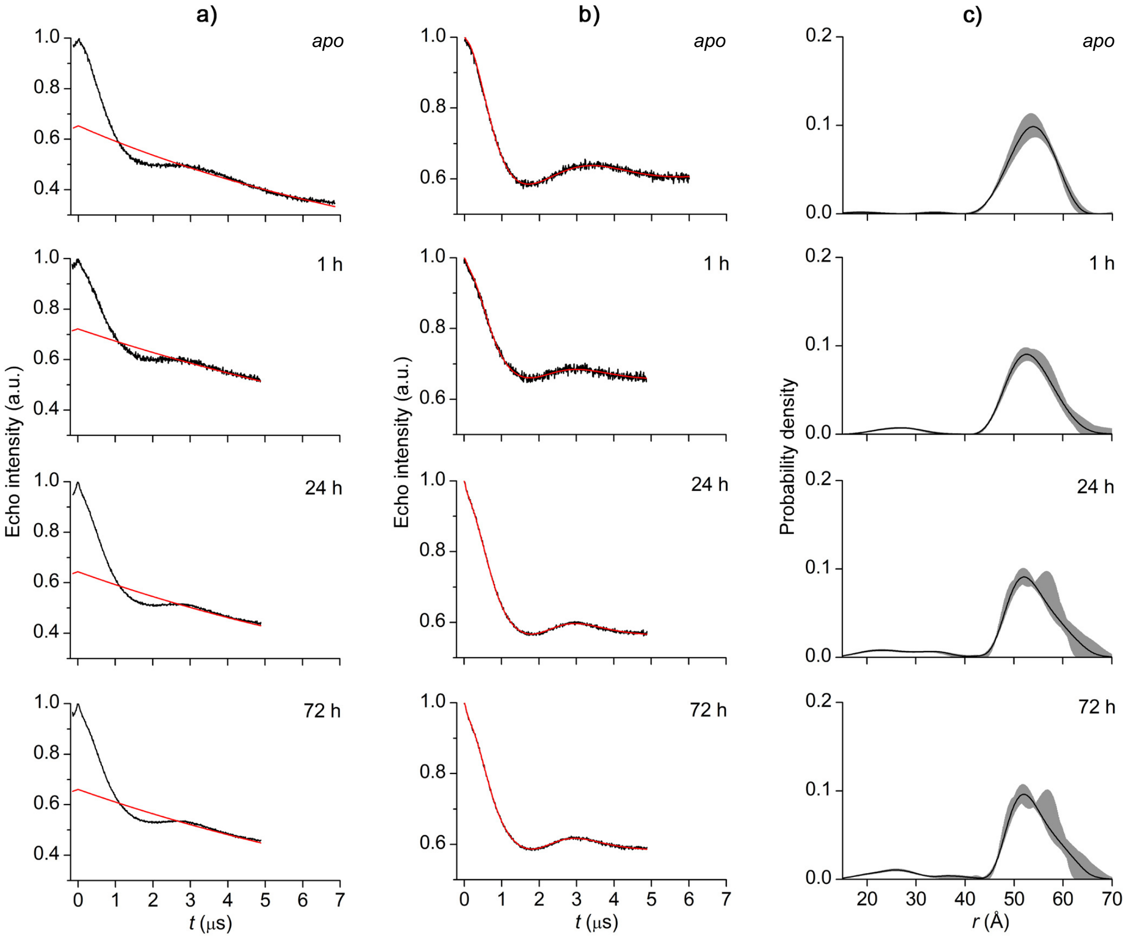

Figure 2.15: PELDOR measurements on TGT^{G87R1} incubated over 1, 24, and 72 h with ligand **2.2**. a) Original PELDOR time traces (black lines) and their background fits (red lines). b) Background-corrected PELDOR time traces and their fits (red lines). c) PELDOR-derived inter-nitroxide distance distributions (black lines). Gray shades depict the error estimates for the distance distributions.

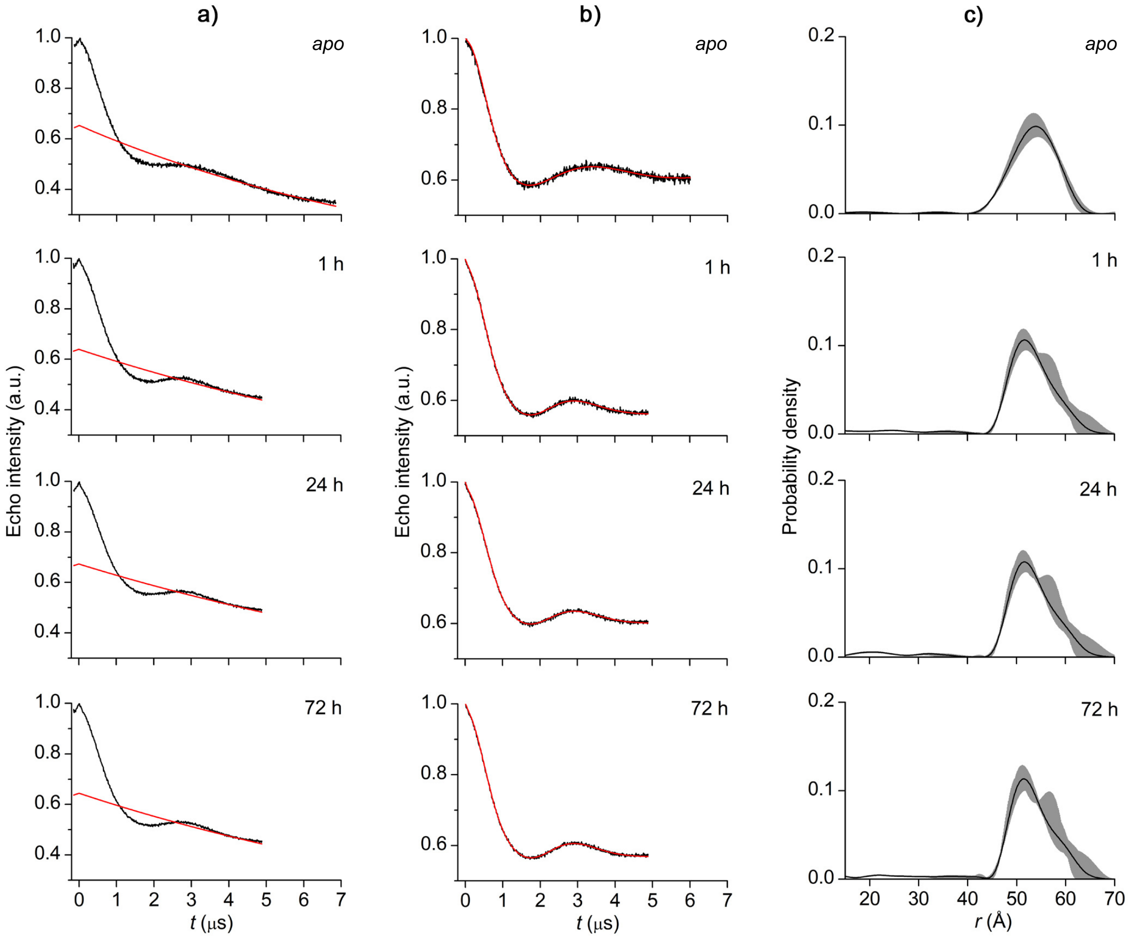

Figure 2.16: PELDOR measurements on TGT^{G87R1} incubated over 1, 24, and 72 h with ligand **2.3**. a) Original PELDOR time traces (black lines) and their background fits (red lines). b) Background-corrected PELDOR time traces and their fits (red lines). c) PELDOR-derived inter-nitroxide distance distributions (black lines). Gray shades depict the error estimates for the distance distributions.

3

Targeting a Transient Binding Pocket by Disulfide-Induced Break-Up of the Homodimeric TGT Interface

3.1 Introduction

In order to ensure proper cellular functions, a vast number of proteins need to be carefully orchestrated. A particular form of intermolecular communication between proteins is represented by protein–protein interactions (PPIs), which play an essential role in the regulation of signaling.[77] Accordingly, it is not surprising that malfunctions of PPIs are often linked to the development of diseases ranging from cancer to infections.[78] Drug research has started to focus on the interference of PPIs as attractive opportunity for therapeutic intervention.[79–82] However, due to their lack of addressable cavities and their usually flat and large interface areas, drugging PPIs with small molecules has long been considered as “high-hanging fruit” in pharmaceutical drug design.[83] The PPIs of permanent homodimeric proteins are especially difficult to target, since their monomer–monomer interactions are long-lived and the individual protomer subunits cannot be easily studied separately.[84,85] Mutagenesis studies such as alanine scanning can be used to dissect the “hot spot” residues as the key determinants of binding free energy that drive oligomer interface formation.[86,87] Using this knowledge, strategies such as covalent fragment tethering[88] or structure–activity relationship (SAR) by NMR[89] may be applied to find small molecules that bind near these hot spots and ultimately facilitate the design of PPI modulators.[90]

3.1.1 Discovery of a pseudomonomeric TGT variant

In order to discover new interface binding sites near the aromatic hot spot residues, Trp326, Tyr330, His333, and Phe92', in homodimeric tRNA-guanine transglycosylase (TGT), specific cysteine mutantions were strategically introduced for a fragment tethering approach.[91] An in-house tethering library consisting of different thiol-containing fragments was screened against a TGT$^{\mathrm{F92C/C158S/C281S}}$ variant and the modification rate was tracked via mass spectrometry. Low modification rates (up to 36 %[91]), likely due to the poor accessibility of Cys92, led to the design of a second variant TGT$^{\mathrm{Y330C}}$. Surprisingly, this mutant crystallized in two different crystal forms resulting in both, the usual functional dimer in the monoclinic space group *C*2 and a newly observed covalently linked dimer in the hexagonal space group $P6_522$ (Figure 3.1). The formation of the new disulfide bridge between Cys330–Cys330', which coincides with the crystallographic twofold symmetry axis, involves a tilting of one monomer subunit against the other, which significantly shrinks the monomer–monomer contact area from over 1600 Å^2 to only 537 Å^2.[91] This rearrangement is aided by the point mutation of Tyr330 to a cysteine which decreases the energetic contribution of an essential hot spot residue and thereby increases the dissociation rate of the functional TGT homodimer to a monomeric state as evidenced by native nanoESI-MS experiments.[22] Importantly, with respect to the original interface area, the new dimer formation exposes a large part of the previously inaccessible dimer interface, thus representing a "pseudomonomeric" TGT structure.

In the *C*2-symmetrical reduced form, the effect of the Y330C point mutation only shows a moderate structural effect on the aromatic stacking pattern of the functional dimer, such as a flip of the Trp326 sidechain by 180° (Figure 3.1a). Contrary, the hot spot residues are placed in a completely different environment in the oxidized pseudomonomeric structure with the disulfide bridge. The residues Trp326 and His333 now form a new contact patch with Trp326' and His333' of the dimer mate and thereby enclose the Cys330–Cys330' disulfide bridge (Figure 3.1b). The residue Phe92', that contributed to the original wild type dimer packing, is found far remote from the other hot spot residues. Apart from the aromatic hot spot, the opened dimer interface now allows the β1α1-loop (residues Gly46–Lys55), a part of the loop–helix motif, to adopt a new previously not observed conformation. The conformational multiplicity of this motif was precedingly studied using the wealth of crystal structures determined from the wild type enzyme,[18] its inhibitor complexes,[29,33,34] and mutated variants.[21–23] We hypothesized that this loop is crucial for the establishment and stability of the dimer interface. Supposedly, in the functional wild type enzyme, the loop–helix motif is disordered in solution and adopts an ordered geometry upon dimer formation.[91] Most likely, the loop–helix motif operates as an additional shield to further prevent the access of water molecules to the interface, which otherwise would interfere with the aromatic hot spot. Important enough, the new conformation of the β1α1-loop would be incompatible with the functional dimer packing for steric reasons.

These findings motivated us to envision a strategy to raise small-molecule binders against this geometrically morphed motif to stabilize the loop geometry in the conformation incompatible with interface formation. A similar concept was successfully applied in the development of small-molecule modulators against interleukin-2 to prevent the binding of this cytokine to its receptor.[92]

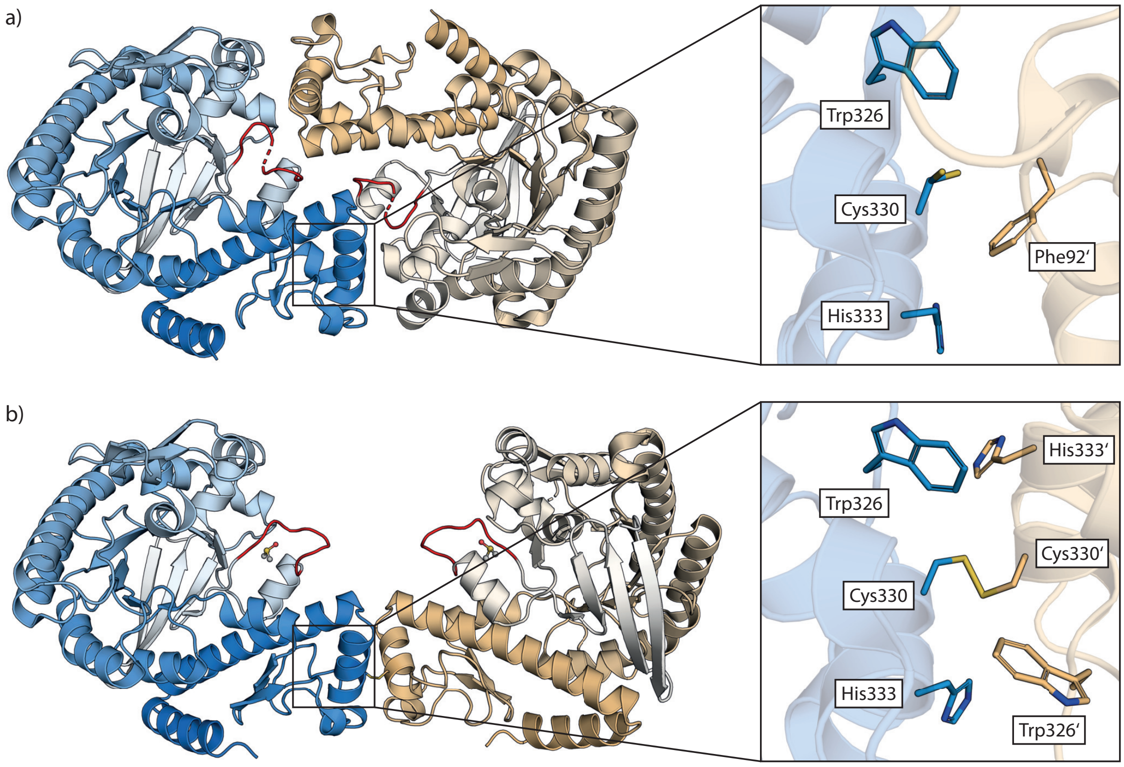

Figure 3.1: Structural comparison of TGT^{Y330C} in the a) functional dimer (PDB ID: 4HTB[91]) vs. the b) disulfide-linked dimer (PDB ID: 4JBR[91]). The β1α1-loop is highlighted in red and ill-defined residues are shown as dashes. The Cys330–Cys330' disulfide bridge is shown as sticks and the bound DMSO molecule is shown as a ball-and-stick model. The hot spot residues are shown as sticks in the subpanels.

3.1.2 Druggability of the β1α1-loop

Interestingly, the novel trace of the β1α1-loop opens a small hydrophobic pocket flanked by amino acids Gly46–Ala49, Ala53, Pro56, and Trp95. In the crystal structure, the binding pocket is occupied by a dimethyl sulfoxide (DMSO, **3.1**) molecule and an adjacent cluster of four water molecules (Figure 3.2a). Remarkably, DMSO was not present in the crystallization buffer but must be picked up from the cryo-buffer used to dip the crystals prior to flash-freezing for the diffraction experiment. We therefore believe that the pocket exists prior to DMSO accommodation and the bound DMSO molecule represents a true fragment complex.[91]

Furthermore, the conformational dynamics of the β1α1-loop was studied *in silico* by molecular dynamic simulations.[93] The resulting probability distribution suggests that a significant amount of the extended loop conformation, as shown in the PDB entry 4JBR[91], is present in TGT monomers at room temperature without the presence of DMSO. Hence, the transient binding pocket, opened by the β1α1-loop extension (Figure 3.2b), should be addressable by small molecules to stabilize its geometry in this state. Further docking experiments led to the acquisition of 15 commercially available sulfoxide-containing fragments to be tested crystallographically (Figure 3.2c).[93] The new findings might provide further structural insights on the conformational stability of the β1α1-loop and ultimately on how the modulation of this loop motif by small molecules could influence dimer formation in TGT. Long-term perspective of this strategy is to enhance the affinity of a small-molecule binder to this pocket so that, also without the artificially introduced disulfide bridge, the interface formation of the TGT homodimer could be blocked by the small molecule.

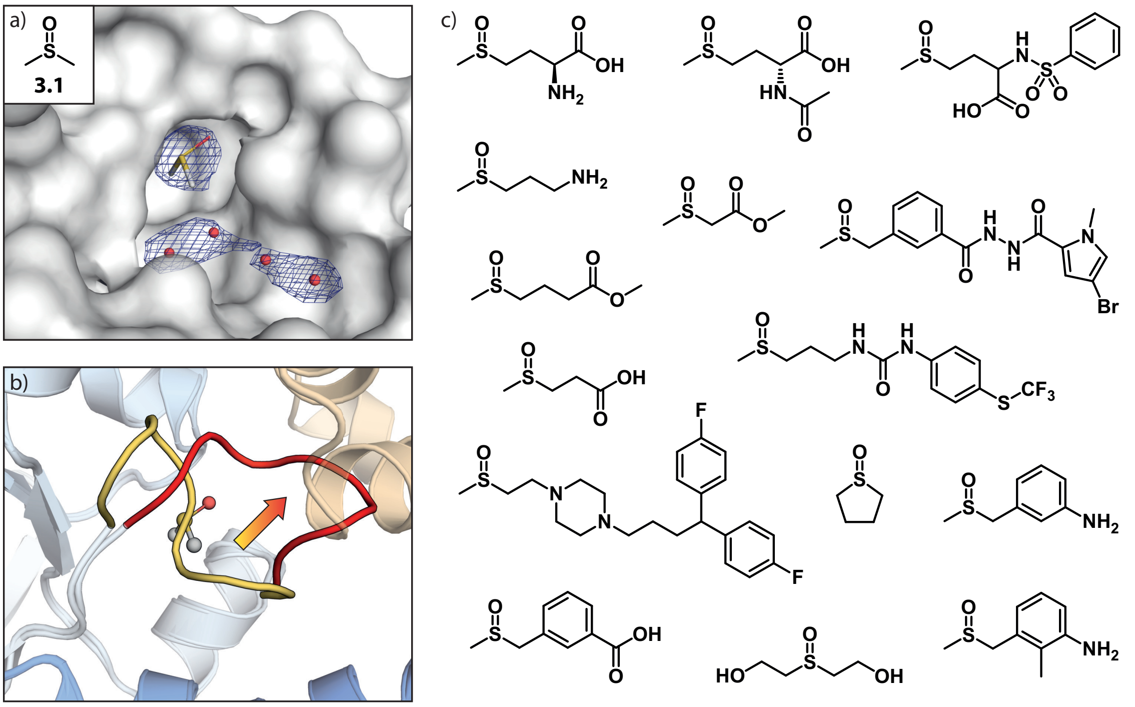

Figure 3.2: a) Surface representation of the opened interface pocket of $\text{TGT}^{\text{Y330C}}$ (PDB ID: 4JBR[91]) occupied by a DMSO molecule (shown as sticks) and an adjacent water cluster (as spheres). Electron densities from the $2mF_\text{o} - DF_\text{c}$ map are contoured at $1.0\,\sigma$. For reasons of clarity, residue Thr47 is not shown. b) Cartoon representation of the β1α1-loop extension from the functional dimer (yellow, PDB ID: 1PUD[18]) to the disulfide-linked dimer (red, PDB ID: 4JBR[91]) which clashes with the functional dimer mate (orange). The loop movement is indicated by an arrow. The bound DMSO molecule is shown as a ball-and-stick model. c) Chemical structures of the investigated sulfoxide fragments.

3.2 Results and Discussion

3.2.1 Preface

This work comprises the structural and biophysical analyses of small molecule fragments bound to the transient interface pocket of a novel disulfide-linked TGT homodimer. The original disulfide-linked dimer was discovered and characterized by **Stephan Jakobi** from the group of **Gerhard Klebe** (Philipps-Universität Marburg). Molecular dynamics simulations and fragment docking experiments on the β1α1-loop were performed **Felix Terwesten** from the same group. Mutagenesis, recombinant protein production, biophysical characterization and crystallization experiments were initially performed by **T. X. Phong Nguyen** from the same group and continued by **Andreas Nguyen** and the author of this thesis. Crystal solvent channels were analyzed *in silico* by **Katharina Holzapfel** and the author of this thesis. NMR experiments were performed and analyzed by **Xiulan Xie** (Philipps-Universität Marburg). The used fragments were purchased from Molport and Enamine. The used *lin*-benzoguanine inhibitors were synthesized by **Luzi J. Barandun** and **Levon D. Movsisyan** from the group of **François Diederich** (ETH Zürich).

3.2.2 Design and characterization of a stabilized disulfide-linked TGT variant

The presence of both TGT^{Y330C} dimer crystal structures, in space groups $C2$ and $P6_522$, points to the existence of both states, the reduced and the oxidized form, in solution and the predominating redox conditions, important to establish the disulfide bridge. The reaction to the oxidized disulfide-linked form could depend on protein concentration as higher concentrations would favor the formation of a more stable dimer interface. Most likely, the abundant oxygen is sufficient to trigger the reaction. Apparently, the functional dimer represents the energetically more favorable arrangement due to its larger interface area compared to the disulfide-linked dimer. The large structural rearrangement in the disulfide-linked dimer indicates that, in addition to the reduced state of the thiol groups, prior dissociation of the functional dimer might be required for the successful oxidative formation of an inter-monomer disulfide bridge.[91] As a matter of fact, protein concentration will significantly exceed locally upon crystallization, thus favoring monomer–monomer association even though the stability of the formed dimer is weakened by mutagenesis of hot spot residues.

Therefore, we hypothesized that an additional weakening of the aromatic hot spot might further increase the dissociation of the functional dimer, hence driving the equilibrium towards the disulfide-linked species. Subsequently, the previously described H333A point mutation[23] was introduced to the Y330C construct. Additionally, the conservative mutations C158S and C281S were introduced to avoid unspecific intermolecular disulfide crosslinks. The resulting TGT$^{C158S/C281S/Y330C/H333A}$ construct, in the following denoted as TGT$^{330/333}$, was screened for optimal crystallization conditions and crystals with hexagonal bipyramidal morphology were obtained from 0.1 M magnesium formate (Figure 3.3a). No DMSO was used for cryo-protection to yield a DMSO-free structure.

No significant structural deviation was detected compared to the previously investigated TGT^{Y330C} variant (PDB ID: 4JBR[91]). The β1α1-loop adopts virtually the same conformation as in the DMSO-bound structure, thus indicating that incorporation of the DMSO molecule is not mandatory to stabilize the loop. Instead, the binding pocket is occupied by a water cluster that mainly interacts with the amide backbone of residues Thr47, Leu54, and Met93 as well as the hydroxy group of the Thr47 sidechain (Figure 3.3b and c). The stable conformation of the β1α1-loop in the DMSO-free *apo* crystal structure of TGT$^{330/333}$ underpins the results from our molecular dynamics simulations on TGT^{Y330C}[93] (PDB ID: 4JBR[91]) for the existence of the extended loop conformation in the monomeric state of TGT. Likely, the loop extension is reverted upon monomer–monomer association to adopt a stable conformation within the homodimer interface. More importantly, the new TGT$^{330/333}$ variant could be crystallized in conditions (0.1 M TRIS, pH 8.5, 4–5 % (w/v) PEG 6000) suitable for soaking and diffraction experiments in terms of handling, durability and improved resolution (up to 1.59 Å vs. 2.92 Å in PDB entry 4JBR[91]).

Furthermore, the new TGT$^{330/333}$ variant was analyzed by analytical gel filtration compared to the wild type TGT dimer and the monomeric TGT^{Y330D} mutant[22] (Figure 3.3d). In contrast to the two control variants that represent the mainly populated dimeric and monomeric species, respectively, TGT$^{330/333}$ showed two distinct peaks in its elution profile. Although this indicates the presence of a dimer–monomer equilibrium, the peak for the dimer could amount for a mixture of both, the functional dimer as well as the disulfide-linked dimer. Nevertheless, the gel elution profile clarifies the increased dissociation of the TGT homodimer by perturbations within the aromatic hot spot at positions 330 and 333. This coincides well with the findings from our thermal shift studies (Figure 3.3e) where the mutations in the TGT$^{330/333}$ variant caused a decrease in protein stability compared to the wild type enzyme. This is indicated by the decrease of ~6.6 °C in the melting temperature of TGT$^{330/333}$ (T_m = 62.0 ± 0.8 °C vs. T_m = 68.6 ± 0.3 °C for TGT$^{330/333}$ and WT TGT, respectively) while it is still ~2.9 °C higher compared to the completely dissociated variant (T_m = 59.1 ± 0.2 °C for TGT^{Y330D}). However, the results from the thermal shift assay are ensemble-weighted and only reflect an averaged value from the melting process without distinguishing between dimer dissociation and overall protein unfolding.

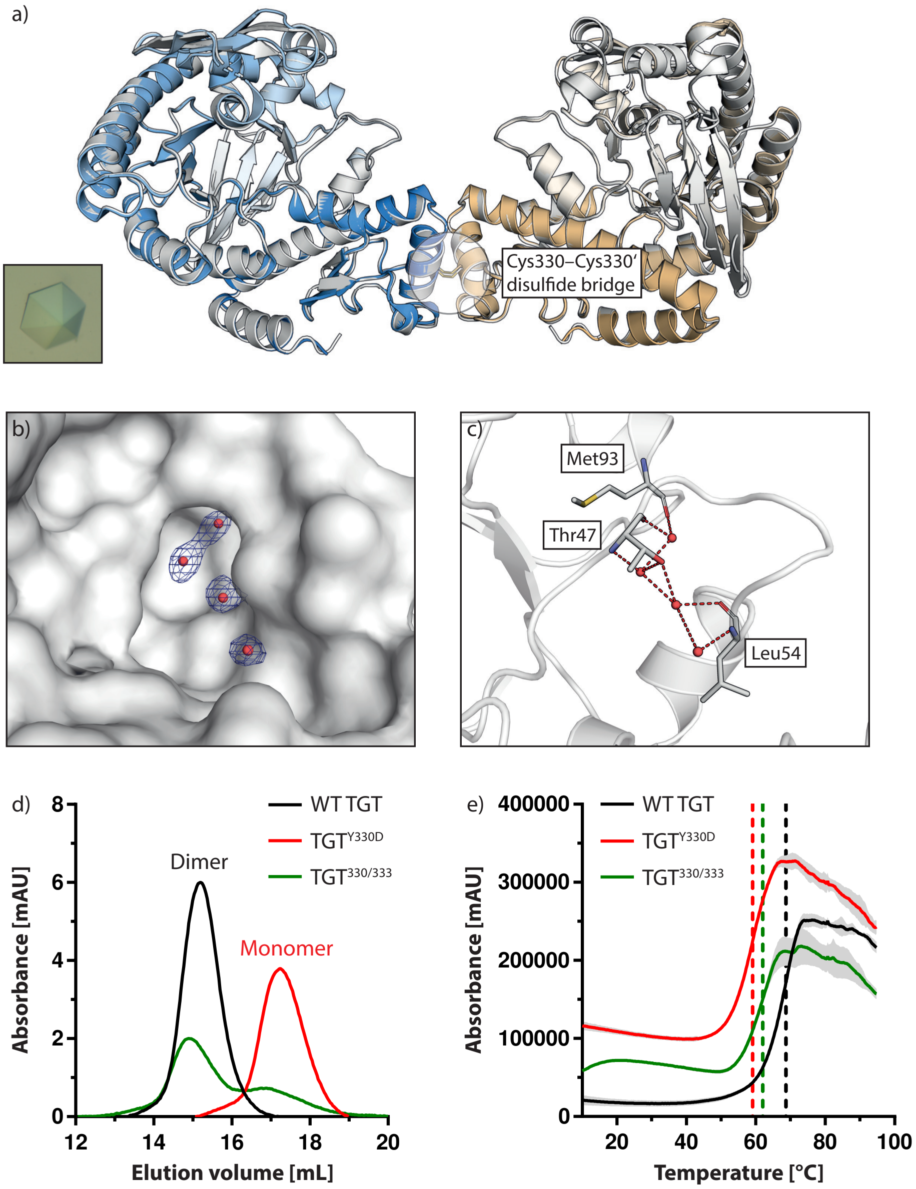

Figure 3.3: Structural and biophysical characterization of TGT$^{330/333}$ and the interface binding pocket. a) Hexagonal bipyramidal crystal morphology and resulting structure of *apo* TGT$^{330/333}$ (gray, PDB ID: 7ADN) compared to TGT^{Y330C} (blue/orange, PDB ID: 4JBR[91]). The Cys330–Cys330’ disulfide bridge is encircled. DMSO is not shown for clarity reasons. b) Detailed view of the interface binding pocket occupied by water molecules. Electron densities from the 2mF_o−DF_c map are contoured at 1.0 σ. For reasons of clarity, residue Thr47 is not shown. c) Representation of the water interaction network in the interface binding pocket. hydrogen-bond interactions are indicated as red dashes. d) Gel filtration elution profiles of TGT variants at 10 µM. e) Melting curves from the thermal shift assay. Standard deviations are depicted as gray shades. The respective melting temperatures are marked with dashed lines.

3.2.3 Soaking of sulfoxide fragments

The 15 previously docked and purchased sulfoxide fragments[93] (Figure 3.2c) were screened via crystal soaking experiments. Therefore, new crystallization conditions (0.1 M TRIS, pH 8.5, 4–5 % PEG 6000) were used for growing the TGT$^{330/333}$ crystals making them more suitable for the soaking procedure. If required, the fragments were dissolved and added in crystallization buffer instead of DMSO to avoid competition with the higher concentrated DMSO for the binding site. In some cases, fragment soaking was applied in combination with cryo-protection of the crystals in a solution containing 30 % glycerol as cryo-protectant.

For the sake of comparability, a TGT$^{330/333}$–DMSO (**3.1**, PDB ID: 7A4X) soaking structure was solved. Surprisingly, the DMSO molecule adopts a twisted binding mode compared to the TGT$^{\text{Y330C}}$–DMSO complex (**3.1**, PDB ID: 4JBR[91], Figure 3.4a) whereby the sulfoxide oxygen now interacts with the amide NH of Thr47 (S=O···(H)N: 2.9 Å) instead of Ala49 (S=O···(H)N: 3.2 Å) (Figure 3.4b). This can be explained due to the poorer electron density from the 4JBR entry[91] (at 2.92 Å resolution) making the assessment of the sulfoxide oxygen compared to the methyl groups in the model more difficult (Figure 3.4a). Nevertheless, the conformation of the β1α1-loop seems unaltered in both structures further underpinning that the formed interactions with the bound DMSO molecule are not mandatory for opening and stabilizing the pocket.

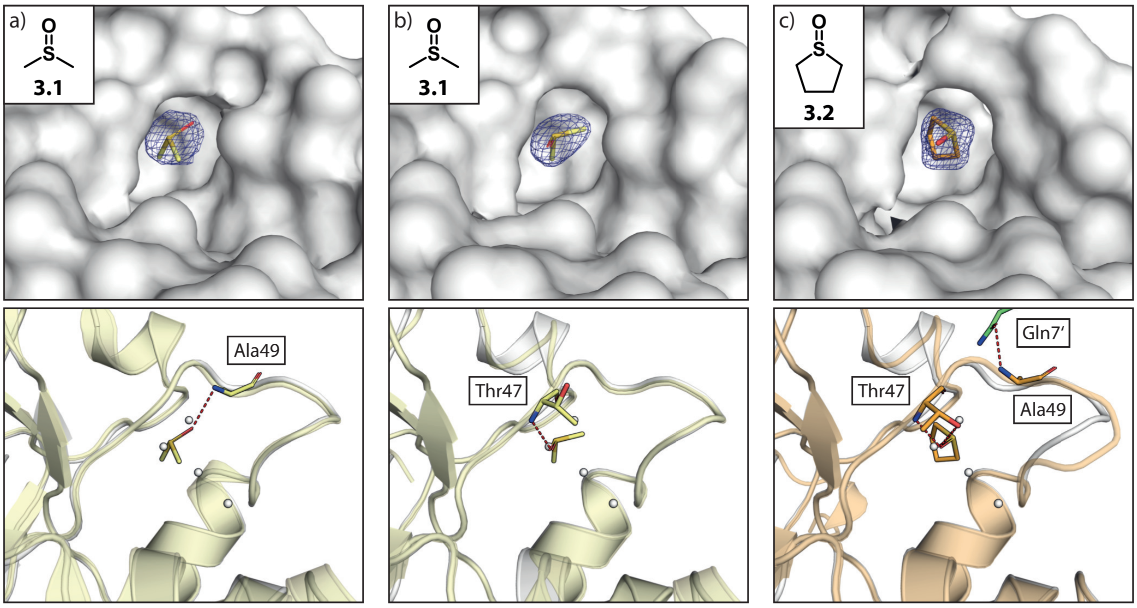

Figure 3.4: Detailed view of the occupied interface binding pocket and interaction network of complexes a) TGT$^{\text{Y330C}}$–**3.1** (yellow, PDB ID: 4JBR[91]), b) TGT$^{330/333}$–**3.1** (yellow, PDB ID: 7A4X), and c) TGT$^{330/333}$–**3.2** (orange, PDB ID: 7A4K) each compared to the *apo* TGT$^{330/333}$ structure including the bound water cluster shown as spheres (gray, PDB ID: 7ADN). For reasons of clarity, residue Thr47 is not shown in the surface representations (top). Electron densities from the $2mF_\text{o} - DF_\text{c}$ map are contoured at $1.0\,\sigma$. Fragments and interacting residues are shown as sticks (bottom). Hydrogen-bonds are indicated as red dashes.

Out of the 15 tested sulfoxide fragments, only tetramethylene sulfoxide (**3.2**) could be accommodated by the binding pocket with a refined occupancy of 80 % (Figure 3.4c). The sulfoxide group forms a hydrogen-bond to the amide NH of Thr47 (S=O···(H)N: 2.8 Å). However, Thr47 is pushed back around 1.6 Å to avoid a steric clash of the backbone with the ring moiety of the fragment. Additionally, a twisted Thr47 sidechain enables a second hydrogen-bond interaction between the sidechain hydroxy group and the sulfoxide of fragment **3.2** (S=O···(H)O: 3.6 Å). Interestingly, the whole β1α1-loop adopts a deviating conformation which could be explained by the pushback of Thr47. Moreover, the new loop conformation allows a stabilizing interaction between Ala49 and the Gln7' sidechain (N(H)···O=C: 3.0 Å) of an adjacent crystal mate. Unexpectedly, the N-terminal tail, which is usually not resolved in TGT crystal structures, could be modeled up to residue Glu3 (Figure 3.5a), thus, providing the basis for an additional project which is discussed in Chapter 4.

A closer look into the quaternary structure of the TGT$^{330/333}$–**3.2** complex reveals the interaction between the crystal mates. The N-terminal tails of the protomers bind onto the opened dimer interface of an adjacent crystal mate in an interlocking fashion (Figure 3.5b). This interaction is neither observed in the *apo* structure nor in the DMSO-bound structure due to the delocalized N-terminal tail. This indicates that the conformational shift of the β1α1-loop, caused by the accommodation of fragment **3.2** in the interface pocket, drives the stabilization of the residues Glu3–Arg11. Interestingly, the newly established interaction of the N-terminal tail with the β1α1-loop of another crystal mate seems to narrow the accessibility of the pocket which is already flanked by two monomeric subunits.

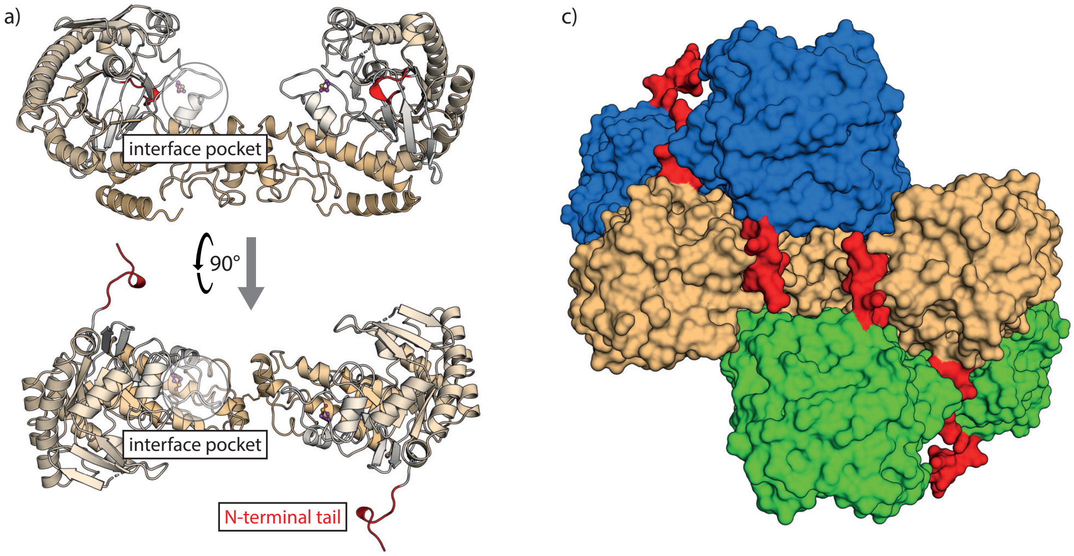

Figure 3.5: Depiction of the stabilizing interaction between the N-terminal tail and the opened dimer interface in TGT$^{330/333}$–**3.2**. a) Cartoon representations of TGT$^{330/333}$–**3.2** (orange, PDB ID: 7A4K). Fragment **3.2** is shown in magenta as ball-and-stick model. Residues Glu3–Arg11 and Glu3'–Arg11' are highlighted in red. b) Surface representation of the TGT$^{330/333}$–**3.2** complex (orange) with two adjacent crystallographic dimer mates (blue and green).

3.2.4 Solvent channel and soakability analysis

The reason why only one out of 15 docked fragment could be verified in soaking experiments required a more detailed investigation. One explanation could be the altered position and interaction of the DMSO molecule found in the TGT$^{330/333}$–**3.1** complex (Figure 3.4b). The fragments were originally selected to displace the nearby water cluster in the TGT^{Y330C}–**3.1** complex by growing the DMSO molecule at one of its methyl groups (Figure 3.2a). However, the docking was based on the wrongly assumed pose found in the low-resolution structure and this might have negatively influenced the selection of promising fragment candidates by the computational method.

Another reasonable explanation for the low hit rate could be an inefficient soakability of the obtained TGT$^{330/333}$ crystals. To test this hypothesis, the *lin*-benzoguanine inhibitor **3.3** was soaked into a TGT$^{330/333}$ crystal and a diffraction dataset was collected at 3.6 Å resolution with an in-house X-ray source (data not deposited in PDB). Electron densities from the $2mF_o - DF_c$ as well as $mF_o - DF_c$ maps were observed in the guanine-34/preQ$_1$ binding pocket. The ligand model fits well into the electron density of both maps, thus verifying the soakability of inhibitor **3.3** in the hexagonal TGT$^{330/333}$ crystals (Figure 3.6). Although this result confirms the soakability of compounds targeting the active site of TGT, the soakability cannot be generalized for the transient interface pocket since diffusion to the latter binding site and the catalytic center could emerge from different solvent channels in the crystal.

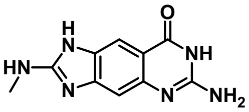

3.3

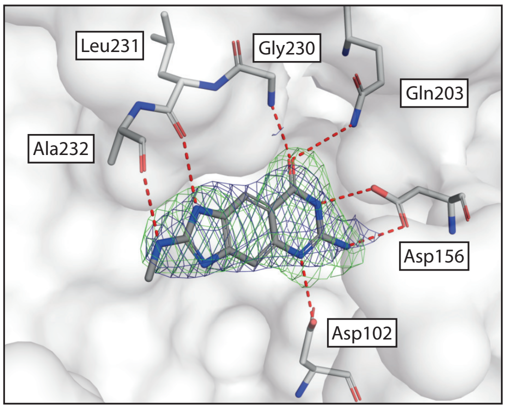

Figure 3.6: Detailed view of the guanine-34/preQ$_1$ binding pocket of the TGT$^{330/333}$ variant occupied by *lin*-benzoguanine inhibitor **3.3** (shown as gray sticks) via soaking (data not deposited in PDB). Residues within the hydrogen-bond interaction network of inhibitor **3.3** are shown as sticks. Electron densities from the $2mF_o - DF_c$ map (blue) and $mF_o - DF_c$ map (green) are contoured at 1.0 σ and 3.0 σ, respectively. Hydrogen-bond and charged interactions are indicated as red dashes. For reasons of clarity, residue Tyr106 is not shown.

Moreover, since both bound fragments accommodated near the β1α1-loop are quite low in molecular size (78.13 g mol^{-1} and 104.17 g mol^{-1} for fragments **3.1** and **3.2**, respectively), the respective solvent channel might be too narrow, thus, preventing successful diffusion of larger ligand molecules to this particular binding site. Therefore, the solvent channels of the *apo* $TGT^{330/333}$ (PDB ID: 7ADN) crystal structure were analyzed *in silico* using the program *MAP_CHANNELS*.[94] A projection along the *c*-axis revealed three distinct pores A–C traveling through the crystal packing (Figure 3.7a) with apparent radii of ca. 22.5, 22.5, and 7.0 Å, respectively, while the view down the *b*-axis indicated one major pore D (Figure 3.7b) with a radius of ca. 14.5 Å. However, these pores are suggested from a two-dimensional projection and no three-dimensional information can be extracted. *MAP_CHANNELS* allows the visualization and characterization of three-dimensional solvent channels throughout the crystal. The resulting solvent channel parameters are summarized in Table 3.1.

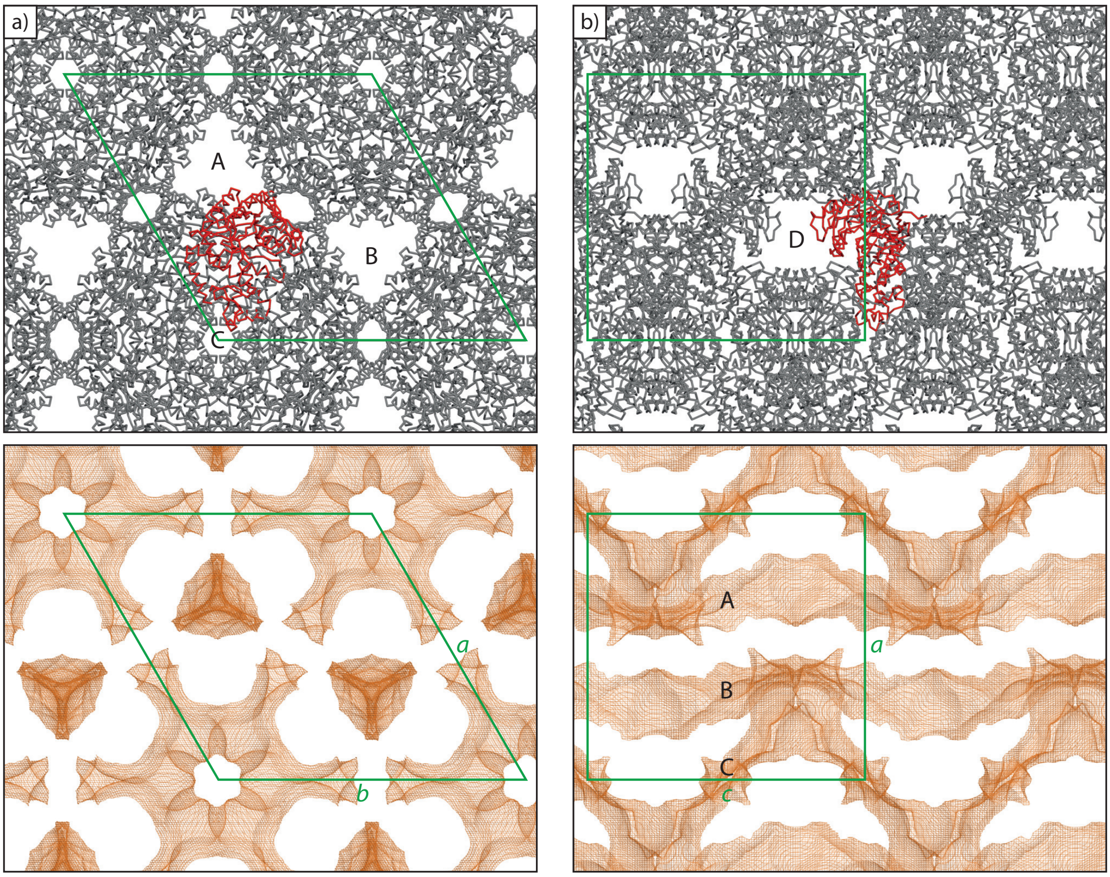

Figure 3.7: Two perspectives on the solvent channels in *apo* $TGT^{330/333}$ (PDB ID: 7ADN) along the a) *c*-axis and b) *b*-axis of the unit cell. Protein units are represented as gray main chain ribbons and the symmetry mates are aligned along the respective unit cell axis (top). One monomer unit is highlighted in red. The unit cell axes are shown in green. Apparent pores are noted as A–D. Solvent channels are displayed as distance maps (shown as orange mesh) in the same orientation as in the ribbon representations (bottom). The distance maps were calculated via *MAP_CHANNELS*[94] and contoured at 11.5 Å.

Table 3.1: Solvent channel analysis of the apo TGT$^{330/333}$ structure (PDB ID: 7ADN) by *MAP_CHANNELS*[94].

Solvent content [%]	63
Matthews coefficient [$Å^3$ Da^{-1}]	3.36
Maximum distance to protein [Å]	16.35
For 3D / 2D / 1D traversion through the unit cell:	
Maximum cutoff radius [Å]	10.80 / 10.80 / 13.60
Projected effective radius [Å]	10.33 / 10.34 / 12.75
For 1D channel along *c*-axis:	
Minimum / maximum tortuosity	1.12 / 4.19
Minimum / maximum width variation	−0.41 / 1.18

In the case of *apo* TGT$^{330/333}$ (PDB ID: 7ADN), three-dimensional traversion through the crystal is possible for spherical objects with radii lower than 10.8 Å (Table 3.1). At higher radii, solvent channels along the *a*-axis and *b*-axis become inaccessible. To visualize the remaining channels along the *c*-axis, distance maps were calculated via *MAP_CHANNELS* at a contour level of 11.5 Å. The resulting map indicates the surfaces on which a sphere with a radius of 11.5 Å can be positioned with its center without causing steric clashes with the protein. A closer view of the distance map revealed three continuous and similarly sized channels in the unit cell with maximum radii of 12.6–12.7 Å (Figure 3.7c and d). Two of the three channels, at pores A and B, are characterized with a tortuosity of 4.2 while the third helical channel around pore C shows a slightly lower tortuosity of 3.8. These three channel types allow diffusion of spherical objects with radii up to 11.5 Å along the *c*-axis of the crystal. No solvent channel was observed along the *b*-axis for the apparent pore D at the given contouring level. At 13.2 Å only the two channels at pores A and B remain up until a bottleneck radius of 13.6 Å after which the last two channels break up into smaller patches (Table 3.1). These results indicate that spheres with radii larger than 13.6 Å are prohibited from entering and traversing through the crystal.

Figure 3.8 depicts a detailed view on the accessibility of the interface binding pocket by a small adjacent channel connection between channels B and C ((marked with a yellow sphere). The distance maps at contour levels of 2.5, 3.0, and 3.5 Å indicate that molecules with radii lower than 2.5, 3.0, and 3.5 Å, respectively, can traverse along the map without steric clash with the protein units. An increase of the contour level from 2.5 to 3.0 Å narrows the channel connection near the pocket entry site (Figure 3.8a and b). At a contour level of 3.5 Å, the channel connection is broken into smaller patches and, thus, no longer traversable (Figure 3.8c). This suggests that, in a crystallographic soaking experiment, the entry for the interface binding pocket becomes inaccessible for molecules with radii larger than ~3 Å. However, it has to be noted that the size of the solvent channels including their cutoff radii could be dynamically influenced by thermal motion of the protein within the crystal, which has not been included in the calculation of the distance maps as the *MAP_CHANNELS* tool assumes a static protein model. The radii of the investigated fragments were estimated using the program *RADI*[95] and are listed in Table 3.6 (Experimental Section 3.4.7).

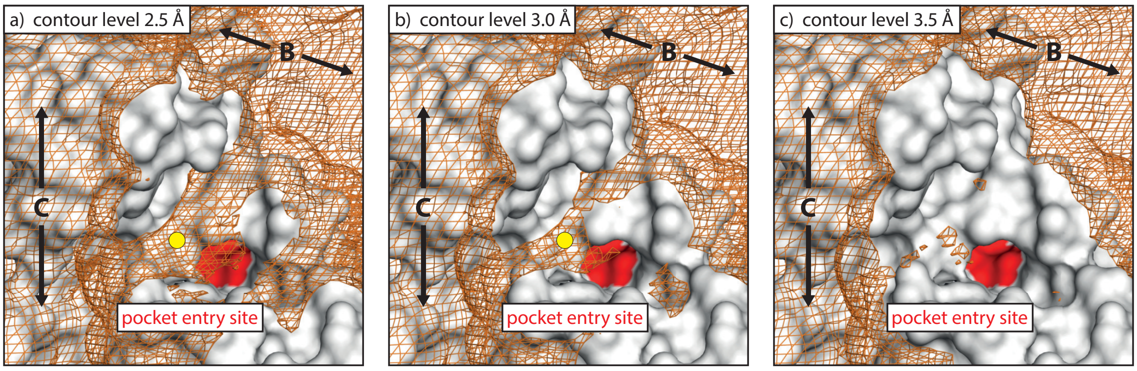

Figure 3.8: Detailed view of the interface binding pocket accessibility and the surrounding solvent channels in the *apo* TGT$^{330/333}$ crystal structure (PDB ID: 7ADN). The distance maps are shown as orange mesh at contour levels of a) 2.5 Å, b) 3.0 Å, and c) 3.5 Å. The protein unit is shown as surface representation. The trajectories of channels B and C are marked with arrows and the channel connection is marked with a yellow sphere. The interface pocket entry site is highlighted in red.

3.2.5 Soaking of sulfone fragments

The results from the solvent channel analysis suggested that only molecules with radii smaller than ~3.0 Å might be capable of diffusing to the interface binding pocket. In the following, additional small sulfone fragments were screened via soaking. Moreover, the use of sulfones adds an acceptor functionality and additionally eliminates the chirality center of sulfoxides. Ethyl methyl sulfone (**3.4**) bound to the pocket by forming a hydrogen-bond from its sulfonyl group to the amide NH of Thr47 (S=O···(H)N: 3.0 Å) in a similar pose to the sulfoxides **3.1** and **3.2** (Figure 3.9a). Unexpectedly, a second ethyl methyl sulfone molecule was accommodated adjacent to the first molecule by establishing another hydrogen-bond interaction to the amide NH of Leu54 (S=O···(H)N: 2.9 Å). This can be explained by the applied high fragment concentration used for the soaking experiment (0.64 м) despite short incubation times with the fragment (~2 min).

Additionally, the sulfone derivative of the cyclic sulfoxide **3.2**, sulfolane (**3.5**), was found to occupy the pocket twice similarly to sulfone **3.4** (Figure 3.9b). A similar interaction pattern is observed between the first fragment with Thr47 (S=O···(H)N: 3.5 Å) and the second fragment with Leu54 (S=O···(H)N: 2.8 Å) compared to TGT$^{330/333}$–**3.4**. The fragment concentration used for the soaking experiment was comparably high (0.66 м) although the incubation time was drastically shorter (~5 s). Presumably, the small size of fragment **3.5** allows a quick and efficient diffusion through the protein crystal. Interestingly, the sulfonyl group of the first molecule is shifted by 1.4 Å compared to the binding pose of sulfone **3.4**, likely to accommodate the five-membered ring. The shift weakens the interaction to Thr47 by increasing the interaction distance and places the first sulfolane molecule closer to helix α1.

Here, an unusual interaction of the sulfonyl group with the $C_\alpha H$ of Pro56 ($S{=}O\cdots(H)C_\alpha$: 3.8 Å) is observed in addition to van der Waals interactions. The $C_\alpha H$ group of amino acids is considered to be polarized and can thus act as a hydrogen-bond donor, although interactions of sulfones with classical hydrogen-bond donors would be preferred.[96] In fact, sulfonyl groups have been demonstrated to engage with polarized CH groups of proteins as was shown, e. g., for an inhibitor binding pose within the S2 pocket of human cathepsin S (PDB ID: 2FRA). The protein–inhibitor complex contained three $S{=}O\cdots(H)C_\alpha$ interactions with interaction distances of ≤3.7 Å to a single sulfonyl group, which was maintained in the core scaffold in the course of inhibitor optimization.[97] Contrary to the sulfoxide equivalent, Thr47 does not get pushed back by the accommodation of fragment **3.5** since the ring moiety of the first molecule adopts an altered binding pose compared to fragment **3.4**. This allows the fixation of the sulfonyl group between residues Thr47 and Pro56. Residue Thr50 was omitted from the final model as the residue is ill-defined in the electron density map. Both complex structures with sulfones **3.4** and **3.5** support the addressability of the interface pocket by displacing the water cluster with small fragments. Two out of three water network interactions with the surrounding residues could be mimicked (Figure 3.9a and b).

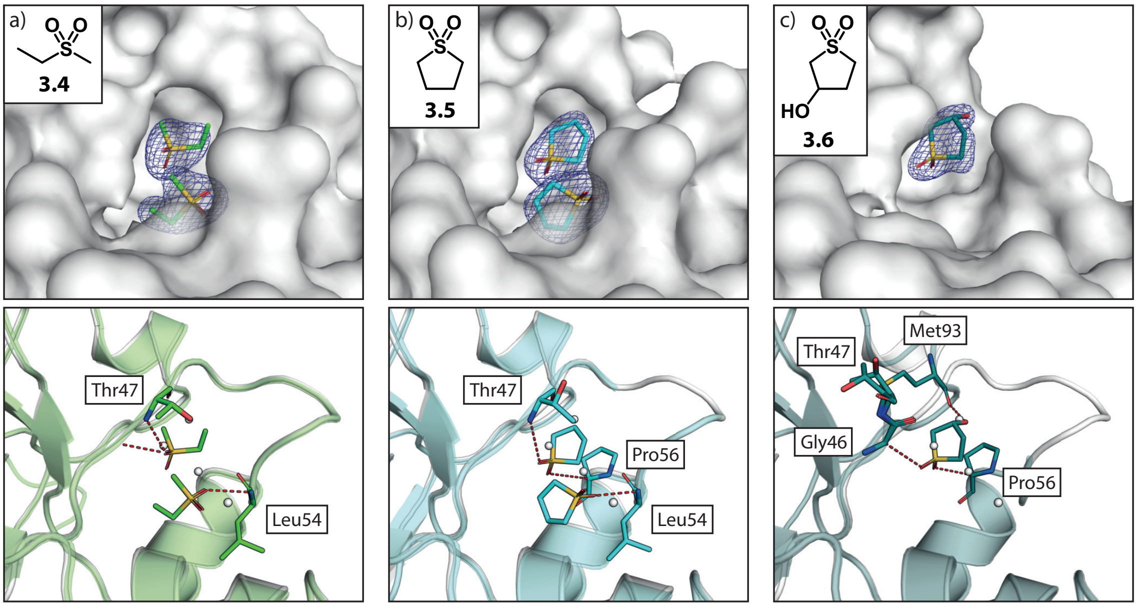

Figure 3.9: Detailed view of the occupied interface binding pocket and interaction network of complexes a) TGT$^{330/333}$–**3.4** (green, PDB ID: 7A9E), b) TGT$^{330/333}$–**3.5** (cyan, PDB ID: 7A3X), and c) TGT$^{330/333}$–**3.6** (teal, PDB ID: 7A3V) each compared to the *apo* TGT$^{330/333}$ structure including the bound water cluster shown as spheres (gray, PDB ID: 7ADN). For reasons of clarity, residue Thr47 is not shown in the surface representations (top). Electron densities from the $2mF_o - DF_c$ map are contoured at 1.0 σ. Fragments and interacting residues are shown as sticks (bottom). Hydrogen-bonds are indicated as red dashes.

The backbone carbonyl of the remaining residue, Met93, could be addressed by expanding the ring moiety of fragment **3.5** at carbon C3 position with a hydrogen-bond donor function such as a hydroxy group. As a consequence, racemic 3-hydroxysulfolane (**3.6**) has been tested in a soaking experiment and the (*R*)-enantiomer has been identified as a hit fragment (Figure 3.9c). The binding pose of fragment (*R*)-**3.6** is similar to the situation in TGT$^{330/333}$–**3.4** although a closer look reveals minor discrepancies. The added hydroxy functionality at C3 of fragment (*R*)-**3.6** successfully forms a hydrogen-bond with the amide carbonyl of Met93 (O(H)···O=C: 2.7 Å). Yet, the short interaction distance to Met93 forces a molecular tilt movement of about 19° measured from the sulfur atom of the fragment. To avoid a clash of the tilted ring moiety with the amide carbonyl of Thr47, the residue gets shifted by about 2.6 Å out the position adopted by fragment–**3.5** in the unsubstituted case. The resulting increased flexibility of residue Thr47 is further underpinned by the existence of two almost equally occupied conformations (47 and 53 %). Ultimately, the fragment-induced shift of Thr47 results in a collapse of the β1α1-loop motif between residues Ala48–Lys52 as the latter residues become ill-defined in the electron density. The previously observed interaction between the sulfonyl group and the amide NH of Thr47 is no longer visible due to the delocalization of the loop. Instead, the sulfonyl oxygen is anchored by another non-classical hydrogen-bond to the polarized $C_\alpha H$ of Gly46 (S=O···(H)C_α: 3.4 Å). The other sulfonyl oxygen forms a similar interaction to $C_\alpha H$ of Pro56 (S=O···(H)C_α: 3.5 Å) as seen for fragment **3.5**. Compared to the S=O···(H)C_α interaction in sulfone **3.5**, the interaction distance is shortened due to the molecular tilt movement which is caused by the establishment of the new hydrogen-bond to Met93.

Moreover, a third molecule of sulfone **3.5** and a second molecule of sulfone **3.6** were found to bind at a different location on the surface of the protein (Figure 3.10). While sulfone **3.5** only forms one hydrogen-bond interaction to the sidechain of Glu292 (S=O···(H)N: 3.4 Å, Figure 3.10a), sulfone **3.6** is accommodated in a comprehensive hydrogen-bond network of Ala80 (S=O···(H)N: 2.9 Å), Glu81 (S=O···(H)N: 3.1 Å), His133 (O(H)···N_δ: 2.8 Å), and a water-assisted hydrogen-bond to the backbone of Met134 (O(H)···W: 2.7 Å, W···(H)N: 3.0 Å, W···O=C: 3.3 Å, Figure 3.10b). The latter surface binding site has already been identified during a fragment-based screen for wild type TGT led by Hassaan *et al.*[30]

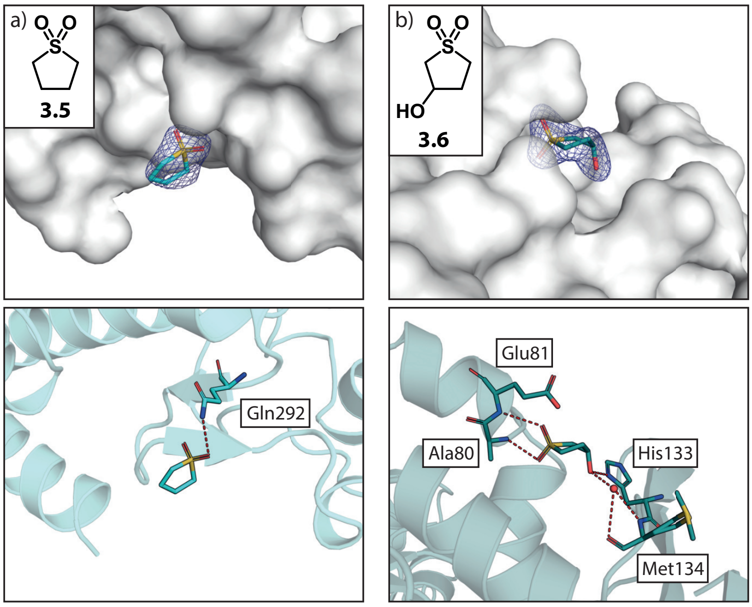

Figure 3.10: Detailed view and interaction network of fragments a) **3.5** (cyan, PDB ID: 7A3X) and b) **3.6** (teal, PDB ID: 7A3V) binding on the surface of TGT$^{330/333}$. Electron densities from the $2mF_o-DF_c$ map are contoured at 1.0 σ (top). Fragments and interacting residues are shown as sticks (bottom). The water molecule is shown as a red sphere. Hydrogen-bonds are indicated as red dashes.

3.2.6 Soaking of cyclic diols and other sulfolane derivatives

On the one hand, the binding of fragment **3.6** enabled the designed interaction to the backbone of Met93 but on the other hand the previous hydrogen-bond interaction with Thr47 was lost. In order to restore the interaction with residue Thr47, a second hydroxy group was introduced to the C4 carbon in *endo* position adjacent to the hydroxy group at C3. The resulting 3,4-dihydroxysulfolane (**3.7**) was tested in a soaking experiment either as the pure *cis* isomer or as a racemic mixture of the *trans* enantiomers. Only the (*R*,*R*)-enantiomer of the fragment **3.7** was accommodated in the interface pocket of TGT$^{330/333}$ in a similar fashion as fragment **3.6** (Figure 3.11a). The three established interactions to residues Gly46 (S=O···(H)C_α: 3.5 Å), Pro56 (S=O···(H)C_α: 3.4 Å) and Met93 (O(H)···O=C: 2.6 Å) have been maintained in the TGT$^{330/333}$–(*R*,*R*)-**3.7** complex. Importantly, the shift of residue Thr47 observed in the TGT$^{330/333}$–**3.6** complex was reverted by the establishment of two additional hydrogen-bond interactions with the introduced hydroxy group in fragment (*R*,*R*)-**3.7** to the amide NH (O(H)···(H)N: 2.9 Å) and to the sidechain hydroxy group of Thr47 (O(H)···(H)O: 3.0 Å). The additional interactions with Thr47 rescued the previously disordered β1α1-loop as it adopts a stabilized conformation similarly to the *apo* structure of TGT$^{330/333}$.

In contrast to the non-classical CH interactions, we hypothesize that the interactions formed by the vicinal diol structure contribute more of the fragment binding free energy. Therefore, a bioisosteric replacement strategy for the sulfonyl group was attempted to find additional fragment hits.

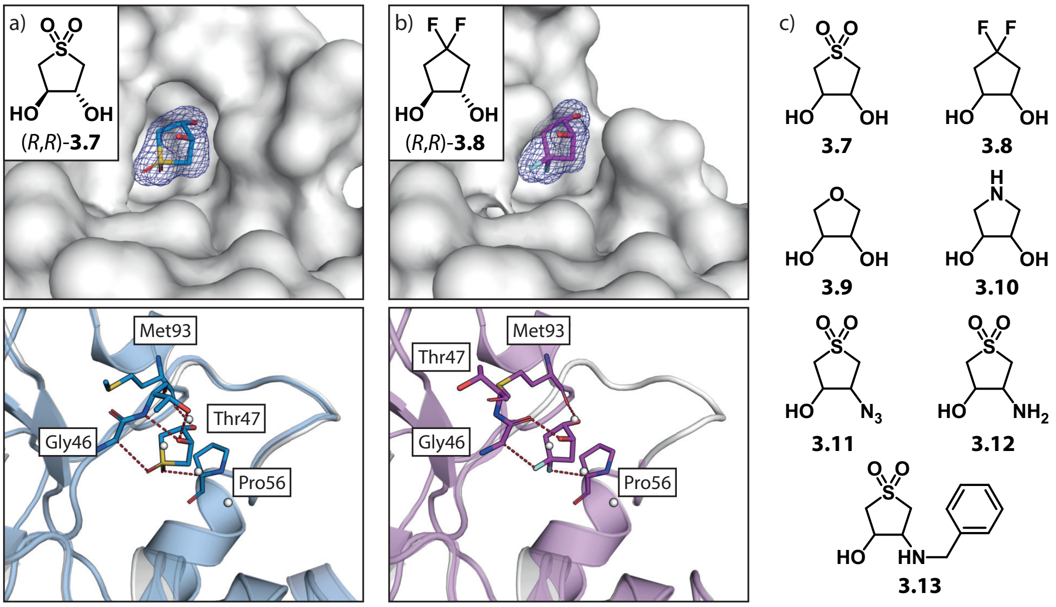

Figure 3.11: Detailed view of the occupied interface binding pocket and interaction network of complexes a) TGT$^{330/333}$–**3.7** (blue, PDB ID: 7A0B) and TGT$^{330/333}$–**3.8** (purple, PDB ID: 7A6D) each compared to the *apo* TGT$^{330/333}$ structure including the bound water cluster shown as spheres (gray, PDB ID: 7ADN). For reasons of clarity, residue Thr47 is not shown in the surface representations (top). Electron densities from the 2mF_o–DF_c map are contoured at 1.0 σ. Fragments and interacting residues are shown as sticks (bottom). Hydrogen-bonds are indicated as red dashes. c) Chemical structures of the investigated fragments **3.7**–**3.13**.

In the first trial, three additional cyclic diols, 4,4-difluorocyclopentane-1,2-diol (**3.8**), tetrahydrofuran-3,4-diol (**3.9**) and pyrrolidine-3,4-diol (**3.10**), were each tested as racemic mixtures of the respective *trans* enantiomers. Surprisingly, only (*R*,*R*)-**3.8** was accommodated by the interface pocket of TGT$^{330/333}$ (Figure 3.11b). The fragment (*R*,*R*)-**3.8** adopts a comparable binding pose as fragment (*R*,*R*)-**3.7**. Apparently, the *gem*-difluoromethylene group also forms non-classical CH-bond interactions with Gly46 (C–F···(H)C_α: 3.6 Å) and Pro56 (C–F···(H)C_α: 3.4 Å), due to the favorable alignment with the C–F-bond dipole.[96] The diols **3.9** and **3.10** will not be able to form the expected interactions with residues Gly46 and Pro56, since both fragments lack a strong polarized group and cannot satisfy the required interactions in terms of distances and angles.

Similarly to the TGT$^{330/333}$ structures with sulfones **3.5** and **3.6**, a second molecule of both diols **3.7** and **3.8** each bound on the surface of the protein. The disubstituted fragment (*R*,*R*)-**3.7** adopts an identical binding pose as the monosubstituted equivalent observed in TGT$^{330/333}$–**3.6**. Also, a similar hydrogen-bond network is formed with residues Ala80 (S=O···(H)N: 2.9 Å), Glu81 (S=O···(H)N: 3.1 Å), His133 (O(H)···N_δ: 2.7 Å), and Met134 (O(H)···W: 2.6 Å, W···(H)N: 3.0 Å, W···O=C: 3.5 Å, Figure 3.12a). No apparent interaction was observed for the second hydroxy group of fragment (*R*,*R*)-**3.7**.

In case of fragment **3.8**, the (*S*,*S*)-enantiomer bound on the protein surface between two crystal mates. The interaction with the surface of TGT$^{330/333}$ is mainly driven by the vicinal diol structure of fragment (*S*,*S*)-**3.8** which forms hydrogen-bonds to the backbone NH of Gly94 and Gly94' of the adjacent crystal mate (O(H)···(H)N: 2.5 Å) as well as to the sidechain of Asp96 and Asp96' (O(H)···(H)O: 2.9 Å, Figure 3.12b).

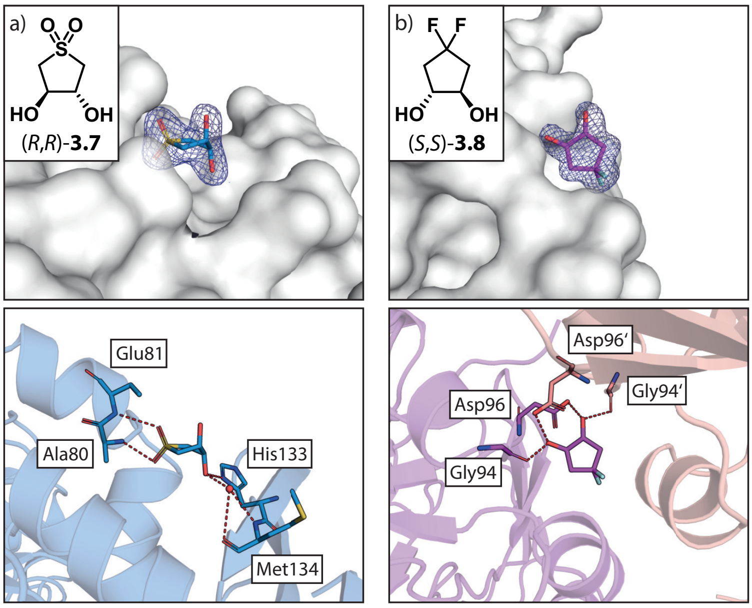

Figure 3.12: Detailed view and interaction network of fragments a) (*R*,*R*)-**3.7** (blue, PDB ID: 7A0B) and b) (*S*,*S*)-**3.8** (purple, PDB ID: 7A6D) binding on the surface of TGT$^{330/333}$. Electron densities from the $2mF_o - DF_c$ map are contoured at 1.0 σ (top). Fragments and interacting residues are shown as sticks (bottom). The water molecule is shown as a red sphere. Hydrogen-bonds are indicated as red dashes. In case of TGT$^{330/333}$–(*S*,*S*)-**3.8**, the crystal mate is shown as cartoon representation (salmon).

Firstly, the findings from the soaking experiments with the cyclic diols indicate that the classical hydrogen-bond interactions of the vicinal diol do not alone ensure successful fragment binding to the interface pocket. Secondly, it also emphasizes the role of the non-classical hydrogen-bond interactions that are formed by the SO_2 and CF_2 groups in fragments **3.7** and **3.8**, respectively. However, contrary to the TGT$^{330/333}$–**3.7** complex, the conformation of the β1α1-loop is destabilized and ill-defined due to a similar displacement of Thr47, as previously described in the TGT$^{330/333}$–**3.6** complex. The hydroxy group at the *endo* carbon C4 now interacts as a hydrogen-bond donor with the flipped amide carbonyl of Thr47 (O(H)···O=C: 2.7 Å). We suspect that a trifluoroacetic acid (TFA) contamination of the sample, which is discussed in section 3.2.7, could be able to drastically reduce the pH in the crystal environment prior to flash freezing. As the crystal was incubated with the fragment at a final concentration of 0.2 M overnight, the buffer capacity of the crystallization solution containing 0.1 M TRIS at pH 8.5 has obviously not been able to stabilize the original pH.

A shift toward a more acidic environment could prove to be detrimental for the stability of the loop–helix motif that comprises the β1α1-loop. This has been shown in our previous study, that draws attention to the collapse of the loop–helix motif in TGT crystals that were grown at pH 5.5 in the presence of a dimer interface-destabilizing mutation.[23]

Additional soaking experiments with the *cis* isomers of diols **3.7** and **3.8** yielded no bound complex structure. This underpins the importance of the required stereochemistry within the fragment, as only the (*R*,*R*)-*trans* isomer was accommodated by the binding pocket in both cases. Furthermore, derivatives of sulfone **3.7**, where one hydroxy group has been replaced by an azide group (**3.11**), amino group (**3.12**), and aminobenzyl group (**3.13**) have been tested via soaking. None of the fragments bound to $TGT^{330/333}$ under the established experimental conditions.

3.2.7 ^{19}F NMR experiments

The discovery of fragment **3.8** as a binder of the transient interface pocket of $TGT^{330/333}$, prompted us to investigate the potential to use the fragment as a probe for ^{19}F NMR-based screening applications. The sensitivity of the NMR signal of a nucleus is proportional to the cubic of its gyromagnetic ratio. The isotope ^{19}F possesses a gyromagnetic ratio of 94 % of that of a proton. Thus, the sensitivity of the ^{19}F signal is 83 % of that of a ^{1}H spectrum, which is followed by ^{31}P with just 6 % the sensitivity of ^{1}H, among all the hetero nuclei. The ^{19}F NMR spectroscopy is unique that its resonance frequency and, thus, its sensitivity is much higher than that of the other hetero nuclei. As compared to ^{1}H spectroscopy, another advantage of ^{19}F is the much larger range of its chemical shifts, about 50 times that of ^{1}H. As a consequence, signal overlap, which is often the case in ^{1}H spectra, is a rare problem in ^{19}F spectra. Recently, another feature of ^{19}F, the large chemical shift anisotropy, which appears as a second-order effect as observed in the effective linewidth of the resonance signals in solution, has been developed into an effective assay for ligand-based NMR screening.[98–100] The established ^{19}F detection assay, labeled as fluorine chemical shift anisotropy and exchange for screening (FAXS), has been used with a fluorinated fragment library designed by Novartis, which has been used for screening purposes, e. g., against bovine trypsin. In the study led by Vulpetti *et al.*, one fragment of the library was highlighted as a weak binder as fragment binding could only be validated through X-ray crystal structure determination and a weak ^{19}F signal attenuation via the FAXS method. This demonstrated the feasibility of FAXS as a screening method to detect low-affinity binders.[101]

The FAXS approach was carried out on the fluorine-containing fragment *rac-trans*-**3.8** with TGT mutants TGT^{H333D} and TGT^{Y330D}. The mutants were chosen based on the hypothesis that the interface pocket is only accessible by small molecules in the monomeric state. Point mutations of the aromatic hot spot residues have been shown to destabilize the dimer interface subsequently resulting in higher dissociation of the TGT homodimer into its monomeric species in solution, thereby enabling the β1α1-loop to adopt the extended conformation and the opening of the transient interface pocket.

We believe that the pocket would be buried and, hence, not accessible in the wild type enzyme since native nanoESI-MS studies revealed a dimer-to-monomer ratio of 98:2 as well as a slow dissociation rate over many hours.[22,23] Contrary, the TGT^{H333D} mutant has a dimer-to-monomer ratio of 58:42, while that of TGT^{Y330D} is 1:99, according to the results of nanoESI-MS.[22] However, mass spectrometric experiments were performed at protein concentrations as low as 10 μM. Since NMR measurements could use protein samples at higher protein concentrations, the oligomeric state was assessed by analytical gel filtration at a concentration of 10 mg mL^{-1} (~233 μM). The elution profiles for wild type TGT and TGT^{Y330D} are distinct as previously seen at lower protein concentrations and can therefore be assessed as the profiles of the dimeric and monomeric TGT species, respectively (Figure 3.13). Surprisingly, instead of two distinct peaks, the elution profile of the TGT^{H333D} variant shows a single intermediate peak between the two reference peaks. This indicates a co-elution of both, the monomeric and dimeric TGT species, which likely results from a rapid monomer–dimer equilibrium.[102] The gel filtration elution profiles correlate well with the native nanoESI-MS data described above as an increase in dimer dissociation leads to higher elution volumes.

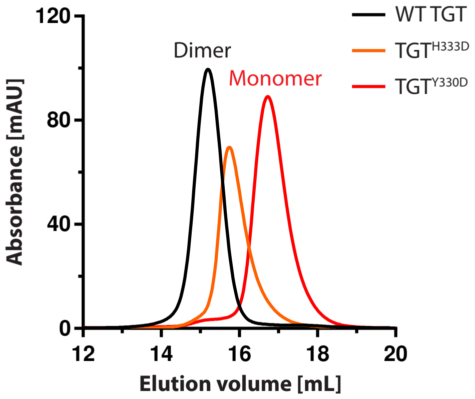

Figure 3.13: Gel filtration elution profiles of TGT variants at 10 mg mL^{-1}.

A known ligand with a CF_3 group, the *lin*-benzoguanine inhibitor **3.14**, which binds well to TGT[64], was chosen as a positive control. A singlet at −62.2 ppm was observed for the CF_3 group of inhibitor **3.14**, which disappeared upon addition of TGT^{H333D} thus indicating successful binding of inhibitor **3.14** at 20 μM TGT^{H333D} and a molar ratio of 25:1 (Figure 3.14). The signal at −122 ppm likely results from an impurity and could potentially serve as a negative control.

For fragment *rac*-*trans*-**3.8**, a quintet signal at −84.3 ppm was observed corresponding to the CF_2 group (Figure 3.15a). The quintet pattern results from scalar coupling of the CF_2 group with the four neighboring protons at carbons C3 and C5 since ^{19}F spectra were recorded without ^{1}H decoupling. Likely, the additional signal at −75.6 ppm originates from a TFA impurity, as no further impurity traces can be found in the corresponding ^{1}H spectrum (Figure 3.21, Experimental section 3.4.6).

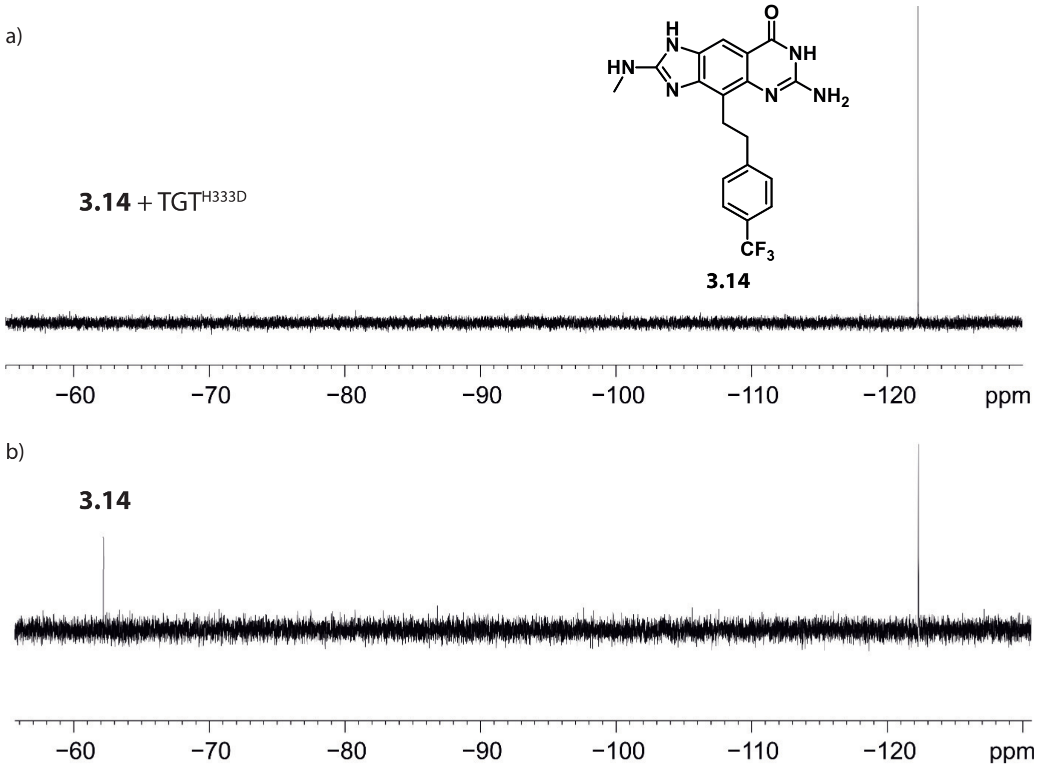

Figure 3.14: ^{19}F spectra of a) inhibitor **3.14** (<0.5 mM due to the very low solubility in buffer) and b) inhibitor **3.14** with 20 µM TGT^{H333D} in D_2O buffer at 298 K.

In fact, TFA was used in the synthesis of the compound and a subsequent removal was attempted by the responsible chemist via evaporation, as verified by the vendor (personal communication). Furthermore, a known fragment, 3-(trifluoromethyl)benzylamine (**3.15**), which is a non-binder of TGT was chosen as a negative control. For fragment **3.15**, a singlet at −62.4 ppm was observed (Figure 3.15b and c). T_2-filters with echo periods up to 320 ms produced non-observable signal changes, which revealed reasonable long relaxation (T_2) for free ligand in solution.

Mixing of 0.5 mM *rac-trans*-**3.8** with 0.5 mM of fragment **3.15** and addition of the mutant TGT^{H333D} at concentrations of 20 and 40 µM in buffer that was **3.8**:**3.15**:TGT^{H333D} at molar ratio of 25:25:1 and 12.5:12.5:1, respectively, resulted in no observable changes to all ^{19}F signals (Figure 7). According to Vulpetti *et al.*[100], in addition to the binding constant K_d, the concentration of the ligand plays an important role to the observation of signal changes in the FAXS assay. Therefore, a FAXS assay at much lower concentration was carried out on the binding of *rac-trans*-**3.8** with mutant TGT^{Y330D}. Thus, we mixed *rac-trans*-**3.8** and fragment **3.12** at concentrations of 300, 100, and 50 µM, each with 25 µM of TGT^{Y330D}. The respective molar ratios were 12:12:1, 4:4:1 and 2:2:1. Both with and without T_2-filter, no changes, neither in chemical shift nor in signal width, were observed in the ^{19}F signals. We thus concluded that in the case of *rac-trans*-**3.8** binding with TGT mutants TGT^{H333D} and TGT^{Y330D}, where binding was not strong, the FAXS assay failed in producing any information into the involved binding process.

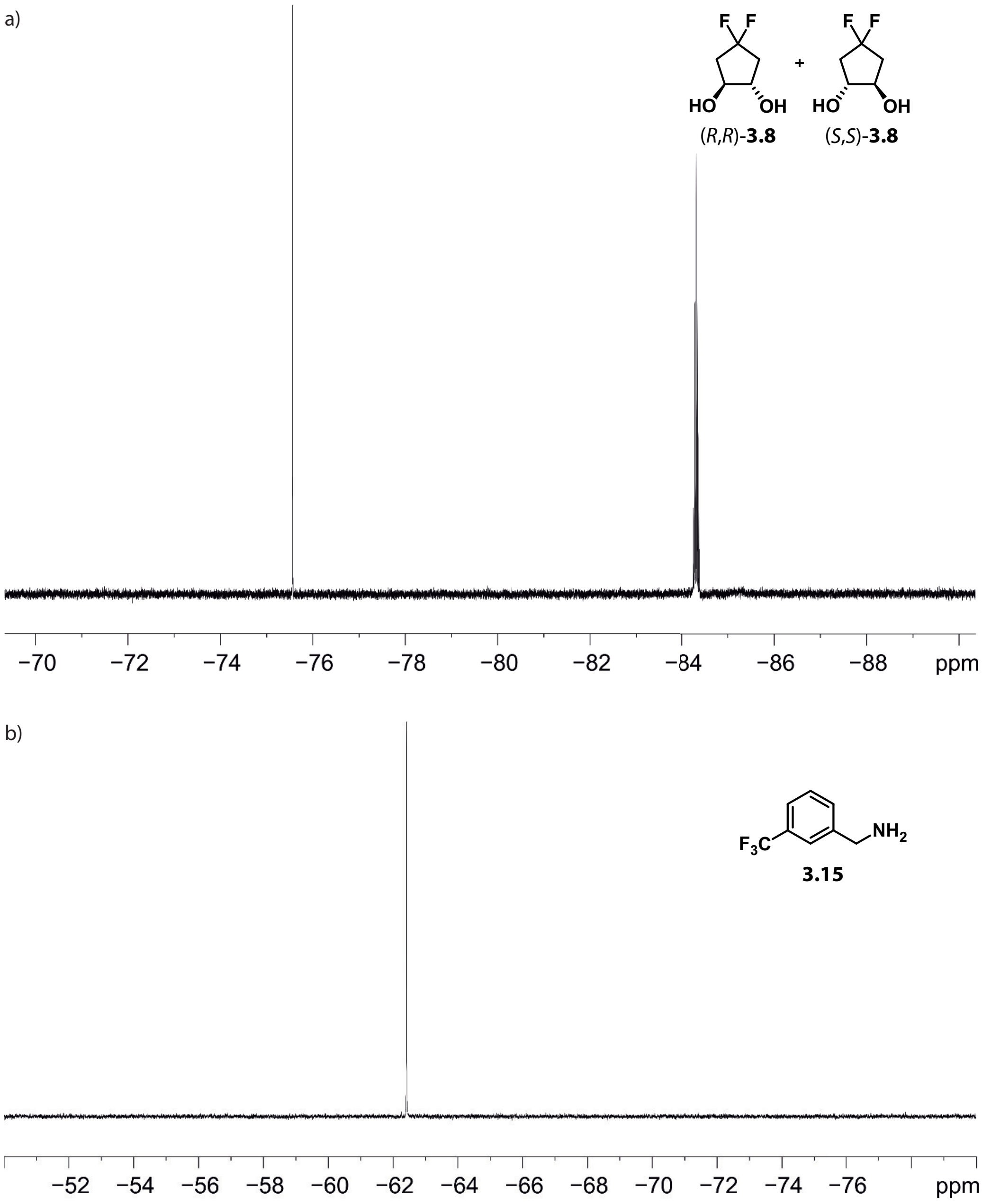

Figure 3.15: ^{19}F spectra of a) 0.5 mM *rac-trans*-**3.8** and b) 1.0 mM **3.15** in D_2O buffer at 298 K. A T_2-filter was used with 2τ of 40 ms and an echo period of 160 ms.

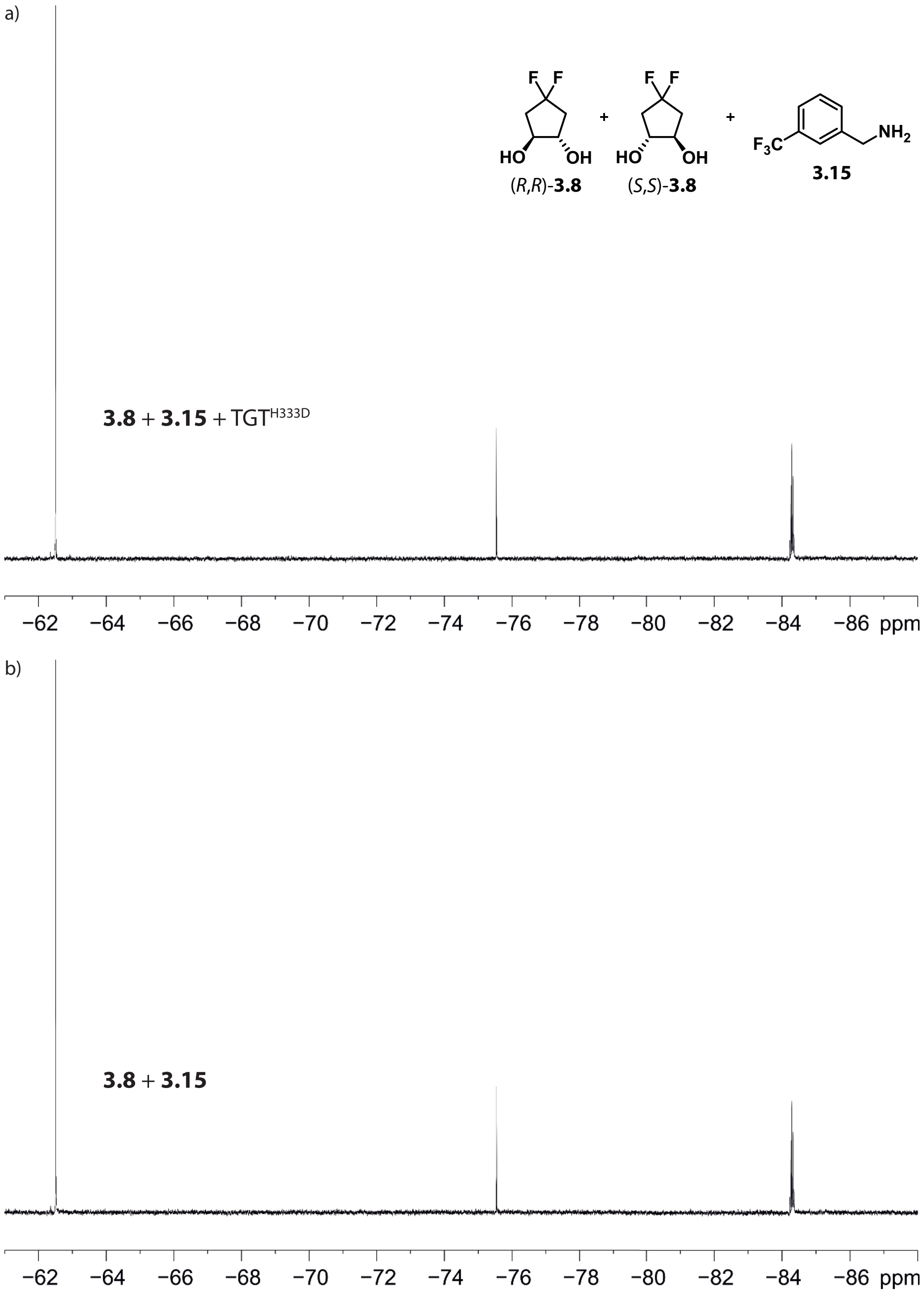

Figure 3.16: ^{19}F spectra of 0.5 mM *rac-trans*-**3.8** and 0.5 mM **3.15** mixed with 20 µM TGT^{H333D} and b) without TGT^{H333D} in D_2O buffer at 298 K. A T_2-filter was used with 2τ of 40 ms and an echo period of 160 ms.

3.2.8 PFG diffusion studies

The use of magnetic field gradients across a living body realized the magnetic resonance imaging technique, which fulfilled the first reconstruction of a hydrogen spin density map into anatomical and physiologically useful pictures.[103] Besides this popular medical application, the pulsed field gradients (PFG) play a fundamental role in modern NMR techniques, both in one- and two-dimensional spectroscopies, where only the coherences of those interesting signals are selected and the remaining signals are suppressed.[104] Compared to the classical way of phase cycling of the radio-frequency pulses, the use of PFG accelerated the experiments and improved the spectral quality tremendously. A third application of PFG is the measuring of self-diffusion coefficients of small molecules as well as macromolecules.[105,106] The PFG NMR diffusion experiment was further developed into a new methodology, the so-called DOSY (diffusion-ordered spectroscopy), which is a pseudo-2D presentation displaying the molecular diffusion coefficients vs. the one-dimensional chemical shifts.[107] DOSY has proved to be a very powerful method with a wide range of applications,[108] among which are the analysis of mixtures without a physical separation of the constituents,[109] the study of aggregates in solution,[110–114] and the characterization of protein–ligand binding interactions.[115–119] In the following, the important features of DOSY and its usage in protein–ligand binding studies are summarized.

In a PFG diffusion experiment, a pair of pulsed field gradients are implemented into a spin-echo with an echo delay. Due to changes in the molecules spatial position caused by their translational diffusion, incomplete refocusing of the signal occurs. Such incomplete refocusing results in an attenuation of the signal intensity, which can be correlated to the duration of the delay, the strength of the applied gradients, and the diffusion coefficient of the molecule, as described by the Stejskel-Tanner relation in equation (3.1):

$$I = I_0 \exp\left[-D\,\gamma^2\,\delta^2\,g^2\left(\Delta - \frac{\delta}{3}\right)\right] \tag{3.1}$$

I_0 = signal intensity in absence of applied gradient
γ = gyromagnetic ratio of the nucleus in concern
δ = gradient pulse duration
g = gradient strength
Δ = total diffusion delay

In a typical DOSY experiment, the signal attenuation is detected by varying the gradient strength g while holding the gradient pulse duration δ and the diffusion delay Δ constant. By fitting the experimental data to a non-linear exponential decay using equation (3.1), the diffusion coefficient D can be extracted. The results are usually presented as a Stejskal-Tanner plot, a typical one being shown in Figure 3.17.

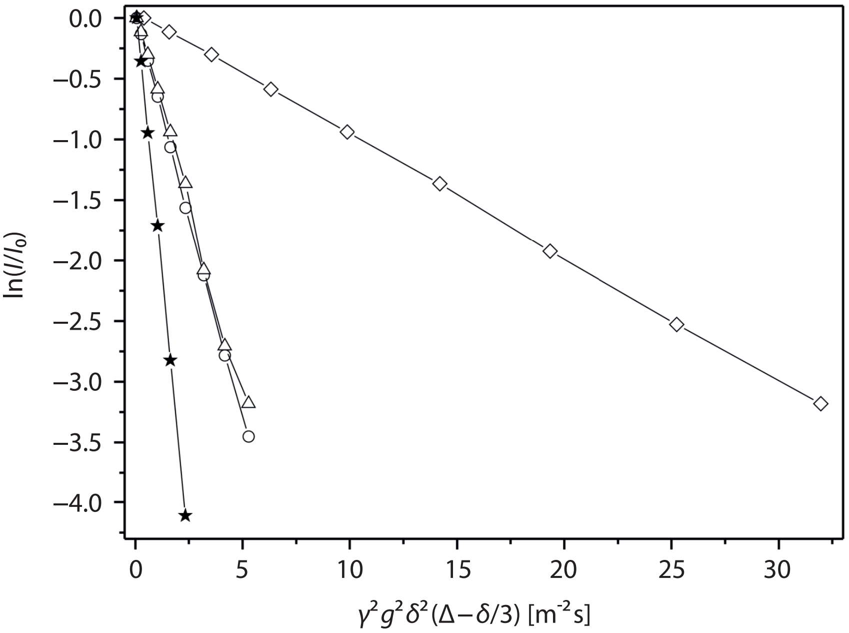

Figure 3.17: Stejskal-Tanner plot of the solvent D_2O (filled stars), TGT^{H333D} (diamonds), the free fragment *rac-trans*-**3.8** (circles) and its mixture with TGT^{H333D} (triangles) in D_2O buffer at 298 K.

In a DOSY assay of a protein–ligand interaction study, mixing of an active ligand with its protein target causes an equilibrium, as shown in equation (3.2),

$$\mathrm{L + P \rightleftharpoons LP} \tag{3.2}$$

where L stands for the ligand, P for the protein and LP for the protein–ligand complex. A dissociation constant, K_d, is introduced to describe the strength of the protein–ligand interaction depending on the concentrations of the single equilibrium components, as shown in equation (3.3).

$$K_\mathrm{d} = \frac{[L][P]}{[LP]} \tag{3.3}$$

In the limit of fast chemical exchange on the time scale of NMR measurements, a single set of resonance signals is observed. The measured spectra represent the average behavior of the ligand in its free and bound states. Thus, the observed diffusion coefficient, D_o, is the weighted average one for the ligand in the free and bound states:

$$D_\mathrm{o} = F_\mathrm{f}\, D_\mathrm{f} + F_\mathrm{b}\, D_\mathrm{b} \tag{3.4}$$

$$F_\mathrm{f} + F_\mathrm{b} = 1 \tag{3.5}$$

where F_f and F_b are fraction of the free and the bound ligands, respectively. Since proteins usually have masses two orders of magnitude as large as those of ligands, the diffusion coefficient of the protein can be used to approximate the diffusion coefficient of the ligand in the bound state D_b. The diffusion coefficient of the free ligand D_f can be measured under the same experimental condition separately. Taking the total concentration of the protein and the ligand P_{tot} and L_{tot}, respectively, as the additional known parameters, the dissociation K_d can be readily determined according to equation (3.6).

$$K_d = P_{tot} \times \frac{D_o - D_b}{D_f - D_o} - L_{tot} \times \frac{D_o - D_b}{D_f - D_o} \tag{3.6}$$

The accuracy in the calculation of K_d is of great challenge. As revealed by equation (3.6), the inaccuracy in K_d is inversely proportional to the square of $(D_f - D_o)$, the difference between the diffusion coefficient of the free ligand and the observed one of the ligand in a protein–ligand mixture. Therefore, the error in K_d rises drastically when the measured diffusion coefficients of the ligand in the free state and in the protein–ligand mixture become very close. A close inspection of equations (3.4)–(3.6) revealed that the expected change in the diffusion coefficients $\Delta D = D_f - D_o$ is closely related to F_b, which depends on P_{tot}, L_{tot}, and K_d in a highly complicated way. These dependencies are described in equations (3.7)–(3.10).

$$F_f = \frac{D_o - D_b}{D_f - D_b} \tag{3.7}$$

$$F_b = \frac{D_f - D_o}{D_f - D_b} \tag{3.8}$$

$$F_b = \frac{(P_{tot} + L_{tot} + K_d) - \sqrt{(P_{tot} + L_{tot} + K_d)^2 - 4\,L_{tot}\,P_{tot}}}{2\,L_{tot}} \tag{3.9}$$

$$\Delta D = D_f - D_o = F_b \times (D_f - D_b) \tag{3.10}$$

Simulated curves of F_b and ΔD against L_{tot} for K_d in the range of the binding systems in this study are shown in Figure 3.18. As revealed in Figure 3.18a, for K_d of 0.1 mM and the ligand concentration at 0.25 mM, about 10 % of the ligand is in the bound state, whereas this fraction drops to about 3 % at a K_d of 1.0 mM. The corresponding expected changes in the diffusion coefficients of the ligand upon binding are 0.7 and $0.2 \times 10^{-10}\ \mathrm{m^2\,s^{-1}}$, respectively. According to the DOSY experimental results, $\pm 0.1 \times 10^{-10}\ \mathrm{m^2\,s^{-1}}$ is the error range of those measured values of the diffusion coefficients. Furthermore, since ΔK_d is proportional to $1/[\Delta D^2]$, we can conclude that the DOSY assay is valid for the binding studies of protein–ligand systems with a least binding strength of 1 mM. The Stejskal-Tanner plots in Figure 3.17 show signal attenuation observed in the DOSY measurements on free ligand, the fragment *rac-trans*-**3.8**, the protein TGT^{H333D} alone, and a mixture of *rac-trans*-**3.8** and TGT^{H333D} at a molar ratio of 6.25:1, with a concentration of *rac-trans*-**3.8** of 0.25 mM in D_2O buffer.

Plots in Figure 3.17 cover a range of two orders of magnitude of the diffusion coefficients involved. Therefore, diffusion coefficients are 1.86×10^{-9}, 6.7×10^{-10}, 6.1×10^{-10}, and 4.3×10^{-11} m^2 s^{-1}, respectively. Nevertheless, the difference between free *rac-trans*-**3.8** and the observed one of *rac-trans*-**3.8** in its mixture with TGT^{H333D} is marginally weak, which is the consequence of a binding constant of 0.09 mᴍ.

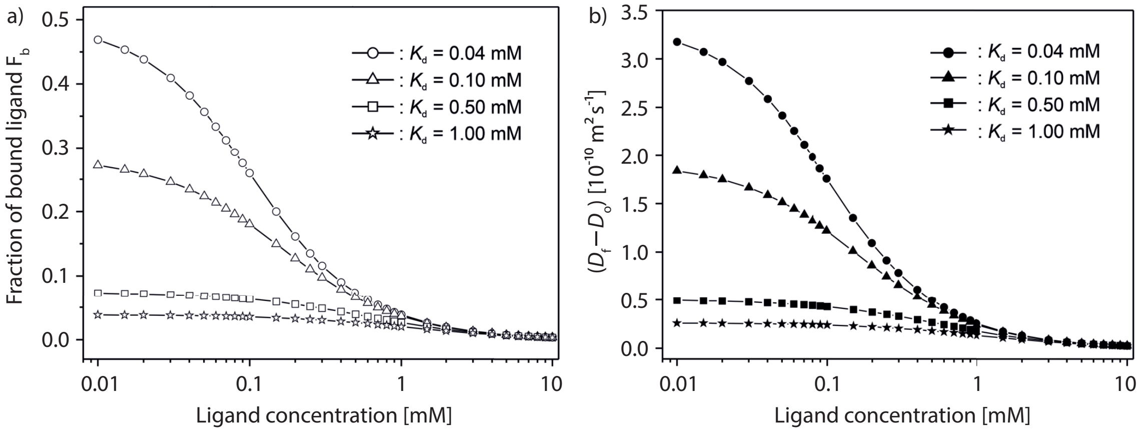

Figure 3.18: Simulated dependency of a) the fraction of bound ligand on the ligand concentration, on the basis of equation (3.9), assuming a protein concentration of 40 μᴍ, and b) the expected change in diffusion coefficient of the ligand ($D_f - D_o$) on the ligand concentration, on the basis of (3.10), assuming a protein concentration of 40 μᴍ, a protein diffusion coefficient of 0.43×10^{-10} m^2 s^{-1}, and a free ligand diffusion coefficient of 7.20×10^{-10} m^2 s^{-1}.

DOSY assays were carried out on six fragments with two protein mutants, as summarized in Table 3.2. The corresponding ^{1}H and two-dimensional ^{1}H–^{13}C HSQC spectra are displayed in Figures 3.20–3.26 (Experimental Section 3.4.6). All fragments were used in their racemic form except for the achiral *meso-cis*-**3.8**. The analyses of the experiments with racemic samples were done assuming that only one of the racemates binds to the protein with a single binding mode. The calculated K_d values range from 0.04 to 0.5 mᴍ. The DOSY assays were able to observe binding events for fragments *rac-trans*-**3.8** and *trans*-**3.12** with mutants TGT^{H333D} and TGT^{Y330D}. It seems that the binding is marginally stronger in the TGT^{H333D} variant compared to TGT^{Y330D}. If the binding of the transient interface pocket is assessed by DOSY, this finding could be explained by the varying conformational dynamics of the β1α1-loop in solution. While for the mainly monomeric species, as would be expected in TGT^{Y330D}, the loop could be able to adopt a high number of disordered states, the rapid dimer–monomer equilibrium in case of TGT^{H333D} could result in more pre-formed loop conformations that favor fragment accommodation.

However, multiple binding of the same fragment to the dimer interface binding pocket or additional binding events on the surface of the protein, as observed in the crystal structures with TGT$^{330/333}$, could lead to an averaged observation in DOSY and, hence, cannot be excluded.

Furthermore, the sensitivity range of DOSY NMR does not account for binding events with an affinity weaker than 1 mM. Unexpectedly, no binding could be detected for the sulfone fragment *rac-trans*-**3.7** as opposed to the observation from the crystal structure. Strangely, the fragment shows the fastest diffusion in our measurements although in size it is slightly larger than fragment *rac-trans*-**3.8** and similar to fragment *rac-trans*-**3.12**. This behavior could be replicated in samples with fragment *rac-trans*-**3.7** alone as well as with mixtures including both TGT variants, $\text{TGT}^{\text{H333D}}$ and $\text{TGT}^{\text{Y330D}}$. One explanation would be that the fragment degrades to a molecule of smaller size during the measurement process, hence, increasing its diffusion rate. This seems, however, less likely, since sulfolanes are usually quite stable and only degrade at harsh conditions via oxidative ring opening to their alkyl sulfonate analogues. Accordingly, the true reason for the unaltered diffusion coefficient between the pure fragment *trans*-**3.7** and the protein–fragment mixture remains unclear at this point.

Table 3.2: DOSY results in D_2O buffer at 298 K.

Sample	$\boldsymbol{D}$ [10^{-9} m^2 s^{-1}]	$\boldsymbol{K_d}$ [mM]
rac-trans-**3.7**	0.74	-
rac-trans-**3.7**–$\text{TGT}^{\text{H333D}}$	0.75	none
rac-trans-**3.7**–$\text{TGT}^{\text{Y330D}}$	0.75	none
rac-trans-**3.8**	0.67	-
rac-trans-**3.8**–$\text{TGT}^{\text{H333D}}$	0.61	0.09
rac-trans-**3.8**–$\text{TGT}^{\text{Y330D}}$	0.63	0.13
cis-**3.8**	0.70	-
cis-**3.8**–$\text{TGT}^{\text{Y330D}}$	0.68	none
rac-trans-**3.12**	0.70	-
rac-trans-**3.12**–$\text{TGT}^{\text{H333D}}$	0.58	0.09
rac-trans-**3.12**–$\text{TGT}^{\text{Y330D}}$	0.66	0.54
rac-cis-**3.12**	0.73	-
rac-cis-**3.12**–$\text{TGT}^{\text{H333D}}$	0.76	none
rac-trans-**3.13**	0.52	-
rac-trans-**3.13**–$\text{TGT}^{\text{H333D}}$	0.50	none
rac-trans-**3.13**–$\text{TGT}^{\text{Y330D}}$	0.50	none
Control measurements:		
3.15	0.58	-
3.15–$\text{TGT}^{\text{H333D}}$	0.58	none
3.15–$\text{TGT}^{\text{Y330D}}$	0.59	none
$\text{TGT}^{\text{H333D}}$	0.043	-
$\text{TGT}^{\text{Y330D}}$	0.046	-

3.3 Conclusion

The design of putative binders raised against a particular conformer of the loop–helix motif requires reliable information about the geometry of this motif in the monomeric state. Even though some of the previously investigated TGT variants show complete dissociation in solution, as evidenced by native nanoESI-MS experiments, we have so far only succeeded in crystallizing the *apo* enzyme in space group *C*2 where the conserved homodimeric arrangement is imposed by a crystallographic twofold axis. Supposedly, the protein arranges very efficiently with this organization in the solid state. This fact explains why it is so difficult to develop reliable descriptors to discriminate permanent PPIs from transient crystal packing contacts by analyzing crystallographic data only. Apart from this, an additional aspect has to be taken into account. With increasing protein concentration, dimer formation should be favored under equilibrium conditions. This concentration dependence is evidenced by our mass spectrometric experiments, which indicate increasing dimer populations at higher concentrations. At this point, it becomes evident that from an experimental point of view, the development of small-molecule modulators against a homodimer is much more delicate than against a heterodimer where the individual components forming the complex can be manipulated and studied separately. Thus, to successfully study the monomeric form of a homodimeric protein, an alternative concept is required. In 2006, Banatao *et al.* reported a method for the synthetic homodimerization of monomers in crystals by inducing disulfide formation via engineered cysteine mutagenesis.[120] In this study, we demonstrate the re-purposing of the mentioned technique using site-directed mutagenesis to find conditions allowing the crystallization of the TGT enzyme in a pseudomonomeric state.

Based on intial findings of Stephan Jakobi[91], who discovered a new hexagonal crystallization packing for the TGT^{Y330C} variant, a new variant, TGT$^{C158S/C281S/Y330C/H333A}$, has been designed to stabilize the disulfide-linked dimer arrangement, which has never been observed before in other crystalline TGT variants. Remarkably, the monomer units of the protein are presented with virtually conserved structure. However, the loop–helix motif, which shows enhanced flexibility in multiple crystal structures, adopts a new, previously not yet observed conformation. Important enough, this conformation would be incompatible for steric reasons with the dimer coinciding with the twofold axis in space group *C*2 as seen in the wild type enzyme. With some care, we hypothesize that this conformer of the loop–helix motif also occurs in solution, however, only with the monomeric form of TGT. This latter state is artificially captured, once the dimeric protein is geometrically split apart by the successfully introduced disulfide bridge.

Using the novel disulfide-linked TGT$^{330/333}$ variant, the now exposed original homodimer interface, which supposedly resembles with some feature the monomeric state, facilitated a crystallographic fragment-based investigation to address a novel transient binding pocket within the dimer interface. Derived fragments, based on the initial hit of a DMSO-bound structure, were soaked into the crystal and studied using structural data obtained from X-ray diffraction experiments.

Including DMSO, in total seven fragments were accomodated by the interface pocket from which two entities bound in the same pocket adjacent to the first molecule (fragments **3.4** and **3.5**) and another four fragment molecules also on the protein surface or between crystal mates (fragments **3.5**–**3.8**). Interestingly, the fragment hits are rather low in size containing only ≤11 non-hydrogen atoms. Likely, the solvent channels of the crystals impose bottlenecks that exclude larger fragments from entering and diffusing through the crystal, as analyzed by the *MAP_CHANNELS*[94] software.

Fine-tuning of the functional groups during fragment selection allowed the formation of new hydrogen-bond interactions with the adjacent amino acids flanking the binding pocket. Moreover, we demonstrated that the design of an additional interaction between a hydroxy group and Met93, as seen for fragment **3.6**, leads to a tilt of the sulfolane ring moiety, ultimately causing a positional shift of Thr47 and a subsequent collapse of the β1α1-loop. Astoundingly, the destabilization of the loop can be reverted by the design of an additional hydroxy function yielding fragment **3.7**, which forms hydrogen-bonds to the backbone and sidechain of residue Thr47, thereby restoring the residue and the β1α1-loop back to their original conformations. The following investigation on cyclic diols and other sulfolane derivatives only resulted in a CF_2-containing fragment **3.8** as additional hit. Likely, the bio-isosteric exchange of a SO_2 to the CF_2 group increases the lipophilicity of the fragment, which could be advantageous for later cell permeability applications. The same bio-isosteric replacement was successfully applied in an optimization process for the development of potent and permeable ATAD2 inhibitors.[121]

Since the obtained fragment hits are considered rather small in size, the biophysical assessment of fragment binding was challenging due to the presumed low binding affinity. We therefore sought to investigate a subset of the fragments using NMR techniques. Although the establishment of an ^{19}F-based screening failed, the binding of two fragments, *rac-trans*-**3.8** and *rac-trans*-**3.12**, could be verified and estimated via 2D DOSY NMR measurements. Moreover, the DOSY studies underpin the importance of the correct stereochemistry for the vicinal diols, as only the trans isomers are capable to bind to TGT as observed in the complex structures with the pseudomonomeric $TGT^{330/333}$ variant. According to the DOSY assay, the fragments show a binding constant in the two- to three-digit micromolar range.

In conclusion, this study provides the experimental prove for the addressability of the transient interface pocket of TGT using a protein variant with an articially introduced disulfide bridge. Nonetheless, the described procedure could be a general protocol to obtain structural information about a pseudomonomeric state of initially homodimeric proteins. The following investigation of small molecule fragments via soaking experiments yielded seven hits that were structurally characterized, from which some show the capability to modulate the dynamics of the β1α1-loop. We believe that these findings serve as starting points for the development of more potent compounds targeting the transient interface pocket. These compounds might have the potential to inhibit TGT using this novel mode-of-action by modulation of homodimer interface formation.

3.4 Experimental Section

3.4.1 Mutagenesis and recombinant production of *Z. mobilis* TGT

Mutagenesis and expression of the *Z. mobilis tgt* gene and its mutated variants were performed as previously described by site-directed mutation and plasmid-based expression of the vector pPR-IBA2 (IBA Lifesciences).[22] Plasmids encoding the required mutated TGT variants were prepared using the PureYield™ Plasmid Miniprep System (Promega). The mutations were introduced via the QuikChange Lightning Site-Directed Mutagenesis Kit (Agilent) according to the vendor instructions. DNA primers were purchased from Eurofins Genomics (Ebersberg, Germany) and are summarized in Table 3.3. The primers for the TGT^{Y330D} and TGT^{H333D} variants are listed in Table 4.2 (Chapter 4, Experimental Section 4.4.1). In each case, the new construct was re-sequenced by Eurofins Genomics to confirm the presence of the desired mutations as well as the absence of any further unwanted mutation. The final constructs were each transformed into *Escherichia coli* BL21-CodonPlus (DE3)-RIPL cells (Agilent).

A single colony was picked from the freshly transformed agar plate and grown overnight in 100 mL of lysogeny broth (LB) medium supplemented with 100 $\mu g\,mL^{-1}$ ampicillin and 34 $\mu g\,mL^{-1}$ chloramphenicol while shaking at 37 °C. The next day, a large-scale culture in LB medium, supplemented with 100 $\mu g\,mL^{-1}$ ampicillin and 34 $\mu g\,mL^{-1}$ chloramphenicol, was inoculated with 10 mL of overnight culture per liter. The culture was grown at 37 °C by shaking at 140 rpm until the optical density at 600 nm (OD_{600}) reached a value between 0.6 to 0.7 and was then cooled to 16 °C while shaking. After 1 h, overnight protein expression was induced by the addition of 1 mM IPTG. The cells were harvested the next day by centrifugation using a JA-10 rotor (Beckman Coulter) at 4 °C and 10 000 rpm for 10 min. The collected cells were disrupted by sonication using a Branson Sonifier™ 250 in 100 mL lysis buffer (20 mM TRIS, pH 7.8, 10 mM EDTA, 1 mM DTT and 1 cOmplete™-Protease Inhibitor Cocktail Tablet (Roche) per 4 L of bacterial culture). Subsequently, the cell debris was removed by centrifugation using a JA-25.50 rotor (Beckman Coulter) at 4 °C and 20 000 rpm for 1 h. The supernatant was collected and loaded onto a Q Sepharose® Fast Flow anion exchange column (XK 26/15, GE Healthcare) conditioned with buffer A (10 mM TRIS, pH 7.8, 1 mM EDTA, 1 mM DTT). After washing with buffer A, the target protein was eluted by applying a linear NaCl gradient from 0 to 100 % (v/v) buffer B (buffer A plus 1 M NaCl). The protein-containing fractions, endowed with an N-terminal Strep-tag® II, were then loaded onto a Strep-Tactin® Superflow® column (XK 16/10, IBA Lifesciences) or Strep-Tactin®XT cartridge (IBA Lifesciences) conditioned with buffer W (100 mM TRIS, pH 7.8, 1 mM EDTA, 1 M or 150 mM NaCl). After washing the column with buffer W, the protein was eluted with buffer E (buffer W plus 2.5 mM D-desthiobiotin) from the Strep-Tactin® Superflow® column or with buffer BXT (buffer W plus 50 mM D-biotin) from the Strep-Tactin®XT cartridge.

All chromatographic steps were carried out at room temperature using an ÄKTAprime™ plus FPLC system (GE Healthcare). All TGT-containing fractions were combined and concentrated to ca. 2 mg mL^{-1} in buffer W or high-salt buffer (10 mM TRIS, pH 7.8, 1 mM EDTA, 2 M NaCl) using Vivaspin® 20 centrifugal concentrators (30 000 MWCO, Sartorius). Subsequently, the Strep-tag® II was chipped off and separated from the target protein by means of the Thrombin Cleavage Capture Kit (Novagen®) according to the manufacturer's instructions. After tag cleavage, the sample was dialyzed against buffer W or high-salt buffer and concentrated via Vivaspin® 20 centrifugal concentrators to ca. 10 mg mL^{-1}. Successful tag cleavage was verified by mass spectrometry (Figure 3.19; mass spectra for the wild type TGT, TGT$^{\text{Y330D}}$, and TGT$^{\text{H333D}}$ variants are depicted in Chapter 4, Experimental Section 4.4.1). 100 µL aliquots of the samples were flash-frozen in liquid nitrogen and stored at −80 °C until further usage.

Table 3.3: DNA primer sequences used for mutagenesis. Nucleobases deviating from the original *tgt* sequence are underlined.

Mutation / Primer ID	Sequence
C158S_f[22]	5'-GGCATTTGATGAAT$\underline{\text{C}}$TACCCCGTATCCGG-3'
C158S_r[22]	5'-CCGGATACGGGGTA$\underline{\text{G}}$ATTCATCAAATGCC-3'
C281S_f[22]	5'-CGATATGTTTGATT$\underline{\text{C}}$TGTTCTGCCGACCCG-3'
C281S_r[22]	5'-CGGGTCGGCAGAACA$\underline{\text{G}}$AATCAAACATATCG-3'
Y330C_f[22]	5'-CAGAAATGGAGCCGTGCCT$\underline{\text{G}}$TATTCATCATCTGATTCG-3'
Y330C_r[22]	5'-CGAATCAGATGATGAATA$\underline{\text{C}}$AGGCACGGCTCCATTTCTG-3'
H333A_f	5'-CCGTGCCTATATTCAT$\underline{\text{GCG}}$CTGATTCGTGCAGGTG-3'
H333A_r	5'-CACCTGCACGAATCAG$\underline{\text{CGC}}$ATGAATATAGGCACGG-3'

3.4.2 Crystallization and fragment soaking

Crystallization of TGT$^{330/333}$ and its complexes was performed using the hanging-drop vapor diffusion method at 10 °C. For *apo* TGT$^{330/333}$ crystals, the protein solutions (10 mg mL^{-1} in buffer W) were mixed with reservoir solution (0.1 M magnesium formate or 0.1 M TRIS, pH 8.5, 4–5 % (w/v) PEG 6000) in a 2:1 volume ratio. Crystals grew within one month in the presence of 500 µL reservoir solution in the plate wells. For soaking experiments, the fragments were either added directly to the drop containing the *apo* crystal or dissolved in reservoir or cryo-protectant solution in which a crystal was transferred. The final fragment concentration ranged between 0.2 and 0.7 M. To enable diffusion of the fragment into the crystal, the crystal–fragment mixture was incubated between 5 s and 16 h. Prior to data collection, if no cryo-protectant was present during the incubation period, the crystals were transferred to a reservoir solution containing 30 % (v/v) glycerol as cryo-protectant for a few seconds and vitrified in liquid nitrogen.

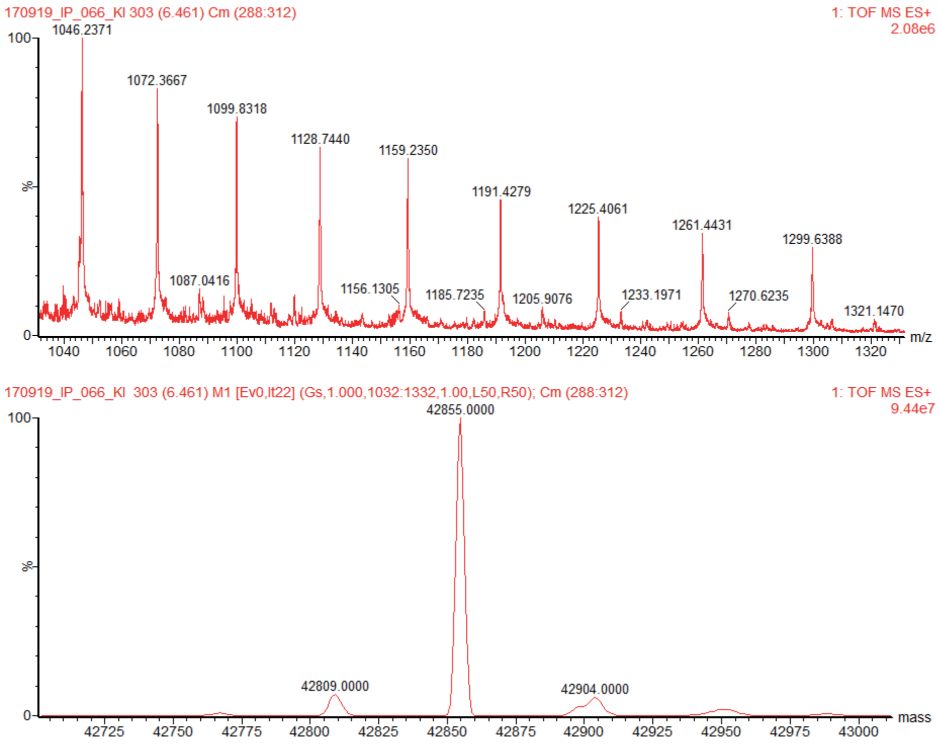

Figure 3.19: Mass spectrum and deconvoluted spectrum of TGT$^{\mathrm{C158S/C281S/Y330C/H333A}}$ (calculated mass: 42 855.6 Da).

3.4.3 Data collection and structure determination

Diffraction data were collected at a temperature of 100 K at the synchrotron beamline P13 or P14 at DESY (EMBL Hamburg) or at beamline 14.1 at BESSY II (Helmholtz-Zentrum Berlin). Indexing, processing and scaling of the diffraction images were done using *XDS*[66] and *XDSAPP*[67]. The structures were determined via molecular replacement using the program *Phaser*[68] from the *CCP4 suite*[69] with the PDB entry 1PUD[18] as initial search model. Model building was done in *Coot*[70] and the program *PHENIX*[71] was used for structure refinement. The used beam wavelengths as well as data collection and refinement statistics are summarized in Tables 3.4 and 3.5.

3.4.4 Analytical gel filtration

Analytical size exclusion chromatography was performed using an ÄKTAprime™ plus FPLC system (GE Healthcare) at room temperature. The protein samples were diluted to 10 µM in high-salt buffer (10 mM TRIS, pH 7.8, 1 mM EDTA, 2 M NaCl) and 100 µL of each sample was loaded onto a pre-equilibrated Superdex™ 200 10/300 GL column. The samples were run at a flowrate of 0.5 mL min^{-1} and protein absorbance was tracked at 280 nm wavelength. Data were processed with *GraphPad Prism 6*.

Table 3.4: Crystallographic data collection, processing and refinement statistics of PDB entries 7ADN, 7A4X, 7A4K and 7A9E.

Protein / Fragment	*apo* TGT$^{330/333}$	TGT$^{330/333}$–**3.1**	TGT$^{330/333}$–**3.2**	TGT$^{330/333}$–**3.4**
PDB ID (Fragment ID)	**7ADN**	**7A4X (DMS)**	**7A4K (QZT)**	**7A9E (R4W)**
(A) Data collection and processing				
Collection site	DESY BL P14	DESY BL P13	BESSY II MX 14.1	BESSY II MX 14.1
Wavelength [Å]	0.97950	0.79990	0.91841	0.91841
Unit cell parameters:				
Space group	$P6_522$ (179)	$P6_522$ (179)	$P6_522$ (179)	$P6_522$ (179)
a, b, c [Å]	127.79 127.79 115.46	128.12 128.12 114.41	128.27 128.27 114.97	128.00 128.00 115.38
α, β, γ [°]	90.0 90.0 120.0	90.0 90.0 120.0	90.0 90.0 120.0	90.0 90.0 120.0
(B) Overall diffraction data (values for highest resolution shell in parentheses)				
Resolution range [Å]	42.85–1.92 (2.03–1.92)	64.06–2.05 (2.17–2.05)	42.81–1.68 (1.78–1.68)	42.85–1.75 (1.87–1.75)
No. of unique reflections	43128 (6777)	35368 (5626)	63158 (10078)	55465 (8761)
R_{sym}[a] [%]	6.2 (49.3)	10.0 (50.8)	6.8 (174.9)	8.9 (147.8)
Completeness [%]	99.7 (98.5)	99.9 (95.7)	98.2 (99.2)	99.7 (99.3)
Multiplicity	24.8 (20.0)	21.9 (22.3)	15.6 (15.8)	10.9 (10.4)
Mean I/σ	31.6 (6.9)	22.3 (5.7)	25.9 (1.6)	16.9 (1.5)
R_{meas}[a] [%]	6.3 (50.6)	10.2 (52.0)	7.0 (180.8)	9.4 (155.5)
$CC_{1/2}$ [%]	99.9 (96.3)	99.9 (95.7)	100.0 (61.5)	99.9 (60.7)
Matthews coefficient [Å^3 Da^{-1}]	3.2	3.2	3.2	3.2
Solvent content [%]	61.3	61.1	61.3	62.1
Wilson B-factor [Å^2]	31.6	31.7	27.7	28.1
No. of proteins in asymmetric unit	1	1	1	1
(C) Refinement with *PHENIX*[71] (version 1.16_3549)				
Resolution range [Å]	42.85–1.92	64.06–2.05	42.81–1.68	42.85–1.75
No. of used reflections	43112	35322	63155	55463
R_{work}[b] / R_{free}[c] [%]	17.2 / 18.8	17.1 / 20.6	15.4 / 18.9	18.2 / 20.5
No. of atoms (non-hydrogen):				
Protein atoms	2967	2942	3042	2945
Water molecules	203	184	278	233
Zinc	1	1	1	1
Solvent ligand atoms	15	16	18	16
Fragment atoms	-	4	6	12
rmsd from ideal values:				
Bond lengths [Å]	0.007	0.007	0.008	0.007
Bond angles [°]	0.8	0.8	0.9	0.8
Ramachandran plot[d]:				
Most favored [%]	94.7	95.0	93.0	94.2
Additionally allowed [%]	5.0	4.3	6.7	5.5
Generously allowed [%]	0.3	0.6	0.3	0.3
Mean *B*-factors[e] [Å^2]:				
Protein atoms	38.7	38.4	42.4	36.9
Water molecules	45.9	43.7	45.9	44.9
Zinc ion	24.4	23.0	22.6	21.5
Solvent ligand atoms	44.5	41.5	38.1	41.6
Fragment atoms	-	40.6	32.6	45.2

[a] $R_{\text{sym}} = \dfrac{\sum_{\text{hkl}} \sum_{\text{i}} |I_{\text{hkl,i}} - \langle I_{\text{hkl}} \rangle|}{\sum_{\text{hkl}} \sum_{\text{i}} I_{\text{hkl,i}}}$; $R_{\text{meas}} = \dfrac{\sum_{\text{hkl}} \sqrt{\frac{\text{n}}{\text{n}-1}} \sum_{\text{i}} |I_{\text{hkl,i}} - \langle I_{\text{hkl}} \rangle|}{\sum_{\text{hkl}} \sum_{\text{i}} I_{\text{hkl,i}}}$.[72]

[b] $R_{\text{work}} = \dfrac{\sum_{\text{hkl}} |F_{\text{o}} - F_{\text{c}}|}{\sum_{\text{hkl}} F_{\text{o}}}$.[72]

[c] R_{free} was calculated as R_{work} but on 5 % of the data excluded from the refinement.

[d] Calculated via *PROCHECK*[73].

[e] Calculated via *MOLEMAN*[74].

Table 3.5: Crystallographic data collection, processing and refinement statistics of PDB entries 7A3X, 7A3V, 7A0B and 7A6D.

Protein / Fragment	TGT$^{330/333}$–**3.5**	TGT$^{330/333}$–**3.6**	TGT$^{330/333}$–**3.7**	TGT$^{330/333}$–**3.8**
PDB ID (Fragment ID)	**7A3X (QXB)**	**7A3V (QXE)**	**7A0B (QTQ)**	**7A6D (R1E/RGN)**
(A) Data collection and processing				
Collection site	BESSY II MX 14.1	BESSY II MX 14.1	BESSY II MX 14.1	BESSY II MX 14.1
Wavelength [Å]	0.91841	0.91841	0.91841	0.91841
Unit cell parameters:				
Space group	$P6_522$ (179)	$P6_522$ (179)	$P6_522$ (179)	$P6_522$ (179)
a, b, c [Å]	128.29 128.29 114.86	127.96 127.96 115.52	127.86 127.86 115.73	127.87 127.87 115.19
α, β, γ [°]	90.0 90.0 120.0	90.0 90.0 120.0	90.0 90.0 120.0	90.0 90.0 120.0
(B) Overall diffraction data (values for highest resolution shell in parentheses)				
Resolution range [Å]	42.80–1.85 (2.05–1.85)	42.87–1.70 (1.80–1.70)	42.90–1.77 (1.88–1.77)	42.79–1.59 (1.68–1.59)
No. of unique reflections	47943 (7607)	61476 (9767)	54711 (8690)	74885 (11815)
R_{sym}[a] [%]	11.1 (160.6)	12.4 (164.1)	8.2 (152.8)	8.0 (205.8)
Completeness [%]	99.9 (99.9)	99.7 (98.4)	99.9 (99.8)	99.8 (99.1)
Multiplicity	9.9 (10.2)	17.1 (15.2)	11.0 (11.2)	17.5 (17.9)
Mean I/σ	12.8 (1.4)	13.5 (1.3)	17.9 (1.5)	21.7 (1.4)
R_{meas}[a] [%]	11.7 (169.1)	12.8 (172.3)	8.7 (160.1)	8.3 (211.9)
$\mathrm{CC}_{1/2}$ [%]	99.8 (61.1)	99.8 (60.1)	99.9 (61.3)	100.0 (60.9)
Matthews coefficient [$Å^3$ Da^{-1}]	3.2	3.3	3.2	3.2
Solvent content [%]	61.3	62.9	61.4	61.2
Wilson B-factor [$Å^2$]	31.5	27.0	29.6	25.1
No. of proteins in asymmetric unit	1	1	1	1
(C) Refinement with *PHENIX*[71] (version 1.16_3549)				
Resolution range [Å]	42.79–1.85	42.87–1.70	42.90–1.77	42.79–1.59
No. of used reflections	47939	61290	54710	74767
R_{work}[b] / R_{free}[c] [%]	20.3 / 22.6	18.1 / 20.0	18.3 / 20.2	14.8 / 17.8
No. of atoms (non-hydrogen):				
Protein atoms	2798	2918	2934	2974
Water molecules	179	213	183	262
Zinc	1	1	1	1
Solvent ligand atoms	12	16	34	26
Fragment atoms	21	16	18	18
rmsd from ideal values:				
Bond lengths [Å]	0.007	0.007	0.007	0.008
Bond angles [°]	0.8	0.8	0.8	1.0
Ramachandran plot[d]:				
Most favored [%]	96.0	94.3	94.4	94.0
Additionally allowed [%]	3.6	5.4	5.3	5.7
Generously allowed [%]	0.3	0.3	0.3	0.3
Mean *B*-factors[e] [$Å^2$]:				
Protein atoms	39.6	34.7	37.7	37.5
Water molecules	44.4	45.4	45.0	43.4
Zinc ion	25.4	21.3	23.4	20.4
Solvent ligand atoms	45.8	41.9	47.2	49.4
Fragment atoms	50.6	39.9	37.5	42.4

[a] $R_{\mathrm{sym}} = \dfrac{\sum_{\mathrm{hkl}} \sum_{\mathrm{i}} |I_{\mathrm{hkl,i}} - \langle I_{\mathrm{hkl}} \rangle|}{\sum_{\mathrm{hkl}} \sum_{\mathrm{i}} I_{\mathrm{hkl,i}}}$; $R_{\mathrm{meas}} = \dfrac{\sum_{\mathrm{hkl}} \sqrt{\frac{\mathrm{n}}{\mathrm{n}-1}} \sum_{\mathrm{i}} |I_{\mathrm{hkl,i}} - \langle I_{\mathrm{hkl}} \rangle|}{\sum_{\mathrm{hkl}} \sum_{\mathrm{i}} I_{\mathrm{hkl,i}}}$.[72]

[b] $R_{\mathrm{work}} = \dfrac{\sum_{\mathrm{hkl}} |F_{\mathrm{o}} - F_{\mathrm{c}}|}{\sum_{\mathrm{hkl}} F_{\mathrm{o}}}$.[72]

[c] R_{free} was calculated as R_{work} but on 5 % of the data excluded from the refinement.

[d] Calculated via *PROCHECK*[73].

[e] Calculated via *MOLEMAN*[74].

3.4.5 Thermal shift assay

Protein unfolding was monitored via the fluorescence of SYPRO™ Orange (Invitrogen) within a temperature range between 10 and 100 °C in 320 increments as described by Niesen *et al.*[122] Thermal shift experiments were done in triplicate using a QuantStudio™ 3 Real-Time PCR System (Thermo Fisher Scientific) equipped with a MicroAmp™ Fast Optical 96-Well Reaction Plate (0.1 mL) (Applied Biosystems). The total volume of each sample was 20 µL with 24 µg of protein diluted in high-salt buffer (10 mм TRIS, pH 7.8, 1 mм EDTA, 2 м NaCl) and 2× SYPRO Orange dye (Invitrogen). The wavelengths for excitation and emission of the dye were 470 ± 15 nm and 575 ± 15 nm, respectively. The melting temperature, T_m, was determined as the maximum of the first derivative of each melting curve. Data were processed with *GraphPad Prism 6*.

3.4.6 NMR spectroscopy

All measurements were performed on a Bruker AVANCE™ III 500 MHz spectrometer equipped with a CryoProbe Prodigy BB-H&F-D-05 with Z-gradient at 298 K. The temperature was calibrated with Bruker standard 4 % methanol in methanol-d_4. Stock solutions of fragments *rac-trans*-**3.7**, *rac-trans*-**3.8**, *cis*-**3.8**, *rac-trans*-**3.12**, *rac-cis*-**3.12**, *rac-cis*-**3.12** and *rac-trans*-**3.13** at a concentration of 100 mм in 50 mм of sodium phosphate buffer supplemented with 150 mм of NaCl in D_2O at pD of 7.40 were prepared and stored at 4 °C for use. The buffer was triply lyophilized from D_2O to fulfill the hydrogen/deuterium exchange. Control ligands **3.14** and **3.15** were prepared in DMSO-d_6 at 100 mм as stock solution and stored at 4 °C for use. As for proteins, the TGT^{H333D} mutant was prepared in the same D_2O buffer at a concentration of 200 µм as a stock solution, while the mutant TGT^{Y330D} was in the same buffer at a concentration of 450 µм. The samples were prepared by diluting those stock solutions with the D_2O buffer to a final solution of 200 µL and put in Wilmad 3 mm tubes (Rototec Spintec). For proteins with limited sample amount, a 3 mm Shigemi tube (Shigemi Inc.) with a sample volume of 100 µL was used.

^{19}F NMR spectra were recorded on ligand samples at 0.1, 0.5, and 1.0 mм. Single pulse without ^{1}H decoupling was not possible due to technical restriction of the Prodigy BB-H&F probe, where ^{1}H and ^{19}F resonances share one channel. The chemical shift of ^{19}F was referenced to $CFCl_3$ externally. Spectra were recorded with 256 to 4096 transients and a relaxation delay of 3 s.

DOSY experiments were done using the stimulated echo method with bipolar gradient pulses and long eddy current delay to avoid disturbances in the detection of resonance peaks.[123,124] The pulse sequence was *ledbpgp3s* from Bruker pulse program library. The gradient shape used was smoothed square SMSQ10.100 and gradient length was between 1 and 2 ms, which resulted in δ of 2 and 4 ms, respectively. The optimized diffusion delays Δ were between 30 ms for the ligands and 100 ms for proteins. Diffusion attenuation was realized with 9 steps in gradient ramp. The DOSY 2D spectra were recorded with 9 experiments and each with 256 to 512 transients. Relaxation delays were 3 s.

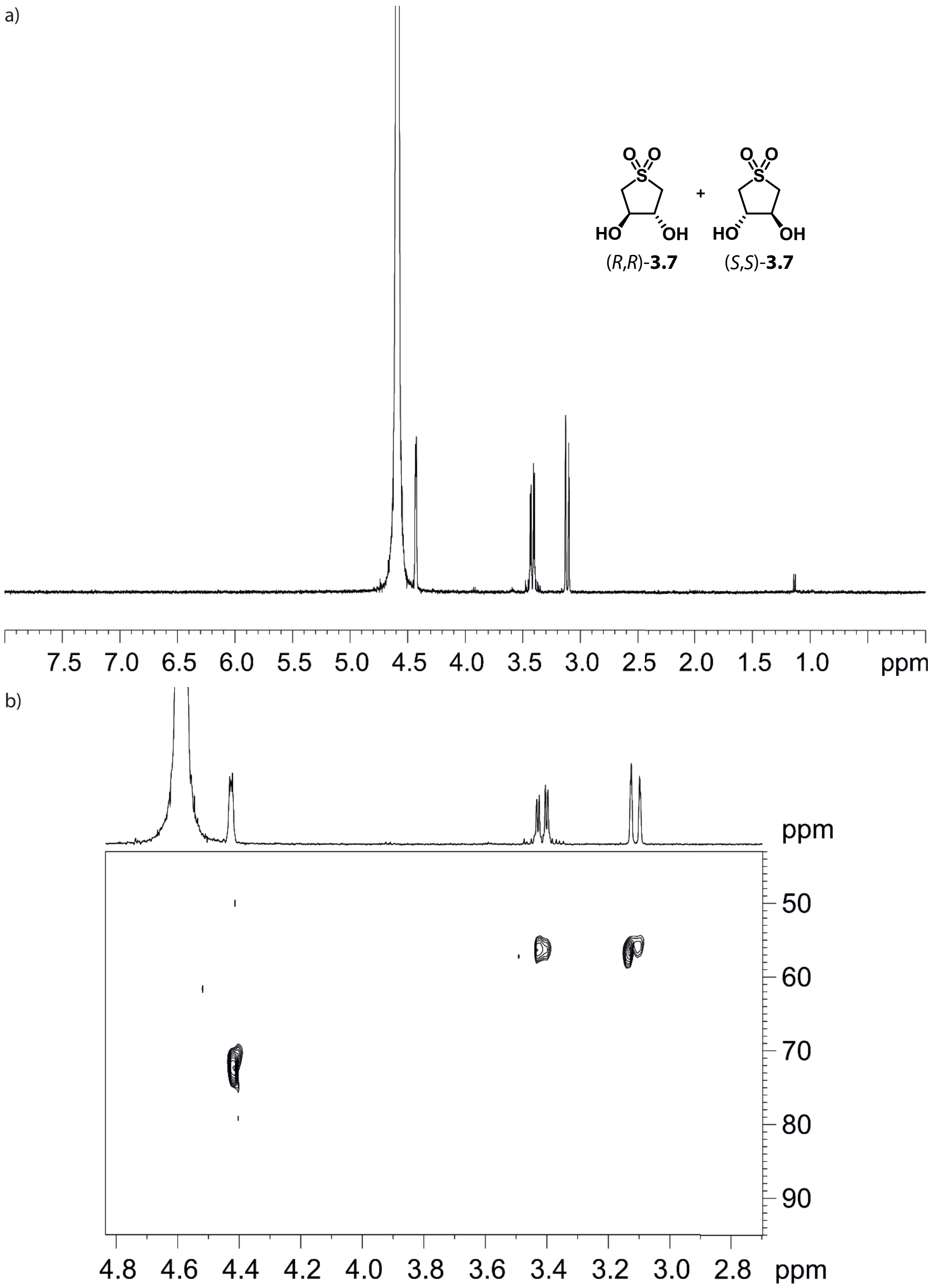

Figure 3.20: a) ^{1}H spectrum and b) ^{1}H–^{13}C HSQC spectrum of 1 mM *rac-trans*-**3.7** in D_2O buffer at 298 K.

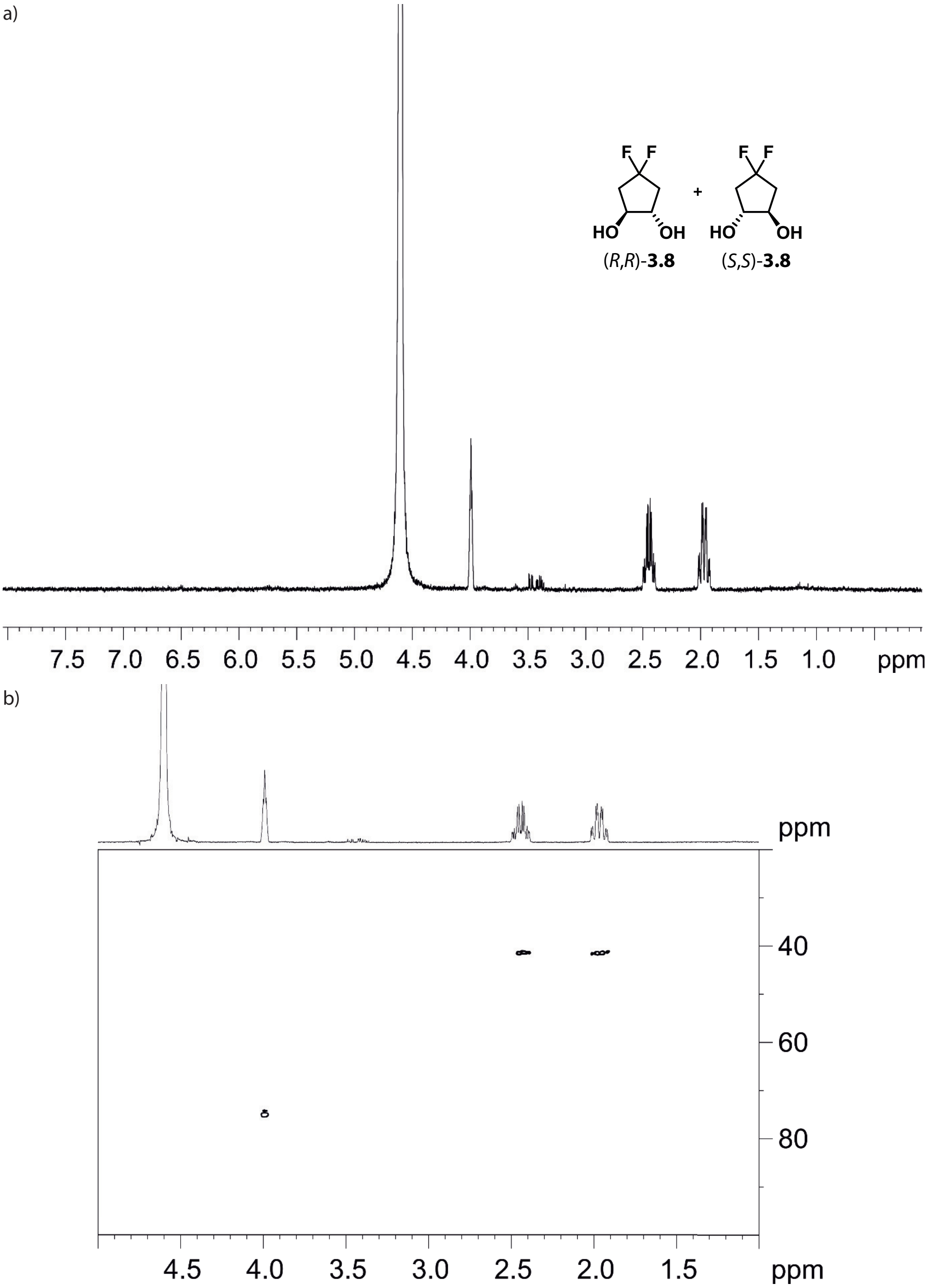

Figure 3.21: a) ^{1}H spectrum and b) ^{1}H–^{13}C HSQC spectrum of 1 mM *rac-trans*-**3.8** in D_2O buffer at 298 K.

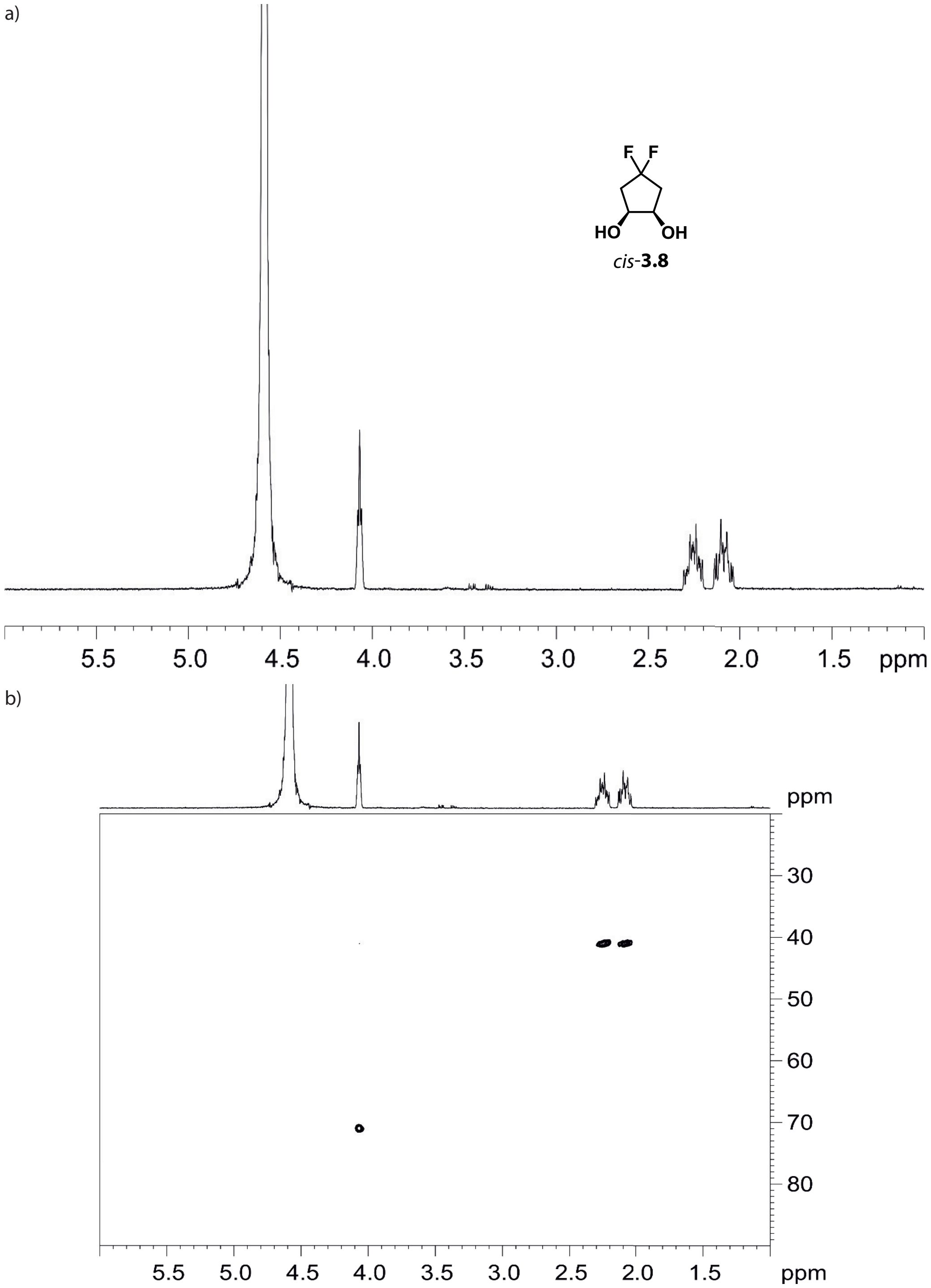

Figure 3.22: a) ^{1}H spectrum and b) ^{1}H–^{13}C HSQC spectrum of 1 mM *cis*-**3.8** in D_2O buffer at 298 K.

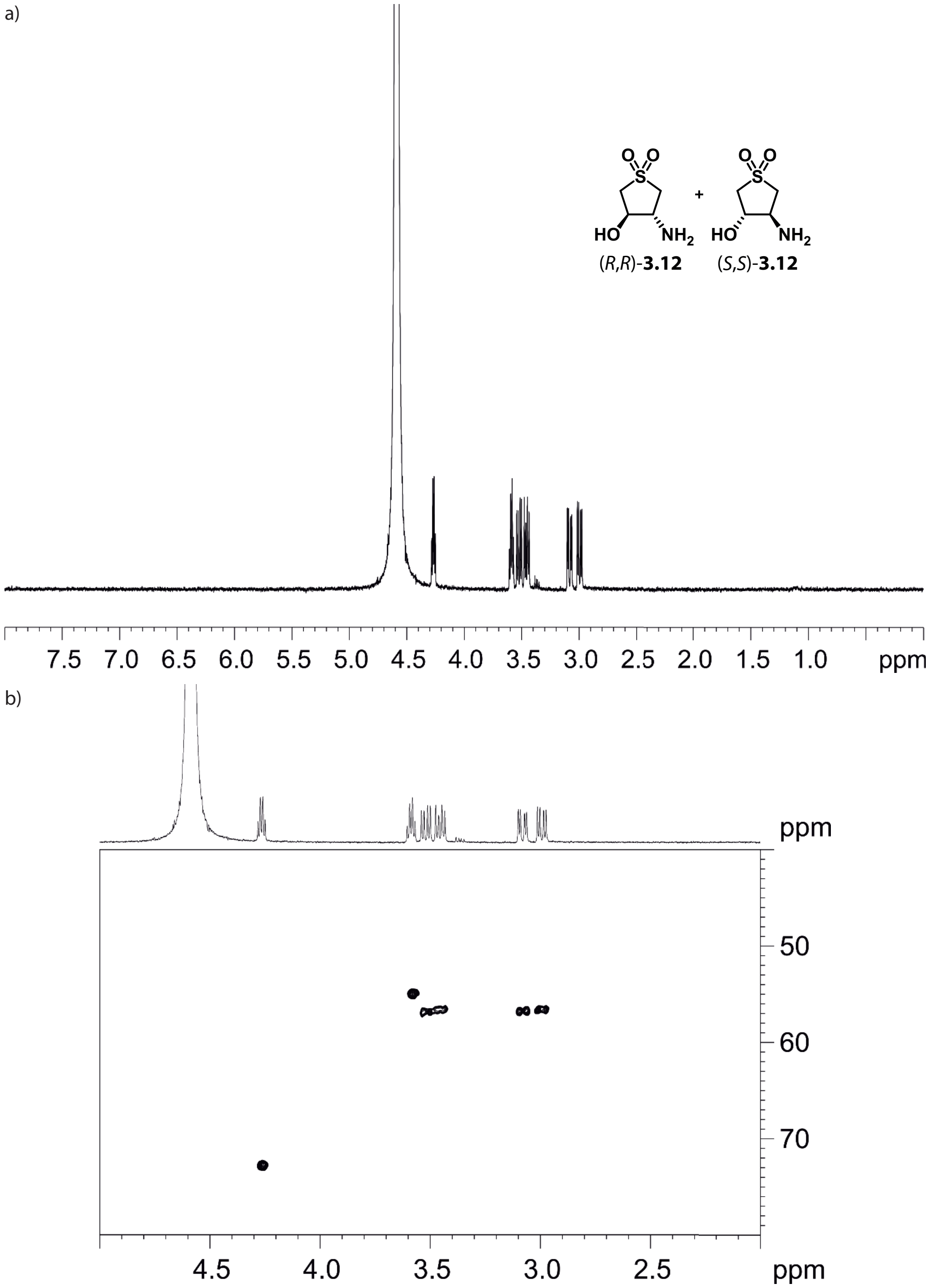

Figure 3.23: a) ^1H spectrum and b) ^1H–^{13}C HSQC spectrum of 1 mM *rac-trans*-**3.12** in D_2O buffer at 298 K.

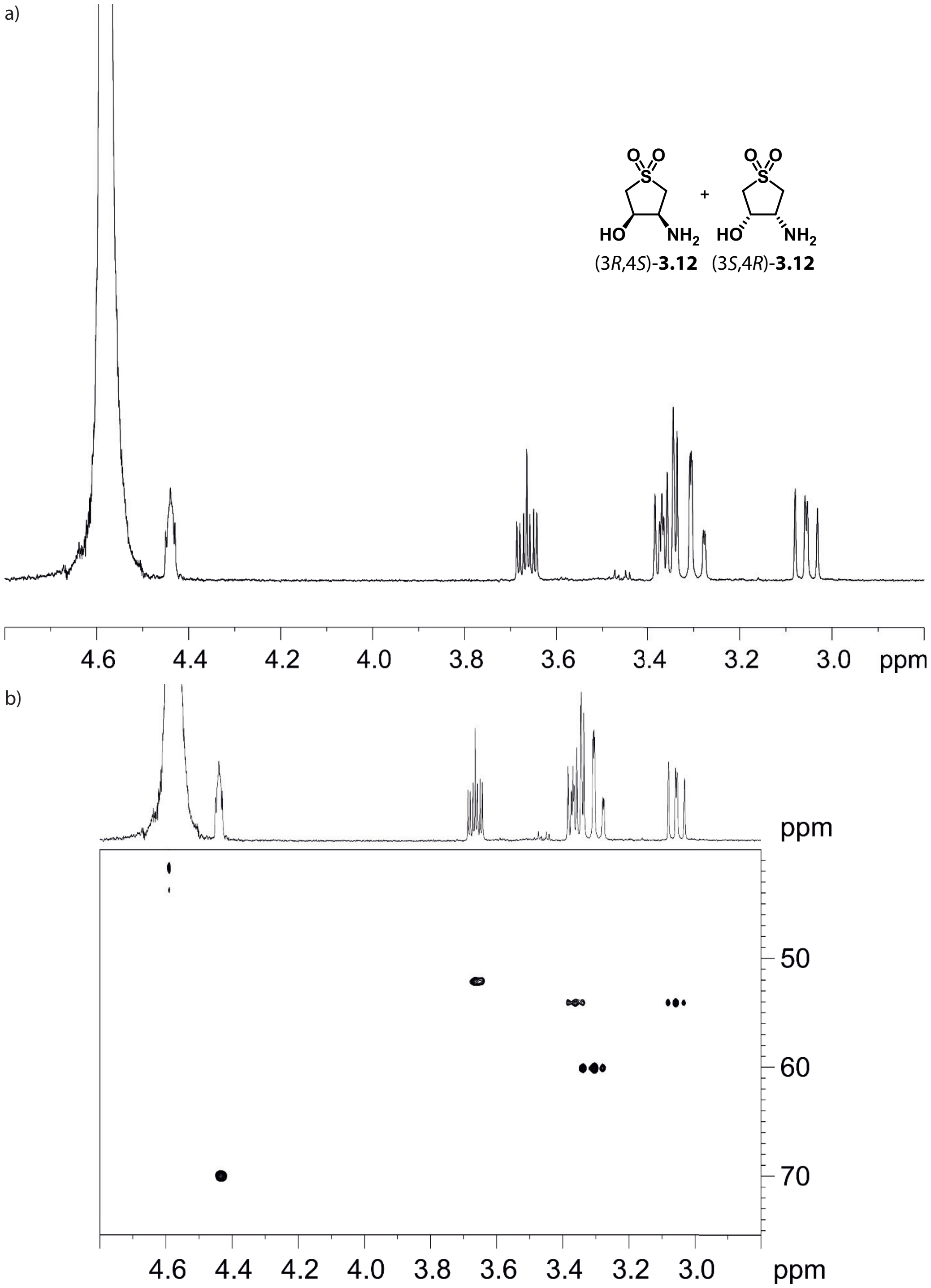

Figure 3.24: a) ^{1}H spectrum and b) ^{1}H–^{13}C HSQC spectrum of 1 mM *rac-cis*-**3.12** in D_2O buffer at 298 K.

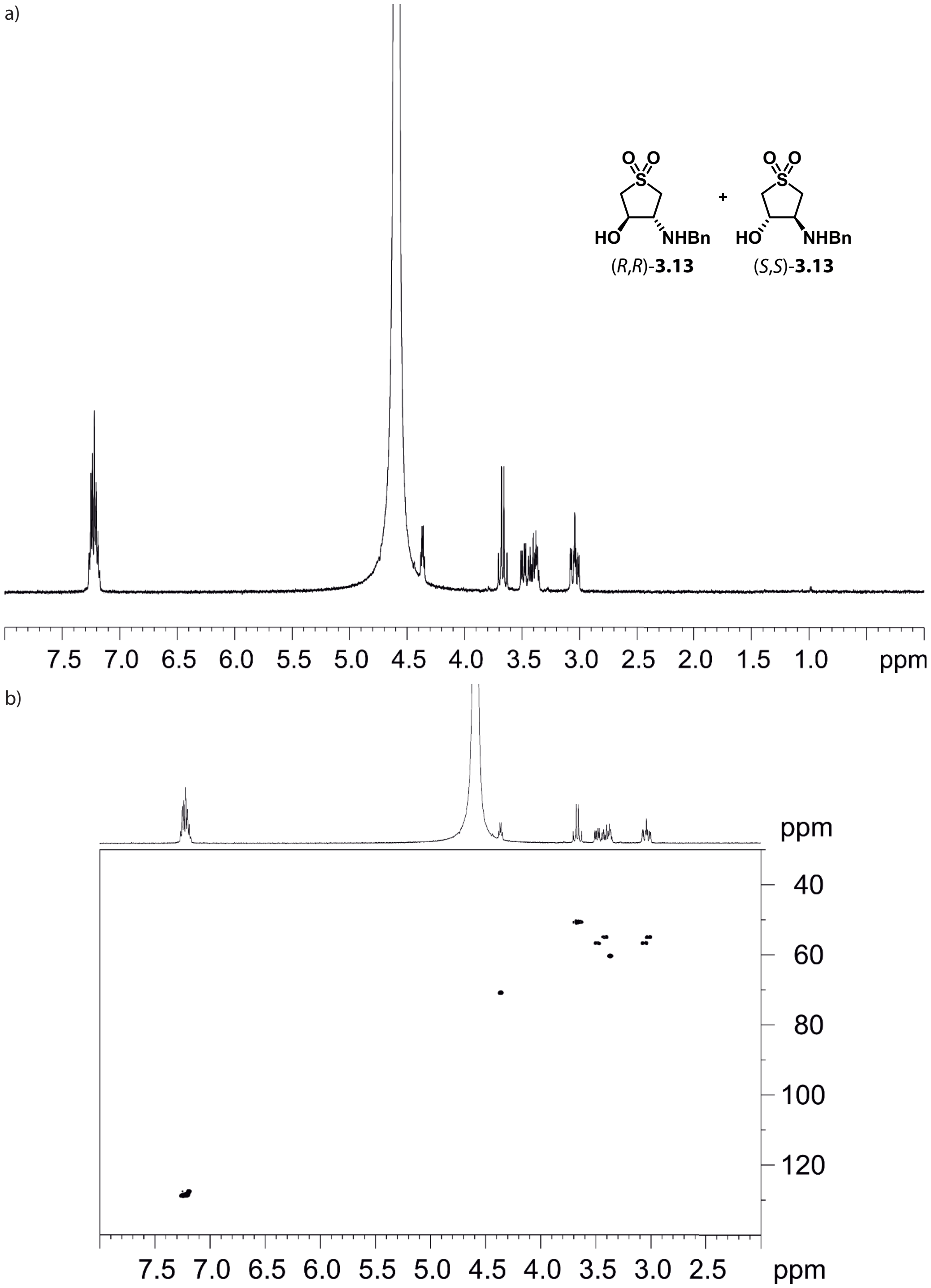

Figure 3.25: a) ^{1}H spectrum and b) ^{1}H–^{13}C HSQC spectrum of 1 mM *rac-trans*-**3.13** in D_2O buffer at 298 K.

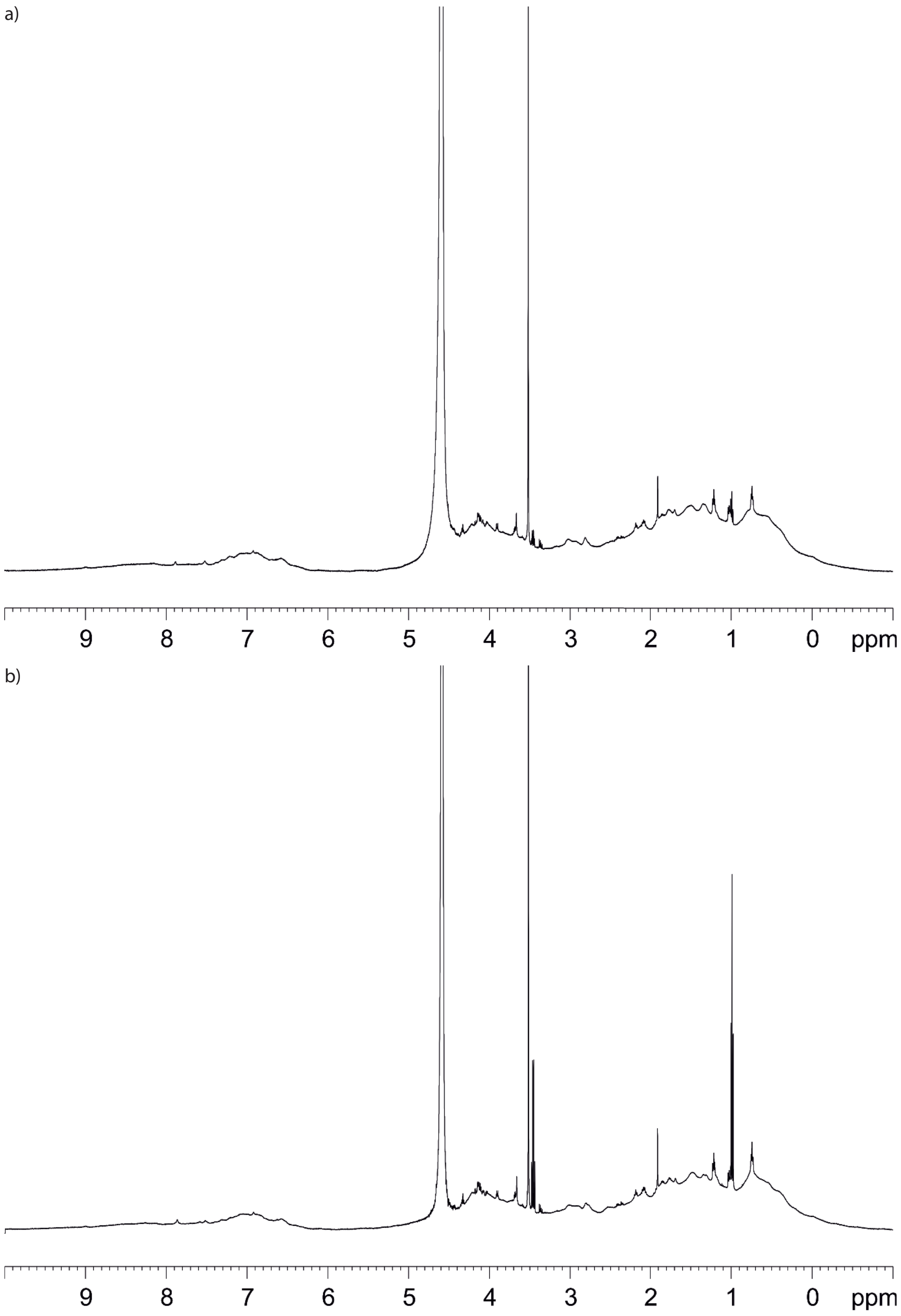

Figure 3.26: ^{1}H spectra of a) 381 µM TGT^{H333D} and b) 459 µM TGT^{Y330D} in D_2O buffer at 298 K.

3.4.7 List of investigated compounds

Table 3.6: Chemical structures and size descriptors of investigated compounds. Only one isomer structure is shown if two isomers are possible.

ID	Chemical structure	Molecular weight [g mol^{-1}]	Molecular volume[a] [Å^3]	Minimal cylindric height[b] / radius[b] [Å]
3.1	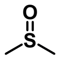	78.13	80.7 ± 5.4	1.59 / 2.33
3.2	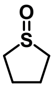	104.17	104.2 ± 5.8	2.60 / 2.24
3.3	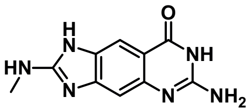	230.23	219.9 ± 7.5	1.74 / 6.02
3.4	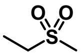	108.16	109.1 ± 5.9	2.40 / 2.93
3.5	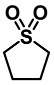	120.17	116.3 ± 6.1	2.43 / 2.22
3.6	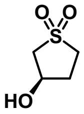	136.17	125.7 ± 6.2	2.89 / 2.37
cis–**3.7**	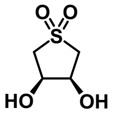	152.16	141.1 ± 6.5	2.85 / 2.69
trans–**3.7**	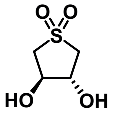	152.16	140.9 ± 6.5	2.61 / 2.71
cis–**3.8**	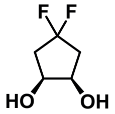	138.11	136.8 ± 6.4	2.89 / 2.53
trans–**3.8**	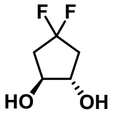	138.11	137.4 ± 6.4	2.55 / 2.69
trans–**3.9**	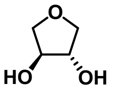	104.11	112.0 ± 6.0	2.71 / 2.38
trans–**3.10**	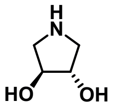	103.12	113.1 ± 6.0	2.56 / 2.68

ID	**Chemical structure**	**Molecular weight** [g mol^{-1}]	**Molecular volume**[a] [Å^3]	**Minimal cylindric height**[b] **/ radius**[b] [Å]
trans–**3.11**	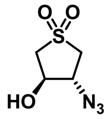	177.18	157.0 ± 6.7	2.61 / 3.29
cis–**3.12**	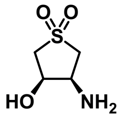	151.18	145.6 ± 6.5	3.16 / 2.81
trans–**3.12**	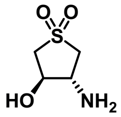	151.18	145.7 ± 6.5	2.64 / 2.85
trans–**3.13**	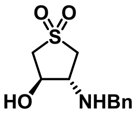	241.31	229.3 ± 7.6	3.53 / 4.96
S1	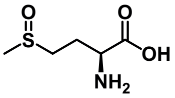	165.21	165.7 ± 6.8	2.80 / 4.05
S2	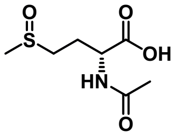	207.24	208.3 ± 7.4	2.94 / 4.48
S3	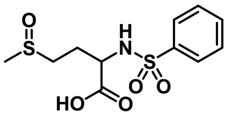	305.36	291.3 ± 8.2	4.33 / 5.68
S4	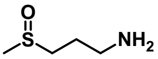	121.20	132.2 ± 6.3	2.12 / 3.76
S5	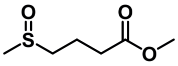	164.22	171.9 ± 6.9	2.94 / 4.98
S6	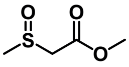	136.17	135.1 ± 6.4	2.76 / 3.33
S7	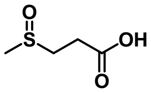	136.17	135.2 ± 6.4	2.57 / 3.71
S8	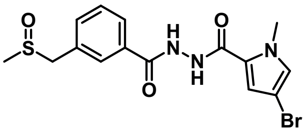	398.28	331.3 ± 8.6	4.25 / 7.28
S9	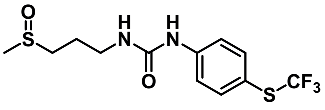	340.38	317.8 ± 8.5	3.64 / 8.15

ID	**Chemical structure**	**Molecular weight** [g mol^{-1}]	**Molecular volume**[a] [Å^3]	**Minimal cylindric height**[b] **/ radius**[b] [Å]
S10	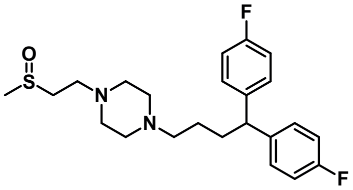	420.56	433.1 ± 9.4	6.71 / 6.30
S11	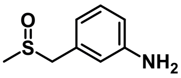	169.24	172.5 ± 6.9	2.29 / 4.11
S12	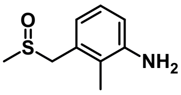	183.27	187.6 ± 7.1	3.12 / 4.30
S13	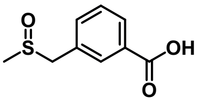	198.24	191.3 ± 7.1	2.24 / 4.89
S14	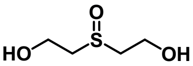	138.18	141.9 ± 6.5	2.53 / 4.50

[a] Calculated via *VEGA ZZ*[125].

[b] Calculated via *RADI*[95].

4

Disrupting the Bacterial TGT Homodimer with Interface-Derived Peptides

4.1 Introduction

Protein–protein interactions (PPIs) are fundamental to a wide variety of cellular processes, as they are involved in large communication networks between proteins. Rational modulation of PPIs can interfere with these processes and may ultimately lead to therapeutic intervention.[79–82] Recent advancements in our knowledge of PPIs have spurred interest in the design of PPI modulators to perturb the biological function of proteins that are involved in disease.[83,126] Since protein–protein interfaces are generally flat and lack deep hydrophobic cavities, druggable by small molecules, research has turned its attention to peptides as they can interact with larger surfaces and represent mimics of natural interaction partners. The advantages of peptides as drug candidates comprise, *inter alia*, their structural flexibility and high modularity, thus allowing them to adapt to large binding surfaces in structurally diverse ways.[127,128] On the contrary, the use of peptides as potential drug candidates is impaired by challenging drawbacks, such as their low stability against proteolytic degradation, insufficient membrane permeability and poor oral bioavailability.[128,129] However, several approaches in peptide modifications, such as the introduction of β-amino acids into peptide backbones,[130] conformational constraints using macrocyclization techniques,[131,132] and the development of so-called cell-penetrating peptides (CPPs),[133,134] have been successfully demonstrated to tackle these bottlenecks. Finally, these success stories emphasize the underestimated potential of peptides as PPI modulators.

4.1.1 Peptides as homodimer disruptors

Peptide-based approaches have been successfully developed to modulate homodimeric protein–protein interactions. For instance, Toro *et al.* investigated a set of peptides derived from an α-helix within the homodimeric interface of *Leishmania infantum* trypanothione reductase (Li-TryR). Supported by molecular dynamics simulations, the peptides were rationally designed and found to inhibit the enzyme by competitive binding to the interface which led to an increased dissociation of the dimer.[135] Further studies led by Ruiz-Santaquiteria *et al.* optimized the peptides through cyclization strategies, such as lactam bridging and all-hydrocarbon stapling, resulting in potent dimer interface modulators with *in vitro* anti-leishmanial activity.[136,137] Another example include peptides by Cardinale *et al.* that were derived from an interfacial β-hairpin structure of the human thymidylate synthase to target its homodimeric interface resulting in growth inhibition of ovarian cancer cells. Further structural and biophysical studies revealed a new mechanism of action, whereby the peptide does not act as a dissociative interface inhibitor but rather stabilizes an inactive form of the dimer.[138] Another example highlights the use of the protein grafting technique, whereby essential residues are grafted onto a stable α-helical protein such as avian pancreatic polypeptide (aPP). With this method, a chimeric peptide was designed that contained essential residues from an interfacial α-helix of the KSHV protease to disrupt its biologically active homodimeric structure.[38] The findings from this study led to a high-throughput screening of a helical mimetic compound library and ultimately to the discovery of DD2, a small molecule capable of inhibit KSHV protease activity by disrupting its dimerization.[39]

4.1.2 Discovery of an interface target site in homodimeric TGT occupied by structural peptide motifs

Since bacterial tRNA-guanine transglycosylase (TGT) is allegedly only active as a homodimer,[19,20] disturbing the homodimer formation by peptides represents an attractive approach to modulate TGT function. In the course of an investigation on a pseudomonomeric TGT variant in which the dimer interface was broken up due to an introduced disulfide bridge (Chapter 3), one protein–fragment complex structure (PDB ID: 7A4K) showed a stabilized N-terminal tail that has never been observed before in a TGT crystal structure, due to pronounced disorder. However, in this structure, the N-terminal amino acids could be resolved in the electron density up to residue Glu3' and are stabilized in an interaction network comprising residues Ala49, Arg77, Arg82, Ser91, and Phe92 (Figure 4.1a). Interestingly, the position of the N-terminal tail closely corresponds to helix αE (residues Arg328'–Arg336') in the functional dimer interface (PDB ID: 1PUD[18], Figure 4.1b). Notably, helix αE harbors two aromatic hotspot residues, Tyr330 and His333, which significantly contribute to the formation of the stable TGT homodimer. Thus, the N-terminal tail as well as helix αE serve as excellent starting points for the investigation of interface-probing peptides.

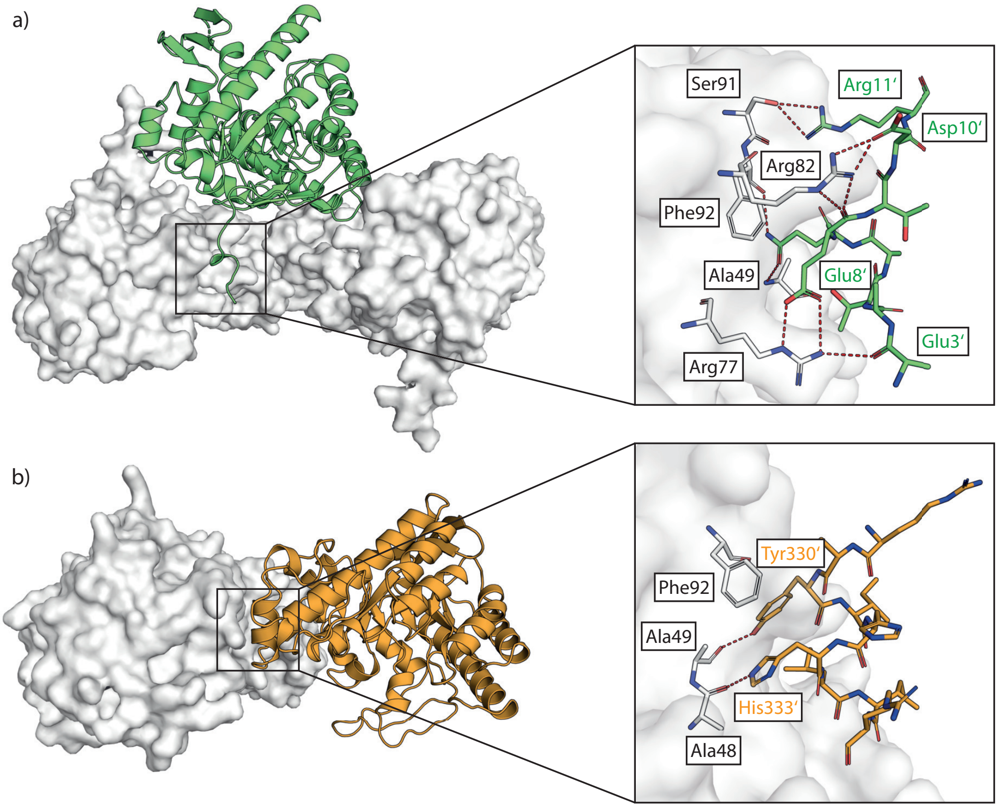

Figure 4.1: Starting points for the study of putative interface-binding peptides: a) N-terminal tail (orange, residues Glu3’–Arg11’) of the crystal mate of the disulfide-linked dimer (PDB ID: 7A4K) and b) helix αE (green, residues Arg328’–Arg336’) of the functional dimer mate (PDB ID: 1PUD[18]).

4.2 Results and Discussion

4.2.1 Preface

This chapter comprises initial investigations on the search for peptides as disruptors for the TGT homodimer. The recombinant expression and purification, biophysical characterization of the protein samples, crystallization experiments and microarray binding assays were performed by the author of this thesis. Peptide synthesis and initial fluorescence polarization experiments were performed by **Lea Albert** from the group of **Olalla Vázquez** (Philipps-Universität Marburg). Further peptide binding studies were continued by **Mujia Li** (Albert-Ludwigs-Universität Freiburg), **Raquel Reilly** (Fairfield University), and the author of this thesis. Enzyme kinetic studies were performed by **Maurice Sebastiani** and **Stefanie Dörr** from the group of **Klaus Reuter** (Philipps-Universität Marburg). The assays for the assessment of dimerization constants were conducted by the author of this thesis. The assay for studying host cell invasion by *Shigella flexneri* was established by the author of this thesis together with **Harshavardhan Janga** and **Leon N. Schulte** (Philipps-Universität Marburg). The *S. flexneri* strains were provided by **Glenn R. Björk** (Umeå University).

4.2.2 Epitope mapping and peptide design using peptide microarrays

We sought to apply peptide-based approaches to prevent homodimer formation of TGT as an alternative strategy to hamper the function of TGT. Therefore, the stabilized N-terminal tail observed in a crystal structure of a disulfide-linked variant (Chapter 3) and helix αE were used as starting points for a further search using peptide arrays. Peptide arrays consist of custom peptide libraries, usually synthesized via SPOT synthesis and immobilized on a membrane.[139] This enables rapid binding evaluation of multiple peptide entities to a target macromolecule.[140] To map the binding epitope of the TGT dimer interface, we acquired peptide microarrays from peptides&elephants (Hennigsdorf, Germany). The array consisted of 27 N-acetylated peptides synthesized in small spots on a 4,7,10-trioxa-1,13-tridecanediamine (TOTD) membrane. For the determination of the peptide binding region using an epitope scan, peptides were synthesized with a frame shift between two or six amino acids starting from a 15-mer peptide derived from helix αE and its flanking amino acids (residues Lys325–Glu339) and a 10-mer peptide from the N-terminal tail (residues Met1–Asp10). Also, a scan of truncated species was applied to determine the minimal binding sequence. In addition to the peptides based on helix αE and the N-terminal tail, peptides derived from the β1α1-loop (residues Thr47–Thr55) and grafted peptide chimeras using a stable helical peptide[141] have been investigated with the array. Successful binding between the peptides and the respective protein tagged with an N-terminal Strep-tag® II, was visualized by a luminol chemiluminesence reaction caused by the addition of a Strep-Tactin®-horseradish peroxidase (HRP) conjugate, which binds to the tagged protein. Since the peptides were designed to bind at the homodimer interface of TGT, the destabilized TGT^{H333A} variant, which shows an enhanced proportion of the monomeric form, was initially used for the assay to ensure proper peptide–TGT binding. Figure 4.2a shows the results with the first peptide array on TGT^{H333A}. The binding affinity of the peptides was estimated from the spot intensities. Only peptides derived from helix αE and the N-terminal tail indicated binding to TGT^{H333A}, with the 13-mer sequence Ac-SRAYIHHLIRAGE (residues Ser327^{P}–Glu339^{P}, peptide numbering indicated with ^{P}) and the 6-mer sequence Ac-TAQETD (residues Thr5^{P}–Asp10^{P}) being the most promising binders.

Based on these results, a second round of array design was accomplished including one-residue frame shifts to locate the precise peptide binding sequence of both parent peptides. Additionally, an alanine scan was performed in which single residues in the parent sequence were mutated to alanine to identify the residues essential for binding. Table 4.4 lists the peptide sequences of the second array design (Experimental Section 4.4.6). Two identical copies of the array were tested against the predominantly monomeric TGT^{Y330D} mutant and wild type TGT. The results indicate similar binding behavior of the peptides against the two TGT variants with the 10-mer peptide Ac-YIHHLIRAGE (residues Tyr330^{P}–Glu339^{P}) derived from helix αE being the superior binding motif (Figure 4.2b and c).

Interestingly, the alanine mutational scan revealed a loss of binding upon mutation of residues Arg328^P, Tyr330^P, His333^P, Arg336^P, and Glu339^P to alanine. This effect was expected for the point mutations Y330A^P (B4), H333A^P (B7), and E339A^P (C4), as they have been identified as hotspot residues in previous studies.[21,23,60] Contrary, the observed binding loss for the mutations R328A^P (B3) and R336A^P (C2) were rather surprising, as both arginine residues are not oriented towards the interface and, thus, should not be involved in dimer formation. One explanation could be that the arginine residues stabilize the helical integrity of the interacting peptide. The reason for this finding remains to be elucidated. Moreover, none of the peptides derived from the N-terminal tail showed binding in the microarray and, hence, were not progressed further.

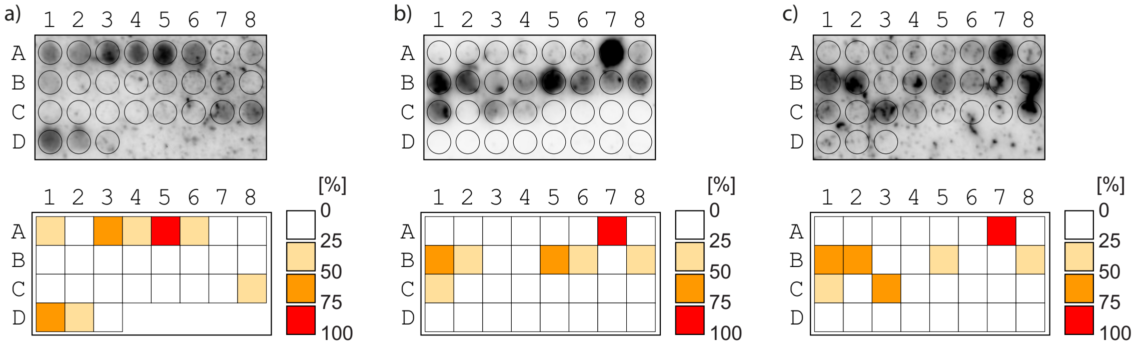

A5: Ac-SRAYIHHLIRAGE
D1: Ac-TAQETD

A7: Ac-YIHHLIRAGE
B1: Ac-SRAYIHHLIRAGE

A7: Ac-YIHHLIRAGE
B1: Ac-SRAYIHHLIRAGE

Figure 4.2: Peptide array results with a) TGT^{H333A}, b) TGT^{Y330D}, and c) wild type TGT. Binding strength of the peptides was estimated by spot intensity. The sequences of the two best binding peptides are displayed. Full sequences of the array are listed in Tables 4.3 and 4.4 (Experimental Section 4.4.6).

4.2.3 Peptide binding by fluorescence polarization

Fluorescently labeled peptides, based on the sequence YIHHLIRAGE, were synthesized for further characterization via fluorescence polarization (FP, also termed fluorescence anisotropy) binding studies. The fluorescence polarization method is based on the detection of changes in the effective molecular volume of a fluorescent protein–ligand complex. After excitation of a fluorophore with plane-polarized light, FP is measured by the fluorescence emission in two planes. The relation between the detected intensities in the parallel ($I_{\parallel}$) and perpendicular ($I_{\perp}$) planes and anisotropy (A) are depicted in equation 4.1[142,143] as:

$$A = \frac{I_{\parallel} - I_{\perp}}{I_{\parallel} + 2I_{\perp}} \tag{4.1}$$

In literature, the terms polarization (P) or millipolarization (mP) are frequently used which can be interchanged with anisotropy values using equations 4.2 and 4.3:[143]

$$P = \frac{3A}{2 + A} \tag{4.2}$$

$$A = \frac{2P}{3 - P} \tag{4.3}$$

The measured anisotropy depends on the angle (ζ) between the excitation and emission dipoles, as shown in equation 4.4,[144] and can reach a theoretical maximum value of $A = 0.4$ if both dipoles are oriented in parallel ($\zeta = 0°$). In such a case, where an excited fluorophore remains immobilized during the lifetime of its excited state, 60 % of the emitted light will remain polarized.

$$A = \frac{3\cos^2\zeta - 1}{5} \tag{4.4}$$

However, rapid molecular tumbling of a small-sized fluorophore, such as a peptide in solution, causes the emitted light to be mainly depolarized with $A = 0$ when $I_{\parallel} = I_{\perp}$. This is due to the reorientation of the fluorophore during its fluorescence lifetime. The degree of anisotropy depends on the rotational tumbling speed, which is inversely proportional to the molecular volume as described by the Stokes' equation 4.5[145]:

$$\rho = \frac{3\eta V}{RT} \tag{4.5}$$

ρ = rotational relaxation time
η = viscosity
V = molecular volume
R = universal gas constant
T = temperature

If the small fluorophore gets immobilized, e. g, by binding to a larger sized molecule, such as a protein, the rotational tumbling will be much slower resulting in a smaller degree of fluorophore reorientation and a higher degree of maintained polarized light. Thus, the observed change in FP can be used to track bound and unbound fluorophore species and, thus, characterize protein–ligand binding events. Figure 4.3 summarizes the rationale for using the FP method to study protein–ligand interactions. The synthesized peptides were fluorescently labeled with 5(6)-carboxyfluorescein (FAM) either at the N-terminus or near the C-terminus and are referred to as "tracers" in the context of FP experiments. A summary of the investigated peptides is given in Table 4.1.

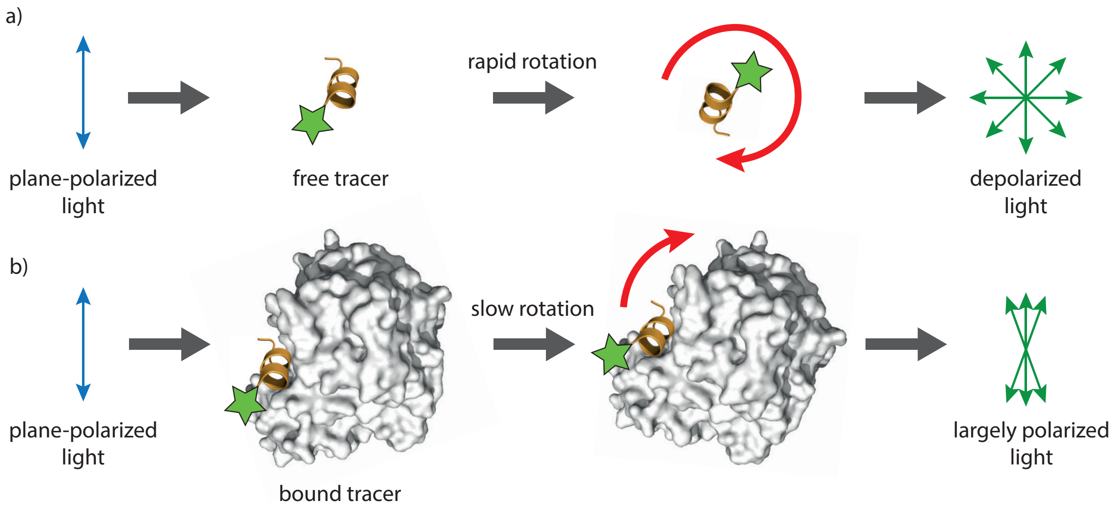

Figure 4.3: Schematic representation of the basic principle behind fluorescence polarization measurements. a) A peptide tracer (orange helix) marked with a fluorophore (green star) gets excited by plane-polarized light. The rapid molecular tumbling of the tracer and the associated high reorientation of the fluorophore during its fluorescence lifetime causes the emitted light to be depolarized. b) The binding of the tracer a larger interaction partner (gray surface) leads to a slower tumbling, low fluorophore reorientation, and, therefore, emission of largely polarization-retained light.

Table 4.1: Peptides for FP binding studies. The fluorophore is highlighted in green. Cysteines at *i*/*i*+4 positions are highlighted in red with the linker represented as an arc.

ID	Tracer peptide sequence
4.1	FAM-YIHHLIRAGE-CONH$_2$
4.2	Ac-YIHHLIRAGE-Ahx-Ahx-K(FAM)-CONH$_2$
4.3	FAM-YCHHLCRAGE-Ahx-Ahx-K(Ac)-CONH$_2$
4.4	FAM-Y$\overset{\frown}{\text{CHHLC}}$RAGE-Ahx-Ahx-K(Ac)-CONH$_2$

An initial FP experiment with N-terminally labeled linear tracer **4.1** at a fixed concentration of 1 µM was performed with wild type TGT (Figure 4.4). FP was measured at specific time points with a total incubation time of 5 h. The lower plateau of the binding curve shows the fraction of unbound tracer. A measurable signal increase could only be observed at the highest protein concentration, which indicates that higher concentrations of TGT are needed to bind a substantial amount of the tracer. Although the signal change can be measured right after mixing the components, a steady increase is observed over time. This points to a shift in the tracer–TGT binding equilibrium, which could be explained by the fact that only a small amount of the wild type enzyme is available in its monomeric state at which the tracer can bind. The tracer binding to the TGT monomer could slowly shift the dimer–monomer equilibrium towards the monomeric species and, hence, increase the chance for binding further tracer molecules. Therefore, TGT mutants with greater dimer dissociation rates, TGT^{Y330D} or TGT^{H333D}, were used for further experiments.

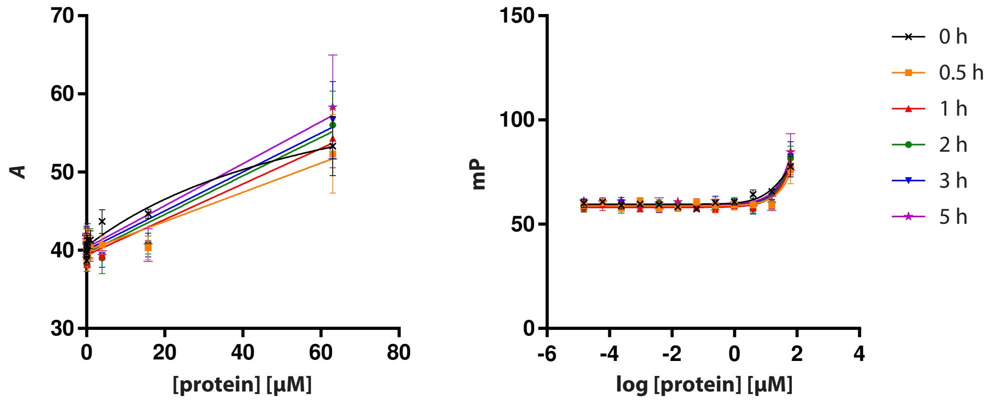

Figure 4.4: Saturation binding curve of 1 µM tracer **4.1** with wild type TGT (left) and dose-response curve for the same FP experiment (right).

A similar approach was pursued by Wang *et al.*, where a phosphorylated variant of the Rho-kinase was used for FP experiment. The phosphorylation prevented the homodimerization of the kinase, hence enabling the direct binding of the investigated peptides to the Rho-kinase monomer.[146]

Although the point mutations at positions 330 and 333 reside in the hotspot region of the dimer interface of TGT, the binding site of helix αE, from which the tracers are derived, is located far remote from the area and, thus, should not substantially influence tracer binding. After optimizing the experimental conditions, such as lowering the tracer concentration from 1 µM to 50 nM and increasing the maximum protein concentration to 419 µM, the FP measurement was repeated with the same tracer and TGT^{Y330D} (Figure 4.5). Although no second plateau for the completely bound tracer could be observed, a large FP signal increase could be measured at high protein concentrations indicating an increased fraction of bound tracer. The dissocation constant of weak-binding tracer **4.1** to TGT^{Y330D} can be estimated to K_d > 1.7 mM. Interestingly, a significant time-dependent signal shift was not observed as in the previous experiment with the wild type enzyme. This could be due to the missing dimer–monomer equilibrium which is likely not present for the TGT^{Y330D} variant.

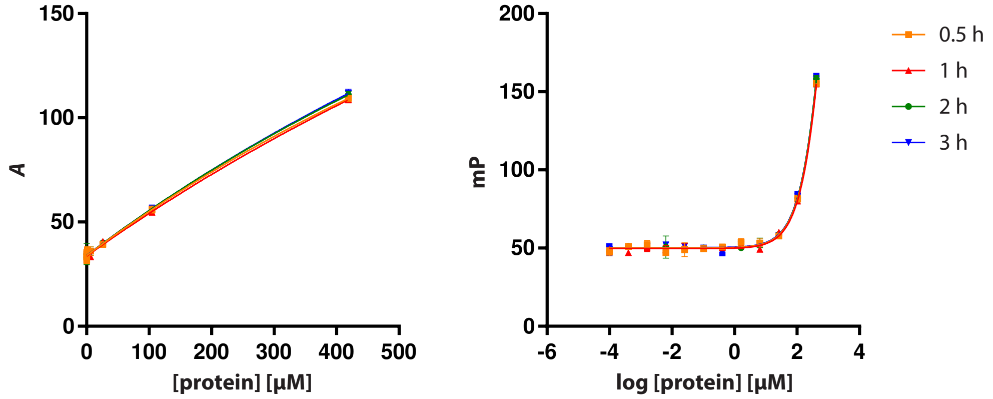

Figure 4.5: Saturation binding curve of 50 nM tracer **4.1** with TGT^{Y330D} (left) and dose-response curve for the same FP experiment (right).

Furthermore, a C-terminally FAM-labeled tracer (**4.2**) was synthesized to test an additional fluorophore labeling site and whether one site influences the binding of the tracer to TGT. No measurable change in FP was detected for tracer **4.2** with the TGT^{Y330D} variant (Figure 4.6). This indicates that the introduced C-terminal linker including the FAM label either interferes with binding or exhibits high residual flexibility leading to the so-called "propeller effect" in which the mobile fluorophore label negatively affects the anisotropy in the bound state.[147] As a consequence, the N-terminal labeling site was retained in further investigated tracers.

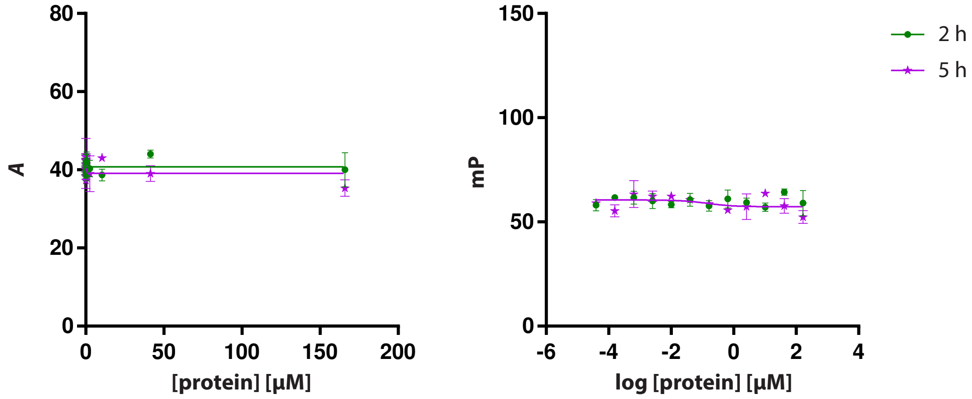

Figure 4.6: Saturation binding curve of 20 nM tracer **4.2** with TGT^{Y330D} (left) and dose-response curve for the same FP experiment (right).

In order to increase the binding affinity of the tracer to TGT, a peptide cyclization approach was attempted since cyclic peptides are more rigid and lower the entropic penalty upon binding. Moreover, the cross-linked backbone of the peptide is more resistant to proteolytic degradation, thus enhancing the stability of the cyclic peptide compared to its linear surrogate.[131,132] Since the tracers were derived from helix αE, we proposed that cyclization via peptide stapling may stabilize the helical geometry of the peptides, which is required for successful binding to the dimer interface.

Stapled helical peptides have been successfully developed as dimer disruptors, as demonstrated for the inhibition of homodimeric Li-TryR reported by Ruiz-Santaquiteria *et al.* A similar stapling approach for $i/i+4$ positions, the spacing at which two amino acid sidechains are in close proximity in an α-helix, was applied on the parent peptide **4.2**. Since cyclization approaches via lactam-bridges failed, cysteine mutations were introduced at residues Ile331^{P} and Ile335^{P} in peptide **4.2** to provide the precursor peptide **4.3** enabling thiol-based cyclization reactions. The peptide stapling strategy was facilitated by perfluoroarylation of the two introduced cysteine residues by hexafluorobenzene yielding the stapled peptide **4.4** (Figure 4.7).[148]

FP of the linear parent tracer **4.3** and stapled tracer **4.4** was measured over an incubation time of 48 h with an additional measurement after 12 d (Figure 4.8). A signal increase at higher protein concentrations can be observed for both tracers after 48 h and 12 d. After 12 d, stronger deviations in the signals are measured which become clear in case of tracer **4.3**. This can be attributed to irregular evaporation of the samples, which were stored in a lid-covered, but not sealed, 96-well plate.

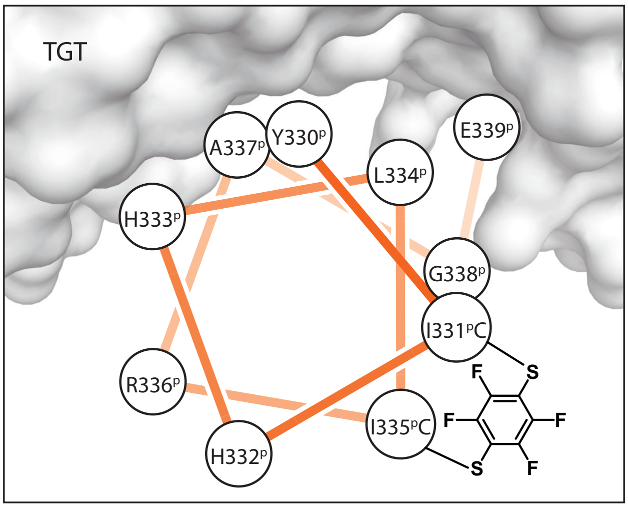
TGT
A337P
Y330P
E339P
L334P
H333P
G338P
I331PC
R336P
I335PC
H332P
F
S
F
F
S
F

Figure 4.7: Helical wheel diagram of the YIHHLIRAGE peptide sequence (residues Tyr330^{P}–Glu339^{P}). A *i*/*i*+4 stapling by a tetrafluorobenzene linker between the introduced cysteine mutations I331C and I335C is shown.

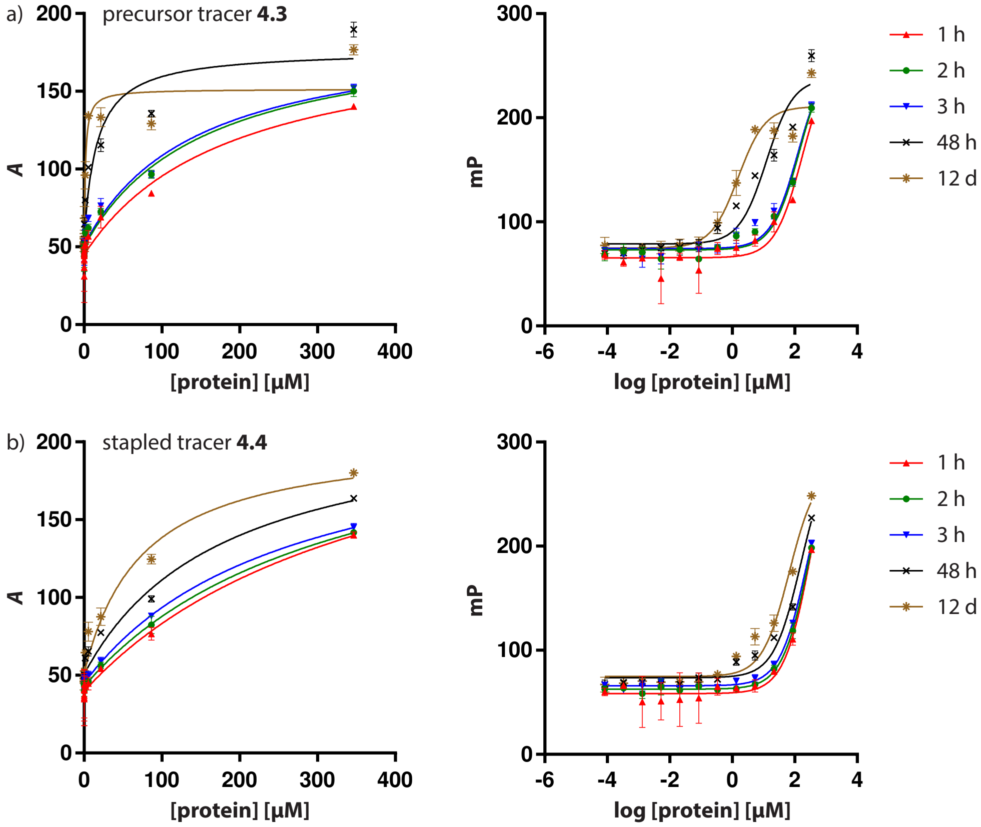

Figure 4.8: Saturation binding curves of a) 20 nM tracer **4.3** and b) 20 nM tracer **4.4** with TGT^{Y330D} (left) and dose-response curves for the same FP experiments (right).

At a later point, the FP experiments were repeated with another interface mutant variant TGT^{H333D}. In Chapter 3, DOSY NMR studies have shown that two investigated small molecule fragments, which bind in a transient pocket of the dimer interface of TGT, have a higher binding affinity towards TGT^{H333D} than to the TGT^{Y330D} variant. This could be explained by the rapid dimer–monomer equilibrium of TGT^{H333D}, which could provide stable interface conformations that would otherwise be altered in a permanent monomeric species. In this study, we investigated if the findings from the DOSY NMR studies apply to our interface-binding peptides as well. Therefore, FP of the linear tracer **4.1** and stapled tracer **4.4** was measured with TGT^{H333D} (Figure 4.9). The results for the linear tracer **4.1** are similar to the ones observed with wild type TGT and TGT^{Y330D} (Figures 4.4 and 4.5, respectively) with no measurable saturation and no significant change in FP signal over an incubation time of 24 h. Remarkably, the results for the stapled tracer **4.4** already indicated a saturation of the tracer binding after 1 h with a measurable dissociation constant of K_d = 9.2 ± 2.0 μM. Interestingly enough, a significant signal shift is observed over time, during which saturation occurs at lower protein concentrations, thus, shifting the binding constant of the tracer to K_d = 4.8 ± 0.4, 3.8 ± 0.2, and 1.0 ± 0.1 μM at 2, 3, and 24 h, respectively. This involves an improvement in binding affinity by a factor ~9 comparing the measurements of incubation times between 1 and 24 h.

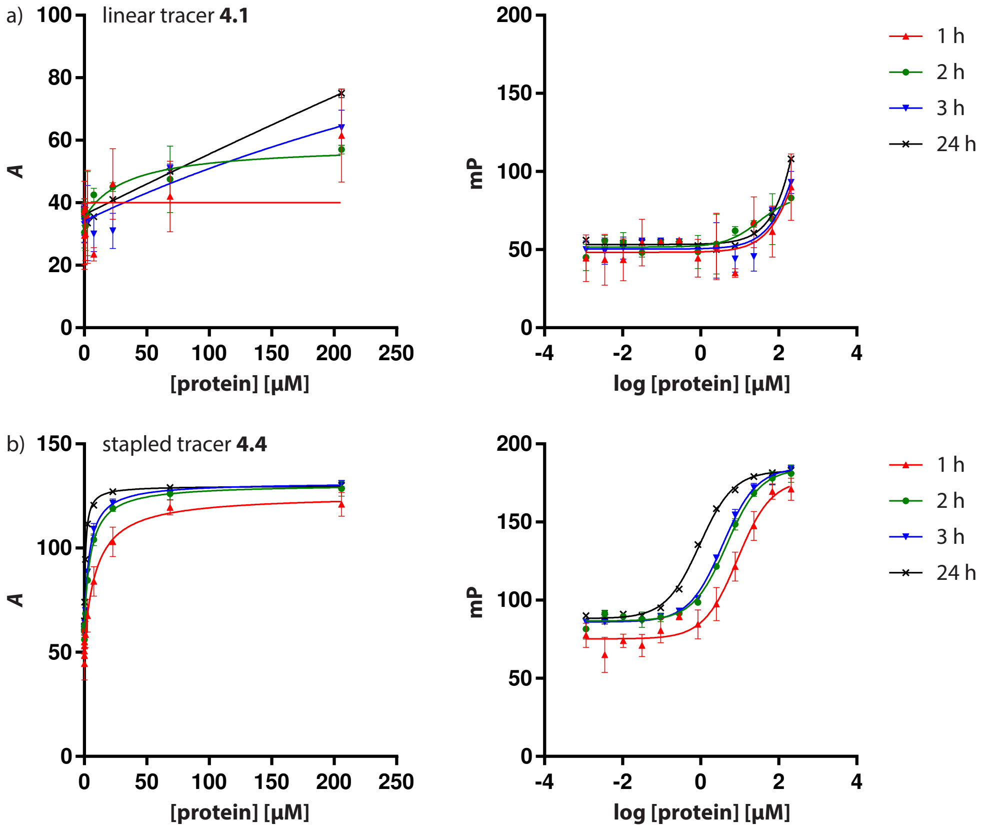

Figure 4.9: Saturation binding curves of a) 20 nM tracer **4.1** and b) 20 nM tracer **4.4** with TGT^{H333D} (left) and dose-response curves for the same FP experiments (right).

The tracer stock solution of peptide **4.4** was freshly prepared for the FP experiment with TGT^{Y330D}, but was stored in assay buffer at 4 °C for a total duration of ~9 months until the experiment was repeated with TGT^{H333D}. To test, whether the signal shift of the previous measurement was an artifact or caused by long storage time, a comparative FP experiment was performed with the same old stock and a freshly prepared stock of tracer **4.4**, and both stocks were prepared from the same synthesis batch (Figure 4.10). The time-dependent signal shift of the previous FP experiment could be reproduced by the use of the old stock solution of tracer **4.4** with a measured $K_d = 2.6 \pm 1.1$ and 0.5 ± 0.1 µM at 1 and 30 h, respectively. However, this effect could not be observed when using a freshly prepared stock solution of the same tracer. For all measured time points, a significant FP signal change of the tracer could only be measured at high protein concentrations with an estimated dissociation constant of $K_d > 50$ µM. Notably, the shift observed in the old tracer stock could be reverted by the addition of a reducing agent, such as tris(2-carboxyethyl)phosphine (TCEP), while no difference was detected for the freshly prepared tracer stock upon TCEP addition. This shows that the signal shift in the old stock is based on oxidative effect which might have occured to the stock solution over the storage time.

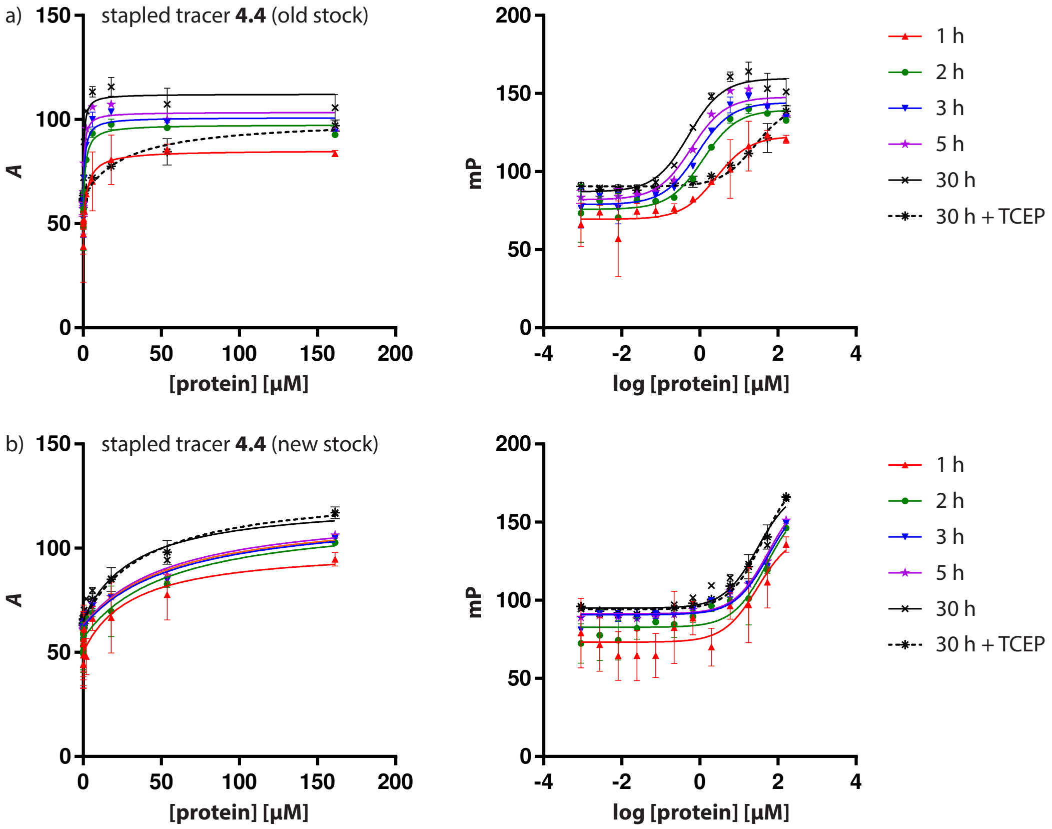

Figure 4.10: Saturation binding curves of 5 nM tracer **4.4** from a) an old and b) freshly prepared stock solution with TGT^{H333D} (left) and dose-response curves for the same FP experiments (right).

One explanation could be explained by the introduction of cysteine residues to the parent peptide **4.3**. Although the thiol groups are converted to stable thioether groups in the stapled peptide **4.4**, a possible degradation or decyclization of the product cannot be excluded. Free cysteine thiol groups may undergo oxidation reactions to form unspecific by-products from which one is able to potently bind to TGT. Another possibility would be the covalent attachment of the peptide through the formation of intermolecular disulfide bridges between the peptide and TGT, as TGT harbors multiple cysteine residues on the protein surface, such as Cys158 or Cys281. This hypothesis could be easily tested by repeating the FP experiments with TGT variants that additionally contain the conservative Cys-to-Ser mutations, as used in Chapter 2. Potential self-aggregation of the tracer seems unlikely since all samples contained a constant amount of tracer and no change in FP could be observed for low protein concentrations. One possible explanation for this result could be that higher protein concentrations force the bound tracer to adopt a new conformation which subsequently triggers aggregation of further tracer molecules to the bound tracer.

To investigate the difference between the old and new stock solution of tracer **4.4**, we attempted a comparative study using MS-coupled high-performance liquid chromatography (HPLC-MS). Therefore, both stock solutions were analyzed each before and after treatment with 10 mM dithiothreitol (DTT) as a reducing agent (Figure 4.11). The freshly prepared stock of tracer **4.4** showed two elution peaks of equal mass at 19.1 and 19.7 min (Figure 4.11b), which likely originate from the two isomers of the 5(6)-FAM mixture used for peptide labeling. Obviously, the 9-month storage of the tracer stock solution resulted in chemical changes of the stapled peptide **4.4**, which can be observed as multiple peaks at lower retention times in the HPLC chromatogram (Figure 4.11a). Upon addition of DTT, no observable change could be detected in the chromatogram of the freshly prepared tracer solution besides the peak at 5.4 min, which corresponds to DTT. In case of the old tracer solution, only small changes could be detected such as an additional elution peak at 16.2 min and a fading of the peak at 19.5 min. The late elution peak at 32.8 min can be observed in all chromatograms and likely corresponds to a component in the assay buffer.

a) stapled tracer **4.4** (old stock)

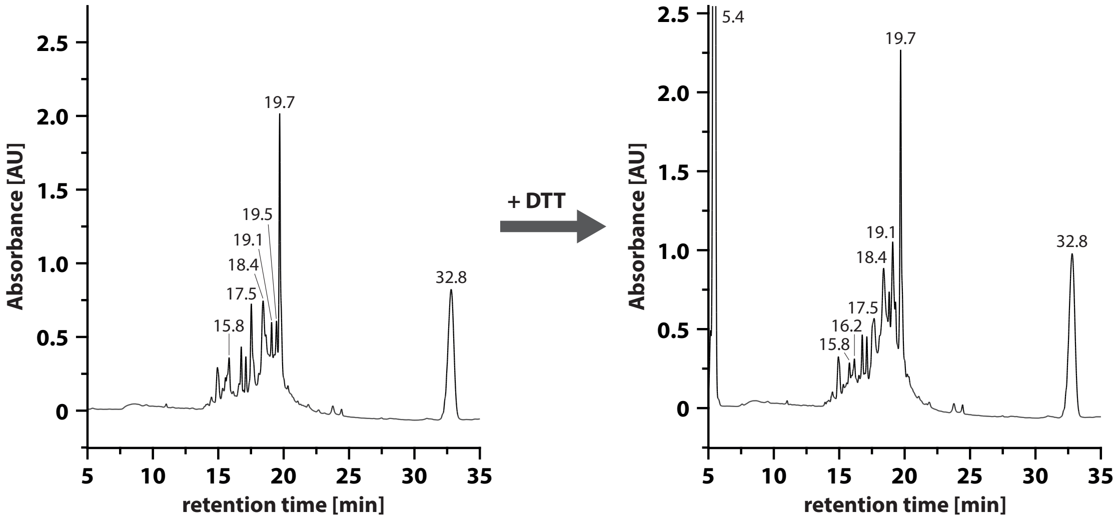

b) stapled tracer **4.4** (new stock)

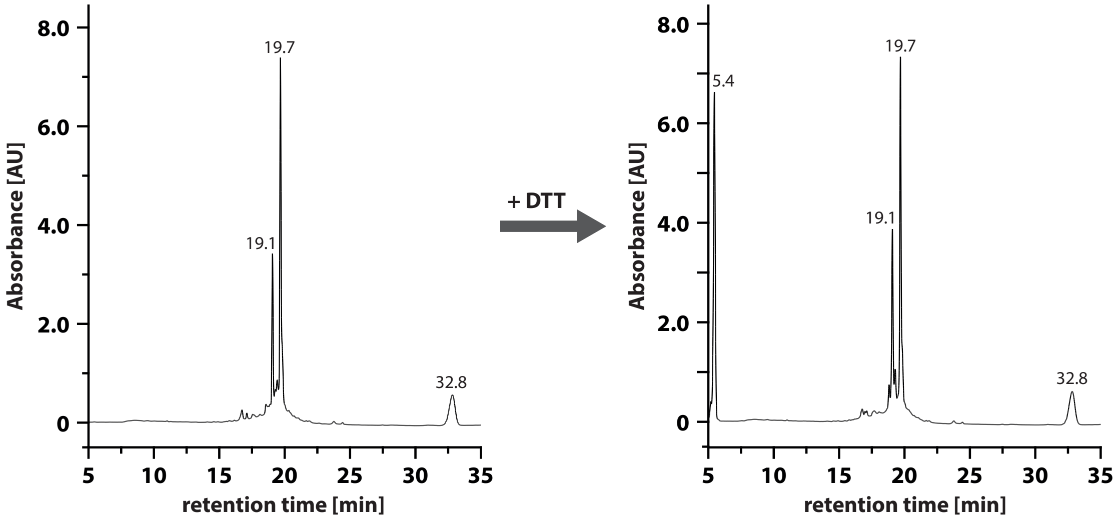

Figure 4.11: HPLC chromatograms of tracer **4.4** prepared from a) the old and b) new stock solution each treated without and with 10 mᴍ DTT. The absorbance was tracked at 260 nm wavelength.

Analysis of the corresponding mass spectra (Figure 4.12) revealed a set of four mass-to-charge ratio (m/z) peaks that originate from different ionic species of the stapled peptide **4.4** (calculated MW: 2088.2 Da): 696.8 Da ($[M+3\,H]^{3+}$), 1044.6 Da ($[M+2\,H]^{2+}$), 1055.7 Da ($[M+H+Na]^{2+}$), and 1066.8 Da ($[M+2\,Na]^{2+}$). Potential protonation sites are located at the sidechains of residues His332^{P}, His333^{P}, and Arg336^{P}. Moreover, it seems that several signals below a m/z of ~650 Da are increased in the old stock solution compared to the freshly prepared one. The m/z-peaks between 376.2–420.2 Da and 555.4–643.5 Da can be assigned to ionic adducts of Triton® X-100, which was present in the assay buffer as a detergent. The observed mass shift of 44 Da correspond to an ethylene oxide monomer unit of the polymer. Additional m/z-peaks at 1392.0 and 1435.3 Da were found although the identification of the corresponding species remains elusive. Interestingly, the peak at 1392.0 Da disappears upon addition of DTT, thus indicating that the species might be redox-sensitive. Furthermore, DTT treatment results in a second set of peaks observed at 747.6 Da, 1120.7 Da, 1131.7 Da, and 1142.6 Da. The related mass shift of ca. 152 Da led to the identification of DTT adducts resulting from the ionic species of the stapled peptide as described above. This observation could be verified in the old as well as new tracer stock solution.

Another aspect to consider is the stability of the buffer during the storage and its effect on the integrity of the stapled peptide. Long-time stability studies of TRIS-based buffers have been investigated elsewhere.[149] Moreover, Song *et al.* provided evidence for the degradation of TRIS buffers at elevated temperatures under release of formaldehyde, which is capable to modify tyrosine residues of a solubilized peptide.[150] In fact, the reactivity of formaldehyde has been evidenced towards multiple amino acids.[151] Although, the degradation of TRIS to formaldehyde was demonstrated at 70 °C, a similar degradation pathway at lower temperatures over a storage time of 9 months cannot be excluded. Nevertheless, an active by-product in the old tracer stock solution, that caused the significant signal shift in the FP measurements, could not be identified by the initial HPLC-MS experiment and remains to be elucidated.

a) stapled tracer **4.4** (old stock)

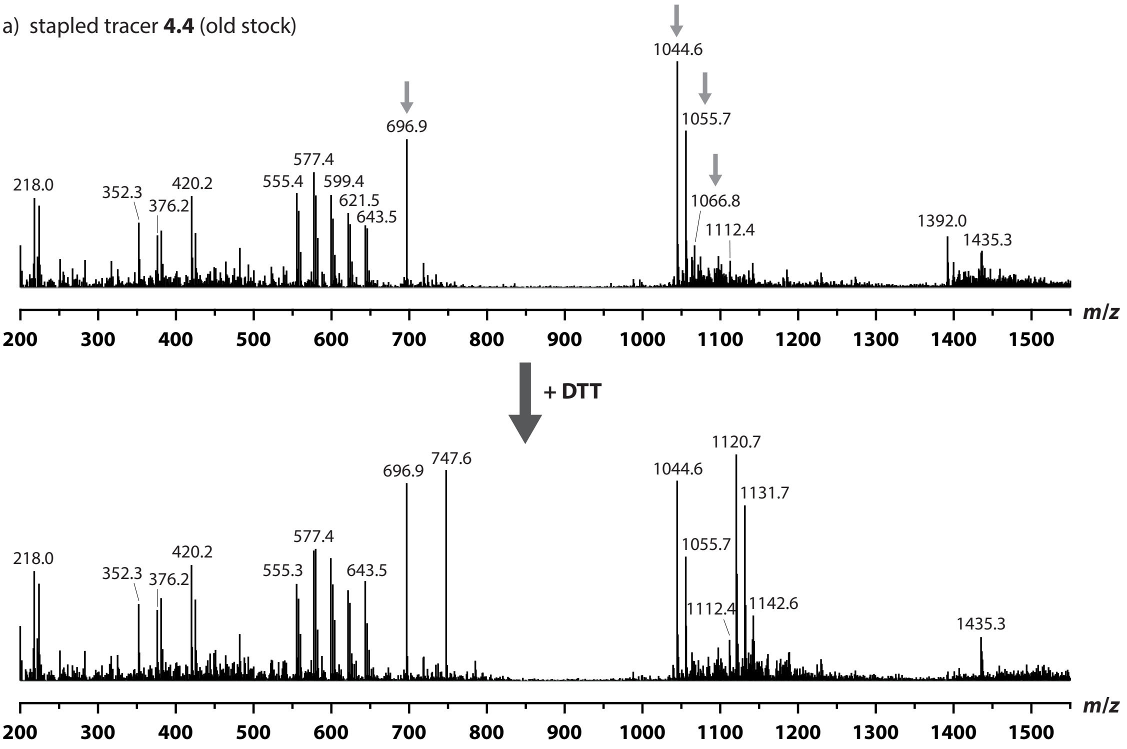

b) stapled tracer **4.4** (new stock)

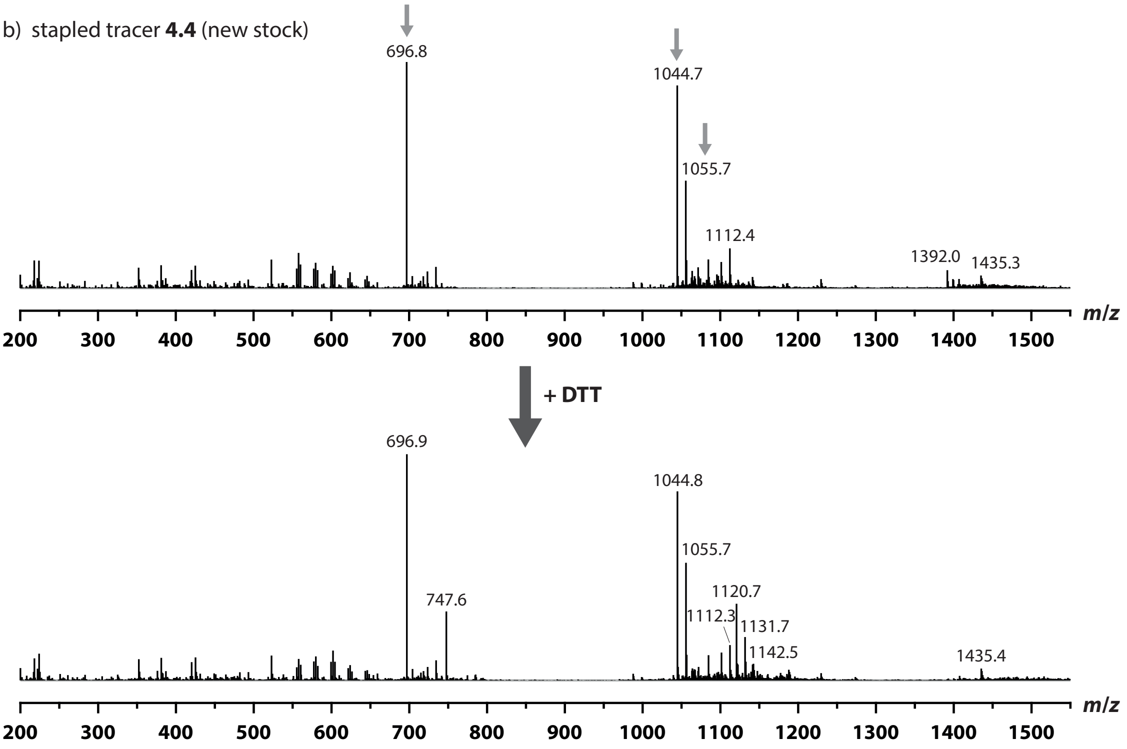

Figure 4.12: Mass spectra of tracer **4.4** prepared from a) the old and b) new stock solution each treated without and with 10 mм DTT. Peaks originating from the ionized peptide species are marked with an arrow.

4.2.4 Crystallization trials and characterization of TGT^{Y330D}

As no diffracting crystals of the TGT^{Y330D} mutant were obtained in a previous study led by Jakobi *et al.*,[22] a new crystallization trial was attempted with the aim to generate new putatively monomeric TGT crystal structure suitable for crystallization with interface-binding peptides. Two needle-like crystal hits were obtained independently from two different crystallization screens under the same crystallization condition (0.1 M tri-sodium citrate, pH 5.6, 1 M lithium sulfate, 0.5 M ammonium sulfate, Figure 4.13a). Although the crystallization was successfully reproduced in-house, only crystals with lattice strains defects were initially obtained (Figure 4.13b), likely due to rapid and uncontrolled nucleation. The use of crystal seeds combined with the streak-seeding technique[152] ultimately yielded single crystals of TGT^{Y330D} (Figure 4.13c).

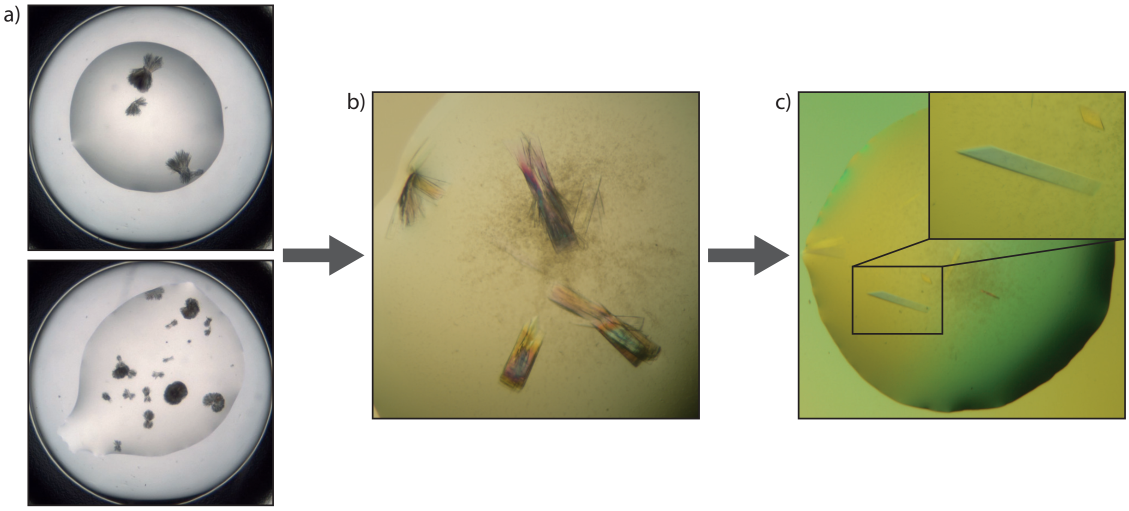

Figure 4.13: Optimization of crystallization conditions for TGT^{Y330D} from a) coarse screen needle-like hits to b) reproduction in-house with lattice strain defects and c) single crystals via seeding.

In the following X-ray diffraction experiments, the crystal growth defects became more obvious as all tested crystals showed splitted reflexes. Thus, the crystals translated to lower data quality, which was indicated by low resolutions around 3 Å, very high overall R_{sym} values of >17 % and the presence of pseudotranslation.[153,154] Despite low quality indicators, the structure of TGT^{Y330D} was presumably solved by molecular replacement in space group $P2_12_12_1$ using the PDB entry 1PUD as a search model (data not deposited in the PDB). With care, our preliminary structural data show a rotated homodimeric structure of TGT^{Y330D}, which deviates from the functional wild type dimer (Figure 4.14a). Interestingly, the new dimer packing resembles the dimeric structure of *Mus musculus* QTRT1 (PDB ID: 6H62), formed by the catalytic subunit of murine TGT only (Figure 4.14b). The latter enzyme is functional as a heterodimer formed from two sequentially different monomer units.

Native nanoESI-MS studies by Behrens *et al.* have shown that QTRT1 does not form a homodimer in solution. Likely, the dimeric assembly in the crystal packing is caused by crystal packing forces and the TGT$^{\mathrm{Y330D}}$ variant exists as a monomer in solution, as supported by native nanoESI-MS[22] and gel filtration experiments (Chapter 3, Figure 3.13). However, an optimization of the crystallization is required to obtain a dataset of higher quality and to fully characterize the structure of TGT$^{\mathrm{Y330D}}$.

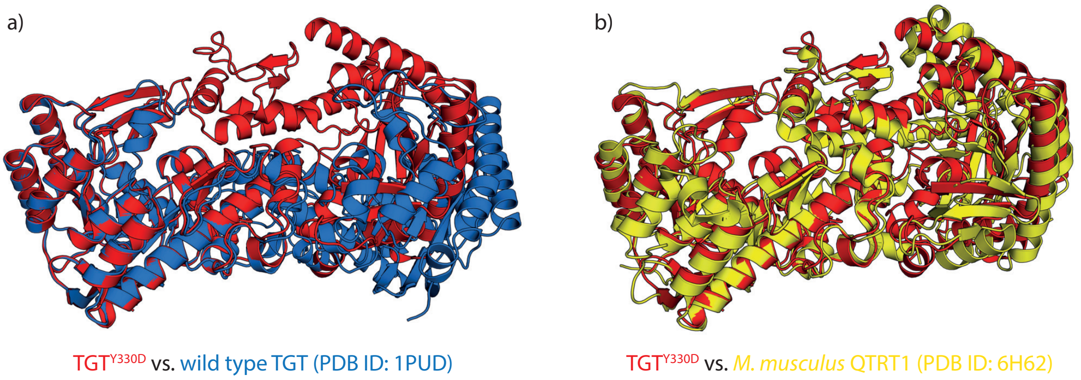
a)
b)
TGTY330D vs. wild type TGT (PDB ID: 1PUD)
TGTY330D vs. M. musculus QTRT1 (PDB ID: 6H62)

Figure 4.14: Structural comparison of TGT$^{\mathrm{Y330D}}$ (red, data not deposited in PDB) with the dimeric structures of a) wild type *Z. mobilis* TGT (blue, PDB ID: 1PUD[18]) and b) *M. musculus* QTRT1 (yellow, PDB ID: 6H62).

Previous mass spectrometric results from the study by Jakobi *et al.* showed that the TGT$^{\mathrm{Y330D}}$ may be post-transcriptionally modified, e. g., by methylation, which was indicated by a mass shift of +14 Da.[22] However, this mass shift was not observed for the variant produced in this study (Figure 4.23, Experimental Section 4.4.1). This can be explained by an altered protein expression protocol in which the formerly used pASK-IBA13plus was replaced by pPR-IBA2 plasmid (IBA Lifesciences). While all expression systems described in this thesis are based on the pPR-IBA2 plasmid, it remains elusive which plasmid was used in the study by Jakobi *et al.*[22,91]

Furthermore, the enzyme kinetics of TGT$^{\mathrm{Y330D}}$ was reassessed (Figure 4.15), as no catalytic turnover was reported for this variant by Jakobi *et al.*[22] Unexpectedly, the catalytic activity of the TGT$^{\mathrm{Y330D}}$ variant is only marginally reduced as k_{cat} is decreased by factor 1.6 compared to the wild type enzyme ($k_{\mathrm{cat}} = (5.7 \pm 0.5) \times 10^{-3}$ and $(9.0 \pm 0.3) \times 10^{-3}\ \mathrm{s}^{-1}$ for TGT$^{\mathrm{Y330D}}$ and wild type TGT, respectively). Furthermore, the Michaelis-Menten constants indicate that the affinity of TGT$^{\mathrm{Y330D}}$ for the tRNA^{Tyr} substrate is slighty decreased in comparison to the wild type ($K_{\mathrm{m}}(\mathrm{tRNA}^{\mathrm{Tyr}}) = 3.5 \pm 0.8$ and $0.8 \pm 0.1\ \mu\mathrm{mol\,L}^{-1}$ for TGT$^{\mathrm{Y330D}}$ and wild type TGT, respectively). Since this mutant is considered to exist predominantly in its monomeric form, as supported by native nanoESI-MS and gel filtration experiments, further investigations are required to examine the cause for the high enzymatic activity of this particular variant.

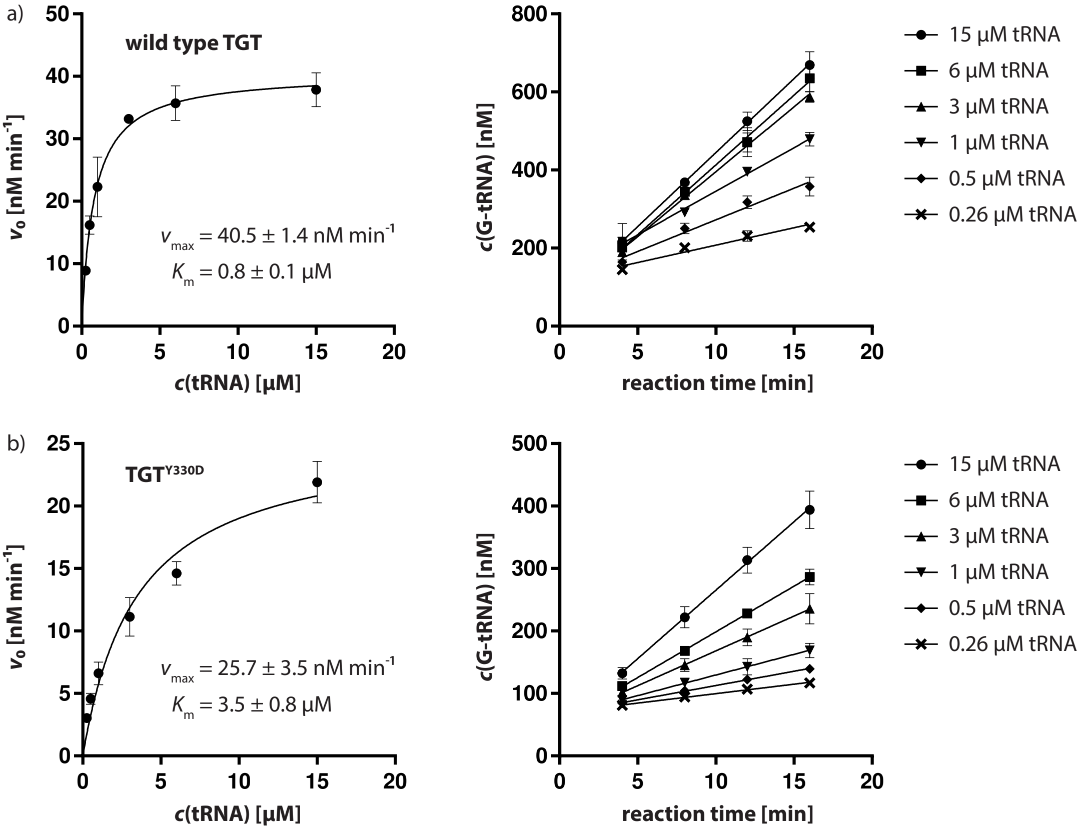

Figure 4.15: Progress curves and the resulting Michaelis-Menten plots of a) wild type TGT and b) TGT^{Y330D}.

4.2.5 Assessment of TGT dimerization constants

In a number of studies that investigated the influence of mutations and dimer-disturbing inhibitors on TGT dimerization, native nanoESI-MS has provided a valuable analytical tool which allowed to quantify the population of the dimeric and monomeric species within the dimer–monomer equilibrium.[22,29,33] Moreover, the kinetics of the monomer–monomer exchange of the TGT homodimer and its mutant variant could be mass spectrometrically assessed.[23] However, the limitations of native MS need to be considered, as measurement occurs in the gas phase under vacuum conditions. In fact, the gas phase environment weakens hydrophobic interactions while charged interaction become stronger, hence, the detected dimer and monomer populations of TGT might deviate from those observed in solution.[155,156] Furthermore, native MS does not provide direct output on the dimerization affinity in form of dissociation constants. As a consequence, two new assays to assess the affinity of TGT dimerization in solution were established.

Dissociation isothermal titration calorimetry

The first assay is based on isothermal titration calorimetry (ITC), which detects changes in heat upon binding of mixed interaction partners. Several binding parameters, such as reaction stoichiometry, dissociation constant (K_d), changes in reaction enthalpy (ΔH), changes in Gibbs free energy (ΔG), and, consequently, changes in entropy (ΔS) can be directly assessed in a usual protein–ligand titration experiment to estimate the thermodynamic binding strength between the partners.[157] Since homodimeric proteins cannot be isolated and studied in a mixing experiment of the individual monomers, the binding strength can only be measured through a dilution experiment.[158] Thereby, a highly concentrated protein solution is stepwise titrated into the calorimetric cell, which contains only buffer. The high protein concentration in the syringe ensures that the dimer species is predominantly populated prior to titration. Initial additions of the protein to the buffer result in the dissociation of the dimer due to the large decrease in concentration, thus, causing a change in heat. Successive injections lead to a progressive increase of protein concentration in the cell and a shift in the dimer–monomer equilibrium, which is defined by the dimer dissociation constant. No significant heat change will be observed when the injected protein dimer no longer dissociates in the cell. It has to be noted that heat signals resulting from dissociation are subject to background heats from dilution. The latter can be estimated from constant heat signals at high protein concentrations toward the end of the titration process and subtracted in the subsequent analysis.

The dissociation ITC method has been applied to characterize the dimer–monomer equilibrium of interleukin-8 and to verify its monomeric state under physiological conditions.[159] The technique also proved to be useful in the investigation of superoxide dismutase 1 (SOD1) and the effect of its mutants on dimer stability, which is associated with amyotrophic lateral sclerosis.[160] In another example, Seetoh *et al.* demonstrated that dissociation ITC experiments can be used to study the influence of small molecule fragments on the dimer–monomer equilibrium of a mutant variant of the CK2β homodimer.[161] It was also shown, that the correct selection of the protein variant is crucial for the detection of concentration-dependent dimerization as some CK2β mutants failed to result in measurable dissociation isotherms.

Three TGT variants, wild type TGT, $\mathrm{TGT}^{\mathrm{H333A}}$, and $\mathrm{TGT}^{\mathrm{H333D}}$, were tested in dissociation ITC experiments at 25 °C. Out of the three variants, only $\mathrm{TGT}^{\mathrm{H333D}}$ showed a well-fitting isotherm in the calorimetric data (Figure 4.16). The heat of dilution was not substracted in this case as it requires further injections for a precise estimation. Analysis of the heat signals by non-linear regression, yielded a dimerization constant of $K_\mathrm{d}(\mathrm{ITC}) = 6.94 \pm 0.36\,\mu\mathrm{M}$. The calorimetric data shows that dissociation of the TGT homodimer is linked to negative enthalpy. This result suggests an entropy-driven dimerization of TGT. An endothermic self-association process was also observed in a study led by Luke *et al.* who investigated the oligomerization thermodynamics of co-chaperonin protein 10.[162] Likely, the dimer stability of TGT is temperature dependent as was shown for SOD1.[160] Therefore, additional measurements at varying temperatures are required.

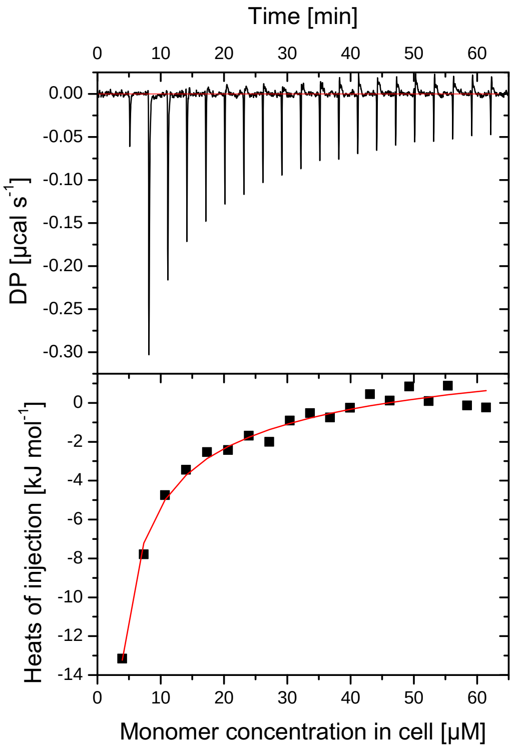

Figure 4.16: Raw thermogram (top) and integrated raw data with the corresponding isotherm (bottom) of the TGT^{H333D} dissociation ITC experiment.

MicroScale thermophoresis

In parallel to dissociation ITC, a second assay based on MicroScale thermophoresis (MST) was established to study TGT dimerization. The method is based on thermophoresis, a controlled movement of molecules along a temperature gradient, which depends on a number of molecular properties, such as molecular size and charge. Changes in these properties are expressed as changes in thermophoresis which can be tracked against time, e. g., by using a fluorescent label. Binding data and dissociation constants can be obtained from dose-response curves converted by the measured time traces at different ligand concentrations. The MST technique has previously been used to evaluate binding data of *lin*-benzoguanine inhibitors to TGT.[29]

By combining mixing experiments of labeled and unlabeled TGT with MST, the dimerization constant can be estimated. This method has been successfully applied to study the dimer–monomer equilibrium of the Grb2 homodimer.[163]

In our study, wild type TGT and TGT^{H333D} were labeled with the amine-reactive RED-NHS dye (NanoTemper Technologies). After labeling, the structural integrity of the labeled variants was validated by a thermal shift assay. Moreover, the stability of the unlabeled TGT^{H333D} was tested in a low-salt and high-salt buffer (150 mM and 1 M NaCl, respectively). The wild type enzyme could not be tested in low-salt conditions due to precipitation.

The resulting melting curves indicate no significant change of the melting temperature between the labeled and unlabeled wild type enzyme (T_m = 73.1 and 72.9 °C, respectively) as well as the labeled and unlabeled $\mathrm{TGT}^{\mathrm{H333D}}$ variant (T_m = 73.2 °C for both) in high-salt conditions (Figure 4.17). Interestingly, the melting temperature for $\mathrm{TGT}^{\mathrm{H333D}}$ in low-salt buffer is decreased by 4.3 °C to the high-salt equivalent (T_m = 68.9 °C). This indicates that TGT is stabilized in buffers with higher ionic strengths. As a consequence, MST measurements were performed in high-salt conditions to ensure stability of both TGT variants.

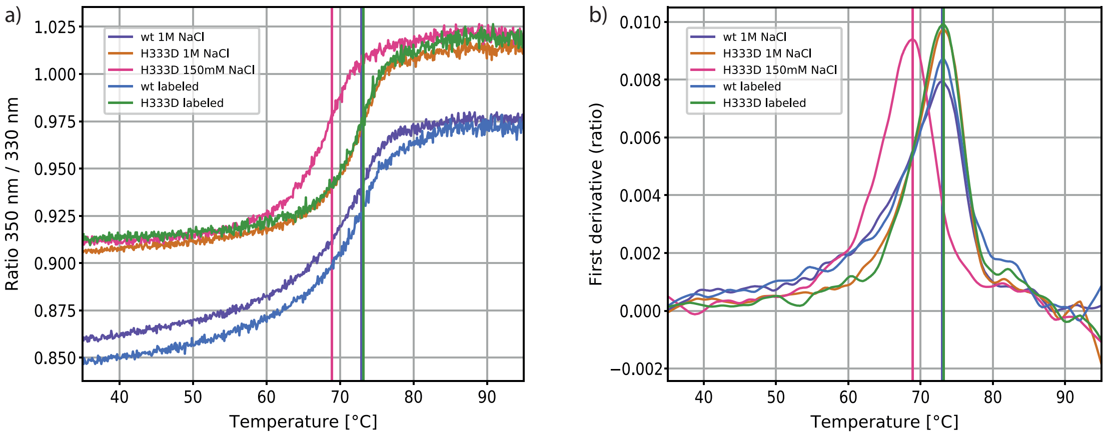

Figure 4.17: Validation of structural integrity of labeled and unlabeled TGT variants by analysis of their a) melting curves and b) corresponding first derivatives.

MST was subsequently measured for wild type TGT and $\mathrm{TGT}^{\mathrm{H333D}}$ resulting in dimerization constants of $K_\mathrm{d}(\mathrm{MST})$ = 202 ± 33 nM and 3.6 ± 0.6 µM, respectively (Figure 4.18). The K_d value for $\mathrm{TGT}^{\mathrm{H333D}}$ agrees well with the one measured by dissociation ITC ($K_\mathrm{d}(\mathrm{ITC})$ = 6.94 ± 0.36 µM).

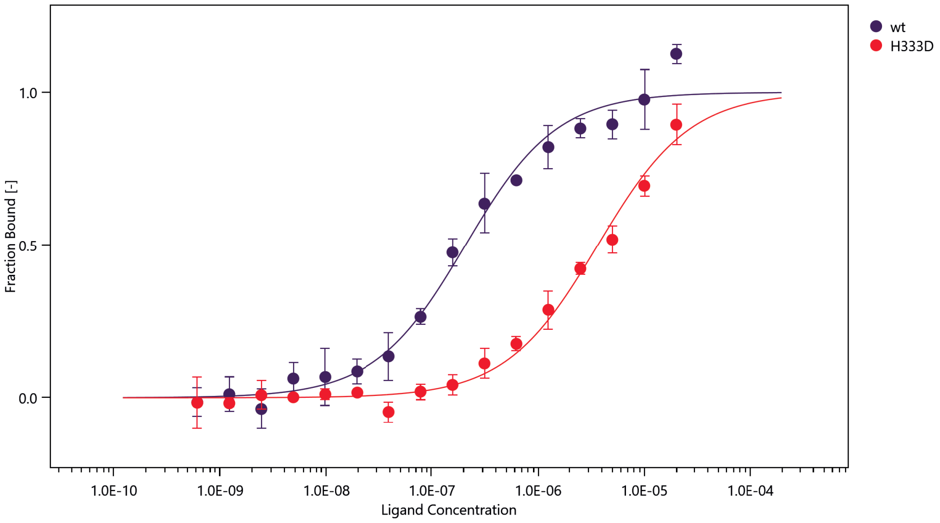

Figure 4.18: Dose-response curves of TGT dimerization measured by MST.

4.2.6 Development of a *Shigella* host cell invasion assay

Since mutations of the *tgt* gene showed a decrease in the expression of the virulence phenotype of *S. flexneri*,[16,17] a host cell invasion assay was developed to assess the effect of a *Shigella* mutant strain containing a deletion of the *tgt* gene (Δ*tgt*) on the *Shigella* invasion pathology. Once established, this assay could provide the basis for further investigations of potential peptide and drug candidates to study their effect on the pathogenicity of *Shigella*. Therefore, the human Caco-2 cell line provided the host cells for the assay as they are capable to form polarized cell monolayers, hence, mimicking the environment of the intestinal epithelium.[164] In this study, the *S. flexneri* serotype 2a Δ*tgt* strain was compared to the virulent 2457T[165] strain. The gene locus, that determines *Shigella* virulence, is located on a ca. 140 MDa plasmid which encodes for virulence factors that are essential for successful penetration into the intestinal epithelium.[166] *Shigella* virulence and the stability of the virulence plasmid respond to different environmental conditions.[167] Maurelli *et al.* demonstrated that the expression of virulence factors depends on the growth temperature of the bacteria, where *Shigella* strains were fully virulent when grown at 37 °C, whereas the bacteria lost their ability to invade intestinal epithelial cells from the Henle-407 cell line[168] when grown at 30 °C.[169] In addition, the invasion efficiency of *Shigella* can be increased by supplementation of sodium deoxycholate to the bacterial growth cultures.[170] The experimental procedures can be found in Experimental Sections 4.4.11 and 4.4.12.

In the present study, both strains, *S. flexneri* 2457T and Δ*tgt*, were grown at 37 °C on Congo red (CR) agar plates, which can be used for phenotypic differentiation of virulent and avirulent *Shigella* colonies since they appear as white or red colonies, respectively (Figure 4.19).[171,172] The growth and invasion protocol was adapted from Koestler *et al.* and modified accordingly.[173] Experimental details can be found in Experimental Sections 4.4.11 and 4.4.12.

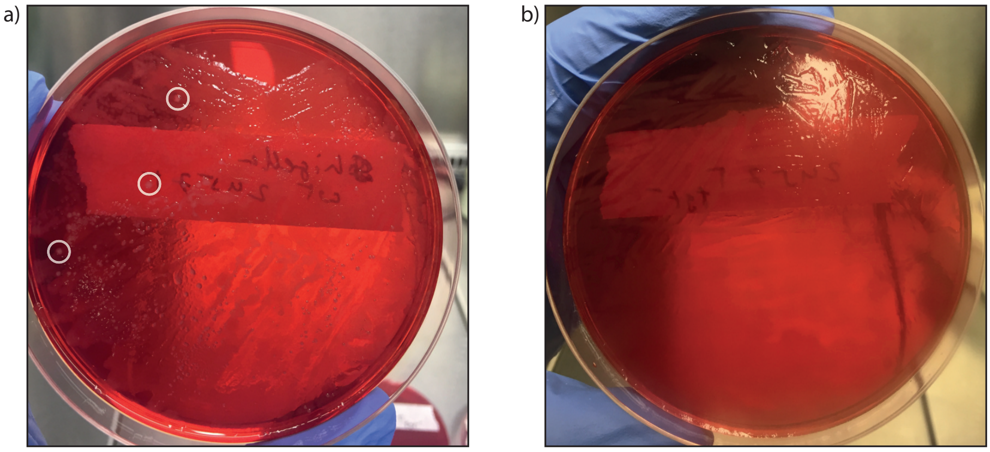

Figure 4.19: Congo red agar plates with grown a) *S. flexneri* 2a 2457T and b) Δ*tgt* strains. Examples for white *Shigella* colonies are encircled in white.

After staining the bacteria with 6-TramTO-3, a novel far-red fluorescent cyanine dye,[174] analysis and quantification of the invasion assay were enabled by fluorescence-activated cell sorting (FACS). First, the optimal multiplicity of infection (MOI) was determined. Therefore, the Caco-2 cells were treated with *S. flexneri* 2a 2457T at different MOI and subsequently analyzed via FACS (Figure 4.20). While at a MOI of 100 more than half of the sampled cells are infected by the stained bacteria, a MOI of 500 resulted in 90 % of measurable *Shigella* invasion. A MOI of 100 was chosen for further experiments to keep the bacterial invasion count of the virulent 2457T strain distinguishable from the Δ*tgt* mutant strain.

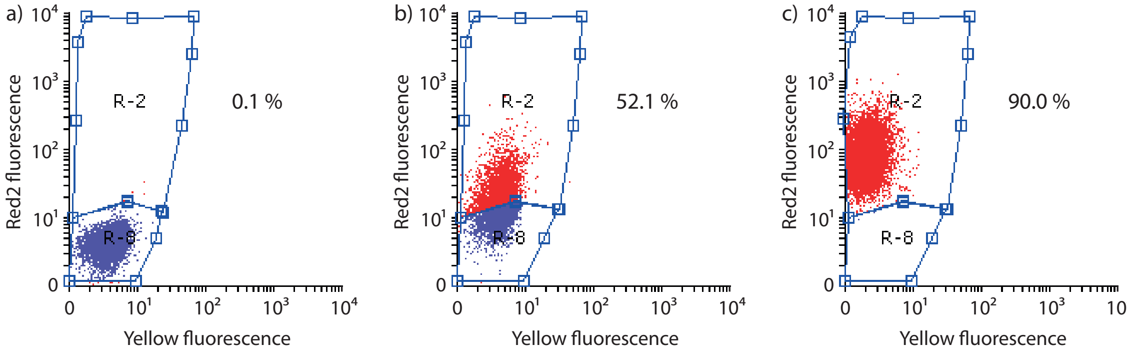

Figure 4.20: Representative dot plots of FACS analysis (red2 and yellow channels) of a) untreated versus bacteria-treated Caco-2 cells at b) MOI of 100 and c) MOI of 500 including quantification of the three independent experiments.

The experiment was repeated with both *S. flexneri* strains, 2457T and Δ*tgt*. Compared to the virulent 2457T strain, which was able to infect almost ~79 % of the Caco-2 cells, the infection rate in the *tgt*-deficient Δ*tgt* strain was reduced by a factor of ~2.9. Clearly, the established assay shows a significant decrease in *Shigella* invasion and, thus, underpins the importance of TGT function for the expression of virulence factors essential for pathogenicity of *Shigella* species.[16,17]

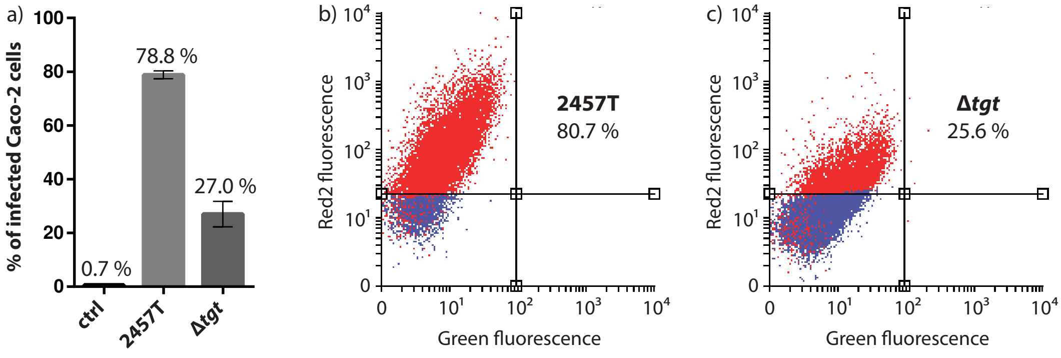

Figure 4.21: a) Infection rate of *S. flexneri* 2a strains and representative dot plots of FACS analysis (red2 and green channels) of Caco-2 cells treated with a) 2457T and b) Δ*tgt* each at MOI of 100 including quantification of the two independent experiments.

4.3 Conclusion

In preceding studies, active-site inhibitor design and fragment-based screening have been applied to search for novel ways of modulating the TGT homodimer. So far, no peptide-based approaches have been reported. In this study, a search for dimer-modulating peptides was initiated resulting from a serendipitous finding of the previous chapter.

A peptide microarray successfully provided sequence information about the binding epitope within the TGT dimer interface. The most promising peptides, derived from helix αE, were synthesized and their binding affinity to different TGT variants was characterized by FP. To improve TGT–peptide binding, a peptide stapling approach was performed to constrain and stabilize the helical structure of the peptide. Further investigations are required to confirm the improved helicity of the stapled peptide, e. g., by circular dichroism (CD) spectroscopy. Unexpectedly, the stapled peptide showed a time-dependent shift of the FP signal towards higher K_d. Although potent binding could be detected, likely this observation resulted from chemical changes to the peptide stock solution during a storage of nine months at 4 °C. Treatment with a reducing agent reverted the signal shift indicating that redox-active species could be the reason for the observation in the FP measurements. Subsequently, different stock solutions of the stapled peptide were treated with DTT and studied by HPLC-MS. Yet, the actual cause for the signal shift requires a more detailed investigation.

Also, two assays based on ITC and MST have been established for the estimation of TGT dimerization constants. While ITC allows a label-free measurement, the MST-based method required labeling of a fluorophore for successful tracking of thermophoresis. Melting curve analysis by thermal shift assays revealed no significant change between the labeled and unlabeled TGT variants. It was demonstrated that MST can be used to study the influence of interface point mutations on the dimerization affinity of the TGT homodimer in solution. Likely, both assays can be used to investigate the modulation of the TGT dimer by peptides and small molecule binders.

Furthermore, a host cell invasion assay was established to study the effect of a Δ*tgt* strain in the pathogenicity of *S. flexneri*. Quantification of the bacterial infection rate by FACS revealed a significantly decreased infection in Caco-2 cells for the *tgt*-deficient *S. flexneri* 2a strain compared to the virulent 2457T strain. This finding highlights the importance of TGT function for virulence development of *S. flexneri*. Moreover, the established invasion assay provides a platform for the screening of antibacterial drug candidates that specifically target and inhibit TGT function. It remains to be elucidated whether the previously developed small molecule inhibitors or potential peptide candidates are capable of reducing the virulence of *Shigella* by inhibition of the TGT enzyme.

4.4 Experimental Section

4.4.1 Preparation of *Z. mobilis* TGT

Mutagenesis and expression of the *Z. mobilis tgt* gene and its mutated variants encoding for $\text{TGT}^{\text{Y330D}}$ and $\text{TGT}^{\text{H333D}}$ were performed as previously described by site-directed mutation and plasmid-based expression of the vector pPR-IBA2 (IBA Lifesciences).[22] The mutations were introduced via the QuikChange Lightning Site-Directed Mutagenesis Kit (Agilent) according to the vendor instructions. DNA primers were purchased from Eurofins Genomics (Ebersberg, Germany) and are summarized in Table 4.2. In each case, the new construct was re-sequenced by Eurofins Genomics to confirm the presence of the desired mutations as well as the absence of any further unwanted mutation. The final constructs were each transformed into *Escherichia coli* BL21-CodonPlus (DE3)-RIPL cells (Agilent).

A single colony was picked from the freshly transformed agar plate and grown overnight in 100 mL of lysogeny broth (LB) medium supplemented with 100 µg mL^{-1} ampicillin and 34 µg mL^{-1} chloramphenicol while shaking at 37 °C. The next day, a large-scale culture in LB medium, supplemented with 100 µg mL^{-1} ampicillin and 34 µg mL^{-1} chloramphenicol, was inoculated with 10 mL of overnight culture per liter. The culture was grown at 37 °C by shaking at 140 rpm until the optical density at 600 nm (OD_{600}) reached a value between 0.6 to 0.7 and was then cooled to 16 °C while shaking. After 1 h, overnight protein expression was induced by the addition of 1 mᴍ IPTG. The cells were harvested the next day by centrifugation using a JA-10 rotor (Beckman Coulter) at 4 °C and 10 000 rpm for 1 h. The collected cells were disrupted by sonication using a Branson Sonifier™ 250 in 100 mL lysis buffer (20 mᴍ TRIS, pH 7.8, 10 mᴍ EDTA, 1 mᴍ DTT and 1 cOmplete™-Protease Inhibitor Cocktail Tablet (Roche) per 4 L of bacterial culture). Subsequently, the cell debris was removed by centrifugation using a JA-25.50 rotor (Beckman Coulter) at 4 °C and 20 000 rpm for 1 h. The supernatant was collected and loaded onto a Q Sepharose® Fast Flow anion exchange column (XK 26/15, GE Healthcare) conditioned with buffer A (10 mᴍ TRIS, pH 7.8, 1 mᴍ EDTA, 1 mᴍ DTT). After washing with buffer A, the target protein was eluted by applying a linear NaCl gradient from 0 to 100 % (v/v) buffer B (buffer A plus 1 ᴍ NaCl). The protein-containing fractions, endowed with an N-terminal Strep-tag® II, were then loaded onto a Strep-Tactin®XT cartridge (IBA Lifesciences) conditioned with buffer W (100 mᴍ TRIS, pH 7.8, 1 mᴍ EDTA, 1 ᴍ or 150 mᴍ NaCl). After washing the column with buffer W, the protein was eluted with buffer BXT (buffer W plus 50 mᴍ ᴅ-biotin) from the Strep-Tactin®XT cartridge. All chromatographic steps were carried out at room temperature using an ÄKTAprime™ plus FPLC system (GE Healthcare). All TGT-containing fractions were combined and concentrated to ca. 2 mg mL^{-1} in buffer W or high-salt buffer (10 mᴍ TRIS, pH 7.8, 1 mᴍ EDTA, 2 ᴍ NaCl) using Vivaspin® 20 centrifugal concentrators (30 000 MWCO, Sartorius). Subsequently, the Strep-tag® II was chipped off and separated from the target protein by means of the Thrombin Cleavage Capture Kit (Novagen®) according to the manufacturer's instructions. After tag cleavage, the sample was dialyzed against buffer W or high-salt buffer and concentrated via Vivaspin® 20 centrifugal concentrators to ca. 15 to 25 mg mL^{-1}.

Successful tag cleavage was verified by mass spectrometry (Figures 4.22–4.24). 100 µL aliquots of the samples were flash-frozen in liquid nitrogen and stored at −80 °C until further usage.

Table 4.2: DNA primer sequences used for mutagenesis. Nucleobases deviating from the original *tgt* sequence are underlined.

Mutation / Primer ID	Sequence
Y330D_f[22]	5'-CAGAAATGGAGCCGTGCCTGTATTCATCATCTGATTCG-3'
Y330D_r[22]	5'-CGAATCAGATGATGAATACAGGCACGGCTCCATTTCTG-3'
H333A_f	5'-CCGTGCCTATATTCATGCGCTGATTCGTGCAGGTG-3'
H333A_r	5'-CACCTGCACGAATCAGCGCATGAATATAGGCACGG-3'

4.4.2 Crystallization and structure determination

Crystallization of TGT^{Y330D} was performed using the hanging-drop vapor diffusion method at 18 °C. The protein solution (19 mg mL^{-1} in buffer W) was mixed with reservoir solution (0.1 M tri-sodium citrate, pH 5.6, 1 M lithium sulfate, 0.5 M ammonium sulfate) in a 1:1 volume ratio. In case of seeding, a horse hair was used to crush crystalline material prior to streaking through a crystallization drop. Crystals grew within a week in the presence of 500 µL reservoir solution in the plate wells. Prior to data collection, the crystals were transferred to a reservoir solution containing 30 % (w/v) D(+)-trehalose as cryo-protectant for a few seconds and vitrified in liquid nitrogen.

Diffraction data were collected at a wavelength of 0.91841 Å and temperature of 100 K at the synchrotron beamline 14.1 at BESSY II (Helmholtz-Zentrum Berlin). Indexing, processing and scaling of the diffraction images were done using *XDS*[66] and *XDSAPP*[67]. The structures were determined via molecular replacement using the program *Phaser*[68] from the *CCP4 suite*[69] with the PDB entry 1PUD[18] as initial search model. Model building was done in *Coot*[70] and the program *PHENIX*[71] was used for structure refinement.

4.4.3 Preparation of tRNA^{Tyr}

The *E. coli* tRNA^{Tyr} (ECY2[75]) was synthesized by *in vitro* transcription using T7 RNA polymerase. The reaction mixture (30 µg of linearized DNA template, 3.75 mM of NTPs, and 1 µM of T7 RNA polymerase in 20 mM $MgCl_2$, 80 mM HEPES, pH 7.5, 1 mM spermidine, 5 mM DTT, 0.05 U pyrophosphatase) was incubated for 4 h at 37 °C. The tRNA transcript was extracted in a 1:1 mixture of acidic phenol/chloroform, pH 4.5, and precipitated upon addition of a 1:20 mixture comprising 3 M sodium acetate, pH 5.2, and ethanol. After centrifugation for 10 min at 16 500 *g*, 4 °C, the supernatant was discarded. The pellet was dried, dissolved in ddH_2O and the tRNA was purified via preparative denaturing (8 M urea) 8 % polyacrylamide electrophoresis (PAGE). The tRNA was eluted from the excised gel slice in 1 M sodium acetate, pH 5.2, overnight while shaking at 900 rpm, 4 °C. The purified tRNA was again precipitated using the above described procedure and finally dried *in vacuo*.

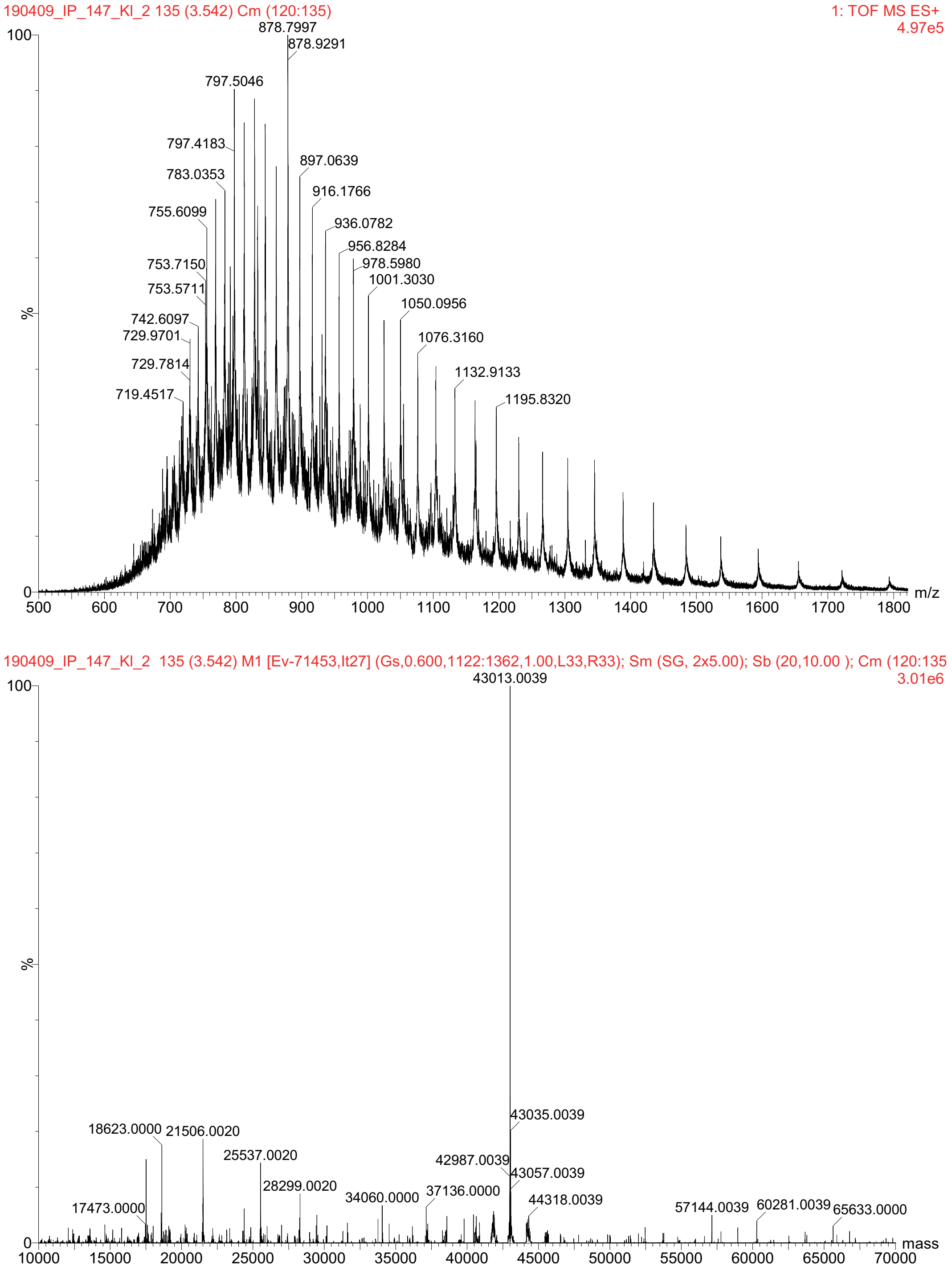

Figure 4.22: Mass spectrum and deconvoluted spectrum of wild type TGT (calculated mass: 43 013.8 Da).

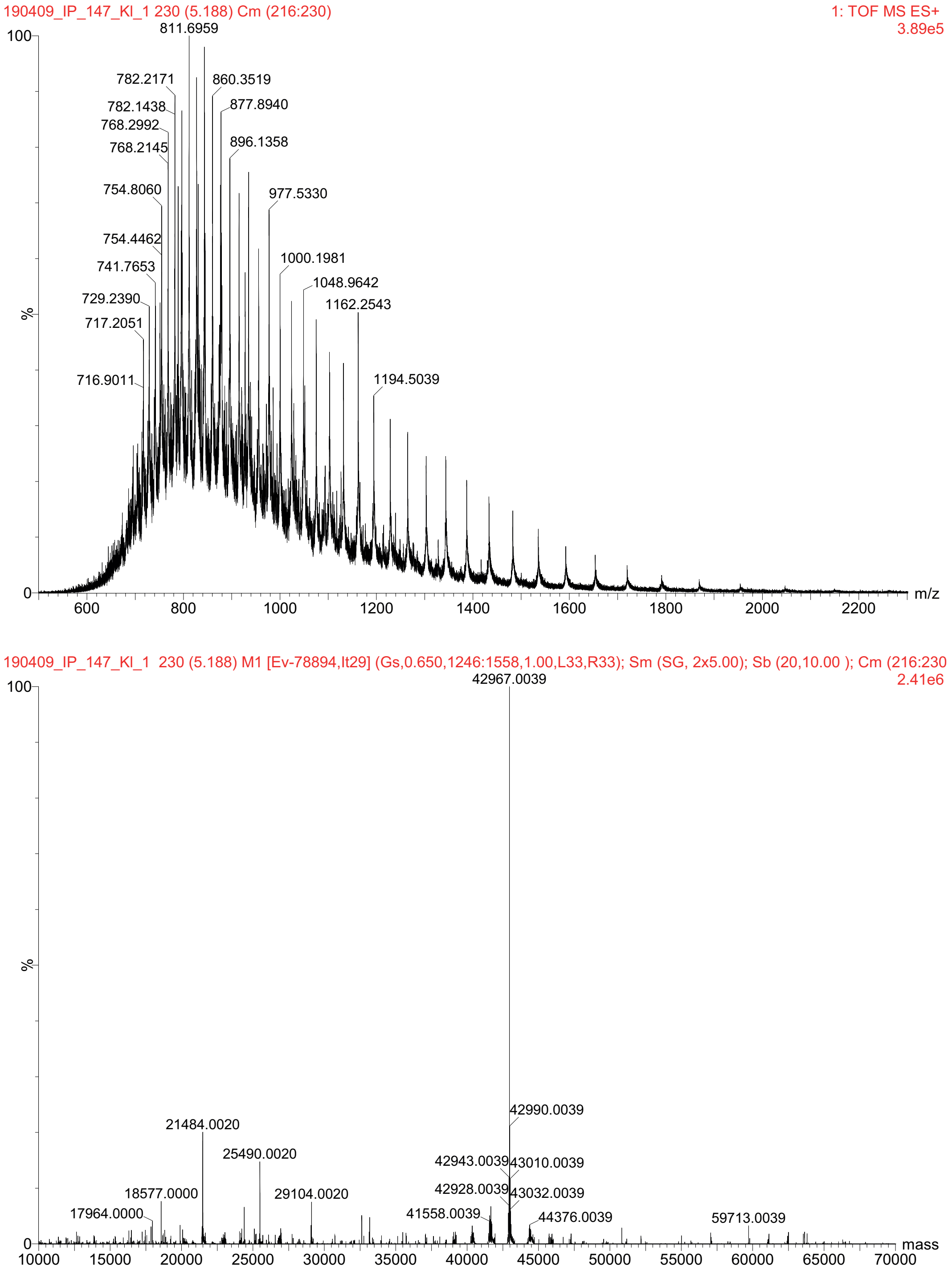

Figure 4.23: Mass spectrum and deconvoluted spectrum of TGT^{Y330D} (calculated mass: 42 965.7 Da).

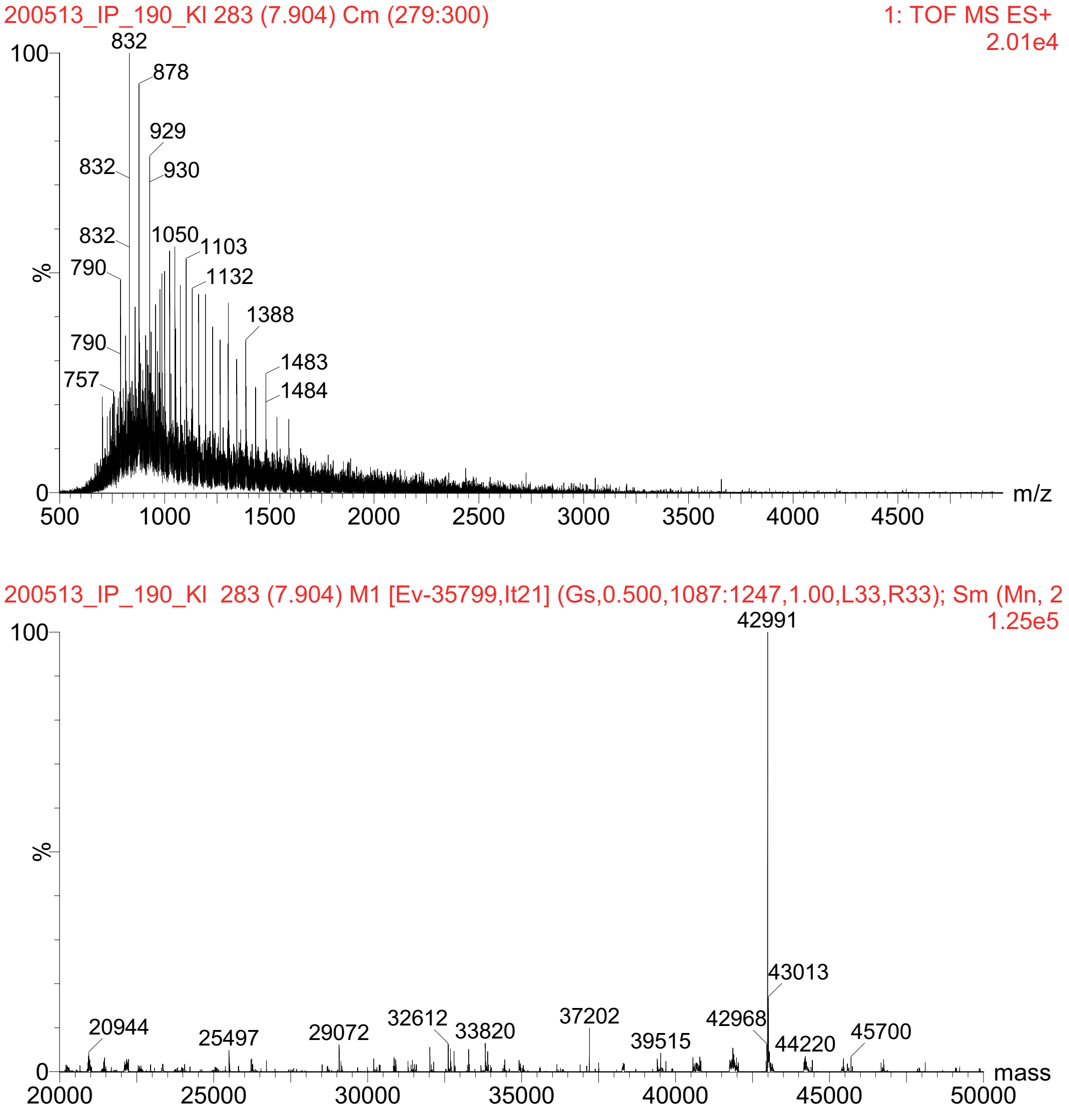

Figure 4.24: Mass spectrum and deconvoluted spectrum of TGT^{H333D} (calculated mass: 42 991.8 Da).

4.4.4 Enzyme kinetic characterization

Michaelis-Menten parameters of wild type TGT and TGT$^{\mathrm{Y330D}}$ were determined by monitoring the incorporation of [8-^{3}H]-labeled guanine (1.5 Ci mmol^{-1}) into tRNA^{Tyr}. The procedure has been described by Biela et al.[25] For each measurement, an enzyme subunit concentration of 150 nᴍ was used and the concentration of [8-^{3}H]-guanine was kept constant at 10 µᴍ. The concentration of tRNA^{Tyr} was varied between 0.26–15 µᴍ. Data were processed with *GraphPad Prism 6*.

4.4.5 Analytical gel filtration

Analytical size exclusion chromatography was performed using an ÄKTAprime™ plus FPLC system (GE Healthcare) at room temperature. The protein samples were diluted to 10 µᴍ in high-salt buffer (10 mᴍ TRIS, pH 7.8, 1 mᴍ EDTA, 2 ᴍ NaCl) and 100 µL of each sample was loaded onto a pre-equilibrated Superdex™ 200 10/300 GL column. The samples were run at a flowrate of 0.5 mL min^{-1} and protein absorbance was tracked at 280 nm wavelength. Data were processed with *GraphPad Prism 6*.

4.4.6 Peptide microarray

Peptide arrays (27 to 32 peptides each, small spots, PEG-3-like spacer, TOTD membrane) were purchased from peptides&elephants (Hennigsdorf, Germany). The membrane was rinsed with methanol, then washed three times with TRIS-buffered saline (TBS; 50 mᴍ TRIS, 27 mᴍ KCl, 136 mᴍ NaCl) and blocked overnight with blocking buffer (TBS-T with 5 % sucrose, 4 % BSA). After blocking, the membrane was washed twice with TBS-T (TBS with 0.05 % Tween® 20) and subsequently once with TBS to remove excess BSA. Strep-tag® II-labeled TGT was added to a final concentration of 1 µᴍ and the mixture was incubated at 4 °C overnight. The next day, the membrane was washed with TBS-T to remove unbound protein and subsequently blocked with blocking buffer at room temperature for 1 h. After washing three times with TBS-T, Strep-Tactin®-HRP conjugate (IBA Lifesciences) was added at a dilution of 1:3000 and the mixture was incubated at room temperature for 2 h. The membrane was washed extensively with TBS-T to remove unbound conjugate. The bound conjugate was detected via chemiluminescence according to the manual of the Clarity™ Western ECL Substrate kit (Bio-Rad) using a ChemiDoc™ Imaging System (Bio-Rad). The chemiluminescence signals were analyzed using *Image Lab 5.0* and classified according to normalized intensity values (“weak” = 5–20 %, “medium” = 20–60 %, “strong” = 60–100 %,).

Table 4.3: Peptide sequences of the first peptide array design.

Position	No. of residues	Peptide sequence
A1	15	KWSRAYIHHLIRAGE
A2	13	KWSRAYIHHLIRA
A3	11	KWSRAYIHHLI
A4	15	SRAYIHHLIRAGEIL
A5	13	SRAYIHHLIRAGE
A6	11	SRAYIHHLIRA
A7	15	AYIHHLIRAGEILGA
A8	13	AYIHHLIRAGEIL
B1	11	AYIHHLIRAGE
B2	11	IRAGEILGAML
B3	9	AGEILGAML
B4	7	EILGAML
B5	12	TAATVKALKPET
B6	10	TAATVKALKP
B7	10	ATVKALKPET
B8	13	SSEEWARNYAAHN
C1	13	SSEEYARNYAAHN
C2	13	SSEEFARNYAAHN
C3	13	SSEEWARNWAAHN
C4	13	SSEEWARNFAAHN
C5	13	SSEEWARNYAAWN
C6	13	SSEEWARNWAALN
C7	10	MVEATAQETD
C8	8	EATAQETD
D1	6	TAQETD
D2	8	TAQETDRP
D3	10	EATAQETDRP

Table 4.4: Peptide sequences of the second peptide array design. Mutations for the alanine are highlighted in red.

Position	No. of residues	Peptide sequence
A1	10	`QKWSRAYIHH`
A2	10	`KWSRAYIHHL`
A3	10	`WSRAYIHHLI`
A4	10	`SRAYIHHLIR`
A5	10	`RAYIHHLIRA`
A6	10	`AYIHHLIRAG`
A7	10	`YIHHLIRAGE`
A8	10	`IHHLIRAGEI`
B1	10	`SRAYIHHLIRAGE`
B2	13	`ARAYIHHLIRAGE`
B3	13	`SAAYIHHLIRAGE`
B4	13	`SRAAIHHLIRAGE`
B5	13	`SRAYAHHLIRAGE`
B6	13	`SRAYIAHLIRAGE`
B7	13	`SRAYIHALI RAGE`
B8	13	`SRAYIHHAIRAGE`
C1	13	`SRAYIHHLARAGE`
C2	13	`SRAYIHHLIAAGE`
C3	13	`SRAYIHHLIRAAE`
C4	13	`SRAYIHHLIRAGA`
C5	6	`MVEATA`
C6	6	`VEATAQ`
C7	6	`EATAQE`
C8	6	`ATAQET`
D1	6	`TAQETD`
D2	6	`AQETDR`
D3	6	`QETDRP`
D4	6	`AAQETD`
D5	6	`TAAETD`
D6	6	`TAQATD`
D7	6	`TAQEAD`
D8	6	`TAQETA`

4.4.7 Fluorescence polarization

All FP-based assays were performed in black 96-well microtiter plates (Greiner) and FP was measured as anisotropy (A) or millipolarization (mP) units on a Spark® 20M plate reader (Tecan) with the following settings: excitation: 485 nm; emission: 530 nm; gain: optimal; Z-position: calculated from control well (0 % inhibition: tracer and protein in assay buffer); number of flashes: 30; G-factor: 1.000. The data was evaluated using *GraphPad Prism 6*. The concentration of the peptides was calculated through UV/Vis measurements on a Spark® 20M plate reader (Tecan).

Dilutions of the TGT protein (3- to 5-fold, 90 µL) were added to 10 µL of a final fixed concentration (between 5 nᴍ and 1 µᴍ) of the fluorescently tagged tracer. Both, protein and tracer, were dissolved in high-salt or FP assay buffer (100 mᴍ TRIS, pH 7.8, 150 mᴍ NaCl, 1 mᴍ EDTA, 0.01 % Triton® X-100). The total volume was 100 µL. Each assay included two controls: blank (buffer only) and tracer only. The plates were incubated at room temperature on a microplate shaker (TiMix Control TH 15, Edmund Bühler) to reach equilibrium and FP was measured after given timepoints. The measurements were done in duplicate or triplicate and the standard deviation was calculated.

The dissociation constant (K_d) was calculated by converting the millipolarization (mP) values into their corresponding anisotropy (A) values. These values were normalized and plotted versus the respective concentrations of the protein with a nonlinear regression according to the following equation[175]:

$$A = A_\mathrm{f} + (A_\mathrm{b} - A_\mathrm{f}) \times \frac{(L_\mathrm{tot} + K_\mathrm{d} + P_\mathrm{tot}) - \sqrt{(L_\mathrm{tot} - K_\mathrm{d} - P_\mathrm{tot})^2 - 4\,L_\mathrm{tot}\,P_\mathrm{tot}}}{2\,L_\mathrm{tot}}$$

4.4.8 Isothermal dilution calorimetry

Dissociation ITC was performed using a MicroCal™ iTC$_{200}$ calorimeter (GE Healthcare) at 25 °C. A protein concentration of ~500 µᴍ in ITC assay buffer (50 mᴍ TRIS, pH 7.8, 1 ᴍ NaCl) was used in the syringe solution. The titration was started with an initial injection of 0.3 µL, after which a total of 19 injections of 2 µL followed every 180 s. Errors for the estimated K_d result from errors of the curve fitting. Data were processed with *Origin 7*.

4.4.9 Thermal shift assay

Protein unfolding was monitored via the fluorescence of the RED-NHS dye (NanoTemper Technologies) within a temperature range between 35 and 95 °C as described by Breitsprecher *et al.*[176] Thermal shift experiments were done in triplicate using a Tycho NT.6 (NanoTemper Technologies) equipped with Tycho NT.6 Capillaries (NanoTemper Technologies). The total volume of each sample was 10 µL of 2 µᴍ protein diluted in MST assay buffer (10 mᴍ HEPES, pH 7.4, 1 ᴍ NaCl, 0.005 % Tween® 20). The diluted samples were incubated at room temperature for at least 30 min before loading the capillaries. The absorbance was tracked at 330 and 350 nm (Figure 4.25). The melting temperature, T_m, was determined as the maximum of the first derivative of each melting curve.

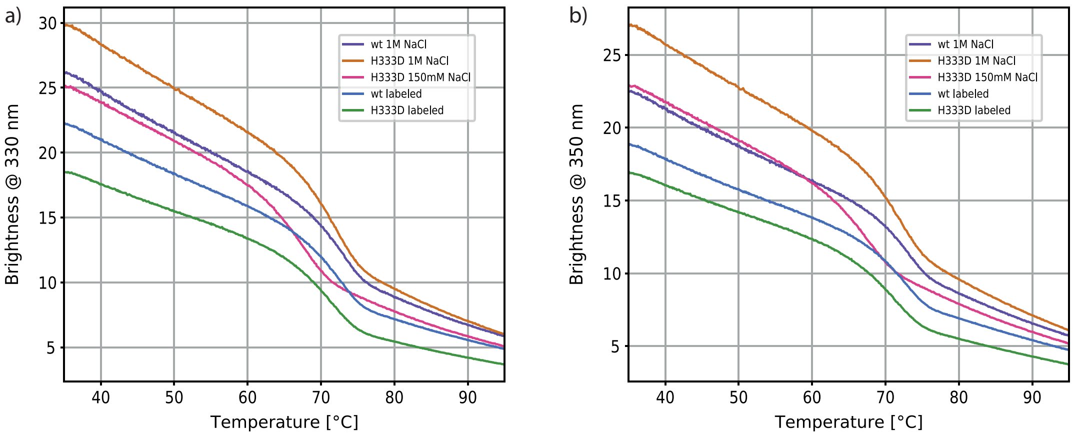

Figure 4.25: Thermal melting curves with intrinsic fluorescence tracked at wavelengths of a) 330 nm and b) 350 nm.

4.4.10 MicroScale thermophoresis

The protein variants were labeled according to the protocol of the Monolith Protein Labeling Kit RED-NHS 2nd Generation (NanoTemper Technologies). The degree-of-labeling was determined to 0.29 and 0.49 for wild type TGT and TGT^{H333D}, respectively. For the MST experiment, a solution of unlabeled TGT was serially diluted to 20 μM–0.6 nM in MST assay buffer (10 mM HEPES, pH 7.4, 1 M NaCl, 1 mM EDTA, 0.005 % Tween® 20) in the presence of 10 nM labeled TGT. The samples were incubated for at least 30 min before loading into Monolith NT.115 Premium Capillaries (NanoTemper Technologies). The MST measurements were performed at room temperature by using medium MST power and 20 % excitation power. Data were processed with *MO.Analysis*.

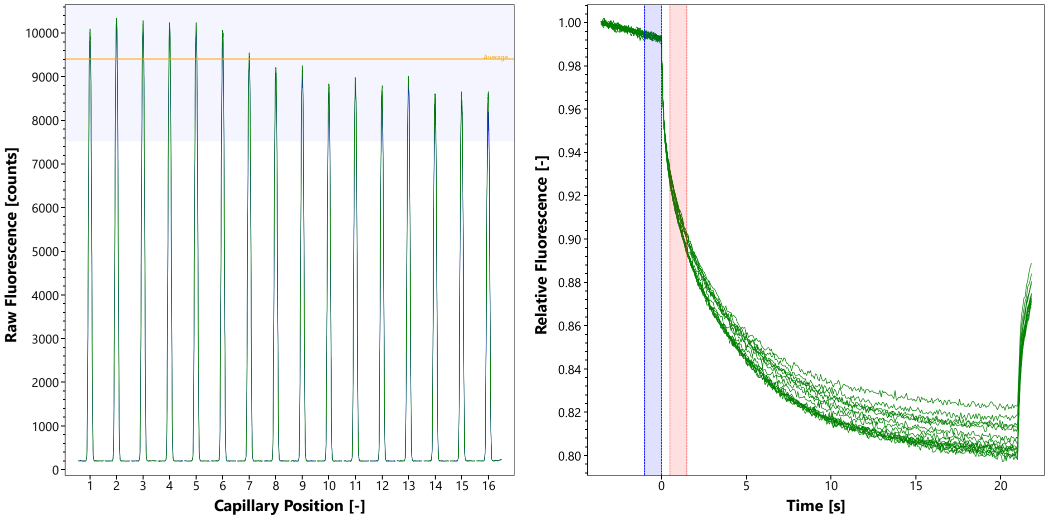

Figure 4.26: Capillary scan (left) and time traces (right) of the MST experiment with WT TGT.

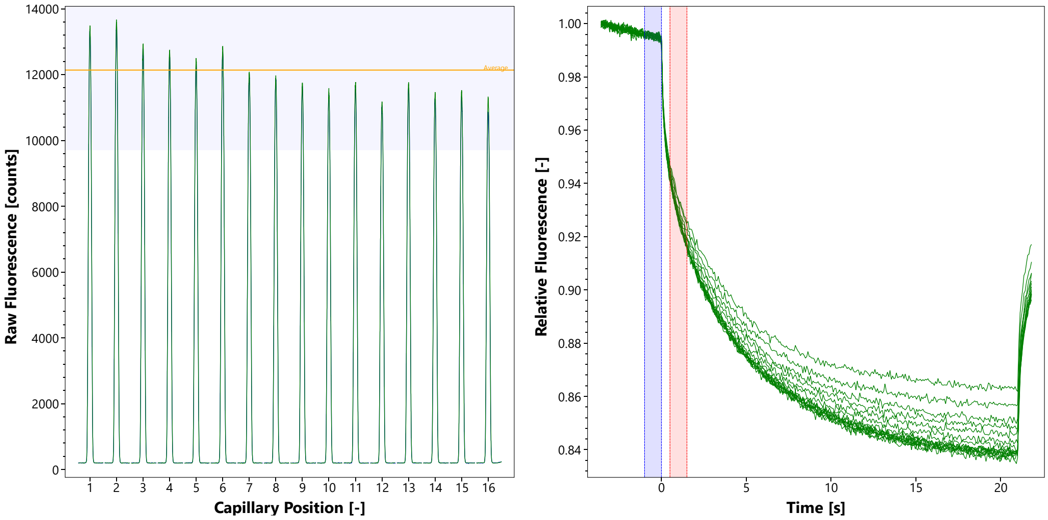

Figure 4.27: Capillary scan (left) and time traces (right) of the MST experiment with TGT^{H333D}.

4.4.11 *Shigella* host cell invasion

The assay protocol was adapted from Koestler *et al.* and slightly modified in this study.[173] Three days prior to infection, Caco-2 cells were seeded on 12-well plates at ca. 100 000 cells per well each filled with 1 mL MEM (Gibco), supplemented with 20 % FCS, or 1 mL RPMI 1640 medium (Gibco), supplemented with 10 % FCS, 1 % GlutaMAX™ (Gibco) and 1 % sodium pyruvate. The plate was incubated at 37 °C in a 5 % CO$_2$ humidified incubator until the Caco-2 cells are confluent at the day of infection (population doubling time around 62 h). One day prior to infection, *S. flexneri* serotype 2a strains (2457T[165] or Δ*tgt*) were streaked from a frozen glycerol stock on CR agar plates (tryptic soy broth, with 0.01 % Congo red and 1.5 % agar) and incubated overnight at 37 °C. The next day, a pre-culture was prepared by suspending red-colored *Shigella* colonies, that were picked from the CR agar plate, in ca. 5 mL LB medium, supplemented with 0.1 % sodium deoxycholate. The pre-culture was diluted to an OD$_{600}$ of 0.2. Subsequently, 2.5 µL of 6-TramTO-3[174] from a 20 mM stock (in DMSO) were added to 5 mL of the pre-culture. The main culture containing 10 mL LB medium, supplemented with 0.1 % sodium deoxycholate, was inoculated with 5 mL of the stained pre-culture and incubated at 37 °C and 160 rpm. After ca. 2 h, the culture reached an OD$_{600}$ of 1.0 and was washed four times with 10 mL phosphate-buffered saline (PBS) each by centrifugation at room temperature and 4400 rpm for 5 min and discarding the supernatant at each step. The bacteria were resuspended and diluted in PBS until an OD$_{600}$ of 1.0 was reached. To start infection, *Shigella* bacteria were added to each well containing Caco-2 cells according to the desired MOI (in case of MOI of 100, 80 µL of diluted bacteria at OD$_{600}$ of 1.0 were added, assuming OD$_{600}$ of 1.0 is equal to 5×10^8 cells/mL) and centrifuged at room temperature and 600 *g* for 1 min. The plate was incubated at 37 °C in a 5 % CO$_2$ humidified incubator.

After 2 h, the infection was stopped by addition of gentamicin to a final concentration of 50 µg mL^{-1} and the plate was incubated for another 1.5 h at 37 °C in a 5 % CO_2 humidified incubator. The medium was then discarded and the cells were washed with 1 mL PBS twice. For detachment of the Caco-2 cells, 150 µL Accutase® solution (Gibco) was added to each well and the plate was incubated for 10 min at room temperature. The cells were resuspended after addition of 250 µL PBS to each well. In case no Accutase® solution was used for cell detachment, the cells were scraped of the wells using a cell scraper and resuspended in 400 µL PBS. In both cases, the cell suspension was filtered through a 100 µm cell strainer and stored on ice until further analysis.

4.4.12 Flow cytometry

The washed and filtered cell suspensions were analyzed using a Guava® easyCyte 5 benchtop flow cytometer (Millipore). Cells were gated in the forward-scatter and side-scatter plot, as shown in Figure 4.28, to exclude cell debris, followed by quadrant gating in plots using the red2 (RED2-LOG, 652–671 nm) and yellow (YLW-LOG, 570–596 nm) or green (GRN-LOG, 510–540 nm) fluorescence channels. Data were processed with *Flowing Software 2.5*.

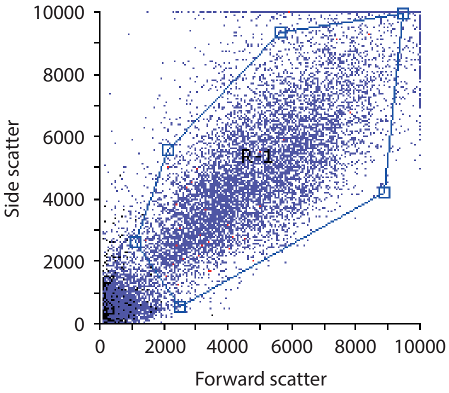

Figure 4.28: Representative forward vs. side scatter plot of Caco-2 cells.

Bibliography

[1] A. Fleming, *Br. J. Exp. Pathol.* **1929**, *10*, 226–236.

[2] L. H. Sternbach, *Prog. Drug Res.* **1978**, *22*, 229–266.

[3] M. Boolell, M. J. Allen, S. A. Ballard, S. Gepi-Attee, G. J. Muirhead, A. M. Naylor, I. H. Osterloh, C. Gingell, *Int. J. Impot. Res.* **1996**, *8*, 47–52.

[4] M. Boolell, S. Gepi-Attee, J. C. Gingell, M. J. Allen, *Br. J. Urol.* **1996**, *78*, 257–261.

[5] H. Kubinyi, *J. Recept. Signal Transduct. Res.* **1999**, *19*, 15–39.

[6] T. A. Ban, *Dialogues Clin. Neurosci.* **2006**, *8*, 335–344.

[7] K. Shiga, *Zentralbl. Bakteriol. Mikrobiol. Hyg.* **1898**, *23*, 599–600.

[8] K. Shiga, *Phil. J. Sci.* **1906**, *1*, 485–500.

[9] I. A. Khalil, C. Troeger, B. F. Blacker, P. C. Rao, A. Brown, D. E. Atherly, T. G. Brewer, C. M. Engmann, E. R. Houpt, G. Kang, K. L. Kotloff, M. M. Levine, S. P. Luby, C. A. MacLennan, W. K. Pan, P. B. Pavlinac, J. A. Platts-Mills, F. Qadri, M. S. Riddle, E. T. Ryan, D. A. Shoultz, A. D. Steele, J. L. Walson, J. W. Sanders, A. H. Mokdad, C. J. L. Murray, S. I. Hay, R. C. Reiner, *Lancet Infect. Dis.* **2018**, *18*, 1229–1240.

[10] H. L. DuPont, M. M. Levine, R. B. Hornick, S. B. Formal, *J. Infect. Dis.* **1989**, *159*, 1126–1128.

[11] World Health Organization, Guidelines for the control of shigellosis, including epidemics due to *Shigella dysenteriae* type 1, Geneva, **2005**.

[12] K. L. Kotloff, M. S. Riddle, J. A. Platts-Mills, P. Pavlinac, A. K. M. Zaidi, *Lancet* **2018**, *391*, 801–812.

[13] G. N. Schroeder, H. Hilbi, *Clin. Microbiol. Rev.* **2008**, *21*, 134–156.

[14] F. Tuorto, C. Legrand, C. Cirzi, G. Federico, R. Liebers, M. Müller, A. E. Ehrenhofer-Murray, G. Dittmar, H.-J. Gröne, F. Lyko, *EMBO J.* **2018**, *37*, e99777.

[15] M. Müller, C. Legrand, F. Tuorto, V. P. Kelly, Y. Atlasi, F. Lyko, A. E. Ehrenhofer-Murray, *Nucl. Acids Res.* **2019**, *47*, 3711–3727.

[16] J. M. Durand, N. Okada, T. Tobe, M. Watarai, I. Fukuda, T. Suzuki, N. Nakata, K. Komatsu, M. Yoshikawa, C. Sasakawa, *J. Bacteriol.* **1994**, *176*, 4627–4634.

[17] G. R. Björk, *Prog. Nucleic Acid Res. Mol. Biol.* **1995**, *50*, 263–338.

[18] C. Romier, K. Reuter, D. Suck, R. Ficner, *EMBO J.* **1996**, *15*, 2850–2857.

[19] W. Xie, X. Liu, R. H. Huang, *Nat. Struct. Biol.* **2003**, *10*, 781–788.

[20] T. Ritschel, C. Atmanene, K. Reuter, A. van Dorsselaer, S. Sanglier-Cianferani, G. Klebe, *J. Mol. Biol.* **2009**, *393*, 833–847.

[21] S. Jakobi, T. X. P. Nguyen, F. Debaene, A. Metz, S. Sanglier-Cianférani, K. Reuter, G. Klebe, *Proteins* **2014**, *82*, 2713–2732.

[22] S. Jakobi, T. X. P. Nguyen, F. Debaene, S. Cianférani, K. Reuter, G. Klebe, *ACS Chem. Biol.* **2015**, *10*, 1897–1907.

[23] A. Nguyen, D. Nguyen, T. X. Phong Nguyen, M. Sebastiani, S. Dörr, O. Hernandez-Alba, F. Debaene, S. Cianférani, A. Heine, G. Klebe, K. Reuter, *ACS Chem. Biol.* **2020**, *15*, 3021–3029.

[24] D. M. Goodenough-Lashua, G. A. Garcia, *Bioorg. Chem.* **2003**, *31*, 331–344.

[25] I. Biela, N. Tidten-Luksch, F. Immekus, S. Glinca, T. X. P. Nguyen, H.-D. Gerber, A. Heine, G. Klebe, K. Reuter, *PLoS ONE* **2013**, *8*, e64240.

[26] S. R. Hörtner, T. Ritschel, B. Stengl, C. Kramer, W. B. Schweizer, B. Wagner, M. Kansy, G. Klebe, F. Diederich, *Angew. Chem. Int. Ed.* **2007**, *46*, 8266–8269.

[27] T. Ritschel, P. C. Kohler, G. Neudert, A. Heine, F. Diederich, G. Klebe, *ChemMedChem* **2009**, *4*, 2012–2023.

[28] B. Stengl, E. A. Meyer, A. Heine, R. Brenk, F. Diederich, G. Klebe, *J. Mol. Biol.* **2007**, *370*, 492–511.

[29] F. Immekus, L. J. Barandun, M. Betz, F. Debaene, S. Petiot, S. Sanglier-Cianferani, K. Reuter, F. Diederich, G. Klebe, *ACS Chem. Biol.* **2013**, *8*, 1163–1178.

[30] E. Hassaan, P.-O. Eriksson, S. Geschwindner, A. Heine, G. Klebe, *ChemMedChem* **2020**, *15*, 324–337.

[31] F. U. Huschmann, J. Linnik, K. Sparta, M. Ühlein, X. Wang, A. Metz, J. Schiebel, A. Heine, G. Klebe, M. S. Weiss, U. Mueller, *Acta Crystallogr. F Struct. Biol. Commun.* **2016**, *72*, 346–355.

[32] E. Hassaan, C. Hohn, F. R. Ehrmann, F. W. Goetzke, L. Movsisyan, T. Hüfner-Wulsdorf, M. Sebastiani, A. Härtsch, K. Reuter, F. Diederich, G. Klebe, *J. Med. Chem.* **2020**, *63*, 6802–6820.

[33] F. R. Ehrmann, J. Stojko, A. Metz, F. Debaene, L. J. Barandun, A. Heine, F. Diederich, S. Cianférani, K. Reuter, G. Klebe, *PLoS ONE* **2017**, *12*, e0175723.

[34] F. R. Ehrmann, J. Kalim, T. Pfaffeneder, B. Bernet, C. Hohn, E. Schäfer, T. Botzanowski, S. Cianférani, A. Heine, K. Reuter, F. Diederich, G. Klebe, *Angew. Chem. Int. Ed.* **2018**, *57*, 10085–10090.

[35] H. Nishi, K. Hashimoto, T. Madej, A. R. Panchenko, *Prog. Mol. Biol. Transl. Sci.* **2013**, *117*, 3–24.

[36] K. Hashimoto, H. Nishi, S. Bryant, A. R. Panchenko, *Phys. Biol.* **2011**, *8*, 035007.

[37] G. G. Hammes, C. W. Wu, *Science* **1971**, *172*, 1205–1211.

[38] N. Shimba, A. M. Nomura, A. B. Marnett, C. S. Craik, *J. Virol.* **2004**, *78*, 6657–6665.

[39] T. Shahian, G. M. Lee, A. Lazic, L. A. Arnold, P. Velusamy, C. M. Roels, R. K. Guy, C. S. Craik, *Nat. Chem. Biol.* **2009**, *5*, 640–646.

[40] T. H. Tran, P. Alexander, S. Dharmaiah, C. Agamasu, D. V. Nissley, F. McCormick, D. Esposito, D. K. Simanshu, A. G. Stephen, T. E. Balius, *Proc. Natl. Acad. Sci.* **2020**, *117*, 3363–3364.

[41] S.-M. Lin, S.-C. Lin, J.-N. Hsu, C.-K. Chang, C.-M. Chien, Y.-S. Wang, H.-Y. Wu, U.-S. Jeng, K. Kehn-Hall, M.-H. Hou, *J. Med. Chem.* **2020**, *63*, 3131–3141.

[42] R. Brenk, M. T. Stubbs, A. Heine, K. Reuter, G. Klebe, *ChemBioChem* **2003**, *4*, 1066–1077.

[43] N. Cox, M. Retegan, F. Neese, D. A. Pantazis, A. Boussac, W. Lubitz, *Science* **2014**, *345*, 804–808.

[44] I. D. Sahu, R. M. McCarrick, G. A. Lorigan, *Biochemistry* **2013**, *52*, 5967–5984.

[45] C. Altenbach, T. Marti, H. G. Khorana, W. L. Hubbell, *Science* **1990**, *248*, 1088–1092.

[46] C. S. Klug, J. B. Feix, *Methods Cell Biol.* **2008**, *84*, 617–658.

[47] J. P. Klare, *Biol. Chem.* **2013**, *394*, 1281–1300.

[48] O. Schiemann, T. F. Prisner, *Q. Rev. Biophys.* **2007**, *40*, 1–53.

[49] G. W. Reginsson, O. Schiemann, *Biochem. J.* **2011**, *434*, 353–363.

[50] G. Jeschke, *Annu. Rev. Phys. Chem.* **2012**, *63*, 419–446.

[51] L. J. Berliner, J. Grunwald, H. Hankovszky, K. Hideg, *Anal. Biochem.* **1982**, *119*, 450–455.

[52] G. Likhtenshtein, J. Yamauchi, S. Nakatsuji, A. I. Smirnov, R. Tamura, *Nitroxides: Applications in Chemistry, Biomedicine, and Materials Science*, Wiley-VCH, Hoboken, **2008**.

[53] G. Likhtenshtein, *Int. Res. J. Pure Appl. Chem.* **2015**, *8*, 1–18.

[54] J. J. Jassoy, A. Berndhäuser, F. Duthie, S. P. Kühn, G. Hagelueken, O. Schiemann, *Angew. Chem. Int. Ed.* **2017**, *56*, 177–181.

[55] J. J. Jassoy, C. A. Heubach, T. Hett, F. Bernhard, F. R. Haege, G. Hagelueken, O. Schiemann, *Molecules* **2019**, *24*, DOI: 10.3390/molecules24152735.

[56] N. Fleck, C. A. Heubach, T. Hett, F. R. Haege, P. P. Bawol, H. Baltruschat, O. Schiemann, *Angew. Chem. Int. Ed.* **2020**, *59*, 9767–9772.

[57] S. Andersson, F. Radner, A. Rydbeek, R. Servin, L.-G. Wistrand, U.S. Patent Application No. 5530140A, **1996**.

[58] Z. Yang, M. D. Bridges, C. J. López, O. Y. Rogozhnikova, D. V. Trukhin, E. K. Brooks, V. Tormyshev, H. J. Halpern, W. L. Hubbell, *J. Magn. Reson.* **2016**, *269*, 50–54.

[59] A. A. Kuzhelev, O. A. Krumkacheva, G. Y. Shevelev, M. Yulikov, M. V. Fedin, E. G. Bagryanskaya, *Phys. Chem. Chem. Phys.* **2018**, *20*, 10224–10230.

[60] A. P. Jagtap, I. Krstic, N. C. Kunjir, R. Hänsel, T. F. Prisner, S. T. Sigurdsson, *Free Radic. Res.* **2015**, *49*, 78–85.

[61] B. Joseph, V. M. Tormyshev, O. Y. Rogozhnikova, D. Akhmetzyanov, E. G. Bagryanskaya, T. F. Prisner, *Angew. Chem. Int. Ed.* **2016**, *55*, 11538–11542.

[62] Y.-N. Chang, E. A. Jaumann, K. Reichel, J. Hartmann, D. Oliver, G. Hummer, B. Joseph, E. R. Geertsma, *Nat. Commun.* **2019**, *10*, 2032.

[63] J. Glaenzer, M. F. Peter, G. Hagelueken, *Methods* **2018**, *147*, 163–175.

[64] A. Nguyen, Dissertation, Philipps-Universität Marburg, Marburg, **2020**.

[65] G. Hagelueken, R. Ward, J. H. Naismith, O. Schiemann, *Appl. Magn. Reson.* **2012**, *42*, 377–391.

[66] W. Kabsch, *Acta Cryst. D* **2010**, *66*, 125–132.

[67] M. Krug, M. S. Weiss, U. Heinemann, U. Mueller, *J. Appl. Crystallogr.* **2012**, *45*, 568–572.

[68] A. J. McCoy, R. W. Grosse-Kunstleve, P. D. Adams, M. D. Winn, L. C. Storoni, R. J. Read, *J. Appl. Crystallogr.* **2007**, *40*, 658–674.

[69] E. Potterton, P. Briggs, M. Turkenburg, E. Dodson, *Acta Cryst. D* **2003**, *59*, 1131–1137.

[70] P. Emsley, B. Lohkamp, W. G. Scott, K. Cowtan, *Acta Cryst. D* **2010**, *66*, 486–501.

[71] P. D. Adams, P. V. Afonine, G. Bunkóczi, V. B. Chen, I. W. Davis, N. Echols, J. J. Headd, L.-W. Hung, G. J. Kapral, R. W. Grosse-Kunstleve, A. J. McCoy, N. W. Moriarty, R. Oeffner, R. J. Read, D. C. Richardson, J. S. Richardson, T. C. Terwilliger, P. H. Zwart, *Acta Cryst. D* **2010**, *66*, 213–221.

[72] K. Diederichs, P. A. Karplus, *Nat. Struct. Biol.* **1997**, *4*, 269–275.

[73] R. A. Laskowski, M. W. MacArthur, D. S. Moss, J. M. Thornton, *J. Appl. Crystallogr.* **1993**, *26*, 283–291.

[74] G. J. Kleywegt, J.-Y. Zou, M. Kjeldgaard, T. A. Jones in *International Tables for Crystallography, Vol. F. Crystallography of Biological Macromolecules*, (Eds.: M. G. Rossmann, E. Arnold), Kluwer Academic Publishers, Dordrecht, **2001**, pp. 353–356, 366–367.

[75] A. W. Curnow, F. L. Kung, K. A. Koch, G. A. Garcia, *Biochemistry* **1993**, *32*, 5239–5246.

[76] G. Jeschke, V. Chechik, P. Ionita, A. Godt, H. Zimmermann, J. Banham, C. R. Timmel, D. Hilger, H. Jung, *Appl. Magn. Reson.* **2006**, *30*, 473–498.

[77] L. Bonetta, *Nature* **2010**, *468*, 851–854.

[78] G. Rabbani, M. H. Baig, K. Ahmad, I. Choi, *Curr. Protein Pept. Sci.* **2018**, *19*, 948–957.

[79] L.-G. Milroy, T. N. Grossmann, S. Hennig, L. Brunsveld, C. Ottmann, *Chem. Rev.* **2014**, *114*, 4695–4748.

[80] A. E. Modell, S. L. Blosser, P. S. Arora, *Trends Pharmacol. Sci.* **2016**, *37*, 702–713.

[81] I. Petta, S. Lievens, C. Libert, J. Tavernier, K. de Bosscher, *Mol. Ther.* **2016**, *24*, 707–718.

[82] L. Mabonga, A. P. Kappo, *Biophys. Rev.* **2019**, *11*, 559–581.

[83] J. A. Wells, C. L. McClendon, *Nature* **2007**, *450*, 1001–1009.

[84] S. Jones, J. M. Thornton, *Prog. Biophys. Mol. Biol.* **1995**, *63*, 31–65.

[85] D. Cardinale, O. M. H. Salo-Ahen, S. Ferrari, G. Ponterini, G. Cruciani, E. Carosati, A. M. Tochowicz, S. Mangani, R. C. Wade, M. P. Costi, *Curr. Med. Chem.* **2010**, *17*, 826–846.

[86] T. Clackson, J. A. Wells, *Science* **1995**, *267*, 383–386.

[87] B. Ma, T. Elkayam, H. Wolfson, R. Nussinov, *Proc. Natl. Acad. Sci.* **2003**, *100*, 5772–5777.

[88] D. A. Erlanson, J. A. Wells, A. C. Braisted, *Annu. Rev. Biophys. Biomol. Struct.* **2004**, *33*, 199–223.

[89] S. B. Shuker, P. J. Hajduk, R. P. Meadows, S. W. Fesik, *Science* **1996**, *274*, 1531–1534.

[90] J. Rudolph, *Nat. Rev. Cancer* **2007**, *7*, 202–211.

[91] S. Jakobi, Dissertation, Philipps-Universität Marburg, Marburg, **2013**.

[92] C. D. Thanos, W. L. DeLano, J. A. Wells, *Proc. Natl. Acad. Sci.* **2006**, *103*, 15422–15427.

[93] F. Terwesten, Dissertation, Philipps-Universität Marburg, Marburg, **2017**.

[94] D. H. Juers, J. Ruffin, *J. Appl. Crystallogr.* **2014**, *47*, 2105–2108.

[95] M. Petitjean, *J. Chem. Inf. Model.* **1992**, *32*, 331–337.

[96] B. Kuhn, E. Gilberg, R. Taylor, J. Cole, O. Korb, *J. Med. Chem.* **2019**, *62*, 10441–10455.

[97] H. Hilpert, H. Mauser, R. Humm, L. Anselm, H. Kuehne, G. Hartmann, S. Gruener, D. W. Banner, J. Benz, B. Gsell, A. Kuglstatter, M. Stihle, R. Thoma, R. A. Sanchez, H. Iding, B. Wirz, W. Haap, *J. Med. Chem.* **2013**, *56*, 9789–9801.

[98] C. Dalvit, P. E. Fagerness, D. T. A. Hadden, R. W. Sarver, B. J. Stockman, *J. Am. Chem. Soc.* **2003**, *125*, 7696–7703.

[99] C. Dalvit, S. Knapp, *Magn. Reson. Chem.* **2017**, *55*, 1091–1095.

[100] C. Dalvit, A. Vulpetti, *J. Med. Chem.* **2019**, *62*, 2218–2244.

[101] A. Vulpetti, N. Schiering, C. Dalvit, *Proteins* **2010**, *78*, 3281–3291.

[102] G. K. Ackers, T. E. Thompson, *Proc. Natl. Acad. Sci.* **1965**, *53*, 342–349.

[103] P. C. Lauterbur, *Nature* **1973**, *242*, 190–191.

[104] T. D. W. Claridge, *High-Resolution NMR Techniques in Organic Chemistry*, 2nd Edition, Elsevier, Amsterdam and London, **2009**.

[105] E. O. Stejskal, J. E. Tanner, *J. Chem. Phys.* **1965**, *42*, 288–292.

[106] W. S. Price, K. Hayamizu, H. Ide, Y. Arata, *J. Magn. Reson.* **1999**, *139*, 205–212.

[107] K. F. Morris, C. S. Johnson, *J. Am. Chem. Soc.* **1992**, *114*, 3139–3141.

[108] C. S. Johnson, *Prog. Nucl. Magn. Reson. Spectrosc.* **1999**, *34*, 203–256.

[109] K. F. Morris, C. S. Johnson, *J. Am. Chem. Soc.* **1993**, *115*, 4291–4299.

[110] I. Keresztes, P. G. Williard, *J. Am. Chem. Soc.* **2000**, *122*, 10228–10229.

[111] M. Valentini, H. Rüegger, P. S. Pregosin, *Helv. Chim. Acta* **2001**, *84*, 2833–2853.

[112] N. E. Schlörer, S. Berger, *Organometallics* **2001**, *20*, 1703–1704.

[113] X. Xie, C. Auel, W. Henze, R. M. Gschwind, *J. Am. Chem. Soc.* **2003**, *125*, 1595–1601.

[114] P. Schweyen, M. Hoffmann, J. Krumsieck, B. Wolfram, X. Xie, M. Bröring, *Angew. Chem. Int. Ed.* **2016**, *55*, 10118–10121.

[115] L. H. Lucas, C. K. Larive, *Concepts Magn. Reson.* **2004**, *20A*, 24–41.

[116] M. Arendt, W. Sun, J. Thomann, X. Xie, T. Schrader, *Chem. Asian J.* **2006**, *1*, 544–554.

[117] S. J. Koch, C. Renner, X. Xie, T. Schrader, *Angew. Chem. Int. Ed.* **2006**, *45*, 6352–6355.

[118] T. S. Derrick, E. F. McCord, C. K. Larive, *J. Magn. Reson.* **2002**, *155*, 217–225.

[119] L. H. Lucas, K. E. Price, C. K. Larive, *J. Am. Chem. Soc.* **2004**, *126*, 14258–14266.

[120] D. R. Banatao, D. Cascio, C. S. Crowley, M. R. Fleissner, H. L. Tienson, T. O. Yeates, *Proc. Natl. Acad. Sci.* **2006**, *103*, 16230–16235.

[121] P. Bamborough, C.-w. Chung, E. H. Demont, R. C. Furze, A. J. Bannister, K. H. Che, H. Diallo, C. Douault, P. Grandi, T. Kouzarides, A.-M. Michon, D. J. Mitchell, R. K. Prinjha, C. Rau, S. Robson, R. J. Sheppard, R. Upton, R. J. Watson, *Angew. Chem. Int. Ed.* **2016**, *128*, 11554–11558.

[122] F. H. Niesen, H. Berglund, M. Vedadi, *Nat. Protoc.* **2007**, *2*, 2212–2221.

[123] D. H. Wu, A. D. Chen, C. S. Johnson, *J. Magn. Reson.* **1995**, *115*, 260–264.

[124] A. Jerschow, N. Müller, *J. Magn. Reson.* **1997**, *125*, 372–375.

[125] A. Pedretti, L. Villa, G. Vistoli, *J. Comp. Aided Mol. Design* **2004**, *18*, 167–173.

[126] M. R. Arkin, J. A. Wells, *Nat. Rev. Drug Discov.* **2004**, *3*, 301–317.

[127] A. P. Higueruelo, H. Jubb, T. L. Blundell, *Curr. Opin. Pharmacol.* **2013**, *13*, 791–796.

[128] L. Nevola, E. Giralt, *Chem. Commun.* **2015**, *51*, 3302–3315.

[129] P. Vlieghe, V. Lisowski, J. Martinez, M. Khrestchatisky, *Drug Discov. Today* **2010**, *15*, 40–56.

[130] R. W. Cheloha, A. Maeda, T. Dean, T. J. Gardella, S. H. Gellman, *Nat. Biotechnol.* **2014**, *32*, 653–655.

[131] T. A. Hill, N. E. Shepherd, F. Diness, D. P. Fairlie, *Angew. Chem. Int. Ed.* **2014**, *53*, 13020–13041.

[132] M. Gao, K. Cheng, H. Yin, *Biopolymers* **2015**, *104*, 310–316.

[133] C. Bechara, S. Sagan, *FEBS Lett.* **2013**, *587*, 1693–1702.

[134] G. Guidotti, L. Brambilla, D. Rossi, *Trends Pharmacol. Sci.* **2017**, *38*, 406–424.

[135] M. A. Toro, P. A. Sánchez-Murcia, D. Moreno, M. Ruiz-Santaquiteria, J. F. Alzate, A. Negri, M.-J. Camarasa, F. Gago, S. Velázquez, A. Jiménez-Ruiz, *ChemBioChem* **2013**, *14*, 1212–1217.

[136] M. Ruiz-Santaquiteria, P. A. Sánchez-Murcia, M. A. Toro, H. de Lucio, K. J. Gutiérrez, S. de Castro, F. A. C. Carneiro, F. Gago, A. Jiménez-Ruiz, M.-J. Camarasa, S. Velázquez, *Eur. J. Med. Chem.* **2017**, *135*, 49–59.

[137] M. Ruiz-Santaquiteria, S. de Castro, M. A. Toro, H. de Lucio, K. J. Gutiérrez, P. A. Sánchez-Murcia, M. Á. Jiménez, F. Gago, A. Jiménez-Ruiz, M.-J. Camarasa, S. Velázquez, *Eur. J. Med. Chem.* **2018**, *149*, 238–247.

[138] D. Cardinale, G. Guaitoli, D. Tondi, R. Luciani, S. Henrich, O. M. H. Salo-Ahen, S. Ferrari, G. Marverti, D. Guerrieri, A. Ligabue, C. Frassineti, C. Pozzi, S. Mangani, D. Fessas, R. Guerrini, G. Ponterini, R. C. Wade, M. P. Costi, *Proc. Natl. Acad. Sci.* **2011**, *108*, E542–9.

[139] R. Frank, *Tetrahedron* **1992**, *48*, 9217–9232.

[140] C. Katz, L. Levy-Beladev, S. Rotem-Bamberger, T. Rito, S. G. D. Rüdiger, A. Friedler, *Chem. Soc. Rev.* **2011**, *40*, 2131–2145.

[141] M. Á. Bonache, B. Balsera, B. López-Méndez, O. Millet, D. Brancaccio, I. Gómez-Monterrey, A. Carotenuto, L. M. Pavone, M. Reille-Seroussi, N. Gagey-Eilstein, M. Vidal, R. de La Torre-Martinez, A. Fernández-Carvajal, A. Ferrer-Montiel, M. T. García-López, M. Martín-Martínez, M. J. P. de Vega, R. González-Muñiz, *ACS Comb. Sci.* **2014**, *16*, 250–258.

[142] A. Jablonski, *Bull. Acad. Pol. Sci. Ser. A* **1960**, 259–264.

[143] J. R. Lakowicz, *Principles of Fluorescence Spectroscopy*, 3rd Edition, Springer, New York, **2010**.

[144] I. N. Serdjuk, N. R. Zaccai, J. Zaccai, *Methods in Molecular Biophysics: Structure, Dynamics, Function for Biology and Medicine*, 2nd Edition, Cambridge University Press, Cambridge, New York, and Port Melbourne, **2017**.

[145] A. M. Rossi, C. W. Taylor, *Nat. Protoc.* **2011**, *6*, 365–387.

[146] X. Wang, D. Hou, W. Dai, W. Gao, S. Ju, H. Cao, L. Zhang, G. Wang, Y. Guo, S. Chen, H. Tian, Z. Li, *Mol. Inform.* **2016**, *35*, 262–267.

[147] N. J. Moerke, *Curr. Protoc. Chem. Biol.* **2009**, *1*, 1–15.

[148] A. M. Spokoyny, Y. Zou, J. J. Ling, H. Yu, Y.-S. Lin, B. L. Pentelute, *J. Am. Chem. Soc.* **2013**, *135*, 5946–5949.

[149] B. V. Nemzer, A. G. Dickson, *Mar. Chem.* **2005**, *96*, 237–242.

[150] Y. Song, R. L. Schowen, R. T. Borchardt, E. M. Topp, *J. Pharm. Sci.* **2001**, *90*, 1198–1203.

[151] J. J. A. G. Kamps, R. J. Hopkinson, C. J. Schofield, T. D. W. Claridge, *Commun. Chem.* **2019**, *2*, DOI: 10.1038/s42004-019-0224-2.

[152] T. Bergfors, *J. Struct. Biol.* **2003**, *142*, 66–76.

[153] P. H. Zwart, R. W. Grosse-Kunstleve, A. A. Lebedev, G. N. Murshudov, P. D. Adams, *Acta Cryst. D* **2008**, *64*, 99–107.

[154] A. A. Lebedev, M. N. Isupov, *Acta Cryst. D* **2014**, *70*, 2430–2443.

[155] E. Boeri Erba, K. Barylyuk, Y. Yang, R. Zenobi, *Anal. Chem.* **2011**, *83*, 9251–9259.

[156] E. Boeri Erba, C. Petosa, *Protein Sci.* **2015**, *24*, 1176–1192.

[157] S. G. Krimmer, G. Klebe, *J. Comp. Aided Mol. Design* **2015**, *29*, 867–883.

[158] A. Velazquez-Campoy, S. A. Leavitt, E. Freire, *Methods Mol. Biol.* **2015**, *1278*, 183–204.

[159] S. D. Burrows, M. L. Doyle, K. P. Murphy, S. G. Franklin, J. R. White, I. Brooks, D. E. McNulty, M. O. Scott, J. R. Knutson, D. Porter, *Biochemistry* **1994**, *33*, 12741–12745.

[160] H. R. Broom, J. A. O. Rumfeldt, K. A. Vassall, E. M. Meiering, *Protein Sci.* **2015**, *24*, 2081–2089.

[161] W.-G. Seetoh, C. Abell, *J. Am. Chem. Soc.* **2016**, *138*, 14303–14311.

[162] K. Luke, D. Apiyo, P. Wittung-Stafshede, *Biophys. J.* **2005**, *89*, 3332–3336.

[163] Z. Ahmed, Z. Timsah, K. M. Suen, N. P. Cook, G. R. Lee, C.-C. Lin, M. Gagea, A. A. Marti, J. E. Ladbury, *Nat. Commun.* **2015**, *6*, 7354.

[164] V. Meunier, M. Bourrié, Y. Berger, G. Fabre, *Cell Biol. Toxicol.* **1995**, *11*, 187–194.

[165] E. H. Labrec, H. Schneider, T. J. Magnani, S. B. Formal, *J. Bacteriol.* **1964**, *88*, 1503–1518.

[166] P. J. Sansonetti, D. J. Kopecko, S. B. Formal, *Infect. Immun.* **1982**, *35*, 852–860.

[167] R. Schuch, A. T. Maurelli, *Infect. Immun.* **1997**, *65*, 3686–3692.

[168] G. Henle, F. Deinhardt, *J. Immunol.* **1957**, *79*, 54–59.

[169] A. T. Maurelli, B. Blackmon, R. Curtis III, *Infect. Immun.* **1984**, *43*, 195–201.

[170] L. M. Pope, K. E. Reed, S. M. Payne, *Infect. Immun.* **1995**, *63*, 3642–3648.

[171] S. M. Payne, R. A. Finkelstein, *Infect. Immun.* **1977**, *18*, 94–98.

[172] F. Qadri, S. A. Hossain, I. Ciznár, K. Haider, A. Ljungh, T. Wadstrom, D. A. Sack, *J. Clin. Microbiol.* **1988**, *26*, 1343–1348.

[173] B. J. Koestler, C. M. Ward, S. M. Payne, *Curr. Protoc. Microbiol.* **2018**, *50*, e57.

[174] L. N. Schulte, B. Heinrich, H. Janga, B. T. Schmeck, O. Vázquez, *Angew. Chem. Int. Ed.* **2018**, *57*, 11564–11568.

[175] Invitrogen Corporation, Technical Resource Guide, Fluorescence Polarization, Madison, **2005**.

[176] D. Breitsprecher, P. A. Fung, N. Tschammer, *Nat. Methods* **2018**, *15*, 298.

[177] M. R. Wilkins, E. Gasteiger, A. Bairoch, J. C. Sanchez, K. L. Williams, R. D. Appel, D. F. Hochstrasser, *Methods Mol. Biol.* **1999**, *112*, 531–552.

Construct Summary

The following section lists the protein sequence of wild type TGT as expressed using the pPR-IBA2 plasmid (IBA Lifesciences) including the N-terminal Strep-tag® II (shown in blue), the thrombin recognition (shown in red) and cleavage site (marked with ∗) followed by the actual target protein sequence (shown in black, starting with Met1 in new line). The molecular weights (MWs) and molar extinction coefficients (ε_{280}) of the used constructs are listed in Table S1.

```
>wild type TGT
MASWSHPQFE KSGGGGGLVP R*GS
MVEATAQETD RPRFSFSIAA REGKARTGTI EMKRGVIRTP AFMPVGTAAT VKALKPETVR ATGADIILGN
TYHLMLRPGA ERIAKLGGLH SFMGWDRPIL TDSGGYQVMS LSSLTKQSEE GVTFKSHLDG SRHMLSPERS
IEIQHLLGSD IVMAFDECTP YPATPSRAAS SMERSMRWAK RSRDAFDSRK EQAENAALFG IQQGSVFENL
RQQSADALAE IGFDGYAVGG LAVGEGQDEM FRVLDFSVPM LPDDKPHYLM GVGKPDDIVG AVERGIDMFD
CVLPTRSGRN GQAFTWDGPI NIRNARFSED LKPLDSECHC AVCQKWSRAY IHHLIRAGEI LGAMLMTEHN
IAFYQQLMQK IRDSISEGRF SQFAQDFRAR YFARNS
```

Table S1: Summary of recombinant *Z. mobilis* TGT constructs including molecular weight (MW) and molar extinction coefficient (ε_{280}), assuming all Cys residues are reduced except in case of TGT$^{C158S/C281S/Y330C/H333A}$. MW and ε_{280} were calculated using *ProtParam*.[177]

Construct	**with Strep-tag® II**		**without Strep-tag® II**	
	MW [Da]	$\boldsymbol{\varepsilon_{280}}$ [L mol^{-1} cm^{-1}]	**MW** [Da]	$\boldsymbol{\varepsilon_{280}}$ [L mol^{-1} cm^{-1}]
WT TGT	45181.3	39420	43013.8	33920
TGT$^{G87R1/C158S/C281S}$	45379.5	39420	43212.1	33920
TGT$^{C158S/C281S/H319R1}$	45299.4	39420	43132.0	33920
TGT$^{C158S/C281S}$	45149.1	39420	42981.7	33920
TGT$^{C158S/C281S/Y330C/H333A}$	45023.0	38180	42855.6	32680
TGT^{Y330D}	45133.2	37930	42965.7	32430
TGT^{H333A}	45115.2	39420	42947.8	33920
TGT^{H333D}	45159.2	39420	42991.8	33920

Materials

The following section summarizes the used materials including their respective vendors. Devices and instruments are listed in Table S2 and chemicals are listed in Table S3.

Table S2: List of used devices and instruments.

Device / instrument type	Designation	Vendor
Autoclave	FVA/2	Fedegari
Biological safety cabinet	HERAsafe™ KS15	Thermo Scientific
Block heater	TCR 100	Carl Roth
Block heater	Thermomixer® comfort	Eppendorf
Calorimeter	MicroCal™ iTC$_{200}$	GE Healthcare
Cell strainer	100 µm Cell Strainer	Corning
Centrifugal concentrator	Vivaspin® 6 30 000 MWCO	Sartorius
Centrifugal concentrator	Vivaspin® 20 30 000 MWCO	Sartorius
Centrifuge	Avanti™ J-25	Beckman Coulter
Centrifuge	Centrifuge 5810 R	Eppendorf
Centrifuge	Multifuge® 3S-R	Heraeus
Column	illustra™ NAP™-25	GE Healthcare
Column	PD-10	GE Healthcare
Column	Q Sepharose® Fast Flow	GE Healthcare
Column	Strep-Tactin® Superflow®	IBA Lifesciences
Column	Strep-Tactin®XT	IBA Lifesciences
Column	Superdex™ 200 10/300 GL	GE Healthcare
Diaphragm vacuum pump	LABOPORT® N 811 KN.18	KNF
Drying cabinet	UF160	Memmert
Electrophoresis module	Mini-PROTEAN® Tetra Cell	Bio-Rad
EPR spectrometer	ELEXSYS E 580	Bruker
Fixed-angle rotor	JA-10	Beckman Coulter
Fixed-angle rotor	JA-25.50	Beckman Coulter
FPLC system	ÄKTAprime™ plus	GE Healthcare
Flow cytometer	Guava® easyCyte 5	Merck Millipore
Gel documentation system	ChemiDoc™ Imaging System	Bio-Rad
Gel documentation system	FastGene® B/G GelPic Box	NIPPON Genetics
Helium flow cryostat	CF935	Oxford Instruments

Device / instrument type	**Designation**	**Vendor**
Image plate detector	mar345	marXperts
Incubator shaker	Innova™ 4200	New Brunswick Scientific
Incubator shaker	Innova™ 4230	New Brunswick Scientific
Incubator shaker	Innova® 43	New Brunswick Scientific
Liquid scintillation analyzer	Tri-Carb® 2810	PerkinElmer
Magnetic stirrer	Hei-Standard	Heidolph
Magnetic stirrer	RH basic 2	IKA
Microbalance	CP2P	Sartorius
Microscope	SZ60	Olympus
Microcentrifuge	Sigma 1-14K	Sigma
Microplate shaker	TiMix Control TH 15	Edmund Bühler
Mini centrifuge	IKA® mini G	IKA
Mini centrifuge	ROTILABO®	Carl Roth
Mini incubator	I5110-230V	Labnet
MST capillaries	Monolith NT.115 Premium Capillaries	NanoTemper Technologies
MST instrument	Monolith NT.115	NanoTemper Technologies
NMR spectrometer	AVANCE™ III 500 MHz	Bruker
Peristaltic pump	Pump P-1	Pharmacia
pH meter	913 pH Meter	Metrohm
Pipetting aid	pipetus®	Hirschmann
Platform shaker	Polymax 1040	Heidolph
Plate reader	Spark® 20M	Tecan
Real-time PCR system	QuantStudio™ 3	Applied Biosystems
Scale	PCB	Kern
Scale	SBC 32	SCALTEC
Scale	SBC 62	SCALTEC
Scale	Type 404/13	SAUTER
Sonicator	Sonifier™ 250	Branson
Spectrophotometer	NanoDrop™ 2000c	Thermo Scientific
Thermal cycler	MiniCycler™ PTC-150	MJ Research
Thermal shift fluorometer	Tycho NT.6	NanoTemper Technologies
Thermal shift capillaries	Tycho NT.6 Capillaries	NanoTemper Technologies
Ultrasonic cleaning unit	Transsonic T310	Elma
Vacuum filter unit	Nalgene™ Rapid-Flow™	Thermo Scientific
Water purification system	PURELAB® 2	ELGA
24-well crystallization plate	VDX™ Plate	Hampton Research
96-well plate	MicroAmp™	Applied Biosystems
96-well plate	Nunc™ F96 MicroWell™	Thermo Scientific
X-ray source	IμS	Incoatec

Table S3: List of used chemicals.

Chemical name	**Vendor**
Accutase®	Gibco
Acetic acid	Carl Roth
Acrylamide, ROTIPHORESE®	Carl Roth
Agar-agar	Carl Roth
Ammonium sulfate	Carl Roth
Ampicillin sodium salt	Carl Roth
D-Biotin	IBA Lifesciences
Biotinylated thrombin	Merck Millipore
Bovine Serum Albumine (BSA)	Sigma Aldrich
Chloramphenicol	Carl Roth
Chloroform	Merck Millipore
cOmplete™ Protease Inhibitor Cocktail Tablet	Roche
Congo red (C.I. 22120)	Carl Roth
Deuterium oxide	Sigma Aldrich
D-Desthiobiotin	IBA Lifesciences
Dimethyl sulfoxide (DMSO)	Carl Roth
Dimethyl sulfoxide-d_8 (DMSO-d_8))	Sigma Aldrich
Dithiothreitol (DTT)	Carl Roth
EDTA disodium salt dihydrate (Titriplex® III)	Merck Millipore
Ethanol	Carl Roth
Fetal Calf Serum (FCS)	Gibco
Fragments used in Chapter 3	Enamine / Molport
Gentamicin sulfate	Carl Roth
GlutaMAX™	Gibco
Glycerol	Carl Roth
Glycerol-d_8	Sigma Aldrich
Guanine [8-^{3}H]	American Radiolabeled Chemicals
HEPES, PUFFERAN®	Carl Roth
Hydrochloric acid	Fisher Scientific
2-(4-Hydroxybenzoyl)benzoic acid (HABA)	Sigma Aldrich
Lithium sulfate monohydrate	Merck Millipore
Magnesium chloride hexahydrate	Carl Roth
Magnesium formate dihydrate	Carl Roth
MES, PUFFERAN®	Carl Roth
Methanol	Fisher Scientific
Minimum Essential Medium (MEM)	Gibco
MTSSL (MTSL)	Biomol
Phenol	Merck Millipore
Phosphate-Buffered Saline (PBS)	Gibco

Chemical name	**Vendor**
Polyethylene glycol 6000	Carl Roth
Polyethylene glycol 8000	Carl Roth
Potassium chloride	Carl Roth
Roswell Park Memorial Institute (RPMI) 1640 Medium	Gibco
Sodium acetate trihydrate	Carl Roth
Sodium chloride	Fisher Scientific
tri-Sodium citrate dihydrate	Carl Roth
Sodium deoxycholate	Sigma Aldrich
Sodium dihydrogen phosphate dihydrate	Carl Roth
Sodium dodecyl sulfate (SDS)	Sigma Aldrich
di-Sodium hydrogen phosphate heptahydrate	Carl Roth
Sodium hydroxide	Fisher Scientific
Sodium pyruvate	Sigma Aldrich
Spermidine	Carl Roth
Strep-Tactin®-HRP	IBA Lifesciences
Sucrose	Carl Roth
SYPRO™ Orange Protein Gel Stain	Invitrogen
TES, PUFFERAN®	Carl Roth
D(+)-Trehalose	Carl Roth
3-(Trifluoromethyl)benzylamine	Sigma Aldrich
TRIS, PUFFERAN®	Carl Roth
Tris(2-carboxyethyl)phosphine (TCEP)	Carl Roth
Triton® X-100	Carl Roth
Tryptic soy broth	BD
Tryptone/peptone	Carl Roth
Tween® 20	Carl Roth
Urea	Carl Roth
Yeast extract	Carl Roth

An den
Vorsitzenden des Promotionsausschusses
des Fachbereichs Pharmazie
Philipps-Universität Marburg
Marbacher Weg 6–10
D-35032 Marburg

Erklärung

gemäß § 10 Abs. 1 der Promotionsordnung der Mathematisch-Naturwissenschaftlichen Fachbereiche und des Medizinischen Fachbereichs für seine mathematisch-naturwissenschaftlichen Fächer der Philipps-Universität Marburg vom 08. Dezember 2010

Ich versichere, dass ich die vorgelegte Dissertation mit dem Titel

From Serendipity to the Rational Design of Protein–Protein Interface Modulators Targeting a tRNA-Modifying Enzyme

selbstständig und ohne fremde Hilfe angefertigt und mich dabei keiner anderen als der von mir ausdrücklich bezeichneten Quellen oder Hilfsmittel bedient habe. Alle vollständig oder sinngemäß übernommenen Zitate sind als solche gekennzeichnet. Die Dissertation wurde in der vorliegenden oder einer ähnlichen Form noch bei keiner anderen in- oder ausländischen Hochschule anlässlich eines Promotionsgesuchs oder zu anderen Prüfungszwecken eingereicht.

Marburg, den 27. November 2020

Dzung Nguyen

Dzung Nguyen